Micromachined Integrated Transducers for Ultrasound Imaging

la Cour, Mette Funding; Jensen, Jørgen Arendt; Thomsen, Erik Vilain

Publication date:
2014

Document Version
Publisher's PDF, also known as Version of record

Citation (APA):
la Cour, M. F., Jensen, J. A., & Thomsen, E. V. (2014). Micromachined Integrated Transducers for Ultrasound Imaging. Technical University of Denmark (DTU).

Technical University of Denmark

Micromachined Integrated Transducers for Ultrasound Imaging

PhD Thesis

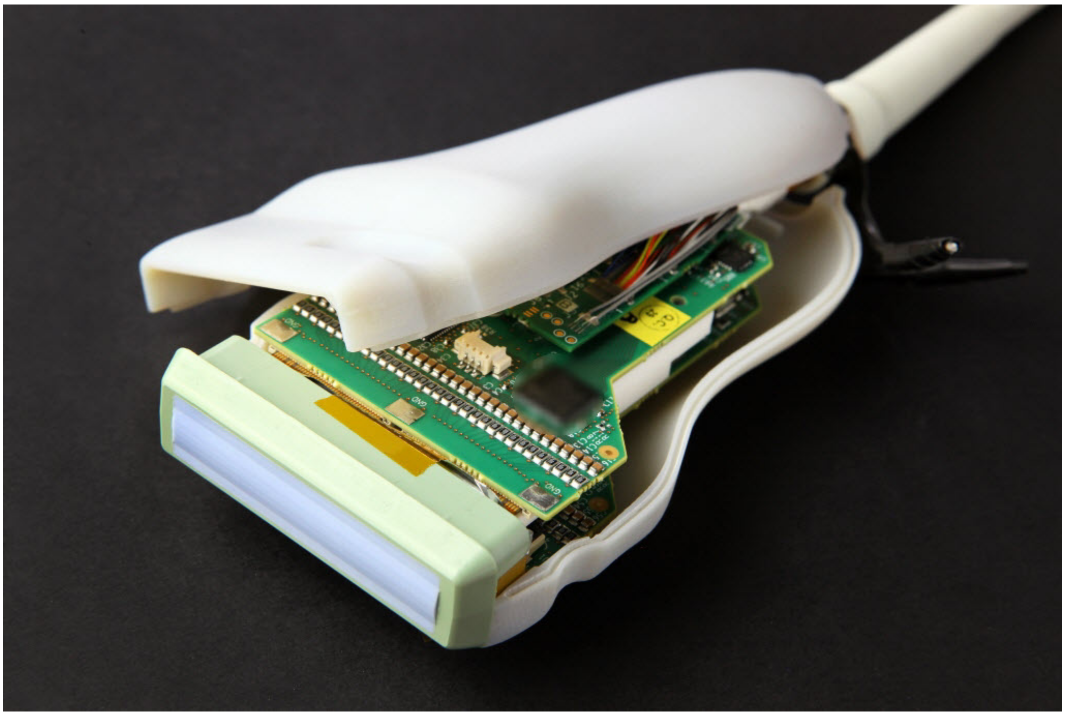

Mette Funding la Cour
September 2014

Supervisors:
Jørgen Arendt Jensen & Erik Vilain Thomsen

DTU Electrical Engineering
Department of Electrical Engineering

DTU Nanotech
Department of Micro- and Nanotechnology

Technical University of Denmark
Department of Electical Engineering
DK-2800 Kgs. Lyngby
Denmark

Submitted in partial fulfillment of the requirements for the degree of Doctor of Philosophy at Technical University of Denmark.

Preface

This PhD dissertation has been submitted to the Technical University of Denmark, in partial fulfillment of the requirements for the degree of Doctor of Philosophy. The work has been supervised by Professor Dr.Techn. Jørgen Arendt Jensen and Professor Erik Vilain Thomsen.

This dissertation consists of a recapitulation of the research work carried out from September 2011 to September 2014 at the Center for Fast Ultrasound Imaging at DTU Electrical Engineering and at DTU Nanotech, Technical University of Denmark. During my work I also had the opportunity to work with professor B. (Pierre) T. Khuri-Yakub at Stanford University for one year which gave me a lot of valuable knowledge for my research. The work both at DTU and Stanford has provided me with the opportunity to explore the field of capacitive micromachined transducers for medical imaging in depth. The work has been challenging and developed my engineering skills to a new level.

The project has furthermore been conducted in close collaboration with BK Medical and Sound Technology Inc. without whom the acoustical testing of the fabricated ultrasonic transducers would not have been possible to raise to the same high level during the three years.

Mette Funding la Cour,
September 2014

Acknowledgement

First of all I would like to thank my supervisors, Jørgen Arendt Jensen and Erik Vilain Thomsen for their guidance throughout this project and for giving me the opportunity and chance to work with both microfabrication and ultrasound imaging on world-class levels. Thank you for showing great enthusiasm in driving my research forward and providing both a focused and optimistic view on thing, creating a very special atmosphere.

A special thanks also goes to B. (Pierre) T. Khuri-Yakub at Stanford University for letting me visit the CMUT group and learn from their experience through 20 years of work within the CMUT field. It has been very important for taking my project as far as it has come within just three years and it has been an honor working with you.

I would like to thankfully mention my colleagues on the CMUT team, Thomas Lehrmann Christiansen, Anders Lei, and Matthias Bo Stuart, for invaluable help and discussions, it would not have been the same without you. I would also like to thank my former master students Martin U. Grønbech and Mads B. Laursen for their contributions to the project and especially Søren Elmin Diederichsen for the huge effort put into the fabrication and development of the TABLA probes. Likewise, I would like to thank all the students who contributed through bachelor projects, physics projects, special projects, and three-week projects. They have all made valuable contributions to the CMUT project in many different ways.

Thanks to our collaborators at BK Medical for designing electronics to operate our devices both in the evaluation test setup and the prototype probe. We could not have fully utilize the potential of the transducer arrays without you. A very special thanks also goes to STI, and especially Christopher Beers, for packaging and assembly of the prototype TABLA probe.

Furthermore, I would like to thank all my former and current colleagues and friends at CFU, Nanotech and Stanford for discussions, inputs, talks, good spirit, and a lot of awesome and unforgettable times! You all gave me a memory for life, and I hope we will continue our friendship for many years.

Last, but definitely not least, I would like to express my sincerest thanks to my family and especially my fiancé Christian Hjortholm Steffensen, who have supported me throughout the project. Thanks for understanding my high commitment and engagement to the project.

Abstract

The purpose of this project is to develop capacitive micromachined ultrasonic transducers (CMUTs) for medical imaging. Medical ultrasound transducers used today are fabricated using piezoelectric materials and bulk processing. To fabricate transducers capable of delivering a higher imaging resolution it is however necessary to develop new fabrication methods that allows fabrication of transducer elements with smaller dimensions. By using microfabrication technology it is possible to push the dimensions down and provide higher design flexibility.

This project is part of a large ultrasound project and collaboration with a lot of partners to improve medical ultrasound imaging. The focus in this part of the project is to design, fabricate and characterize 1D CMUT arrays. Two versions of 1D transducers are made, one at Stanford University and one at DTU. Electrical and acoustical characterizations are carried out successfully for both types of arrays. The arrays made at Stanford is found to suffer from low breakdown voltage of the supporting oxide and was not useful for medical imaging.

The arrays made at DTU are used for various tests, both of the design, performance, possible packaging, and post-processing. The electrical characterization shows serious charging effects in the device which is shown to be reduced by reversing the bias polarity. Furthermore, the wirebonding and glob top packaging scheme shows to cause loose connection for several elements. This is still under investigation, but two possible solutions are suggested. Two devices are assembled into probe handles and initial acoustical characterizations are promising. Even though the sensitivity is currently low, images are produced with recognizable features both on phantoms and volunteers. It can be mentioned that a -6 dB fractional bandwidth of 100-110 % is measured.

Resumé

Formålet med dette project er at udvikle kapacitive mikrofremstillede ultraslydstransducere (CMUTs) til medicinsk billeddannelse. Transducere til medicinsk billeddannelse bliver i dag fremstillet i piezoelektriske materialer med konventionelle processeringsmetoder. For at fremstille transducere, der kan levere billeder med høj opløsning, er det imidlertid nødvendigt at udvikle nye fabrikationsmetoder, som gør det muligt at fremstille transducerelementer med mindre dimensioner. Ved at anvende mikrofabrikationsteknologi vil det være muligt at mindske dimensionerne og samtidig give en højere designfleksibilitet.

Dette projekt er del af et stort ultralydsprojekt, som er et samarbejde mellem mange partnere, og som søger at forbedre medicinsk billeddannelse. Fokusområdet i denne del af projektet er at designe, fremstille og karakterisere 1D CMUT arrays. To versioner er fremstillet, en på Stanford University og en på DTU. Elektrisk karakterisering er udført successfuldt for begge typer af arrays. Transducerne fremstillet på Stanford viste sig at have en lav sammenbrudsspænding af support oxiden, og de var ikke brugbare til billeddannelse.

Transducerne fremstillet på DTU er blevet anvendt til en række test, både for at undersøge designet, ydeevnen, mulige indpakningsmetoder og andet efterprocessering. Elektrisk karakterisering viser seriøse opladningseffekter, men også at dissee kan reduceres ved at vende polariteten af bias spændingen om. Derudover ses der problemer med wirebonding og glob top løsningen, da den resulterer i løse forbindelser til mange elementer. Der arbejdes stadig på en endelig løsning til dette problem, men to muligheder er testet og fundet brugbare. To CMUT'er er monteret i probehåndtag, og de første målinger viser lovende resultater. Selvom sensitiviteten på nuværende tidspunkt er lav, kan der stadig fremstilles billeder med genkendelige features både på fantomer og testpersoner. Det kan nævnes, at en -6 dB relativ båndbredde på $100-110$ % er blevet målt.

Contents

CHAPTER 1

Introduction

Capacitive micromachined ultrasonic transducers (CMUTs) offer the possibility for replacing standard piezoelectric transducers used for medical imaging. CMUTs are said to have superior properties such as larger bandwidth, more design flexibility, easy integration, being lead-free etc. [1–3]. They have existed for 20 years now - so why have they not overtaken the commercial ultrasonic probe market yet? During this project a basic knowledge and understanding of the CMUT device has been obtained and transducers have been fabricated and mounted into both test setups and probe handles to understand, as well as give solutions to, the challenges with this alternative to the standard piezoelectric transducers.

Ultrasound was first used for medical imaging in the 1950s [4]. Back then, the patient was submerged into a water bath for making the images. Now, specially made transducer probes are produced and pressed against the patients skin to produce images. The CMUT technology has the possibility to improve the transducer performance and expand the production of probes for specific applications. The conventional transducers as well as the CMUTs will be discussed in the following to show how the CMUTs may raise the quality of transducers.

Beside medical imaging, CMUTs can be used for a wide range of applications such as therapeutic treatment [5], gas flow metering and air coupled ultrasound [6] and as chemical sensors [7]. Across the application, the technology is based on a resonator, which can either transmit or receive ultrasound. They are all based on the same types of devices which can be also be used for medical imaging, where the transducer needs to be able to both transmit and receive ultrasound waves. This project focuses only on the medical imaging application, and how devices can be fabricated to be optimal for use in this field.

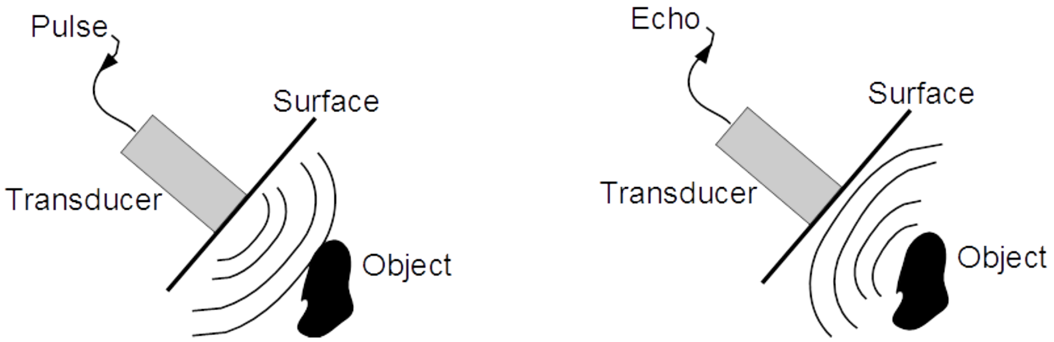

(a) *Generating the ultrasound pulse.*

(b) *Receiving the echo.*

Figure 1.1: *Principle of ultrasound imaging. a) An ultrasound wave is transmitted from a transducer into an object. Depending on the structure and density of the object the signal will be reflected differently, and b) received by the transducer again.*

1.1 Ultrasound

Sound is motion or vibration of particles which propagates as longitudinal waves. Ultrasound is defined as sound waves with a frequency above what the human ear can detect e.g. above 20 kHz. The usual range for ultrasound waves used for medical imaging is 1-20 MHz, and ultrasound transducers for this purpose should therefore be designed to have a resonant frequency within this range for optimal operation.

The principle of ultrasound imaging is to excite the transducer at its resonant frequency to create ultrasound waves or pulses which propagates through the medium in front of the transducer, see Figure 1.1a. Different tissue material then reflects the waves differently as a result of the density of the medium. For example water does not reflect the sound waves, whereas bone reflects them completely. The acoustical impedance of a medium indicates how much pressure is generated at a given frequency. All materials have a characteristic acoustic impedance, Z_{ac}, which is given by

$$Z_{\text{ac}} = \rho c \tag{1.1}$$

where ρ is the density of the medium, and c is the speed of sound in the medium. Examples of different acoustical impedances relevant to medical imaging can be seen in Table 1.1. When the signal is reflected on an object, the wave will travel back to the transducer again and the received signal is called an echo, see Figure 1.1b. An image is created by having multiple transducer elements next to each other which can be addressed and excited separately. By using time delays for the transmissions and observing the received signals and their arrival times, it is possible to beamform an ultrasound image. An example of an ultrasound image can be seen in Figure 1.2, showing a liver.

1.2 Transducers

A transducer is a device which converts one form of energy into an other. In ultrasound imaging, a transducer is used to convert electrical energy to mechanical energy to acoustical energy when transmitting

Table 1.1: *Examples on density, speed of sound and characteristic acoustical impedance for various mediums in the body, air and water [8]. It is noted that water and tissue have similar properties.*

	Density [kg/m^3]	**Speed of sound** [m/s]	**Characteristic acoustic impedance** [kg/(m^2·s)]
Air	1.2	333	0.4×10^3
Blood	1.06×10^3	1575	1.66×10^6
Bone	1.9×10^3	4080	7.75×10^6
Fat	0.92×10^3	1450	1.38×10^6
Liver	1.06×10^3	1590	1.69×10^6
Water	1.00×10^3	1480	1.48×10^6

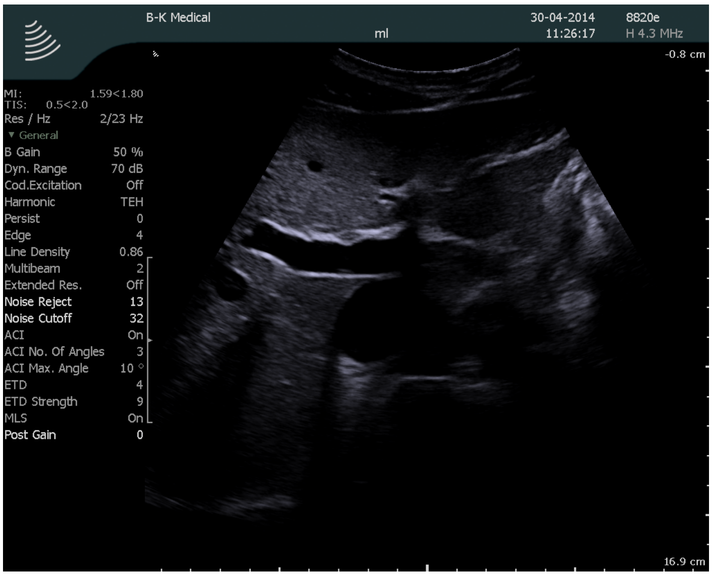

```
MI:              1.59<1.80
TIS:     0.5<2.0
Res / Hz            2/23 Hz
▼ General
B Gain                 50 %
Dyn. Range            70 dB
Cod.Excitation          Off
Harmonic                TEH
Persist                   0
Edge                      4
Line Density           0.86
Multibeam                 2
Extended Res.           Off
Noise Reject             13
Noise Cutoff             32
ACI                      On
ACI No. Of Angles         3
ACI Max. Angle         10 °
ETD                       4
ETD Strength              9
MLS                      On
Post Gain                 0
```

Figure 1.2: *Ultrasound image of a liver. The image is of a healthy volunteer and recorded at Center for Fast Ultrasound Imaging using a BK Medical scanner.*

ultrasound. The opposite order of conversions are happening when receiving the ultrasound.

As mentioned earlier different ways to transmit ultrasound waves exists. The conventional way which is used in most commercial scanners today is using the piezoelectric effect and is illustrated in Figure 1.3a. When a voltage is applied to a piezoelectric material, the material will deform. If an AC voltage in the MHz range is used, an ultrasound wave will be transmitted.

The alternative to this technique is based on a capacitive method and is illustrated in Figure 1.3b. When an AC voltage is applied to two plates with some insulation in between (a capacitor), the movable top plate will deflect and ultrasound waves will be transmitted. Only one of the plates should be able to move, so the bottom plate is usually thick and the top plate thin so it is flexible.

For making an ultrasound image with both kinds of transducers several elements are placed next to each other forming an array. This is illustrated in Figure 1.4 for both types of transducers.

An array for imaging typically consists of 128 or 192 elements. The length of an element is dependent on how deep the ultrasound beam should be focused. The width of the elements is decided from the desired operation frequency. There are two types of arrays that are usually used for imaging: linear and phased arrays. For a linear array a group of elements is active simultaneously and an image is formed as straight lines from each element in the array, see Figure 1.5. For a phased array all elements are active simultaneously and the beam is steered electronically to form a fan shaped image, see Figure 1.6. Linear array imaging usually use an element pitch of the wavelength, λ, and phased array imaging requires an element pitch of half the wavelength, $\lambda/2$. The wavelength is found from the speed of sound, c, and the frequency, f, as

$$\lambda = c/f. \tag{1.2}$$

As an example operating at 5 MHz and using the speed of sound in tissue or water of around 1500 m/s, the pitch for a linear array should be 300 µm and for a phased array it should be 150 µm. Piezoelectric transducers are usually diced into elements by a saw and these dimensions can be really challenging to make using this technique. This is one of the reasons microfabrication can be an advantage.

The operating frequency used for ultrasound imaging determines the resolution and the depth of penetration that can be obtained, and it is a trade off situation. Higher frequency results in a higher resolution but the ultrasound is reflected and absorbed faster. Using a lower frequency on the other hand, a higher penetration can be obtained at the cost of reducing the resolution.

When using the transducer array in a commercial setting, it is contained in a probe handle with some electronics. This is both to shield the electronics from noise and to protect the patient and operator. A sketch of an array in a probe handle, a transducer probe, can be seen in Figure 1.7.

1.2.1 Transducer Comparison

CMUTs are usually made in a cleanroom with standard silicon fabrication techniques. This is an advantage compared to the piezoelectric transducers usually made of PZT. Besides being lead-free, the cleanroom fabrication technology also provides more design flexibility, as the device is built up of layer which is patterned on the surface using light. A 3D structure can then be obtained by etching the different layers. This way it is possible to make any desirable design as long as it can be drawn in a 2D

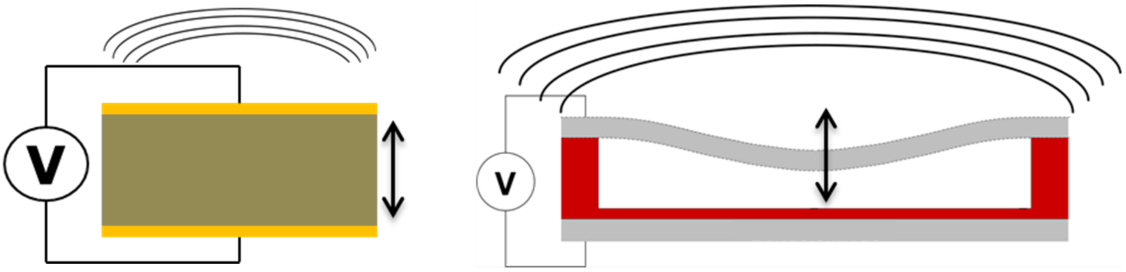

(a) *Piezoelectric transducer.* (b) *Capacitive transducer.*

Figure 1.3: *Principle of ultrasound generation for a) piezoelectric and b) capacitive transducers. For both types an AC voltage is applied which makes the bulk or the flexible top plate vibrate, respectively.*

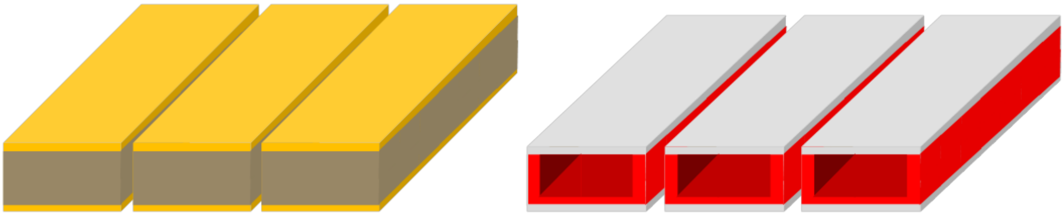

Figure 1.4: *Illustration of 1D array elements for piezoelectric transducers (left) and CMUTs (right). Several elements are placed next to each other in close distance to maximize the active area.*

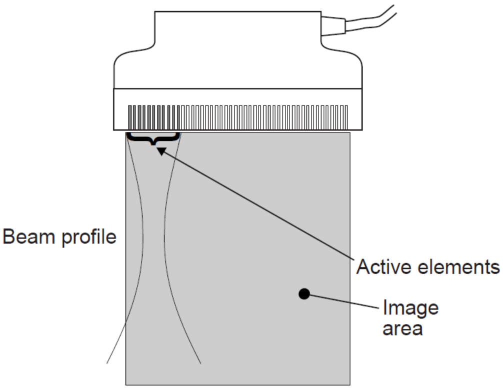

Figure 1.5: *Linear array imaging: a group of active elements at the time to form straight image lines.* [9]

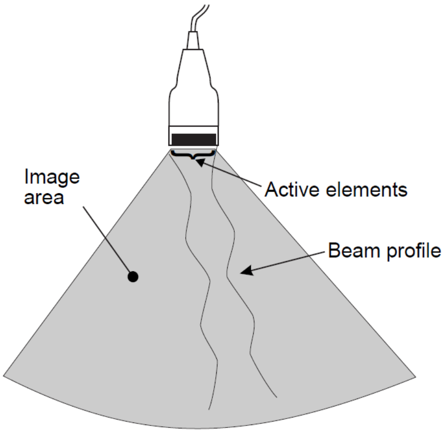

Figure 1.6: *Phased array imaging: all elements active and electronically steered to form a fan shaped image.* [9]

drawing program. The piezoelectric transducers on the other hand is made from a crystal rod which is diced out using a saw. This makes it very cumbersome to make curved structures and furthermore limits the smallest feature size due to aspect ratio of the elements after dicing and width of the blade which limits the smallest possible kerf between elements.

The resonant frequency for the two types of transducers is adjusted to the desired value with different methods. For piezoelectric transducers it is determined from the thickness of the element and for CMUTs it is determined from the radius, stiffness and thickness of the capacitor top plate. To obtain a higher resolution in the ultrasound images a higher frequency is necessary. A higher frequency means smaller elements which can be a challenge to make with the piezoelectric transducer fabrication method, however, for the CMUT the width of the structure is limited only by the wavelength of the light used for patterning the layers and much smaller structures can be obtained.

The CMUT is chosen for the transducers in this project due to the high design flexibility and the large bandwidth which can open up for possible optimization of the transducer itself for more advanced imaging methods.

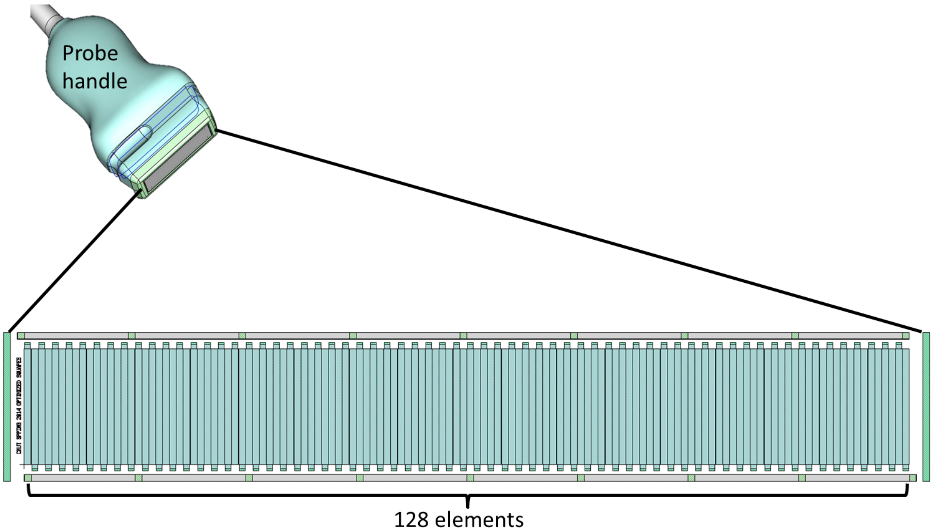

Figure 1.7: *Illustration of a 128 element 1D array in a probe handle. A zoom on the array is seen, in this case a CMUT array.*

1.2.2 CMUT Fabrication

Fabrication of CMUTs can be based on two different fabrication principles: sacrificial release or fusion bonding. Several versions of these processes have been proposed during the years and these will be commented on in section 1.3. Here, the basics of each type of process will be explained together with argumentation for the choice of process in this project. A sketch of a CMUT made with sacrificial release (a) and fusion bonding (b) fabrication processes can be seen in Figure 1.8.

The sacrificial release method, shown in (a), is basically deposition of an insulation layer, a sacrificial layer and another insulation layer followed by etching of the sacrificial layer to form the cavity [10, 11]. An electrode is then made on top of the suspended plate. A huge disadvantage with this process is that the plate will have a high built-in stress after end of fabrication which will affect the bending and

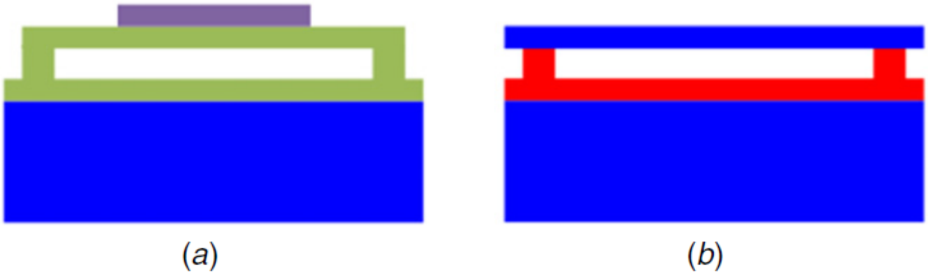

Figure 1.8: *Two basic processes used for fabricating CMUTs [3]. a) Illustrates the sacrificial release process with blue being the bottom silicon electrode, green being the silicon nitride insulation layer and plate, and purple the metal layer for the top electrode. b) Illustrates the fusion bonding process with blue being the silicon bottom electrode and top plate/electrode, and red being the silicon oxide support post and insulation layer.*

vibration in ways that are harder to calculate. Furthermore as the layers are grown or deposited slowly, it limits the reachable thickness of the plate and gap and also etching the sacrificial layer through etching holes can be a challenge.

The simplest possible fusion bonding process, shown in (b), is basically a substrate wafer with an insulation layer, an etched vacuum gap, and then a silicon-on-insulator (SOI) wafer fusion bonded to the supporting posts [12]. Most of the SOI wafer is then etched away to form the plate. With this process it should be easier to control the vertical thickness as fewer layers are required, however, the uniformity of the SOI wafers are not always good which can be a disadvantage. The best uniformity obtained from SOI wafer manufacturers are ± 0.3 μm, which is quite a lot when the plate thickness is in the order of $0.5-5$ μm. Another challenge is the fusion bonding itself which is not a very standard cleanroom fabrication process and requires an extremely flat and clean surface.

In this project it was chosen to use the simplest possible fusion bonding method as a start. The reason is that it was of higher priority to obtain good working devices than to optimize the structure itself with the risk of low yield or unsuccessful processing. Furthermore, the group at DTU Nanotech already had experience in fusion bonding and a process that only needed slight modifications to work for imaging CMUTs already existed.

1.2.3 The CMUT Device

The basic CMUT structure is shown in Figure 1.3b. A more detailed cross section of a CMUT including definition of expressions for the different parts can be found in Figure 1.9. Basically the CMUT consists of a fixed bottom electrode, a flexible top electrode (or plate), a vacuum gap between the electrodes and an insulator called the support post to separate the electrodes. An insulation layer inside the cavity is also needed to avoid leak currents and short circuiting.

For an illustration of definition of device parameters, see Figure 1.10. The plate can be both circular with radius a or square shaped with side length $2L$. The deflection in the center of the plate is called w_0. The plate thickness is h, the vacuum gap g and the insulation layer thickness t_{ox}. An external circuit is used to drive the CMUT which consists of both a DC voltage to pre-deflect the plate for higher

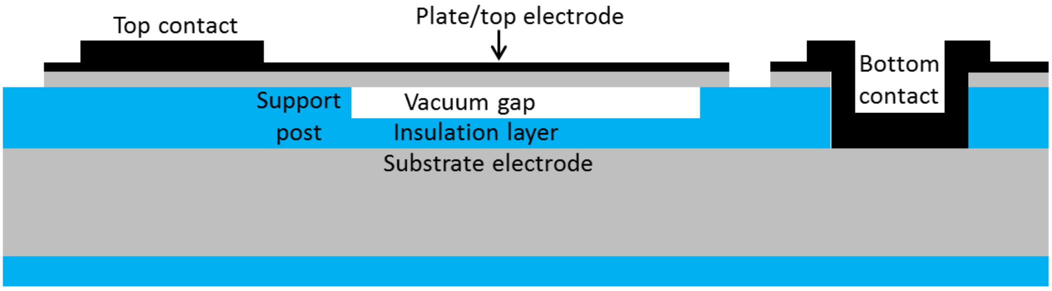

Figure 1.9: *CMUT cross section with device parts illustrated. The CMUT consists of a metilized flexible plate over a vacuum cavity, an insulation layer and a fixed bottom electrode. The supporting insulator is called a post or simply support. The access to the top and bottom electrodes of the capacitor is called top and bottom contacts.*

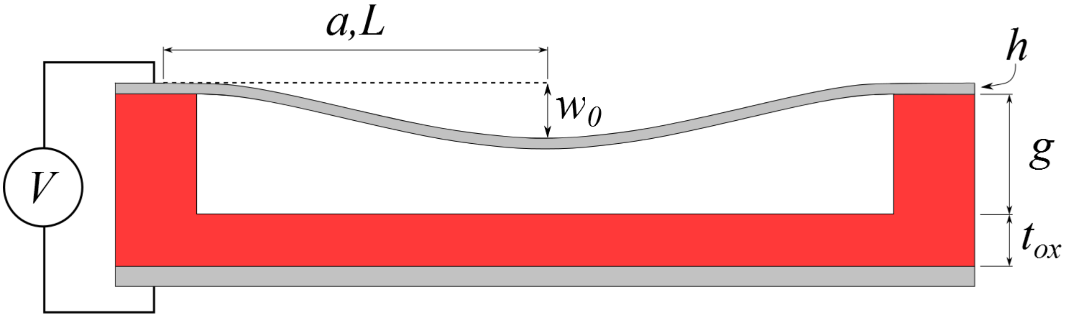

Figure 1.10: *CMUT cross section with device dimensions illustrated. For a square cell half the side length is called L and for a circular cell the radius is called a. The plate thickness is h, the vacuum gap height g and the insulation layer thickness* t_{ox}. *When a voltage V is applied, the plate deflects* w_0 *in the center.*

sensitivity and an AC voltage for generating the ultrasound waves. The most important parameters for the CMUT is its resonant frequency, bandwidth, and pull-in voltage and these are determined by the dimensions of the device. The resonant frequency, f_0, is found from the radius, a, for a circular plate or the sidelength, $2L$, for a square plate and the thickness of the plate, h and scales as

$$f_0 \propto h/a^2. \tag{1.3}$$

The bandwidth, BW, is dependent on the damping, mass and resonant frequency of the CMUT and scales with the thickness of the plate as

$$BW = b/(\omega_0 m) \propto 1/h^2, \tag{1.4}$$

where b is the damping, ω_0 is the angular resonant frequency and m is the mass. From this equation the difference in bandwidth for piezoelectric transducers and CMUTs can be seen. The damping and the resonant frequency are identical for the two, however, the mass of the CMUT is much lower than the mass of a piezo-rod which will result in the larger fractional bandwidth for CMUTs.

Pull-in voltage, V_{PI}, is the applied voltage where the plate is deflected so much that the restoring spring forces cannot balance the attractive electrostatic force anymore. The plate will snap down to the bottom of the cavity. For the conventional mode of operation, this therefore defines the maximum operating voltage, and it scales with gap height, plate thickness, and radius/sidelength as

$$V_{\mathrm{PI}} \propto g^3 h^3 / a^4. \tag{1.5}$$

When increasing the bias voltage the plate will deflect towards to bottom electrode and the higher the bias the softer the plate will be as the effective stiffness is reduced. The electromechanical coupling efficiency increases with bias voltage and approaches unity at the pull-in voltage. This means increased performance the closer to the pull-in the device is operated. The principle of pull-in and pull-out, which happens when lowering the bias again, is illustrated in Figure 1.11.

Examples of dimensions of a CMUT and the resulting resonant frequency and pull-in voltage can be seen in Table 1.2. The fractional bandwidth for CMUTs is usually in the order of 100 % [1, 14].

Using (1.3)-(1.5) as design guidelines, CMUTs with the desired parameters can be produced. Later chapters will go into the specific design and fabrication of the CMUTs in this project.

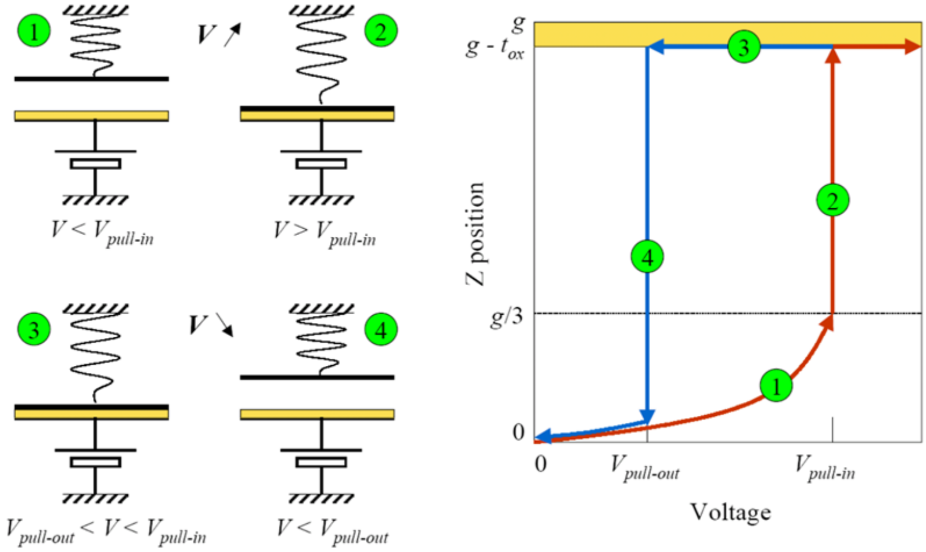

Figure 1.11: *Principle of pull-in and pull-out. In the first phase (1) when increasing the applied voltage the plate moved closer to the other plate, in (2) it reaches the pull-in voltage and the plate snaps down and touches the other plate. Lowering the voltage again the plates are stuck together (3) until the snap back voltage, which is usually lower than the pull-in voltage, is reaches in (4) and the flexible plate is released. Figure from [13]*

Table 1.2: *Example of device dimensions for a circular cell CMUT and the resulting calculated parameters. These are realistic values for CMUTs made for medical imaging.*

Parameter	**Value**
Radius	30 µm
Plate thickness	2 µm
Gap height	300 nm
Resonant frequency	8.4 MHz
Pull-in voltage	104 V

1.2.4 Operating the CMUT

In a real device, the CMUT does not only consist of one cell as the one shown in Figure 1.10. Multiple cells (in the order of 300-500) are placed in an element and connected in parallel to obtain a higher signal when operating at the frequencies used for ultrasound imaging. An illustration of this can be seen in Figure 1.12. Part of an array is shown with a zoom in on one end of two elements. The cells can be seen closely packed within each of the elements to maximize the active area. Each element ends in a contact going to the opposite sides for every second elements. A contact pad for contacting the elements seperately is also seen. Pitch and kerf of the device is furthermore illustrated.

When operating the CMUT in transmit a DC voltage is applied as well as an AC as mentioned earlier. This is to reduce the nonlinear effects. The applied AC voltage has the form $V = V' \sin(\omega t)$. In the theory chapter, it can be seen that the potential energy of the CMUT scales with the voltage squared and without the DC bias this results in

$$V^2 = V'^2 \sin^2(\omega t) = \frac{1}{2} V'^2 (1 - \cos(2\omega t)) \tag{1.6}$$

This way the emitted waves will have the double frequency. This can be avoided by having a DC bias which is significantly larger than the AC voltage such that

$$V^2 = (V_{\text{DC}} + V' \sin(\omega t))^2 = V_{\text{DC}}^2 + V'^2 \sin^2(\omega t) + 2V_{\text{DC}} V' \sin(\omega t), \tag{1.7}$$

and the second term on the right side will be neglectable. Using this operation conditions, the CMUT in transmit will look as sketched in Figure 1.13 with a DC and an AC voltage applied. In the receive

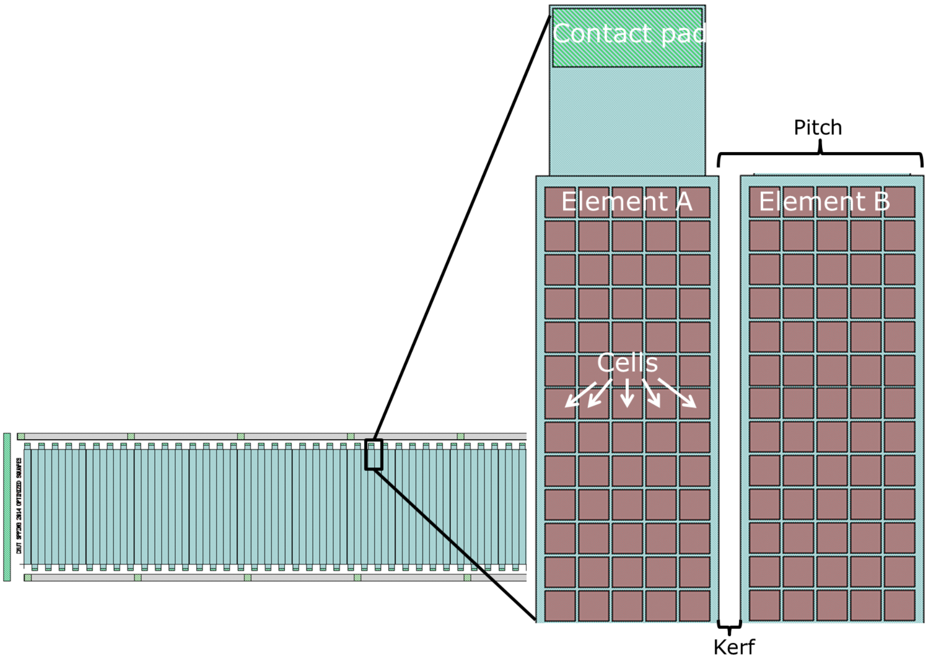

Figure 1.12: *Sketch of 1D CMUT array with a zoom in on two elements to show the cells and the contact pads. Furthermore, the pitch is defined as the distance between two elements and the kerf is defined as the spacing between two elements.*

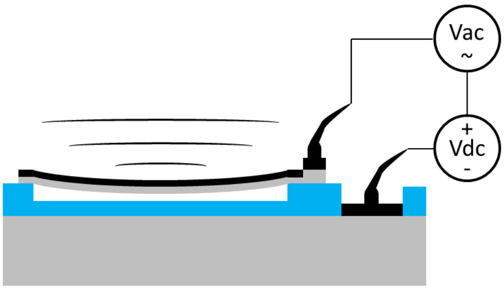

Figure 1.13: *A CMUT in transmit mode with a DC and an AC voltage applied to have the device bias when sending out a signal.*

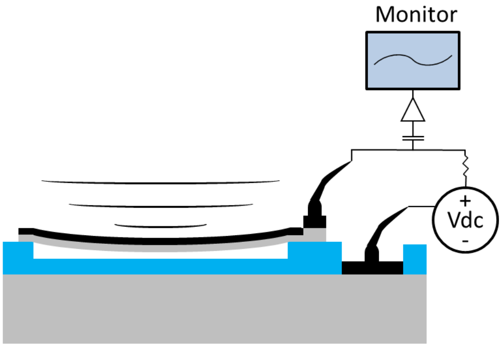

Figure 1.14: *A CMUT in receive mode with a DC applied to increase sensitivity and a monitor to shown the received AC signal.*

mode the situation will be as sketched in Figure 1.14, where the received signal can be collected and shown on a monitor instead of applying an AC signal.

1.3 Literature Review

This review will cover several areas of the CMUT technology. First of all the fabrication, going from the simple processes in the beginning and how CMUTs started through more advanced processes. Furthermore, a review of the theoretical work on CMUTs will also be given before focusing on 1D arrays and CMUTs used for medical imaging applications and probe assembly.

1.3.1 Fabrication

The first capacitive ultrasonic transducers were actually not fully micromachined. For example Schindel et al. [15] made a bottom plate with microfabricated cavities covered by a kapton or mylar film, however these devices are not possible to make vacuum sealed and the resonant frequency can be hard to control. Actual micromachined capacitive transducers (CMUTs) were developed at Stanford University who also holds the majority of publications within the field. Haller and Khuri-Yakub has the first paper in 1994 with a slightly extended version in 1996 [16, 17]. These first papers explain the principle of the micromachined transducer and show devices fabricated by use of sacrificial oxide etch to form the cavities.

The sacrificial release process has been developed a lot since the first processing, starting with Jin et al. in 1998 [10] who changed the sacrificial material to polysilicon for better cell size control (defined by lithography instead of timed etching and higher selectivity to the surrounding insulating silicon nitride layers) and possibility for vacuum sealing.

Many variation of the sacrificial release process has been proposed since, e.g. Caronti et al [11] who used chromium as sacrificial layer, Chen et al. [18] who used phosphosilicate glass (PSG) as sacrificial layer, and Noble et al. [19] who used polyimide as sacrificial layer. The important thing for all the sacrificial release processes is to have high selectivity between the sacrificial layer and the layer surrounding it.

More advances processes and designs have also been proposed, e.g. Cheng et al. [18] who made a miniature CMUT device for invasive imaging purpose by etching the device out from a wafer resulting in a very thin substrate and with the purpose of minimizing the trade off in penetration depth. Another example is the reverse fabrication process made by Caliano et al. [14] where the standard sacrificial release process is turned around so the first layer that is deposited is the plate and backing and protection of wire bonding interconnects can be included automatically.

In 2003 Huang et al. [12] developed a CMUT fabrication process based on fusion bonding. With this process it is possible to control the uniformity and variations in gab height much better as fewer layers of thinfilms are used and the plate is formed by the device layer of a Silicon-on-Insulator (SOI) wafer. Both the fusion bonding process and the sacrificial process is still used today.

A lot of variations has also been proposed for the fusion bonding process to optimise the device structure. Among these are Kupnik et al. in 2007 [20] who extended the insulation layer structure to improve limitations on electrical breakdown, parasitic charging effects, and gap height. Furthermore, it has been desired to make the electrical connection to the bottom electrode through backside of the device, especially for realizing 2D arrays. For this purpose processes was developed which incorporated through wafer vias (also optimized specifically for CMUT applications [21,22]). One of these processes are the thick burried oxide process from Kupnik et al. [23] where the structure is optimised to only have a high electrical field right under the movable plate and still have thickened supporting oxide posts. Another advantage with this process is increase patient safety as ground will be on the top electrode. The challenge with this process is to etch the vias through the thick burried oxide layer with the dimensions required for medical imaging purposes. Another example is the LOCOS process by Park et al. [24] where Local oxidation of silicon (LOCOS) is used to extend the oxide posts and still be able to perform fusion bonding without the need of chemical-mechanical polishing (CMP) (used in [20]). This process has successfully been used for fabricating 1D arrays, however, for 2D arrays it has been a challenge to incorporate the through wafer vias in the process while keeping high enough surface quality to perform fusion bonding. To avoid the through wafer vias and still be able to contact the elements from the backside Zhuang et al. [25] suggested an alternative process based on trench-isolated interconnects with a supporting frame. This process is however very challenging to complete with high yield.

There has also been several more creative suggestions to improve the CMUT structure. These include e.g. piston shaped membranes [26] with extra mass added to the plate to make the movement more piston like and get more power transmitted and substrate-embedded springs for non-flexural plate movement [27].

Almost at the same time as Stanford developed the first CMUTs, Eccardt et al. [28] made a CMUT in a CMOS process also with a sacrificial release process of oxide but without changing the layers of the CMOS. The CMUT-in-CMOS structure has the advantage of easy integration with electronics, however, other limitations such as optimising the CMUT structure itself may be the reason why this method for fabrication is not as widespread. An alternative has been proposed where the CMUT is fabricated as postprocessing of a CMOS wafer (CMUT-on-CMOS) to avoid the space limitations [29,30]. An other process for easing integration with electronics has also been proposed by Tsuji et al. [31] where a low-temperature wafer bonding process was realized by use of a Titanium adhesion layer.

Very alternative device structures has also been proposed. For example having one big plate in an element instead of multiple cells has been proven to work as well [19] (also a low temperature CMOS compatible process) or a split of transmit and receive to avoid the trade off between transmitted power and receive sensitivity by using a grating in the bottom of the cavity and optical read out instead of capacitive [32]. This device has to be made on a glass wafer substrate so it is possible to shine light through the backside. Using atomic layer deposition (ALD) for deposition of the different layers to better thickness and hence device parameter control has also been suggested [33].

Using both the sacrifical release process and the fusion bonding process it is also possible to make curved transducer arrays for convex array imaging [34, 35]. For this imaging method you use the same exitation scheme as for the linear arrays imaging pictured in Figure 1.5 but are able to scan a fan shaped area as for the phased array imaging method shown in Figure 1.6.

1.3.2 Theory

Precise modeling of CMUTs is important for an efficient design process. The deflection of the movable plate is an important parameter that influences several basic CMUT parameters such as pull-in voltage and capacitance. The first decade after CMUTs were invented, various analytical models were presented for circular cells, which included more and more features of the device behaviour [36–38]. However, all of them were based on parallel plate approximations for the deflection leading only to estimates of the critical CMUT parameters. Later, the actual deflection of the movable plate clamped at the edges was taken into account [39–41], where it was used for calculating pull-in voltage and expansions of equivalent circuit models. The effect from having a non-uniform load on the plate was included in solving the plate equation by [40] who used superposition and a concentrically loaded plate, and by [42] who used the Galerkin method. The non-uniform load occurs when the bias voltage is increased, as the electrostatic force will be greater where the gap is smaller, an effect getting more distinct when the deflection is larger. However, it is not necessary to include for the typical CMUT case, where the plate never deflect more than half the gap due to pull-in.

All of these models assumes a circular plate geometry of the CMUT cells. For circular plates, a simple and exact solution for the deflection exists [43], but this is not the case for square plates. Existing solutions for the deflection of square plates is based on series expansions with either trigonometric [44] or polynomial basis functions [45].

Most existing analytical approaches use the isotropic plate equation to calculate the deflection i.e. [39, 46]. However, when using fusion bonding fabrication technology [12], the plate usually consists of crystalline silicon. Having a silicon (001) substrate, which is most often used, Young's modulus and Poisson's ratio are strongly anisotropic. The isotropic approach is then invalid, and this results in deviations in the deflection compared to finite element modeling (FEM) and measurements. Therefore, to get precise modeling of these CMUTs, the anisotropy of silicon needs to be taken into account. None of the above mentioned works, however, take the anisotropy of the plate into account.

For the first fabricated CMUTs there was no need for using anisotropic plate theory, as the plate usually consisted of silicon nitride or polysilicon when fabricated with the sacrificial release method. After the fusion bonding fabrication method was applied to CMUTs, the anisotropy of the plate, which now consisted of crystalline silicon, was considered [47]. However, instead of solving the problem analytically, finite element modeling (FEM) was used to estimate a set of material parameters (Young's modulus and Poisson's ratio) to use in the models to get an approximation as close as possible to the correct anisotropic solution.

In this project solutions to the full anisotropic plate equation for both circular and square plates are presented. The models were initially presented in [48] for an anisotropic plate with circular geometry, and this was then modified and expanded to include square plates as well in [49]. For the circular cells the symmetry reduces the plate equation and an exact solution for the anisotropic case can be obtained similarly to the isotropic solution. The approach used to solve the equation for the square plate is the Galerkin method [50]. Utilizing the symmetry of the silicon crystal, a compact and precise approximation of the deflection of a square plate can be obtained for the anisotropic case.

The plate usually also consists of more than one material. The theory of laminar plates is described in [51, 52] and in this project, the multilayer plate theory including anisotropy is applied to calculate important parameters for a two layer silicon/metal plate typically used for fusion bonded CMUTs.

Having found the deflection of the CMUT plate, a model for the electrostatic behavior of the transducer can be set up. Circular cells have been investigated thoroughly during the years and a full model for this plate geometry has recently been presented [41], whereas the full electrostatic analysis for the square plate has not been investigated previously. Furthermore, none of the existing models include the anisotropy. The full anisotropic electrostatic analysis for both circular and square plates are developed in this project and presented in [48, 49, 53].

1.3.3 Imaging

CMUTs have been developed for imaging purposes all the way from the beginning and the first pulse-echo B-scan images using a 1D CMUT arrays was demonstrated in 2000 by Oralkan et al. [54]. For this demonstration only 16 elements were used, however, similar experiments were conducted a little later with the first pulse-echo images with a 128 element array [1]. Both of these use devices made with the sacrificial release process using poly-silicon as sacrificial layer and a bandwidth of 80 % was observed as well as a center frequency of 2.3 MHz and 3 MHz, respectively.

After proving that CMUTs can be used for medical imaging the next thing is to assemble the transducers into a probe handle and to compare with a standard piezoelectric transducer and both have been done several times. Mills assembled CMUTs made with both fabrication processes into probe handles and compared to a piezoelectric probe and connected the probes to a real ultrasound scanner [55]. A flexible PCB is used for mounting the device and fold the connections backwards. In-vivo images are shown and compared with the conclusion that CMUTs perform slightly better in terms of resolution and bandwidth, however the piezoelectric probe has better depth of penetration. The fractional bandwidth is shown to be 130 %.

Caliano et al. [14] also assembled a surface micromachined CMUT array into a probe and made measurements first in air, then water-based phantoms and then in-vivo. The transducers had 64 elements, wirebonding was used for connections and silicone was used to protect the surface of the device with no acoustical lens applied for this prototype mounting. On average a fractional bandwidth of 100 % is observed for a center frequency of 2.9 MHz. Using a wire phantom a comparison to a piezoelectric array is made and the conclusions are that the CMUT appears to perform better in terms of axial resolution whereas it suffers from lower sensitivity.

In-vitro characterization and comparison between arrays have also been made to compare the image quality more quantitatively [56]. Similar image quality is observed for the two probes despite an environment favouring the piezoelectric transducer, the comparison is done with a standard imaging system, and performance of the CMUT could be increased by using a dedicated system.

A wearable probe has also been mounted using a flexible PCB with the purpose of constant monitoring of patients [57]. Here a PDMS lens is used for focusing and the ultrasound field in the focal point is measured to 750 kPa. Both phantom and in-vivo images were demonstrated. The array is mounted with electronics made in-house.

Savoia et al. [58] have made probe assembly using their reverse fabrication process where mounting of the device is incorporated into the process itself by turning the active side of the device during the processing to avoid through wafer vias but still obtain contact on the backside of the device. The process then also automatically includes backing. A 192 element CMUT array was compared to a piezoelectric array and a bandwidth of 105 % was observed with a center frequency of 11 MHz which is higher than for the piezoelectric probe. Analysis of the 2-way sensitivity showed better performance of the piezoelectric probe. Real-time in-vivo images are shown and compared.

A very alternative device has also been demonstrated to work for imaging on a wirephantom. It is the 21 element needle shaped miniature array made for invasive imaging by Cheng et al. [18]. A bandwidth of 116 % and a center frequency of 3.8 MHz are measured.

Testing of CMUT arrays for medical imaging and development of a flexible system for this purpose is part of the work done in this project as well as assembly of CMUTs into probe handles. For this purpose an investigation of PDMS as coating was also made and presented [53]. Coating of CMUTs is important for insulation between the surface of the elements and the patient when applying the high voltages required for operating CMUTs. Furthermore it also protects the surface of the device against environmental factors and e.g. degradation of the electrodes [59].

A possible coating material should have good acoustical properties such that the impedance matches with the medium for high energy transfer, a glass transition frequency smaller than 1 MHz for operation of the CMUT in the MHz range and a glass transition temperature below room temperature providing a low static Young's modulus for preserving the CMUT's pull-in voltage [60]. Furthermore the coating needs to be biocompatible. Polydimethylsiloxane (PDMS), Sylgard 170, is chosen as coating material in this work as it fulfils these requirements. Its acoustical properties match well with water and tissue (acoustical impedance 1.5 MRayls for water, 1.63 MRayls for tissue and 1.37 MRayls for Sylgard 170).

Other coating materials have previously been investigated e.g. Parylene C [59, 61] which gives good results and has the advantage of being cleanroom compatible but is deposited using Vapor deposition polymerization (VDP). Silicon nitride has also been proposed due to cleanroom compatibility, but the stress in this thinfilm highly affects the device performance [62]. Different PDMS have also been investigated and it is seen that some will increase the output signal due to increased mass loading and others will decrease the influence of the echo from the coating-water interface due to better impedance matching [60, 61]. Many of the experiments regarding coating have been conducted in air using a vibrometer and thus need further testing to check the influence on performance for imaging.

In this project it has been investigated how the Sylgard 170 PDMS coating affects the CMUT performance through comparison of the transmit pressure and receive sensitivity for devices with and without coating [53].

1.4 Scope of Project and Motivations

This project is part of a large ultrasound project funded by the Danish Advanced Technology Foundation. It is a collaboration between Center for Fast Ultrasound Imaging at DTU Electrical Engineering who are experts in ultrasound imaging and the MEMS-Applied Sensors group at DTU Nanotech who possesses a very high level of skills and experience within microfabrication. Furthermore, it is conducted in close collaboration with BK Medical (BK) and Sound Technology Inc. (STI).

First, this project seeks to obtain a basic knowledge and understanding of the CMUT device through analytical modelling. As several models have already been described, the focus in this project is to include the anisotropic effects in the analytical modelling and give a better description of a square plate geometry.

Second, it is desired to design and fabricate 1D CMUT arrays. For the fabrication it is chosen to use the fusion bonding process as the MEMS-Applied Sensors group had a lot of experience with this non-standard cleanroom fabrication technique. The simplest possible process is developed to obtain good working devices with a high yield and short fabrication time.

Third, a test setup for characterization of the fabricated transducers should be made. As it is expected that several transducer designs should be tested within the large ultrasound project, it is important to develop a flexible platform for evaluating CMUTs. This part is made together with BK medical who are in charge of designing PCBs and electronics.

Last, a prototype CMUT probe should be produced. Fabricated devices should be mounted into real probe handles. This prototype assembly is mainly made towards the end of the project with a timeline of 100 days. It should be produced all the way from design and fabrication of new chips (DTU Nanotech), design and production of electronics (BK) and assembly with backing, coating and lens in a probe handle (STI). Next is imaging with the array and a comparison with a piezoelectric probe. This is to observe which challenges would come up during such a probe production process, and the results will be explained in the thesis.

1.5 Thesis Outline

This thesis can be seen as a guide to fabricate, design and characterize 1D CMUT arrays and give an example of how to produce a prototype CMUT probe.

The thesis structure is as follows:

Chapter 1: Introduction - Describing the basis of ultrasound, transducers and the CMUT as well as a litterature review of CMUT fabrication, theory and CMUTs for medical imaging.

Chapter 2: Theory - Describing the electrostatic analysis of CMUTs with anisotropic circular and square plates which was developed in this project with focus on fusion bonded CMUTs. Multilayered plates are also covered and calculated deflections are compared to measurements. Energy considerations are used.

Chapter 3: Stanford Arrays - Describing design, fabrication and measurements of the first 1D arrays in this project. The work was carried out at Stanford University. One array was assembled into a probe by Vermon and the first images were made with CMUTs at DTU. The importance of high quality oxide was realized.

Chapter 4: Baseline Process - Describing development of a baseline process for fabricating CMUTs at DTU. Includes a detailed description of a fabrication run with the process and electrical measurements on the 1D arrays. Issues with charging in the CMUTs was discovered and a possible solution to avoid the charging found.

Chapter 5: Evaluation Platform - Describing development of a flexible platform for testing multiple transducer designs while reusing the electronic parts. The system is developed in collaboration with BK Medical. It is used for evaluation of the coating effects of CMUTs and for medical imaging with the 1D arrays made with the baseline process and different imaging methods.

Chapter 6: TABLA Prototype Probe - Describing the design and assembly of the prototype CMUT probe developed in collaboration with BK Medical and Sound Technology Inc. Initial tests with the two first probes are shown.

Chapter 7: Conclusion and Outlook

CHAPTER 2

Theory

This chapter will cover the essentials of the electrostatic theory for the CMUT. It is submitted for publication in [63] which can be seen in appendix E.

Many important design parameters for CMUTs depend on the deflection of the plate. The full anisotropic plate equation and solutions for both circular and square plates will first be presented. The models were initially presented in [48], see appendix C, for an anisotropic plate with circular geometry, and this was then modified and expanded to include square plates as well in [49], see appendix D,. Furthermore, the multilayer plate theory including anisotropy is applied to a two layer silicon/metal plate typically used for CMUTs. Having found the deflection of the CMUT plate, electrostatic analysis can be performed to find the stable position of the plate, when applying a certain bias voltage. The stable position is the position where the spring force balances the electrostatic and pressure forces. From this the pull-in distance and pull-in voltage can be found.

An illustration of the CMUT cell analysed in this chapter can be seen in Figure 2.1 which shows a cross sectional view of a CMUT cell with an applied voltage. The device parameters are illustrated for both circular and square plates and these notations will be used throughout the analysis.

2.1 Plate Deflection

Conventionally, the deflection $w(x,y)$ of a CMUT with a thin plate is modeled using the isotropic plate equation [44]

$$\frac{\partial^4 w}{\partial x^4} + 2\frac{\partial^4 w}{\partial x^2 \partial y^2} + \frac{\partial^4 w}{\partial y^4} = \frac{p}{D_\mathrm{i}}, \tag{2.1}$$

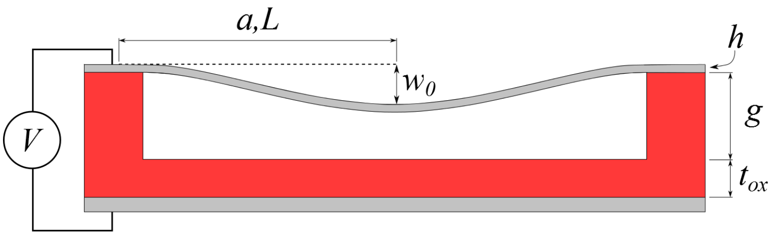

Figure 2.1: *Cross sectional view of CMUT cell with applied voltage. For a square cell the sidelength is* $2L$ *and for a circular cell the radius is a. The plate thickness is h, the vacuum gap height g and the insulation layer thickness* t_{ox}. *When a voltage V is applied, the plate deflects* w_0 *in the center.*

where p is the applied pressure difference across the plate and the flexural rigidity is given by

$$D_{\mathrm{i}} = \frac{E}{12\left(1-\nu^2\right)} h^3, \tag{2.2}$$

with E being Young's modulus, ν being Poisson's ratio, and h being the thickness of the plate.

For thin clamped circular plates, an exact solution exists. For such a plate with radius a, the center deflection is given by [43]

$$w_{0,\mathrm{iso,circ}} = \frac{1}{64}\frac{a^4 p}{D_{\mathrm{i}}}. \tag{2.3}$$

For clamped rectangular and square plates, no simple exact solution exists and approximate methods have to be used. The conventional isotropic approach is based on a series expansion of the deflection, and the center deflection for a thin clamped square plate having side length $2L$ is [44]

$$w_{0,\mathrm{iso,sq}} = 0.020245\frac{L^4 p}{D_{\mathrm{i}}}. \tag{2.4}$$

To take the anisotropy of the plate into account and avoid the inaccuracy from isotropic modeling, the stiffness of the plate needs to be described through the stiffness matrix of the material instead of Young's modulus and Poisson's ratio.

The generalized plate equation is used to include the anisotropic effects. This is a differential equation for the deflection, $w(x,y)$, of a thin anisotropic plate exposed to a uniform load p given by [64, 65]

$$\frac{\partial^4 w}{\partial x^4} + k_1\frac{\partial^4 w}{\partial x^3 \partial y} + k_2\frac{\partial^4 w}{\partial x^2 \partial y^2} + k_3\frac{\partial^4 w}{\partial x \partial y^3} + k_4\frac{\partial^4 w}{\partial y^4} = \frac{p}{D_{\mathrm{a}}}. \tag{2.5}$$

The plate coefficients k_1-k_4 and the anisotropic flexural rigidity, D_{a}, depend on the elastic constants of the plate material

$$k_1 = \frac{4C_{13}^{\mathrm{eff}}}{C_{11}^{\mathrm{eff}}} \quad k_2 = \frac{2\left(C_{12}^{\mathrm{eff}}+2C_{33}^{\mathrm{eff}}\right)}{C_{11}^{\mathrm{eff}}} \quad k_3 = \frac{4C_{23}^{\mathrm{eff}}}{C_{11}^{\mathrm{eff}}} k_4 = \frac{C_{22}^{\mathrm{eff}}}{C_{11}^{\mathrm{eff}}} \quad D_{\mathrm{a}} = \frac{1}{12}h^3 C_{11}^{\mathrm{eff}}, \tag{2.6}$$

where $C_{\mathrm{pq}}^{\mathrm{eff}}$ are elements in the effective stiffness matrix. Note that the stiffness of the plate is no longer expressed through Young's modulus and Poisson's ratio but directly through the stiffness values. The

Table 2.1: *Room temperature (300K) compliance coefficients for n-type crystalline silicon measured by [66] for a substrate with low doping level (150 Ω-cm, $\sim 2.8 \times 10^{13}$ cm^{-3}) and high doping level (3.26 mΩ-cm, $\sim 2.1 \times 10^{19}$ cm^{-3}).*

	Low doping	**High doping**
s^c_{11}	7.691×10^{-12} Pa^{-1}	7.858×10^{-12} Pa^{-1}
s^c_{12}	-2.1420×10^{-12} Pa^{-1}	-2.2254×10^{-12} Pa^{-1}
s^c_{44}	12.577×10^{-12} Pa^{-1}	12.628×10^{-12} Pa^{-1}

Table 2.2: *Selected values for the plate coefficients and anisotropic flexural rigidity for plates on a silicon (001) substrate [64]. Upper values in brackets are for low doping level and lower values for high doping level.*

Orientation	ψ	k_1	k_2	k_3	k_4	$12D_a/h^3$[GPa]
[100]	0	0	2.8133 ± 0.0006 2.8559 ± 0.0006	0	1	140.96 ± 0.03 138.35 ± 0.03
[110]	$\pi/4$	0	1.3241 ± 0.0004 1.2949 ± 0.0004	0	1	169.62 ± 0.03 167.96 ± 0.03

effective stiffness matrix is found from the relation between stress and strain and for silicon it becomes

$$C^{\text{eff}}_{\text{Si(001),[110]}} = \begin{pmatrix} \frac{1}{s^c_{44}} + \frac{1}{2(s^c_{11}+s^c_{12})} & \frac{1}{2(s^c_{11}+s^c_{12})} - \frac{1}{s^c_{44}} & 0 \\ \frac{1}{2(s^c_{11}+s^c_{12})} - \frac{1}{s^c_{44}} & \frac{1}{s^c_{44}} + \frac{1}{2(s^c_{11}+s^c_{12})} & 0 \\ 0 & 0 & \frac{1}{2s^c_{11}-2s^c_{12}} \end{pmatrix}. \tag{2.7}$$

The elements in this matrix are in the crystallographic coordinate system and are known from measurements and shown in Table 2.1 [66]. Equation (2.7) is specifically for having silicon as plate material and performing standard cleanroom fabrication, the plate will usually be on a (001) substrate and aligned to the primary wafer flat. Flat alignment is to the [110] direction. A transformation of the compliance matrix between the two coordinate systems is performed to obtain (2.7) [64].

Using the compliance values for silicon (Table 2.1) and inserting the stiffness elements in (2.7) into (2.6), it follows that $k_1 = k_3 = 0$ and $k_4 = 1$. Thus, aligning the plate to the primary flat simplifies the anisotropic plate equation (2.5). This is also the case for aligning the plate along the [100] direction. For these two special cases, the coefficients in the plate equation are summarized in Table 2.2 for both high and low doping levels of the substrate.

2.1.1 Deflection of Circular Plates

The solution to (2.5) for a circular plate of radius a fixed at the boundary is easily obtained using polar coordinates. The deflection at a point a distance r from the center is given by [43]

$$\frac{w(r)}{w_0} = \left(1 - \left(\frac{r}{a}\right)^2\right)^2. \tag{2.8}$$

Table 2.3: *Young's modulus and Poisson's ratio for silicon (001) and a plate aligned to the [100] and [110] directions as well a the mean values for these.*

	Young's modulus	**Poisson's ratio**
[100] direction	130 GPa	0.278
[110] direction	169 GPa	0.062
Mean value	148 GPa	0.177

This expression is similar to the deflection for the isotropic case, however, the center deflection is different

$$w_{0,\mathrm{circ}} = \frac{1}{8\,(3+k_2+3k_4)}\,\frac{a^4 p}{D_\mathrm{a}}. \tag{2.9}$$

By combining (2.3) and (2.9) it is possible to find an effective flexural rigidity

$$D_\mathrm{eff} = \frac{3+k_2+3k_4}{8} D_\mathrm{a}. \tag{2.10}$$

This can be used to easily change from the isotropic plate equation to the anisotropic plate equation in already existing analytical models of CMUTs. An example of this will be shown in section 2.2. Using the plate coefficient values from Table 2.2 for a highly doped (001) silicon plate aligned to the $\langle 110\rangle$ direction, the effective flexural rigidity becomes $D_\mathrm{eff} = 0.91551 D_\mathrm{a}$.

To compare the anisotropic model with the isotropic approach and FEM simulations, the normalized deflection of a CMUT exposed to a pressure difference is shown in Figure 2.2. The FEM simulations were performed in COMSOL Multiphysics version 4.2a using the full anisotropic stiffness tensor and the curves are normalized to the center deflection of this. The isotropic curves are made using (2.8) and (2.3) and Young's modulus and Poisson's ratio along the [100] and [110] directions (see Table 2.3) to give the dash and dashdot lines, respectively. The anisotropic solution is made using (2.8) and (2.9) and is shown as a solid curve. This is on top of the FEM simulation (circles). Due to the symmetry of the circular plate, any set of parameters from Table 2.2 can be used. Excellent agreement between the anisotropic solution and the finite element calculation is seen with an error of less than 0.3%. The figure also shows that using Young's modulus and Poisson's ratio corresponding to [100] or [110] directions leads to errors in the center deflection of around 10%. To reduce this error, it is common practice to use mean values of Young's modulus and Poisson's ratio (see Table 2.3) which decreases the error to around 1.5%.

As it is seen, using the anisotropic approach for a thin circular CMUT plate on a (001) silicon substrate is simple and the result is exact.

2.1.2 Deflection of Square Plates

Having a square plate makes analytical deflection calculations complicated and approximate methods must be used to solve the anisotropic plate equation. With the anisotropic approach, the Galerkin method [50] can be used to find approximate expressions for the deflection of a thin anisotropic square

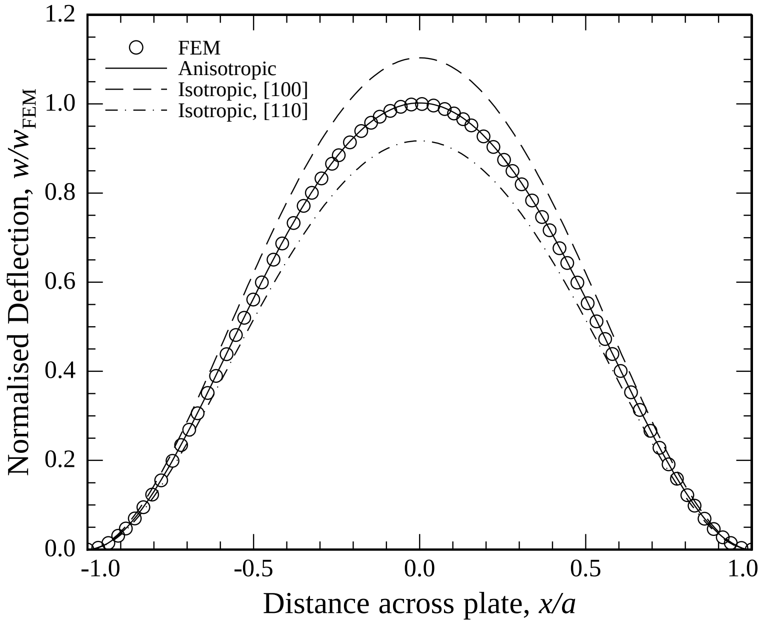

Figure 2.2: *Normalized deflection cross section ($y = 0$) of a thin circular plate of silicon (001) calculated with* (2.8) *using both the isotropic approach* (2.3) *with Young's modulus and Poisson's ratio in the [100] and [110] directions and the anisotropic approach* (2.9)*. The circles represent the deflection calculated by FEM.*

plate. As previously stated, in the most common case for CMUTs, the plate is fabricated on a silicon (001) substrate and aligned to the [110] direction. For this orthotropic square plate with sidelengths $2L$, the relative deflection is found to be [64, 67]

$$\frac{w(x,y)}{w_0} = \left[1-\left(\frac{x}{L}\right)^2\right]^2 \left[1-\left(\frac{y}{L}\right)^2\right]^2 \times \left[1+\beta\left(\frac{x}{L}\right)^2+\beta\left(\frac{y}{L}\right)^2\right], \tag{2.11}$$

where the plate parameter β is defined as

$$\beta = \frac{182+143k_2}{1432+91k_2}. \tag{2.12}$$

Equations (2.11) and (2.12) are also valid when the plate is aligned to the [100] direction on a silicon (001) substrate. For primary flat alignment, it is found by inserting k_2 into (2.12) and using the low doping values $\beta_{\mathrm{low}} = 0.23920$ and using the high doping values $\beta_{\mathrm{high}} = 0.23691$. For the low doping case, this results in a normalized deflection for the plate aligned to the $\langle 110\rangle$ direction given by

$$\left.\frac{w(x,y)}{w_0}\right|_{\mathrm{sq,Si(001)},\langle 110\rangle} = \left[1-(x/L)^2\right]^2\left[1-(y/L)^2\right]^2 \times \left[1+0.23920\left[(x/L)^2+(y/L)^2\right]\right], \tag{2.13}$$

and the center deflection becomes

$$w_{0,\mathrm{sq,Si(001)},\langle 110\rangle} = 0.02196\frac{L^4 p}{D_{\mathrm{a}}}. \tag{2.14}$$

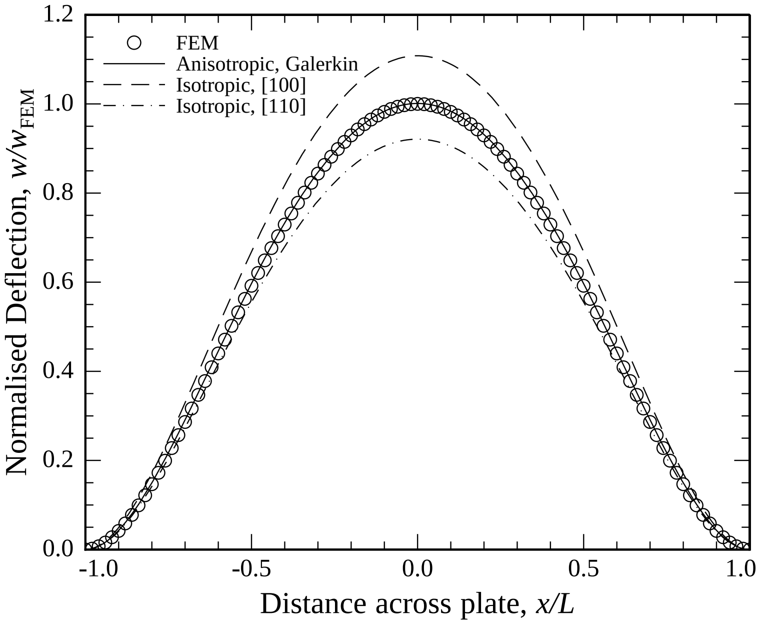

Figure 2.3: *Normalized deflection cross section* ($y = 0$) *of a square plate of silicon (001) calculated with* (2.15) *using both the isotropic approach* (2.4) *with Young's modulus and Poisson's ratio in the [100] and [110] directions and the anisotropic approach* (2.14). *The circles represent the deflection calculated by FEM.*

For the high doping case, the factor in front becomes 0.02204 for the center deflection. Comparing (2.4) and (2.14), it is seen that they are very similar containing the same parameters but different coefficients and the anisotropic instead of the isotropic flexural rigidity.

Figure 2.3 shows the deflection cross section through $y = 0$ of a square plate of silicon (001) given by the reduced version of (2.11)

$$w_{y=0,\mathrm{sq}} = w_0 \left[1 - (x/L)^2\right]^2 \left[1 + \beta\,(x/L)^2\right]. \tag{2.15}$$

The deflection calculated with the anisotropic approach uses $k_2 = 1.3241$ in (2.12) and center deflection (2.14) (solid curve). This is compared to the isotropic approach using $k_2 = 2$ in (2.12) and center deflection (2.4), with Young's modulus and Poisson's ratio in the [100] and [110] directions (dash and dashdot curves), and to a finite element (FEM) simulation made using the full anisotropic compliance matrix (compliance coefficients from Table 2.1) in COMSOL (circles). The calculated deflections are normalized to the FEM center deflection. Excellent agreement is shown between the anisotropic curve and FEM with a deviation of less than 0.1 % whereas the isotropic approach leads to deviations in the center deflection of around 10 % for both [100] and [110] directions.

2.1.3 Multilayer Plates

For the CMUT application, the multilayer plate will often consist of two layers with silicon as the main part and a thin aluminum layer on top for contacts. The aluminum is an isotropic material and the silicon is an orthotropic material (when aligned to [110] direction on a (001) substrate). For this two-layer plate, the total thickness is called h and the ratio $\alpha = h_{\text{Al}}/h$ is defined from the thickness of the aluminum, h_{Al}. When the plate is all silicon $\alpha = 0$ and when the plate is only aluminum $\alpha = 1$. Again utilizing the symmetry of the materials, it can be found that $k_1 = k_3 = 0$ and $k_4 = 1$ so again only k_2 and D_{a} need to be taken into account for the usual CMUT plates.

The expressions for k_2 and the plate stiffness becomes quite long even for the simplified case. Using the compliance values for highly doped silicon in Table 2.1 and Young's modulus of $E = 70$ GPa and Poisson's ratio of $\nu = 0.35$ for aluminum in the expressions, they become [63]

$$D_{\text{AlSi}} = (13.9963\ \text{GPa} - 22.0458\ \text{GPa} \cdot \alpha)h^3 \tag{2.16}$$

$$k_{2,\text{AlSi}} = 1.29493 + 1.00464\alpha. \tag{2.17}$$

Furthermore, it can also be found that when having a sufficiently thin aluminum layer, $\alpha < 0.2$, a series expansion can be used and simple correction formulas can be found. This way, the flexural rigidity of the combined aluminum and silicon plate compared to the flexural rigidity for a plate of only silicon with the same thickness as the total thickness can be expressed as

$$\frac{D_{\text{AlSi}}}{D_{\text{Si}}} = 1 - 1.575\alpha. \tag{2.18}$$

Similarly, for the plate parameter k_2 it is found that

$$\frac{k_{2,\text{AlSi}}}{k_{2,\text{Si}}} = 1 - 0.775822\alpha. \tag{2.19}$$

Equations (2.18) and (2.19) both use the stiffness values for highly doped silicon from Table 2.1.

For a circular plate, the relative center deflection using the same method as above can be found to be

$$\frac{w_{0,\text{AlSi,circ}}}{w_{0,\text{Si,circ}}} = 1 + 1.437\alpha. \tag{2.20}$$

Doing the same for square plates the relation becomes

$$\frac{w_{0,\text{AlSi,Sq}}}{w_{0,\text{Si,Sq}}} = 1 + 1.445\alpha. \tag{2.21}$$

The error between the series expansion and the full result for the center deflection is less than 2 % for $\alpha = 0.2$ for both plate geometries. An example of a typical thicknesses of the layers of the CMUT multilayer plate is ~2 μm silicon and ~0.2 μm aluminum. This gives $\alpha = 0.1$ and the error when using the series expansion is less than 0.5%.

As examples on how the aluminum layer influences the plate parameter, stiffness and center deflection of the circular and square plates, calculations using single and multilayer plate theory can be seen in Table 2.4. Here, calculations are made with dimensions as the fabricated devices found in Table 2.5. For the single layer calculations the aluminum layer is not included and a pure silicon plate is considered. The values for the plate coefficient and flexural rigidity are found in Table 2.2 and for the center deflections (2.9) and (2.14) are used. For the multilayer plate examples the aluminum layer is included in the calculations and (2.17), (2.16), (2.20) and (2.21) are used. It is seen that including the aluminum layer in the calculations affects k_2 with around 7 %, the stiffness of the plate with around 18 % and the center deflection with around 12 % in this case.

Table 2.4: *Examples on k_2, stiffness and center deflection when using single or multilayer plate theory for both circular and square shaped plates.*

	α	k_2	$12D_a/h^3$	w_0
Circ., multi	0.10	1.3954	141.50 GPa	29.4 nm
Circ., Si	-	1.2949	167.96 GPa	25.7 nm
Sq., multi	0.08	1.3753	146.79 GPa	12.5 nm
Sq., Si	-	1.2949	167.96 GPa	11.2 nm

Table 2.5: *Dimensions of devices fabricated using fusion bonding. Both circular and square shaped plates were produced.*

	Circular	**Square**
Size (a, L)	36 μm	32.5 μm
Plate thickness, Si h_{Si}	1.8 μm	2.3 μm
Al thickness h_{Al}	200 nm	200 nm
Gap height (vacuum) g	(uncertain)	405 nm
Insulation layer t_{ox}	195 nm	198 nm

2.1.4 Deflection Measurement

To further validate the deflection of the square plate, CMUTs with square silicon plates have been fabricated using fusion bonding [68]. The dimensions of the fabricated device can be seen in Table 2.5. The deflection was measured with a Sensofar PLu Neox 3D Optical Profiler using white light interferometry. Figure 2.4 shows a measured cross section of the normalized deflection for a fabricated device. It is normalized in both center deflection and distance across the plate to compare the shape of the measured deflection with the calculated deflection. The red curve is a fit made to the measurements using the anisotropic model (2.15). The plate parameter β is fitted to the measurements. As it is seen in the figure, the fitted value for β is 0.243. Using (2.17) for calculating β for this multilayer plate (2 μm highly doped silicon (001) substrate aligned to [110] direction with 200 nm Al) a deviation of only 0.07 % is obtained.

2.2 Electrostatic Analysis

Having found the deflection of the CMUT plate, the device parameters such as stable position, pull-in distance and pull-in voltage can now be found through electrostatic analysis. The relevant parameters will first be derived generally before using the theory on three types of capacitors: the parallel plate capacitor, the circular CMUT plate and the square CMUT plate. The three types will be compared during the analysis.

The analysis is based on energy considerations. The total potential energy U_t consists of three terms,

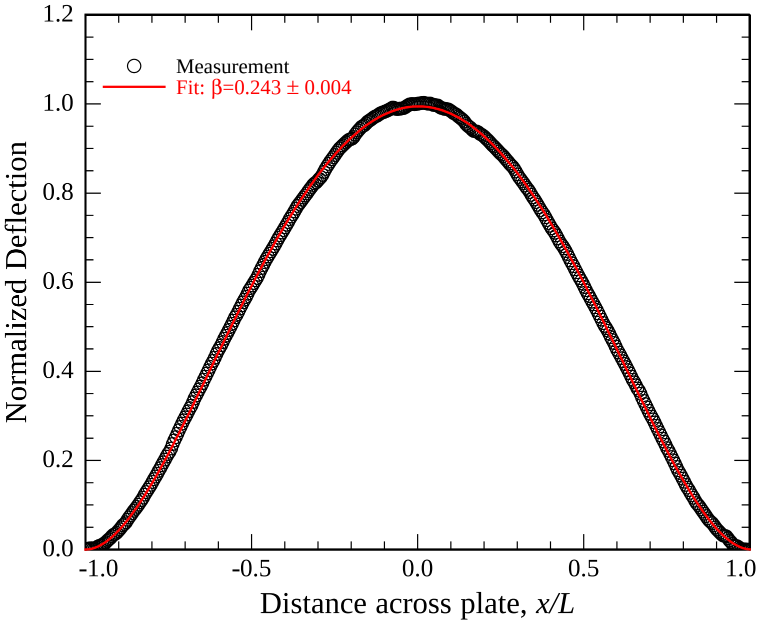

Figure 2.4: *Normalized deflection cross section ($y=0$) from measurement on a fabricated CMUT with square plate of silicon (001) aligned to [110]. The red curve is a fit made from (2.15).*

the strain energy U_s, the electrostatic energy U_e, and the energy from applying a pressure U_p

$$U_\mathrm{t} = U_\mathrm{s} + U_\mathrm{p} + U_\mathrm{e}. \tag{2.22}$$

The method is valid for all systems where the total potential energy is of the form

$$U_\mathrm{t} = \frac{k_0 w_0^2}{2} - pA_\mathrm{eff} w_0 - \frac{1}{2} V^2 C_\mathrm{t}(w_0), \tag{2.23}$$

where k_0 is the generalized spring constant that comes from the calculation of the strain energy, A_eff is the effective area of the plates i.e. the area that goes into calculation of the work performed by deflecting the plate due to applied pressure, V is the applied voltage, p the atmospheric pressure, C_t the total capacitance of the device and w_0 the center deflection of the plate. For the parallel plate $k_0 = k$ and $A_\mathrm{eff} = A$.

The total force on the system, F_t, is found by differentiating the total potential energy with respect to the center deflection, which is used as a reference in this work (any deflection could be used as a reference)

$$F_\mathrm{t} = \frac{\partial U_\mathrm{t}}{\partial w_0} = k_0 w_0 - pA_\mathrm{eff} - \frac{1}{2} V^2 C_\mathrm{t}'(w_0), \tag{2.24}$$

where $C_\mathrm{t}'(w_0)$ denotes the capacitance differentiated with respect to w_0. The stable position of the plate can be found for a given applied voltage as the point where the total force is zero, so solving

$$k_0 w_0 = pA_\mathrm{eff} + \frac{1}{2} V^2 C_\mathrm{t}'(w_0). \tag{2.25}$$

The effective spring constant, k_{eff}, can be found as the second derivative of the total potential energy or by differentiating the total force

$$k_{\mathrm{eff}} = \frac{\partial F_{\mathrm{t}}}{\partial w_0} = k_0 - \frac{1}{2} V^2 C_{\mathrm{t}}''(w_0). \tag{2.26}$$

Pull-in occurs when the effective spring constant is zero and the pull-in voltage V_{PI} can be expressed as

$$V_{\mathrm{PI}} = \frac{2k_0}{C_{\mathrm{t}}''(w_0)}. \tag{2.27}$$

Inserting the pull-in voltage (2.27) into the equation for the stable position (2.25) the pull-in distance can be found by solving the equation

$$k_0 w_0 = pA_{\mathrm{eff}} + \frac{k_0 C_{\mathrm{t}}'(w_0)}{C_{\mathrm{t}}''(w_0)}. \tag{2.28}$$

This can then be inserted into (2.27) to obtain the pull-in voltage. Finding pull-in distance and voltage is therefore a question of solving the two equations (2.25) and (2.28) for the two variables.

In the following, this analysis is shown for both circular and square plates including the anisotropic effects and for a parallel plate capacitor as well for comparison. Similar analysis has previously been shown by others for circular plates i.e. [39, 41] and are therefore shown here in compact form.

2.2.1 Capacitance

An important variable in the electrostatic analysis for CMUTs is the capacitance. The capacitance at zero deflection, C_0, of the plate can for both the circular and square plates be divided into two contributions: The capacitance from the vacuum gap $C_0 = \varepsilon_0 A/g$ and the capacitance from the insulation oxide between in electrodes $C_{\mathrm{ox}} = \varepsilon_0 \varepsilon_{\mathrm{ox}} A/t_{\mathrm{ox}}$. A is the area of the plates, g the vacuum gap, ε_0 the vacuum permittivity, t_{ox} the thickness of the insulation oxide layer, and $\varepsilon_{\mathrm{ox}}$ the relative permittivity of the oxide. The effect from having both contributions can be collected in an effective gap height

$$g_{\mathrm{eff}} = g + \frac{t_{\mathrm{ox}}}{\varepsilon_{\mathrm{ox}}}. \tag{2.29}$$

The total capacitance at zero deflection can then be written

$$C_{\mathrm{t0}} = \left(\frac{1}{C_0} + \frac{1}{C_{\mathrm{ox}}} \right)^{-1} = \frac{\varepsilon_0 A}{g_{\mathrm{eff}}}. \tag{2.30}$$

Taking the deflection of the plate into account, the total capacitance of the device is

$$C_{\mathrm{t}} = \frac{1}{g_{\mathrm{eff}}} \iint \frac{\varepsilon_0}{1 - \eta f(x,y)} \mathrm{d}x \, \mathrm{d}y \tag{2.31}$$

where $\eta = w_0/g_{\mathrm{eff}}$ is the normalized center deflection and $f(x,y)$ is a function describing the shape of the deflection. For circular plates, this function will be (2.8), for square plates it is (2.13), and for the parallel plate $f = 1$.

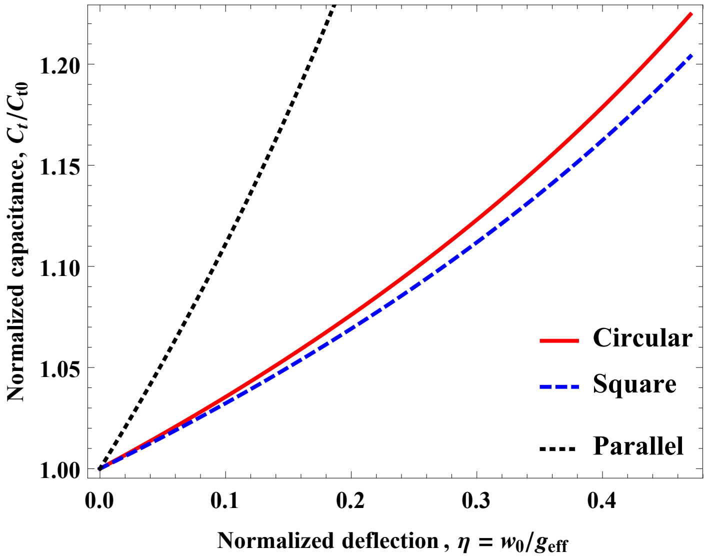

Figure 2.5: *Normalized total capacitance versus normalized deflection for a circular* (2.33) *and a square plate* (2.34). *The parallel plate solution* (2.32) *shown for comparison.*

The total capacitance of a parallel plate capacitor is given by

$$C_{\mathrm{t,parallel}} = C_{\mathrm{t0}} \frac{1}{1-\eta}. \tag{2.32}$$

For the circular plate, the integral can be solved analytically and the total capacitance becomes

$$C_{\mathrm{t,circ}} = C_{\mathrm{t0}} \sqrt{\frac{1}{\eta}}\,\operatorname{arctanh}\sqrt{\eta}. \tag{2.33}$$

For the square plate, there is no analytical solution. The integration in (2.31) is performed numerically and is stored using the interpolation function in Wolfram Mathematica 9. The relative error between the interpolation function and the numerical integration is less than 4×10^{-6} and this function can be used like a normal expression for further calculations. The total capacitance can be written

$$C_{\mathrm{t,sq}} = C_{\mathrm{t0}} f_i(\eta). \tag{2.34}$$

where $f_i(\eta)$ is the interpolation function. Alternatively, a Taylor expansion can be used, however, at least 8 terms is needed to get sufficient accuracy.

Figure 2.5 shows the total capacitance normalized to the total capacitance with no deflection, $C_{\mathrm{t}}/C_{\mathrm{t0}}$, versus the relative deflection, η, for all three cases. It is seen that when normalized, the circular and square plates have similar capacitance responses. For example, at a relative deflection of 0.4 the deviation is 1.4% between the square and circular capacitance, whereas using the parallel plate approximation results in a much larger difference as seen in the figure.

2.2.2 Energy Calculations

The total strain energy is calculated by integrating the strain energy density using the relation between stress and strain and (2.7). Having a thin plate, we can assume plane stress and the expression becomes

$$U_\mathrm{s} = \frac{1}{2} \iiint (\sigma_1 \varepsilon_1 + \sigma_2 \varepsilon_2 + \sigma_6 \varepsilon_6)\, \mathrm{d}x\, \mathrm{d}y\, \mathrm{d}z, \tag{2.35}$$

where the strains are given by

$$\varepsilon_1 = -z \frac{\partial^2 w(x,y)}{\partial x^2}, \varepsilon_2 = -z \frac{\partial^2 w(x,y)}{\partial y^2}, \varepsilon_6 = -2z \frac{\partial^2 w(x,y)}{\partial x \partial y}. \tag{2.36}$$

The energy due to the externally applied pressure is calculated as minus the work performed (i.e. force times length, here pressure times area times length) when deflecting the plate

$$U_\mathrm{p} = -\iint p w(x,y)\, \mathrm{d}x\, \mathrm{d}y. \tag{2.37}$$

The electrostatic energy is expressed through the charge Q or applied voltage V, the vacuum permittivity ε_0, gap height g_eff and the total capacitance C_t of the device

$$U_\mathrm{e} = -\frac{1}{2} V^2 C_\mathrm{t} = -\frac{1}{2} V^2 \iint \frac{\varepsilon_0}{g_\mathrm{eff} - w(x,y)} \mathrm{d}x\, \mathrm{d}y \tag{2.38}$$

The capacitance inserted during the second equalization in (2.38) is valid for all plate geometries, if the right expression for the deflection is used in each case. It can be seen how the deflection of the plate appears, and therefore, the plate geometry and the anisotropy of the plate is included through the deflection.

For a circular plate (2.35), (2.37) and (2.38) become

$$\begin{aligned} U_\mathrm{s,circ} &= \frac{1}{2} \int_{-h/2}^{h/2} \int_0^{2\pi} \int_0^a r\, (\sigma_1 \varepsilon_1 + \sigma_2 \varepsilon_2 + \sigma_6 \varepsilon_6)\, \mathrm{d}r\, \mathrm{d}\theta\, \mathrm{d}z \\ &= \frac{h^3 \pi w_0^2 \left(3C_{11}^\mathrm{eff} + 2C_{12}^\mathrm{eff} + 3C_{22}^\mathrm{eff} + 4C_{33}^\mathrm{eff}\right)}{9a^2}. \end{aligned} \tag{2.39}$$

$$U_\mathrm{p,circ} = -\int_0^a 2\pi p r w dr = -\frac{1}{3} \pi p a^2 w_0. \tag{2.40}$$

$$U_\mathrm{e,circ} = -\frac{1}{2} C_\mathrm{t} V^2 = -\frac{1}{2} V^2 C_\mathrm{t0} \sqrt{\frac{1}{\eta}}\, \mathrm{arctanh} \sqrt{\eta}. \tag{2.41}$$

Using (2.6) it can be seen that the strain energy can be written in terms of the effective flexural rigidity

$$U_\mathrm{s,circ} = \frac{h^3 \pi w_0^2}{9a^2} (3 + k_2 + 3k_4) \frac{12 D_\mathrm{a}}{h^3} = \frac{32 \pi D_\mathrm{eff} w_0^2}{3a^2}. \tag{2.42}$$

By changing the flexural rigidity, it is possible to easily switch between isotropic and anisotropic calculations in (2.42).

Comparing (2.42), (2.39), and (2.40) with (2.23) it can be seen that for the circular plate the general spring constant and the effective area are given by

$$k_{0,\mathrm{circ}} = \frac{2 \cdot 32 D_{\mathrm{eff}} \pi}{3a^2} = \frac{64 D_{\mathrm{eff}} \pi}{3a^2}, \tag{2.43}$$

$$A_{\mathrm{eff,circ}} = \frac{1}{3} \pi a^2. \tag{2.44}$$

For the square plate, only the most common case with a highly doped plate on silicon (001) substrate aligned to the $\langle 110 \rangle$ direction is considered. Using the deflection from (2.13) and the capacitance from (2.34), equations (2.35), (2.37) and (2.38) become

$$\begin{aligned} U_{\mathrm{s,sq}} &= \frac{1}{2} \int_{-h/2}^{h/2} \int_{-L}^{L} \int_{-L}^{L} \left(\sigma_1 \varepsilon_1 + \sigma_2 \varepsilon_2 + \sigma_6 \varepsilon_6 \right) \mathrm{d}x \, \mathrm{d}y \, \mathrm{d}z \\ &= \frac{4096 h^3 w_0^2}{4729725 L^2} \left(\gamma_1 C_{11}^{\mathrm{eff}} + 2\gamma_2 C_{12}^{\mathrm{eff}} + \gamma_1 C_{22}^{\mathrm{eff}} + 4\gamma_2 C_{33}^{\mathrm{eff}} \right), \\ \gamma_1 &= \left(1001 + 468\beta + 476\beta^2 \right), \quad \gamma_2 = 26 \left(11 + 2\beta^2 \right). \end{aligned} \tag{2.45}$$

$$U_{\mathrm{p,sq,Si(001),[110]}} = -\int_{-L}^{L} \int_{-L}^{L} p w(x,y) \, dxdy = -\xi_{\mathrm{p}} p L^2 w_0, \quad \xi_{\mathrm{p}} = 1.215. \tag{2.46}$$

$$U_{\mathrm{e,sq}} = -\frac{1}{2} V^2 C_{\mathrm{t0}} f(\eta). \tag{2.47}$$

Using the value for β_{high}, $\gamma_1 = 1138.5$ and $\gamma_2 = 288.9$. Inserting the plate coefficients from (2.6) into (2.45), it can be seen that the strain energy can be written in terms of the plate coefficients and the anisotropic flexural rigidity

$$U_{\mathrm{s,sq}} = \frac{49152}{4729725} \left(\gamma_1 + \gamma_2 k_2 + \gamma_1 k_4 \right) \frac{D_{\mathrm{a}} w_0^2}{L^2}, \tag{2.48}$$

Using the values from Table 2.2 the strain energy for the square plate of silicon (001) aligned to the $\langle 110 \rangle$ direction becomes

$$U_{\mathrm{s,sq,Si(001),[110]}} = \xi_{\mathrm{s}} \frac{h^3 w_0^2}{L^2}, \quad \xi_{\mathrm{s}} = 385.637 \ \mathrm{GPa}. \tag{2.49}$$

Comparing (2.49) and (2.46) with (2.23) it is seen that for the square plate the general spring constant and the effective area are given by

$$k_{0,\mathrm{sq}} = \frac{2 \cdot \xi_{\mathrm{s}} h^3}{L^2} = \frac{2 h^3 \xi_{\mathrm{s}}}{L^2}, \tag{2.50}$$

$$A_{\mathrm{eff,sq}} = \xi_{\mathrm{p}} L^2. \tag{2.51}$$

2.2.3 Stable Position

Using the expressions (2.42)-(2.41) for the energies and the equation for the stable position (2.25), the stable position for the circular plate becomes

$$\begin{aligned} & V_{\mathrm{stable,circ}} = \\ & \sqrt{\frac{-256 g_{\mathrm{eff}} \eta^{3/2} (-a^4 p \pi / 64 + D_{\mathrm{eff}} \pi \eta g_{\mathrm{eff}})(-1 + \eta)}{3a^2 C_{\mathrm{t0}} \left(-\operatorname{arctanh}\left[\sqrt{\eta}\right] + \eta \operatorname{arctanh}\left[\sqrt{\eta}\right] + \sqrt{\eta} \right)}}. \end{aligned} \tag{2.52}$$

A comparison of the stable position found using the anisotropic approach, (2.52), and measurements on a fabricated device can be found in Section 2.3.

For the square plate, combining the expressions in (2.49), (2.46) and (2.47), the stable position for the highly doped square plate on silicon (001) substrate aligned to the $\langle 110 \rangle$ direction can be found by (2.25)

$$V_{\text{stable,sq}} = \sqrt{\frac{2g_{\text{eff}}\left(-L^4 p \xi_{\text{p}} + 2h^3 \eta \xi_{\text{s}} g_{\text{eff}}\right)}{C_{\text{t0}} L^2 f(\eta)}}. \tag{2.53}$$

Devices with square plates were also fabricated and a comparison of the stable position found using the anisotropic approaches compared to the measured center deflection can be found in Section 2.3.

Originally, the CMUT was modelled by use of a parallel plate approximation [36, 37]. The parallel plate case is also included here for comparison and in this case, the stable position is

$$V_{\text{stable,parallel}} = \sqrt{\frac{2(-1+\eta)^2 g_{\text{eff}}(-Ap + k\eta g_{\text{eff}})}{C_{\text{t0}}}}. \tag{2.54}$$

From the static analysis, it is possible to present a set of general design plots for CMUTs by using adequate normalizations. Hereby, the results for circular, square and parallel plates can be compared. For specific device behavior, the equations for zero applied pressure or voltage can be used to eliminate the normalizations. These expressions are derived in section 2.2.5.

Figure 2.6 shows the stable position of the plate for varying bias voltages. The bias voltage is normalized to the pull-in voltage at zero applied pressure $V/V_{\text{PI,p0}}$ and the deflection to the pull-in distance at zero applied pressure $\eta/\eta_{\text{PI,p0}}$. It is seen that the circular and square plate give almost identical results, whereas the parallel plate has a slight deviation. At 80 % of pull-in, which is where the CMUT is usually designed to operate, the deviation of the square plate result compared to the circular plate result is only 0.01 %. For the parallel plate the deviation is 0.3 % compared to the circular plate result.

2.2.4 Spring Constant

As mentioned earlier, the effective spring constant can be found by performing the double differentiation of the total potential energy with respect to center deflection, see (2.26). The generalized spring constant can be identified from the strain energy for both circular and square plates, (2.43) and (2.50), and for the parallel plate the spring constant is simply just k. All these expressions can be inserted into the generalized effective spring constant (2.26) to obtain the effective spring constant for each plate type. The effect of spring softening is easily seen in (2.26) as the second term and it is seen to depend on the capacitance. Furthermore, it is seen that the spring constant at zero applied voltage is the generalized spring constant.

In Figure 2.7, the effective spring constant relative to the spring constant at zero applied voltage k_{eff}/k_0 is shown versus the normalized relative deflection $\eta/\eta_{\text{PI,p0}}$ (lower axis) or normalized voltage (upper axis). The spring softening effect is clearly seen as the effective spring constant becomes smaller when the deflection and bias voltage increases. Again the circular and square plate behave almost identical

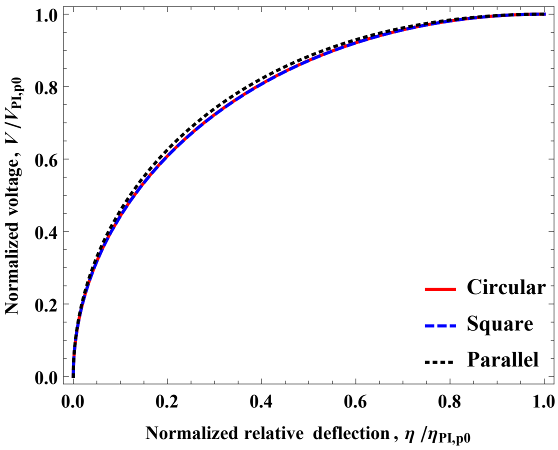

Figure 2.6: *Stable voltage normalized to pull-in voltage at zero applied pressure versus relative center deflection normalized to the pull-in distance at zero applied pressure for circular* (2.52), *square* (2.53) *and parallel plates* (2.54).

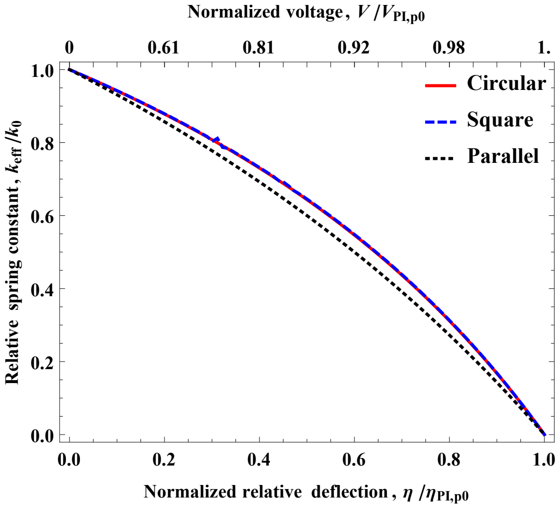

Figure 2.7: *Normalized effective spring constant versus relative center deflection normalized to the pull-in distance for circular, square and parallel plates.*

and the parallel plate approximation differs from the two. Operating at 80% of pull-in the deviation between square and circular plate results is 0.47% and for the parallel plate it is 12.5%.

In general, it is seen from Figs. 2.6 and 2.7 that the overall behaviour of the CMUT is well captured by both the more accurate results for the circular and square plates but also by the parallel plate approximation. The difference lies in the normalizations i.e. the pull-in point calculation which is different for each case when using the actual shape of the deflection. The anisotropic effects are included through these as well. This means that practically the simple expressions can be used to model the CMUTs with good approximations, if using the specific de-normalizations for each plate type.

2.2.5 Pull-in

For the parallel plate, the pull-in distance at zero applied pressure is given by $\eta_{\mathrm{PI,p0,parallel}} = 1/3$. The corresponding pull-in voltage is

$$V_{\mathrm{PI,p0,parallel}} = \sqrt{\frac{8kg_{\mathrm{eff}}^2}{27C_{\mathrm{t0}}}}. \tag{2.55}$$

The pressure dependence on the pull-in distance can be found analytically for this plate type and is given by

$$\eta_{\mathrm{PI,parallel}} = 1/3 + 2/3p_{\mathrm{r}}, \tag{2.56}$$

where the relative pressure is given by $p_{\mathrm{r}} = pA/(g_{\mathrm{eff}}k)$. The relative pressure is the applied pressure normalized to the pressure it takes to deflect the plate the size of the effective gap, p_{g}. Figure 2.8 shows the linear dependence of the pressure on the pull-in distance, (2.56), as the black dotted curve. The pressure dependent pull-in voltage can for the parallel plate also be calculated analytically and is given by

$$V_{\mathrm{PI,parallel}} = \frac{(-Ap + kg_{\mathrm{eff}})^3}{27C_{\mathrm{t0}}k^2g_{\mathrm{eff}}}. \tag{2.57}$$

It is seen that the influence of the pressure on the pull-in distance, and thus also the pull-in voltage, is dependent on the geometry of the device. Defining the relative pull-in voltage as $V_{\mathrm{rel}} = V_{\mathrm{PI}}/V_{\mathrm{PI,p0}}$ and using (2.57) and (2.55), the relative pull-in voltage for the parallel plate yields

$$V_{\mathrm{rel,parallel}} = (1 - p_{\mathrm{r}})^{(3/2)}. \tag{2.58}$$

Figure 2.9 shows a comparison of the relative voltage versus the relative pressure with a black dotted curve for the parallel plate.

Looking at the circular plate and the special case where the applied pressure is zero, the relative pull-in distance becomes $\eta_{\mathrm{PI,p0,circ}} = 0.463$ from (2.28). With this pull-in distance inserted into (2.52), the pull in voltage at zero applied pressure for the circular plate becomes

$$V_{\mathrm{PI,p0,circ}} = \sqrt{\frac{89.4459D_{\mathrm{eff}}g_{\mathrm{eff}}^2}{a^2C_{\mathrm{t0}}}}. \tag{2.59}$$

To find the influence of the pressure on the pull-in distance, (2.28) is evaluated for varying values of the pressure. The result can be seen as red points in Figure 2.8. As also observed by [39, 41], the influence

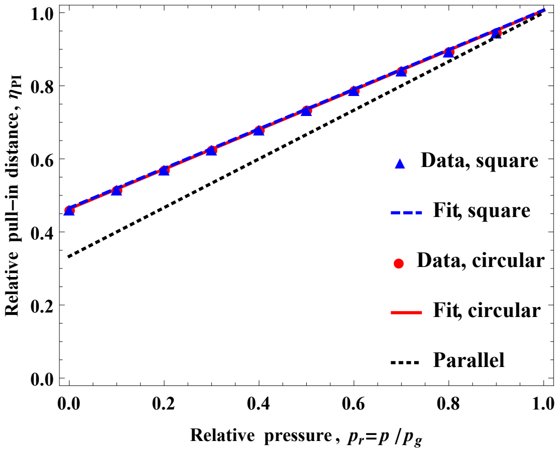

Figure 2.8: *Pull-in distance versus relative pressure. Circles are the full calculation for circular plates, triangles the full model for square plates, the red solid curve a fit for the circular plate* (2.61)*, blue dashed curve a fit for the square plate* (2.64) *and black dotted the analytical expression for the parallel plate* (2.56).

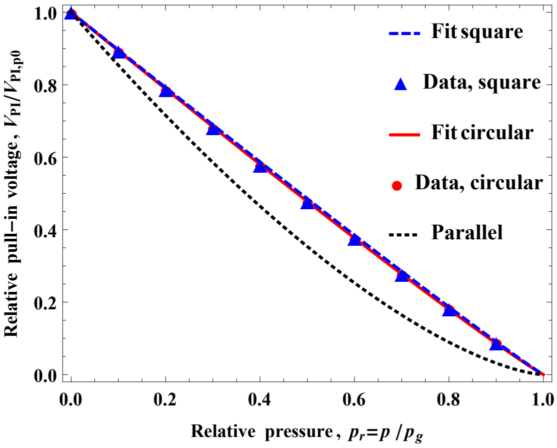

Figure 2.9: *Pull-in voltage relative to pull-in voltage for zero applied pressure versus relative pressure. Circles are the full calculation for circular plates, triangles the full model for square plates, the red solid curve a fit for the circular plate* (2.62)*, blue dashed curve a fit for the square plate* (2.65) *and black dotted the analytical expression for the parallel plate* (2.58).

of the pressure on the pull-in distance is found to be linear as for the parallel plate. The expression can be found by considering the boundary conditions $\eta_{\mathrm{PI}}(0) = \eta_{\mathrm{PI,p0}}$ and $\eta_{\mathrm{PI}}(1) = 1$. Using these conditions the expression for the pressure dependent relative pull-in distance becomes

$$\eta_{\mathrm{PI}} = \eta_{\mathrm{PI,p0}} + (1 - \eta_{\mathrm{PI,p0}})p_{\mathrm{r}}, \tag{2.60}$$

where the relative pressure is given by $p_{\mathrm{r}} = p/p_{\mathrm{g}} = pa^4/(64g_{\mathrm{eff}}D_{\mathrm{eff}})$ for the circular plate. Inserting $\eta_{\mathrm{PI,p0,circ}} = 0.463$ for the circular plate yields

$$\eta_{\mathrm{PI,circ}} = 0.463 + 0.537p_{\mathrm{r}}. \tag{2.61}$$

Eqn. (2.61) is plotted as the red solid curve in Figure 2.8. The maximum deviation between the expression and the data points is 0.6 %. Compared to the parallel plate solution the difference in pull-in distance at zero applied pressure is clearly observed. Furthermore, note that (2.60) also applies for the parallel plate as seen in (2.56).

To see how the pressure affects the pull-in voltage for the circular plate the relative pull-in voltage is again considered. For simplicity, the equation for the pressure dependent pull-in voltage is not shown, but it is found from the pull-in distance, (2.61), inserted into the stable position, (2.52). The resulting equation is evaluated for varying values of pressure and this is shown as red dots in Figure 2.9. It is seen that the pull-in voltage decreases for increasing external pressure as expected, since the plate is deflected due to the applied pressure. To follow the analytical expression obtained for the parallel plate, a fit was made to an expression having the same form as this analytical result $V_{\mathrm{rel}} = (1 - p_{\mathrm{r}})^{(K \cdot 3/2)}$, where K is the fitted parameter. The result from fitting is

$$V_{\mathrm{rel,circ}} = (1 - p_{\mathrm{r}})^{(0.710 \cdot 3/2)}, \tag{2.62}$$

Using this fit a maximum deviation of only 3.9 % is obtained. Also for the pull-in voltage, a difference is observed between the the parallel and circular plate.

To expand this pull-in investigation to square plates as well, the same procedure as for the circular plates is followed. For the square case, the pull-in distance in the special case of zero applied pressure becomes $\eta_{\mathrm{PI,p0,sq}} = 0.466$ which is very close to the circular plate pull-in distance. The corresponding pull-in voltage is

$$V_{\mathrm{PI,p0,sq}} = \sqrt{\frac{2.95118 g_{\mathrm{eff}}^2 h^3 \xi_{\mathrm{s}}}{C_{\mathrm{t0}} L^2}}. \tag{2.63}$$

To find the influence of the pressure on the pull-in distance for the square plate it was calculated for different pressures and plotted as triangular points in Figure 2.8. A linear fit to the data points are shown as a dashed blue line. As for the two other plate geometries, the influence of the pressure on the pull-in distance is found to be linear and using (2.60) it can be described as

$$\eta_{\mathrm{PI,sq}} = 0.466 + 0.534p_{\mathrm{r}}, \tag{2.64}$$

where the relative pressure for the square plate is given by $p_{\mathrm{r}} = 0.021961pL^4/(g_{\mathrm{eff}}D_{\mathrm{a}})$. The maximum deviation between the fit and the data points for the square plate is 0.7%.

In Figure 2.9 it is seen how the pressure affects the pull-in voltage for the square plate shown as triangular points and a fit with a dashed blue line. The calculation method is the same as for the circular

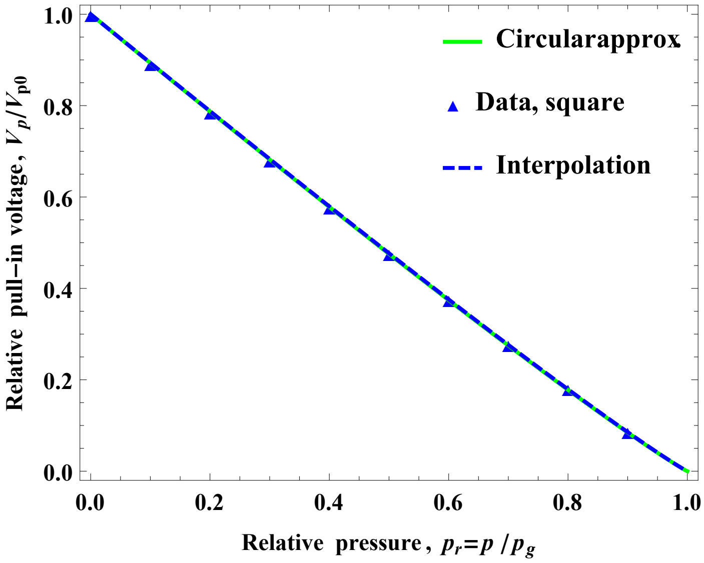

Figure 2.10: *Pull-in voltage relative to pull-in voltage for zero applied pressure versus relative pressure for a square plate using the interpolating function (blue, dashed) and an approximation of the capacitance using the circular expression (green, solid). The triangles are the original data points calculated from the full solution.*

plate, and the same behavior is also observed. A fit of the data points to an expression of the same form as for the parallel plate case yields

$$V_{\mathrm{rel,sq}} = (1 - p_{\mathrm{r}})^{(0.712\cdot 3/2)}, \tag{2.65}$$

resulting in a maximum deviation of 1.7%.

As it can be difficult for others to use the interpolation function in (2.34), and since the results for a circular and square plate are close to each other, the expression for the total capacitance of the circular plate (2.31) can be used for the square plate instead of the interpolation function due to the similarity of the results. If the same pull-in analysis is carried out, the same pull-in distance is obtained and the result for the relative pull-in voltage versus relative pressure can be seen in Figure 2.10. The data points show the result using the interpolation function. The fit to the expression in (2.58) when using the circular capacitance is shown together with the previous fit for the square plate using the interpolating function. The fit of the data points in this approximation case case yields

$$V_{\mathrm{rel,sq}} = (1 - p_{\mathrm{r}})^{(0.715\cdot 3/2)}, \tag{2.66}$$

The two curves look the same and the maximum deviation from the data points is only 1.6 %. The deviation is highest for higher relative pressure and realistic values for CMUTs would be in the lower end. The relative pressure for the fabricated square device, see Table 2.5, is 0.02 which gives a deviation of only 0.01 % when using the circular plate capacitance.

2.3 Measurements

To compare the anisotropic approach for modeling CMUTs to measurements for further validation of the theory for both circular and square plates, devices with both plate types were fabricated using a fusion bonding method [68]. The dimensions of the devices can be seen in Table 2.5.

Measurements of the stable position (presented as the deflection in the center of the plate) for increasing bias voltage were performed on the fabricated devices. The deflections were measured as area scans with a Sensofar PLu Neox 3D Optical Profiler using white light interferometry.

Figure 2.11 shows the measurements of the circular plate device. It is seen how the center deflection varies with the applied voltage and how it deflects more when approaching the pull-in voltage as expected. The center deflection for the measurements is found as the average of 10 cells and gray shaded areas corresponds to plus/minus two standard deviations. For the circular device there was some uncertainty in the final gap height due to the fabrication method. Because of this it was not possible to plot the theoretical stable position for a circular plate, (2.52), together with the measurements. Instead a fit was made which is shown as the theoretical curve in Figure 2.11. From the fit a gap height of 457 nm was found and it is seen that the expression captures the behavior of the device very well. With this gap, the theoretical curve is within the uncertainty interval of the measurements. Also, the pull-in voltage is in good agreement with the experimentally found value, as it was measured to be 140 V, compared to an expected value of 138 V from the anisotropic model (2.62).

Measurements with a DC voltage applied were also performed for the square plate and the results are shown in Figure 2.12. The center deflection for the measurements is found as the average of 10 cells and the gray shaded areas correspond to plus/minus two standard deviations. The theoretical curve is made from the stable position analysis and is for this case plotted directly as the gap height was known from this fabrication run. It is seen that the anisotropic theory matches well with the measurement as it is within the error margin. Also, the pull-in voltages are in good agreement as it was measured to be

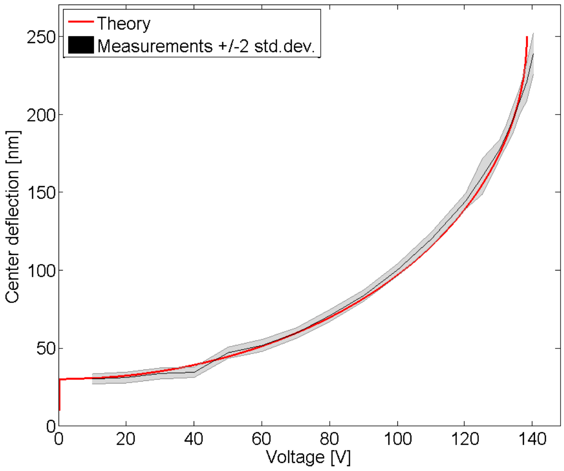

Figure 2.11: *Measured center deflection for increasing bias voltage together with theoretical curves for a circular plate* (2.52).

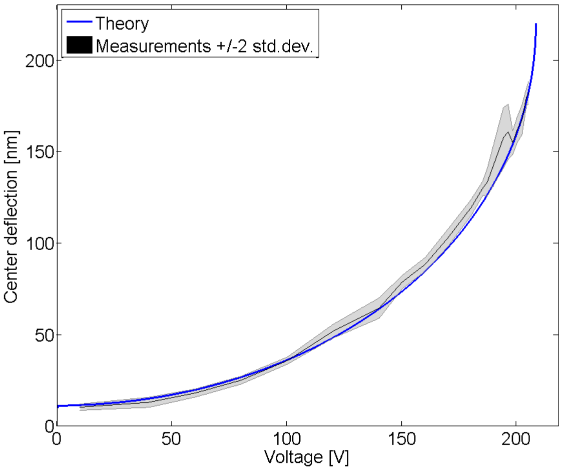

Figure 2.12: *Measured center deflection for increasing bias voltage together with theoretical curves for a square plate* (2.53).

206 V, compared to an expected value of 201 V from the anisotropic model (2.65).

2.4 Summary

In this chapter it was demonstrated how wafer bonded CMUTs with both circular and square plates can be analytically modelled using the full anisotropic properties of single crystalline silicon. The solutions for the deflections were compared to FEM showing a maximum of 0.3 % difference. The theory of multilayer plates was also applied to CMUTs and the result compared to a deflection measurement of a fabricated device.

A full electrostatic analysis including the anisotropic effects was carried out for both circular, square, and parallel plate devices. The analysis was based on energy considerations, and capacitance, effective spring constant, stable position, pull-in distance, and pull-in voltage were all calculated. In the pull-in analysis the pressure dependence was also included. The circular and square plate devices were seen to behave very similar whereas the parallel plate approximation resulted in a slightly higher deviation.

Devices with both circular and square plates were fabricated and the stable position and pull-in voltage measured. Comparing these to the anisotropic theory, it was seen that the theory was within the uncertainty interval of the measurements in both cases.

The analytical models described in this chapter was developed during the project to help the design process and prediction of the device behavior. It was described in two accepted conference papers [48, 49] and one submitted journal paper [63]. For a complete design tool the dynamics of the plate should be included as well which has partly been done through FEM with Comsol. A study of dimensional scaling for CMUT and how this influence the device performance was presented in [69], see appendix G. These models helped in the design process and the description of device in the next two chapters.

CHAPTER 3

Stanford Arrays

The first version of 1D array CMUTs in this project were fabricated at Stanford University. The idea was to utilize an already existing fabrication process to obtain working devices. The purpose of this was to collect knowledge and experience in how to fabricate and characterize the CMUTs and how to operate them to make images.

3.1 Layout and Design

As the process was based on fusion bonding two wafers were used. One was a highly doped silicon substrate wafer and the other a silicon-on-insulator (SOI) wafer with a highly doped device layer. The substrate and device layer needed to be highly doped as they would form the two electrodes of the capacitor.

The masks were reused from a previous process, fixing all lateral dimensions of the devices. The mask layout of a full wafer can be seen in Figure 3.1a and had 15 arrays with square cells and 6 arrays with circular cells. A zoom on one of the square cell arrays can be seen in Figure 3.1b. The CMUT cells are red, the rings to etch edge bumps (explained in the processing section 3.2) are blue, top contact and plate metallizations are grey and bottom contacts are green. The element pitch was defined in the same way as in Figure 1.12 and it was set to be 300 µm for this design. The pitch was the same for the square and circular cell arrays. The sidelength of the square cells were 40 µm, and the radius of the circular cells were 48 µm.

The vertical dimensions could be varied to adjust the resonant frequency of the transducers. Two versions of the process were carried out to make devices with two different resonant frequencies, called type 1 and 2. For the type 1 devices the desired immersion frequency was 5 MHz and for type 2 it was 2.6 MHz. They are designed to make one of them a linear array and the other a phased array.

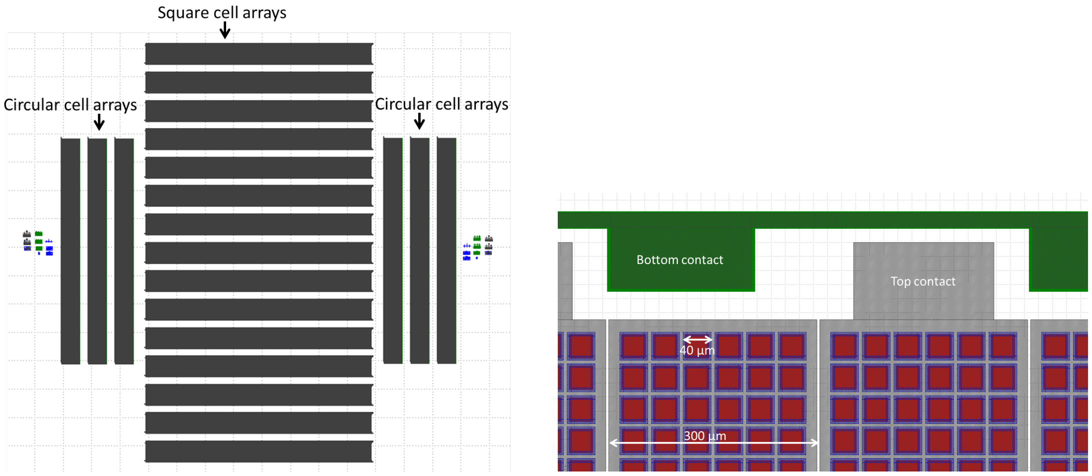

(a) *Full wafer layout.* (b) *Layout of a square cell array.*

Figure 3.1: *Mask layout for 1D Stanford arrays with square and circular cells. a) The full wafer layout showing 15 1D arrays with square cells and 6 1D arrays with circular cells and alignment marks to the sides. b) Zoom on one end of 2 square cell elements, showing bonding pads to opposites for every second element and one long ground pad along the array. The pitch is* 300 µm *and the cell side length* 40 µm.

3.1.1 Device Dimensions

The cell dimension, plate thickness and gap height was decided using the CMUT program developed by the Stanford group. This was a MATLAB program using a Graphical User Interface (GUI) and could model the CMUT using simple plate theory and a lumped element circuit model. The transmitted pressure, the received signal and the plate displacement, when applying a DC voltage, were all analyzed using the GUI program.

The focus of the design process optimization was the square shaped cells, and the results for the circular plates were afterwards checked to be acceptable for obtaining working devices with the final dimensions of each device type. First, the plate thickness was optimized by looking at the transmitted pressure in a non-linear transient response. A sine wave was used as input waveform and an AC voltage of 100 V was used on top of a DC voltage of 130 V. The period of the sine wave was adjusted until a maximum in the signal was obtained (resonance). Plate thicknesses of 1.5 µm and 1.77 µm were obtained for the type 1 and 2 devices, respectively. The final plate thickness was decided from the availability of SOI wafers in stock.

The gap height was now fixed by looking at the displacement of the plate when the device was in transmit mode and applying only a DC voltage. The intention was to maximize the space within the vacuum gap, where the plate could move without reaching pull-in. It was found that the gap should be 400 nm for device type 1 and 300 nm for device type 2. The expected pull-in voltage was also found in this analysis.

Last, the frequency response was checked to make sure the operation frequency was correct. For these devices the resonant frequency would be a bit higher than the operating point, but due to a large

Table 3.1: *Device dimensions for the Stanford arrays of type 1 (linear, 5 MHz) and type 2 (phased, 2.6 MHz).*

	Type 1, square	**Type 1, circular**	**Type 2, square**	**Type 2, circular**
Plate size, $2a$ or $2L$	40 µm	48 µm	40 µm	48 µm
Plate thickness, h	1.77 µm	1.77 µm	1.5 µm	1.5 µm
Vacuum gap height, g	400 nm	400 nm	300 nm	300 nm
Insulation thickness, t_{ox}	200 nm	200 nm	200 nm	200 nm
Pull-in voltage, V_{PI}	(150 V)	188 V	(160 V)	199 V

bandwidth, it should not be a problem. The final desired dimensions for each device type can be seen in Table 3.1. The parentheses for the square cells indicate that the program did not model the square cells very precisely as it only provided estimates for this plate type.

3.2 Fabrication Process

As previously mentioned, the devices were fabricated with a fusion bonding process and the overall process flow is illustrated in Figure 3.2. The details and results from the fabrication will be explained in this section, and the full process flow can be seen in appendix A.

Step 1: Oxidation to Create Support Posts

First step of the process was to oxidize the substrate wafer to create oxide support posts, see Figure 3.2a. The oxidation was performed as a wet oxidation at 1000°C for 1:15 or 1:52 hours in a Thermco furnace. The grown oxide thickness was 365 nm and 450 nm for device type 1 and 2, respectively.

Step 2: Etch of Cavities

The second step was to etch cavities in the oxide, see Figure 3.2b. This was done by a wet etch in 6:1 Buffered Oxide Etch (BOE) solution. This BOE consisted of approximately 6 parts 40 % ammonium fluoride (NH_4F) and 1 part 49 % hydrofluoric acid (HF), thus, it was approximately 34 % NH_4F, 7 % HF, and 59 % water. All wafers were etched for 6 min. As the bonding surface was covered by resist during the etch, the surface roughness of the oxide was unaffected. Figure 3.3 shows microscope pictures of circular and square cells etched in the oxide.

Step 3: Oxidation to Create Insulation Layer

A second oxidation of the substrate wafer was performed to make an insulation layer at the bottom of the cavity, see Figure 3.2c. This was done by dry oxidation to obtain the best quality of the oxide. The process was performed in a Thermco furnace at 1100°C in two steps: one of 1:45 hours where most of

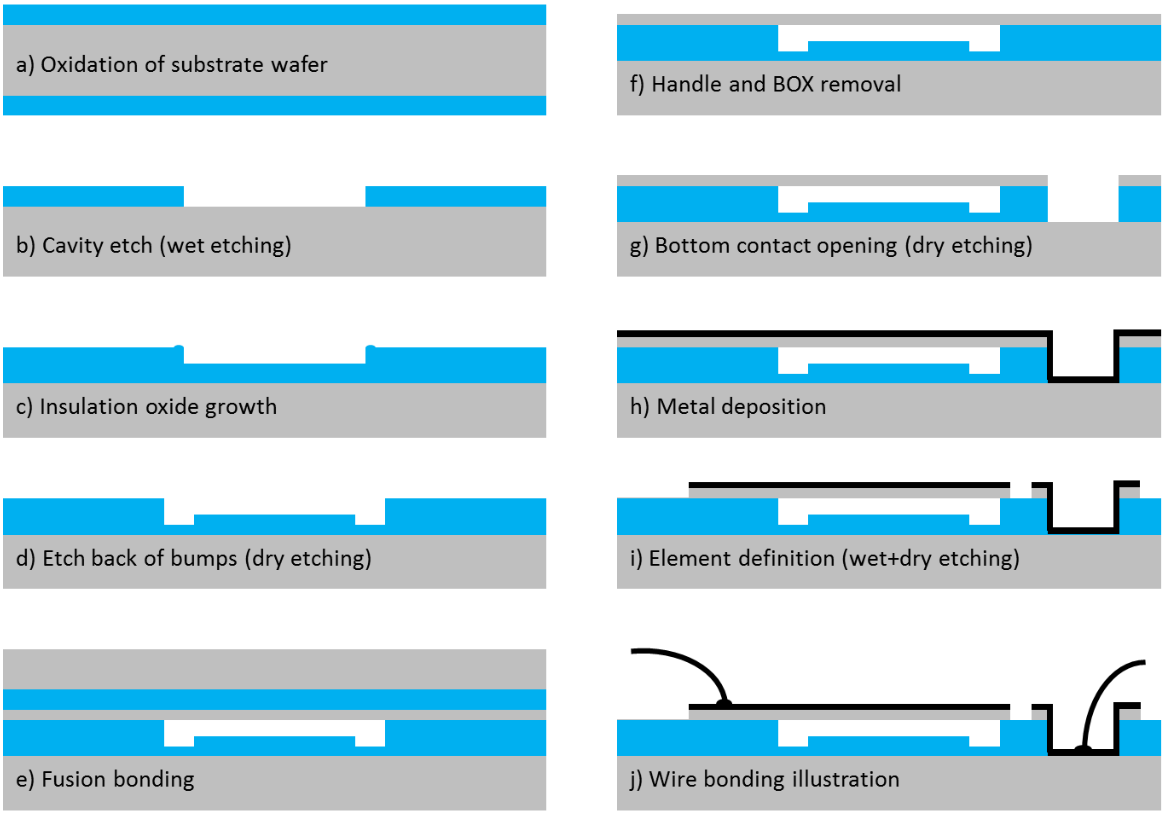

Figure 3.2: *Process flow overview of the fusion bonding process made at Stanford. a) Oxidation of highly doped substrate wafer; b) defining cavities by wet etch of the oxide; c) growth of insulation oxide layer in the bottom of the cavity; d) etch back of oxide bumps at the corners of the cavities; e) fusion bonding to SOI wafer; f) removal of handle and BOX layer of the SOI by grinding and etching; g) opening up to the substrate by etching; h) metal deposition; and i) defining top plates and contacts by etching. j) The finished device after dicing and wirebonded.*

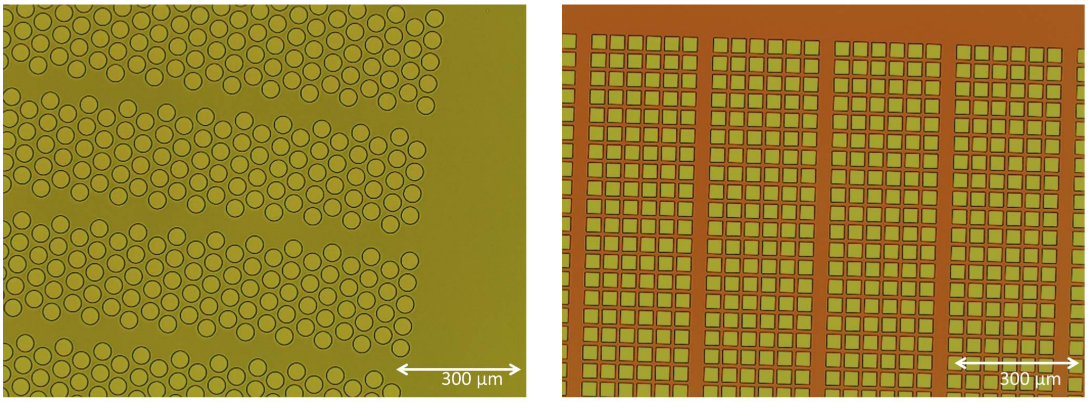

(a) *Circular cells on type 1 device.* (b) *Square cells on type 2 device.*

Figure 3.3: *Microscope pictures of wafers after etching cavities in the oxide. a) Circular cell on a type 1 array and b) square cell on a type 2 array. The color of the oxide is seen to be different for the two array types due to the two thicknesses.*

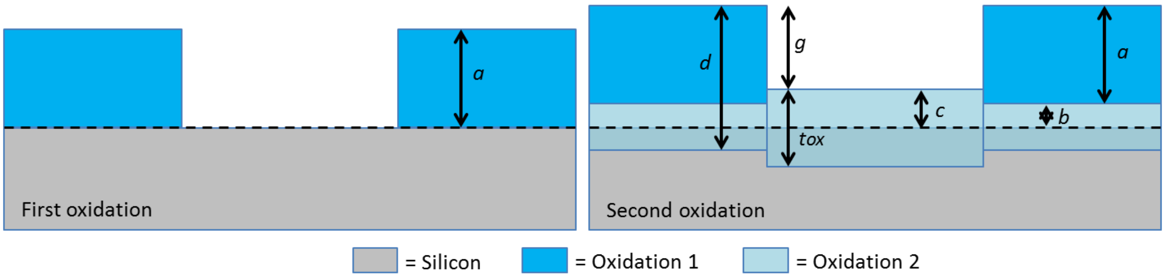

Figure 3.4: *The final depth of the cavities are determined from measuring the various thickness after the double oxidation. The oxide thickness after the first oxidation a is measured as well as the oxide thickness inside t_{ox} and outside d of the cavity after the second oxidation. From this the c and b can be found and the gap height can be calculated.*

the oxide was grown and an other of 30 minutes to grown the rest. This two step process was used to control the thickness of the layer more precisely. The desired thickness was 200 nm and a thickness of 210 nm was obtained.

The depth of the cavity was determined from the measurement of the different oxide thicknesses as illustrated in Figure 3.4. The oxide thickness after the first oxidation, a, was measured to be 365 nm and 450 nm for device type 1 and 2, respectively. The oxide thickness inside the cavity, t_{ox}, after the second oxidation were measured to be 209 nm for both types. The oxide thickness outside the cavity, d, were measured to be 433 nm and 509 nm for device type 1 and 2, respectively. Using the fact that 46 % silicon is consumed during an oxidation, $c = 0.54 \cdot t_{ox}$ and $b = 0.54 \cdot (d - a)$. The gap heights was then calculated as $g = (a + b) - c = a + 0.54 \cdot (d - a) - c$, and the results were 0.289 µm and 0.369 µm for type 1 and 2, respectively. It was taken into account in the oxidation times that the oxide grows faster on the silicon surface than on the silicon-oxide interface. The stated thickness for a, t_{ox} and d were averages obtained from one wafer with 5 measurement points using a Nanospec 210XP (uses spectro-reflectometry). To take into account that the numbers might be slightly different between wafers of the same type, the final values were rounded off. A gap height of 290 nm and 370 nm were obtained for the type 1 and 2 device, respectively. Both devices had an insulation oxide thickness of 210 nm.

The gap heights were also measured using a profiler (Tencor P2 Long Scan Profiler) on test wafers to avoid scratching of the bonding surface. Rounding off the values, 270 nm and 370 nm were measured, respectively, confirming the calculated results.

Step 4: Etch of Oxide Bump

The second oxidation step resulted in oxide bumps at the corners of the first oxide which could ruin the fusion bonding process [68]. To remove these bumps, an extra etching step was made to lower the bumps under the bonding surface, see Figure 3.2d. Etching of the bumps was performed with dry etching of the oxide using the AMT 8100 Plasma Etcher with a standard oxide etch recipe which used mainly CHF_3 and some O_2 gasses. Figure 3.5 show the wafers after etching of the oxide bumps.

Step 5: Fusion Bonding

Before this step was performed the surface roughness of the bonding surface was measured using AFM (Digital Instruments AFM Nanoscope Dimension 3000) to check that it was suitable for fusion bonding after processing of the wafers. As a rule of thumb the surface roughness should be below 0.3 nm to be able to get a strong bonding. If the roughness was too high, the wafers could not be bonded together.

The wafer bow was also monitored with a stress gage (Flexus 2320) after each step in the process and should be minimal before the bonding and preferably be convex rather than concave.

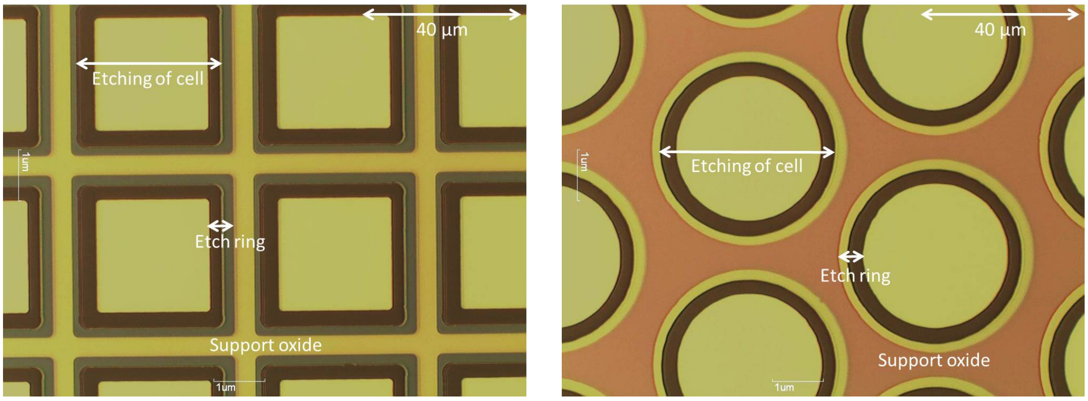

(a) *Square cells on type 1 device.*

(b) *Circular cells on type 2 device.*

Figure 3.5: *Microscope pictures after etching the ring covering the oxidations bumps. a) A type 1 devices with square cells and b) a type 2 device with circular cells. The colors of the support oxide and the insulation layer oxide are seen to be different and the ring is also seen to have two thicknesses.*

The measured surface roughness was around 0.1 nm for a sample on each of the two kind of SOI wafers and the wafer bow was convex with 5-15 μm maximum bending for both substrate and SOI wafers which satisfied the requirements for bonding.

The bonding, see Figure 3.2e, was performed using a Süss wafer bonder at a temperature of 50°C followed by an annealing in a Thermco furnace at 1050°C for 4 hours. The annealing after bonding was done as a wet oxidation to obtain a thick oxide layer on the backside of the wafer, which protected the backside from getting etched, when the handle layer was removed.

Step 6: Grinding and Etching to Release Plate

After fusion bonding most of the handle layer of the SOI was removed by grinding (mechanical removal). The last $220-270$ μm were removed in a TMAH (Tetramethylammonium hydroxide) etch. TMAH temperature was 70-95°C during etching and etch time was around 9 hours.

The handle removal was followed by BOE etching of the buried oxide layer, see Figure 3.2f. The deflection of the plates due to atmospheric pressure was measured using an interferometer. The deflection was 10-30 nm for circular and square cells which was expected from calculations using the CMUT code described earlier.

Step 7: Etching of Bottom Contacts

Next step was opening of the bottom contacts to the substrate wafer, see Figure 3.2g. This was done by dry etching of the silicon device layer and of the support oxide. For opening the silicon a Drytek2 Model 100 was used with the standard recipe for silicon etching which used mostly SF_6 and some F_{22} gasses. For opening the support oxide the AMTecher and the standard oxide receipe also used in step 4 was used again. A microscope picture of a device after etching can be seen in Figure 3.6. Besides the bottom contacts, the cavities can also be seen through the device layer.

Step 8: Metalization of Top Contacts

The last steps of the Stanford process was deposition of metal and definition of the top plates and contacts, see Figure 3.2h-i. A 400 nm thick aluminum layer was deposited (done outside the regular cleanroom) and patterned using wet aluminum etching. A premixed aluminum etchant (AL-11 Cyantek Aluminum Etchant) was used which consisted of 72 % Phosphoric Acid, 3 % Acetic Acid, 3 % Nitric Acid, and 22 % water. The pattern was also transferred to the silicon device layer to remove the highly doped material in the regions outside the top plates. For this the standard silicon recipe, see step 7, in the Drytek2 was used. Figure 3.7 shows a device after etching.

A picture of a finished wafer can be seen in Figure 3.8. The yield was very close to 100 % for this process run as there was only one small void on one of the five wafers, ruining around 10 elements on one of the arrays. Figure 3.9 shows a picture of two of the finished device, one of each type.

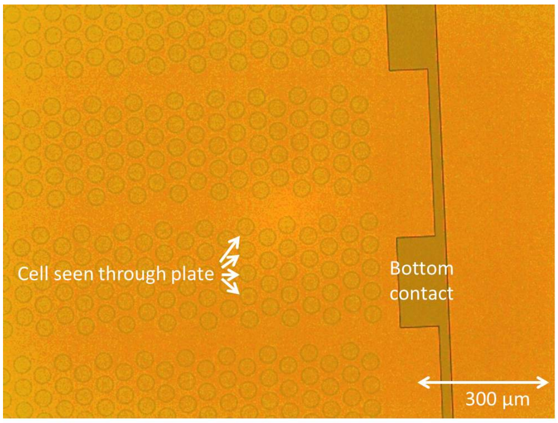

Figure 3.6: *Microscope picture after opening to the bottom substrate. The bonding pads are seen as wider areas for every second element and the cells can be seen through the plate.*

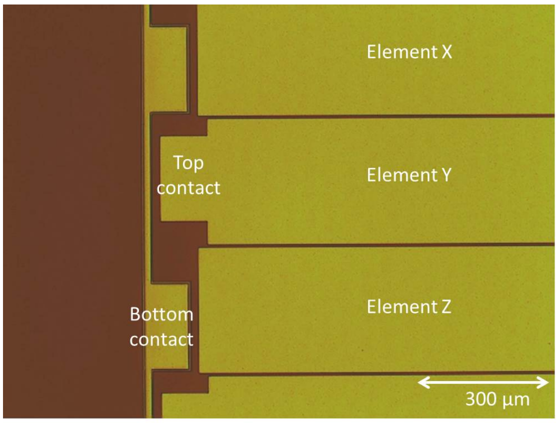

Figure 3.7: *Microscope picture after etching the top plates. Aluminum is used for bottom and top contacts and plate metallization. Three elements are seen with contacts in the ends.*

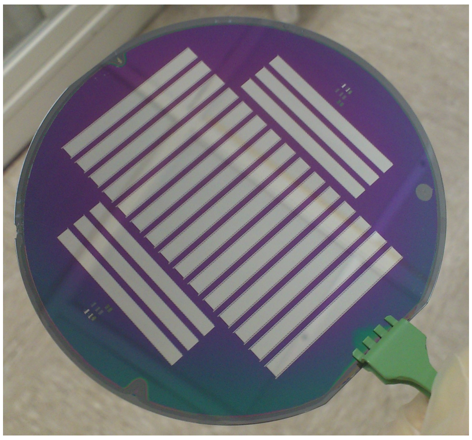

Figure 3.8: *Full wafer after processing. Each wafer yield 21 devices.*

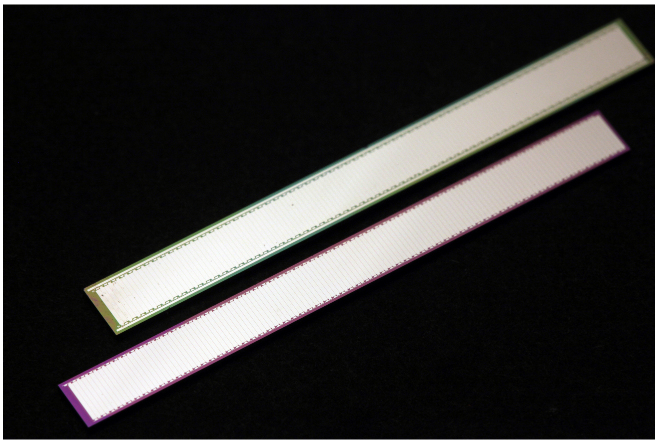

Figure 3.9: *A finished type 1 (green, upper) and type 2 (purple, lower) device.*

3.3 Characterization

A CMUT array should be characterized in several ways after fabrication. First are electrical measurements using an impedance analyzer and these are often followed by acoustical measurements. Both characterizations have been carried out on the Stanford arrays and are described in the following.

3.3.1 Impedance Measurements

The first thing to characterize was if the resonant frequency and the pull-in voltage were as expected. With the impedance analyzer, the measurements were made in air. Measuring in air would result in a higher resonant frequency than the immersion resonant frequency. The desired resonant frequencies

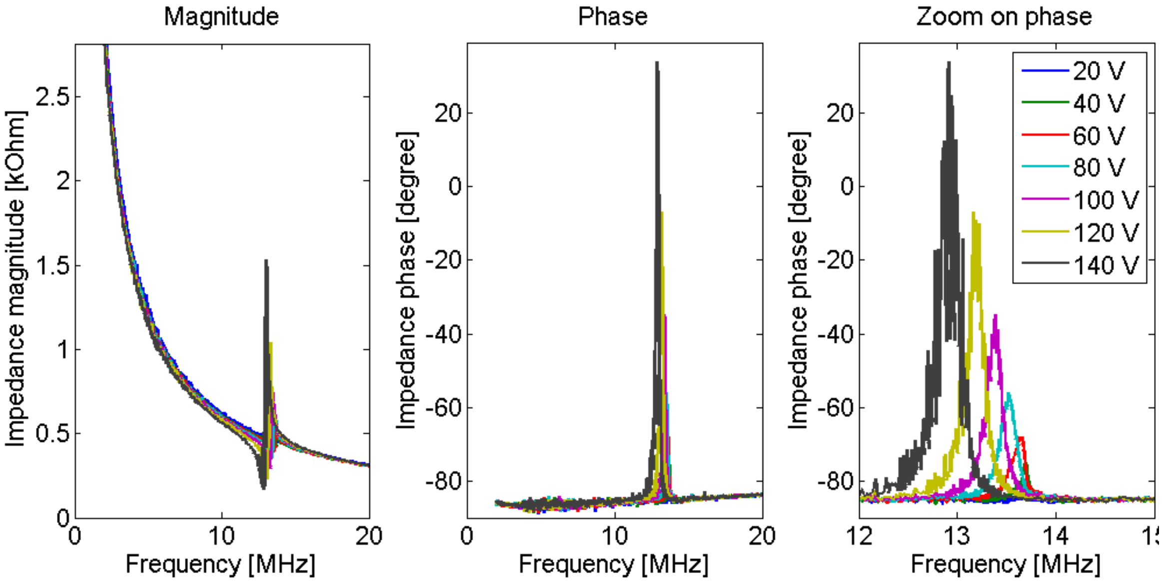

Figure 3.10: *Impedance magnitude and phase for a center element on a type 1 device. The capaciive behavior of the device is seen in the magnitude plot. The resonant frequency is easily found as the peak in the phase plot and the spring softening effect is seen as a lower resonant frequency for higher applied voltages.*

specified during design of the CMUTs were the immersion resonant frequency, and the measured would therefore be higher than the desired frequency.

Impedance measurements on a center element on a type 1 array can be seen in Figure 3.10 for varying bias voltage. The resonant frequency was clearly seen as well as the spring softening effect, which reduced the resonant frequency when the bias was increased. The resonant frequency for type 1 devices was found to be 13.4 MHz. Figure 3.11 shows similar impedance measurements of a type 2 array and the same effects were seen. The resonant frequency for type 2 devices was determined to be 11.7 MHz. It was noted that for both arrays the maximum in phase angle crossed 0° in the phase and reached more than 20°. This was comparable to what others have reported [58] and should be enough signal to make ultrasound images.

Uniformity

It is very important to have a high uniformity across the array, so each element will operate in the same way when making images. The uniformity across the array can be found through impedance measurements. Figure 3.12a shows the resonant frequency found for each element in two different arrays from the same wafer. A bias voltage of 60 V was used and the frequency was found from the maximum of the phase angle measurement. The two arrays were seen to have a mean resonant frequency of 11.83 ± 0.02 MHz and 11.80 ± 0.03 MHz respectively, indicating a very high uniformity both between the two arrays and between the elements. Within one array the deviation of each element from the mean value was less than 1 % as can be seen in Figure 3.12b.

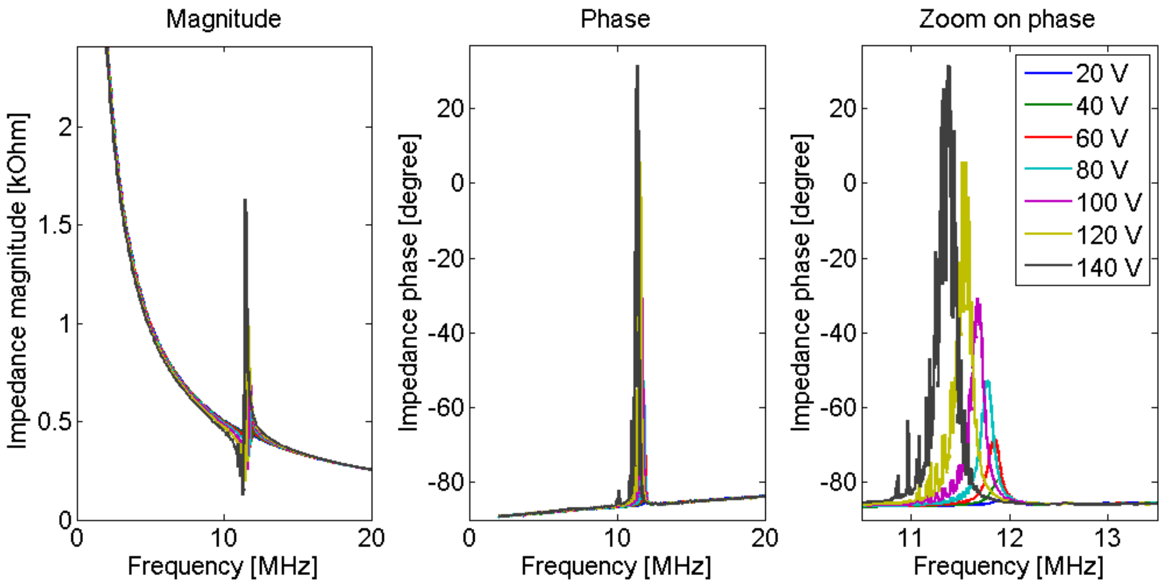

Figure 3.11: *Impedance magnitude and phase for a center element on a type 2 device. The capaciive behavior of the device is seen in the magnitude plot. The resonant frequency is easily found as the peak in the phase plot and the spring softening effect is seen as a lower resonant frequency for higher applied voltages.*

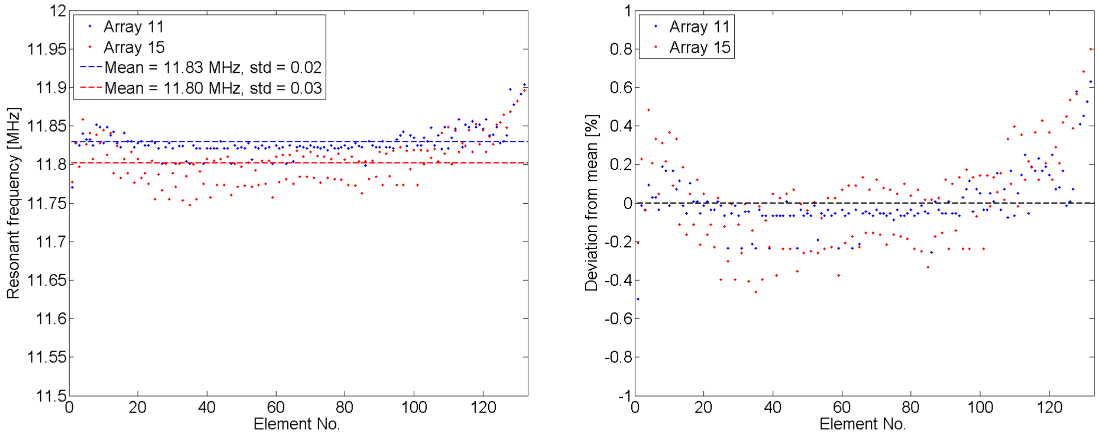

(a) *Resonant frequency found from maximum in phase angle.*

(b) *Deviation of resonant frequency from mean of all elements.*

Figure 3.12: *Uniformity in resonant frequency of all elements of two CMUT arrays of type 2 from the same wafer (a). The uniformities between arrays and between elements are seen to be good with less than 1 % deviation for all elements (b).*

3.3.2 The Vermon Probe

The acoustical testing with the Stanford arrays were done in a slightly unconventional manner. An array was shipped to Vermon (Vermon, Tours, France) and they assembled the chip into a probe handle, complete with electronics. The finished probe can be seen in Figure 3.13a with an unmounted chip in front of it. The probe needed to be operated using a separate DC supply cable besides the standard BK transducer cable. The DC supplies for bias and electronics were made using a push-pull connector (Lemo, Gentofte, Denmark) which can provide the necessary DC voltages both to the electronics and for biasing the CMUT. A special power supply was also made for the probe. All this can be seen in the picture in Figure 3.13b.

Initial Measurements

The probe was connected to the experimental Synthetic Aperture Real-time Ultrasound System (SARUS) [70] at CFU. As seen in the impedance measurements and from the design of these devices, the pull-in voltage should be above 200 V. There had previously been indications that some of the elements had a lower breakdown voltage of the oxide. Vermon provided initial acoustical tests of the probe during mounting and a bias voltage of 60 V was used during these measurements. Turning the DC supply to 60 V bias at DTU caused the probe to stop working. As the electronic configuration was unknown to others than Vermon, it was a challenge to troubleshoot and find the problem. It was found that the problem was a shorted element and the solution was to pull out the pin in the connector for that element, then the rest of the probe worked again. From this it was learned that the elements had a much lower breakdown voltage than expected, and that this probably happened due to low oxide quality. Furthermore, the importance of making sure in the electronics configuration that the probe could work with a shorted element was realized.

An evaluation of which elements were working, a hydrophone was placed around 37 mm from the

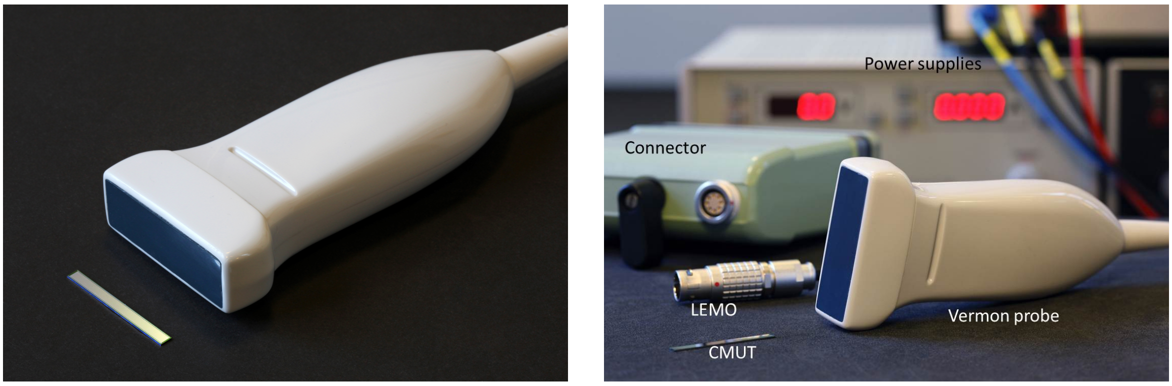

(a) (b)

Figure 3.13: *Stanford chip mounted in probe handle with electronics by Vermon. a) Probe handle with a similar chip in front. b) Probe handle with the lemo connector, transducer cable and power supplies used to operate the probe.*

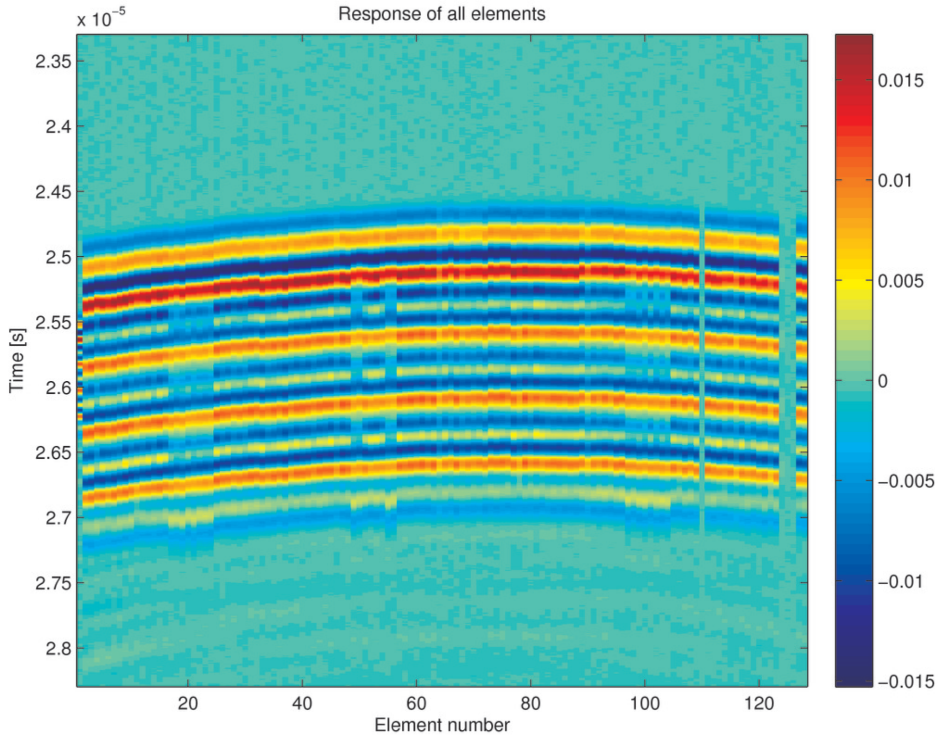

Figure 3.14: *Output signal from all elements in the Vermon probe measured with a hydrophone. Four elements are seen to be acoustically dead in one of the ends. No bias is used and the excitation is 8 pulses with a 25 V AC signal. The colorbar is in volts.*

transducer. The transmitted pressure was measured using an oscilloscope. The bias was in this experiment 0 V and the AC transmit signal was ±25 V. The resulting signals can be seen in Figure 3.14. It is seen that all elements except four are working. The three of these elements had most likely been shorted from the beginning and therefore not connected to the channels in the probe handle by Vermon. It was the short circuiting of the forth element that caused the problems until it was disconnected in the connector.

Ultrasound Imaging

The mounted probe was used to make the very first ultrasound images with CMUTs at DTU. The image can be seen in Figure 3.15 and depicts the hydrophone. The tip of the hydrophone is seen as the white dot in a depth of 55 mm and the sides of it can be distinguished as well. The images was made with the dynamic receive focusing technique using 64 electronically focused elements in transmit with a Hamming apodization across the array at 5 MHz. The focus depth was 55 mm, number of emissions 128, the DC bias 50 V, and the AC voltage 25 V.

Imaging were also performed testing several imaging methods. The tested imaging methods were dynamic receive focusing (DRF), synthetic aperture (STA) imaging and tissue harmonic imaging (THI) combined with both of the first mentioned methods. For DRF the images were made using 64 electronically focused (55 mm) elements in transmit with a Hamming apodization across the array at

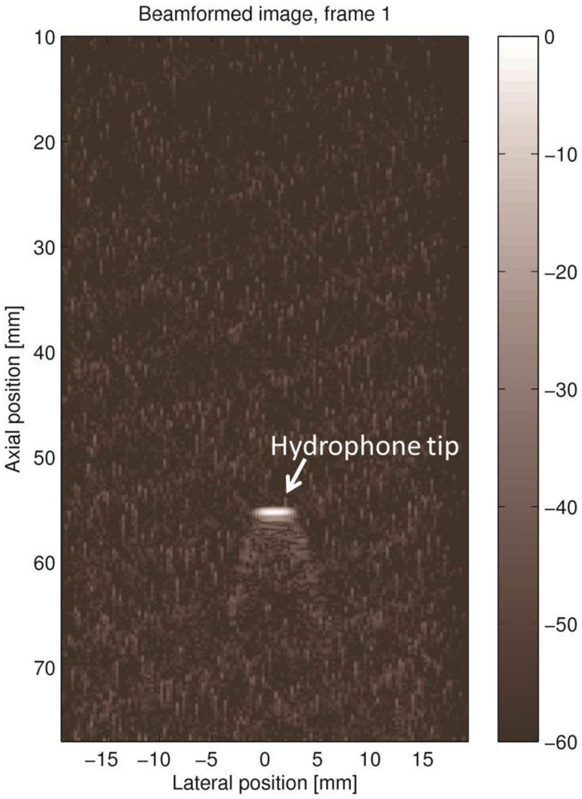

Figure 3.15: *First CMUT image from DTU which uses the Vermon probe. The tip of a hydrophone can be seen in a depth of 55 mm and sides can be distinguished as well. The colorbar indicates dB level.*

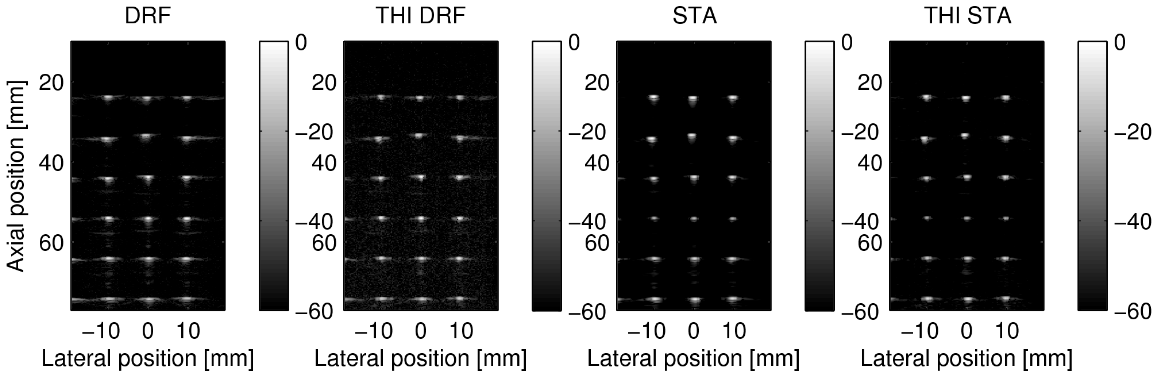

Figure 3.16: *Ultrasound images with the Vermon probe using different imaging methods: Dynamic receive focusing, Tissue harmonic imaging with dynamic receive focusing, Synthetic transmit aperture and Tissue harmonic imaging with Synthetic transmit aperture.*

5 MHz. For the SA imaging, single element emissions at 5 MHz were used. For THI the excitation was a 2 cycle sinusoidal pulse with a center frequency of 3 MHz which was lower than the transducer resonant frequency but within the -6 dB bandwidth. This was in order to have the second harmonic (for which signals are received) within the -6 dB bandwidth. In all cases 128 emissions were used and each image was an average of 10 frames. The probe was operated with a 50 V DC bias and a 25 V AC voltage. The probe was placed on a multiwire phantom and the resulting images can be seen in Figure 3.16. It was seen that STA performs better than DRF, and that THI improves the image slightly. However, it was found that THI was probably not using real pulse inversion since the bias was so low that sound would be emitted at higher harmonic frequencies from the beginning and not generated in the tissue.

3.4 Summary

In this chapter the first 1D arrays fabricated in this project was described. The design of the devices was explained as well as the detailed fabrication process. Devices were fabricated using an existing mask set from Stanford University. The process was based on a double oxidation to form the cavity and the insulation oxide followed by fusion bonding to an SOI wafer to form the thin flexible plate. Connections are made to the front side of the devices.

A yield very close to 100 % was obtained for the fabrication, however measurements showed indications of a much lower breakdown voltage of the support oxide than expected. Impedance measurements on good elements were conducted and the uniformity was found to be very good with a variation of less than 1 % within an array.

One device was mounted into a probe handle by Vermon and used for the first ultrasound measurements with a CMUT at DTU. Images were made both of a hydrophone and of a multiwire phantom using various imaging methods. However, the probe suffered from the low breakdown voltage. The experience from the design, fabrication and characterization of these arrays was used to develop a baseline process for producing CMUTs at DTU.

CHAPTER 4

1D Array Baseline Process

Several versions of CMUTs have been fabricated leading to the development of a reliable baseline process for fabricating CMUTs at DTU. The baseline process can be used for both 1D array fabrication and also for 2D array fabrication with only a few modifications. The focus of this thesis will only be on the 1D arrays.

This chapter will describe the important factors, that was discovered during the processing, for making working CMUTs. Furthermore, the baseline fabrication process for 1D arrays will be explained and electrical characterization of fabricated devices will be shown.

4.1 Development of the Baseline Process

The initial attempt at making CMUTs at DTU was based on an old design of capacitive pressure sensors. The work was performed prior to the work on the 1D array for ultrasound imaging presented in chapter 3. The experience gained from these initial fabrication processes was used for development of a baseline process for CMUT array fabrication at DTU.

4.1.1 Capacitive Pressure Sensor

The capacitive pressure sensor, developed by Thomas Pedersen and Giulio Fragiacomo at DTU [71], was operated by the same principle as a capacitive ultrasonic transducer. The device had two electrodes where one of them was free to move and deflected when pressure was applied, and the other electrode was fixed. Instead of being divided into elements, as a CMUT, the pressure sensor was just one big element with a lot of cells. Figure 4.1 shows the design layout and a photo of a finished pressure sensor.

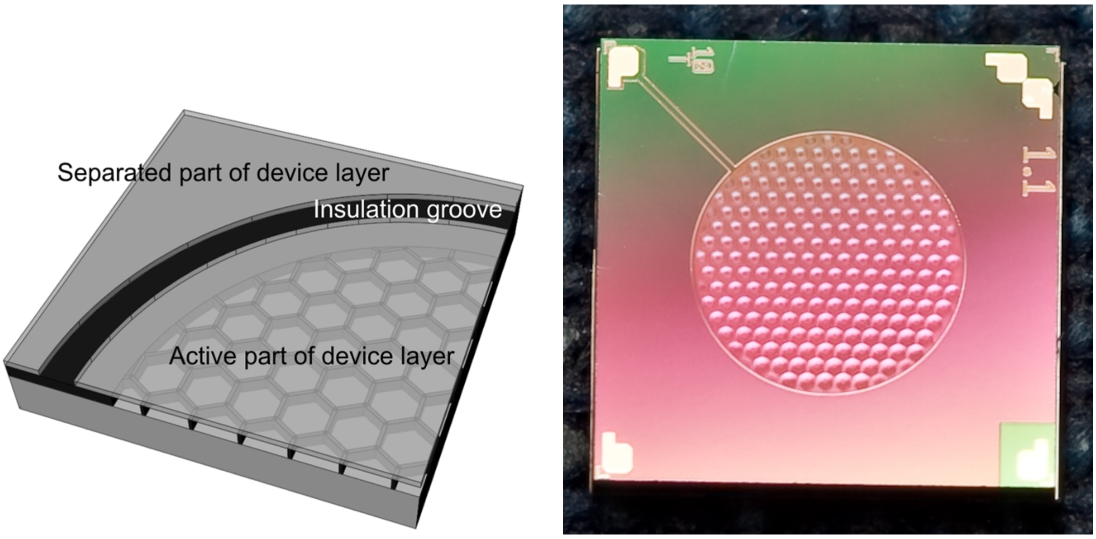

(a) *Illustration of the design.* (b) *Fabricated pressure sensor.*

Figure 4.1: *Capacitive pressure sensor made by Giulio Fragiacomo at DTU Nanotech [72]. a) Illustration of the design with the honeycomb cavity structure and insulation groove around the active area. b) A finished device with contacts in the corners after dicing and visible deflection of the plates in the center. The design was reused for the fabrication of a single element CMUT.*

This design had a hexagonal plate geometry to maximize the active area. The pressure sensor was not designed to operate with a bias voltage, however, this was no problem to add to the existing design.

With this design it was possible to emit ultrasound and measure it using a hydrophone. However, problems with the device performance were discovered. It was found that fabrication of CMUTs requires a particular clean environment for several of the process steps as high voltages need to be applied to the finished device. If the cleanliness during fabrication was not good enough, the oxide between the two capacitor plates would break down and the device would not work. With the first devices, problems with the performance was found mainly to be caused by low oxide breakdown voltage (not measured but devices broke down at a few volts). This resulted in incapability to keep a high bias voltage over the device and thus only producing very low sound transmission.

4.1.2 Optimization of Cleanroom Processes

During the investigation of the problems with the initial single element CMUTs, several factors were found to be of high importance when fabricating CMUTs:

- Particle contamination during wafer bonding
- KOH contamination/contamination from ions
- Contamination from dicing
- Low insulator quality

All of these were considered during development of the baseline process and will now be elaborated on.

Particle Contamination

When performing fusion bonding it was of high importance to have very clean substrates as even a single particle could result in a void (air trap) with a diameter of up to 1 cm. Furthermore, contamination when performing the bonding could cause surface currents to run inside the cavity or it could cause contamination of the insulating oxide. Therefore, having clean wafers was of high importance for the finished device performance. Two precautions should be taken to keep the wafers clean and particle-free:

- *Wafer cleaning*: By default the bonding process included a cleaning step right before the bonding itself. A Piranha combined with an IMEC clean was suggested by DTU Danchip, however, a standard RCA clean was also tested, and it was found that both cleaning methods could be used. The procedures for both cleaning methods can be seen in Table 4.1 and 4.2. As no particular difference was observed when using one cleaning method or the other, it was decided to use the RCA which had a dedicated bench in the Danchip cleanroom.

Table 4.1: *Cleaning procedure for IMEC/Piranha cleaning developed specially for fusion bonding at DTU Danchip.*

Process	**Time**	**Notes**
Piranha	5 min	Mixture: H_2SO_4:H_2O_2 (4:1), 80°C
Rinse	2 min	
IMEC	100 s	Mixture: DI water:5 % HF:IPA (100:10:1), 25°C
Rinse	2 min	
Piranha	20 min	Mixture: H_2SO_4:H_2O_2 (4:1), 80°C
Rinse and spin dry	5 min	

Table 4.2: *Standard RCA cleaning procedure which was found to provide sufficient cleaning before fusion bonding.*

Process	**Time**	**Notes**
RCA1	10 min	Mixture: NH_4OH:H_2O_2:DI water (1:1:5), 70°C
Rinse	3 min	
HF	30 s	
Rinse	20 s + 2 min	20 s in bath for HF cleaning and 2 min in dump rinse
RCA2	10 min	Mixture: HCl:H_2O_2:DI water (1:1:5), 70°C
Rinse	3 min	
HF	30 s	
Rinse and spin dry	20 s + 5 min	20 s in bath for HF cleaning and 5 min in dump rinse

- *Bonding machine*: Another important part was that the bonder itself was clean. A guideline for cleaning the bonder was previously developed by Giulio Fragiacomo [72]. This procedure involved blowing off particles from the machine the evening before bonding and then performing the bonding as early as possible next morning. However, as the developed CMUT process opposed to the pressure sensor process did not use alignment of the wafers before the bonding, it was found that the most important thing was to keep the air exposure of the wafers to a minimum and avoid talking when the wafer box was open. Having the bonder in a room separate from the main part of the cleanroom was helping a lot in fulfilling this.

Bonding of two wafers with 100 % yield have been obtained at DTU Danchip with the current bonding setup and RCA cleaning.

Contamination from Ions

The second possible cause for low breakdown of the devices could be contamination by alkali ions arising from some of the process steps. Indications of such problems were observed from two different sources: using plasma asher for removing photoresist and using a NaOH-based developer for photoresist. These problems, however, were found not to be the main source of failure in device performance and were not considered further.

Later, a TMAH-based developer had become available in the DTU cleanroom, and this would be recommended for future CMUT processing.

Contamination from Dicing

Poor performance of devices was in some cases observed after dicing out the wafer. Breakdown was observed in cases where the dicing was done through the top electrode layer. This can leave contaminating particles or dust from the saw along the edge of the device, causing the bottom and top electrode to be short circuited. To avoid this, the design layout of all CMUTs should include etching away the top electrode around the active plate area. This way the saw will only touch the bottom substrate electrode and the insulation oxide and possible surface currents will have much longer distance to travel. These two ways of dicing are illustrated in Figure 4.2 where the difference in the path of the current is indicated as well.

Insulator Quality

The quality of the oxide was found to be the most important factor for obtaining working devices. As a high voltage is required to operate the CMUTs, the oxide needs to be of high quality to avoid breakdown. If the quality is poor, contaminants in the oxide will cause an electrical breakdown which results in a short in the device.

In theory a high quality oxide should be able to withstand 1 V/nm. When measuring the breakdown voltage of the oxide made at DTU Danchip, it was found that it did not meet the requirements, see

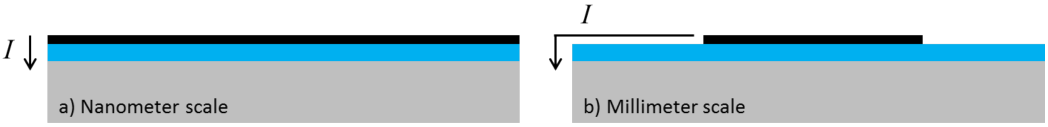

Figure 4.2: *Illustration of surface currents when dicing chips out from wafer. a) Dicing through the metal layer, the current only has to run on a nanometer scale. This can leave contaminating particles or dust from the saw along the edge of the device, causing the bottom and top electrode to be short circuited. b) Etching the metal before dicing, the current has to run on millimeter scale and short circuiting is unlikely.*

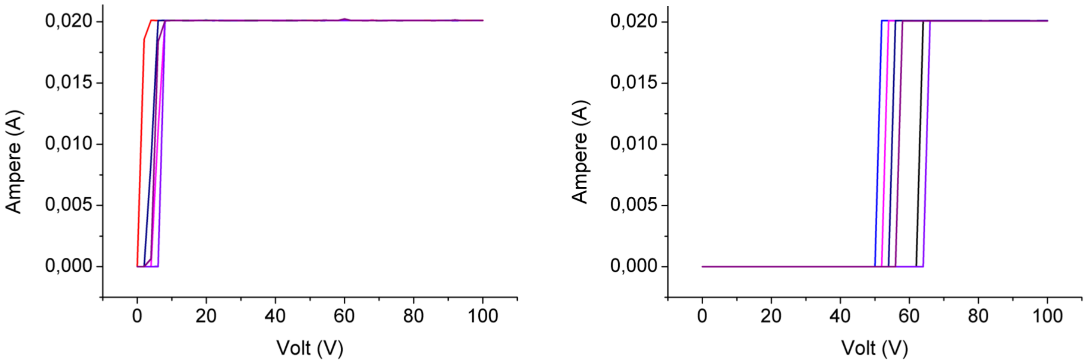

(a) *Oxide with low breakdown value.*

(b) *Oxide with high breakdown value.*

Figure 4.3: *Breakdown voltage measurements on 60 nm thick test oxides grown on a standard silicon wafer. a) The poor oxide quality is seen on the low breakdown voltage whereas for b) the high quality is seen on the high breakdown voltage.*

Figure 4.3a. A breakdown of around 0.08 V/nm was measured. After this discovery, all oxidation tubes had to be changed and the test of the oxide quality was repeated. With the new oxidation tubes, the quality was markedly increased as is seen in Figure 4.3b. A breakdown voltage of around 0.9 V/nm was obtained, almost as high as the theoretical value. The measurements in Figure 4.3 were made on test structures with a 60 nm oxide layer grown on a standard silicon wafer. Contacts of around 1×1 cm were made on the oxide with aluminum using a shadow mask deposition.

To be able to check the oxide quality of each batch of transducers, test structures for measuring breakdown should be included in all designs. The first characterization of oxide quality should be performed after the first oxidation step in order to avoid full processing of wafers with poor oxide quality.

Recommendations for Ensuring High Cleanliness

Considering all these factors for cleanliness a set of guidelines were suggested for designing and fabricating CMUTs:

- Use the standard RCA cleaning before fusion bonding.
- Wear a mouth cover and do not speak during fusion bonding, especially when the wafers are exposed to the air.
- If possible use TMAH-based developer in stead of KOH-based developer.
- Always etch back the metal and device layers everywhere around the plate area.
- Include test structures on the wafer to check oxide quality during and after fabrication.
- Make an initial test of the oxide quality on a dummy wafer right after oxide growth, and stop further processing if the quality is low.
- Use photoresist for protection of device surfaces while dicing wafers.

Recommendations for Designing 1D CMUT Arrays

After having made the initial tests on CMUT arrays some guidelines for designing are proposed:

- *Cavity etch on SOI wafer*: The etch back of the oxide bumps in the Stanford 1D array process (see previous chapter) is not needed if the insulation oxide is made on the substrate wafer and the cavities are made on the SOI wafer. Note that the opposite way results in stresses in the plate due to a silicon-oxide plate and this can give unpredictable performance.
- *Bottom contacts*: Contacts to the bottom plate from front side of device is important as it will cause problems with obtaining proper contact when using the entire backside of the wafer.
- *Insulation layer*: Include the insulation layer in the cavity even though a device is not meant to operate in pull-in, otherwise surface currents will appear, ruining the device.

These are guidelines made from observations during the development of the baseline process and it is recommended to follow these whenever a new design is made. The next sections will present the design layout of the baseline process followed by a process overview and detailed fabrication description.

4.2 Layout and Design

The design of the 1D arrays made with the baseline process developed during this project had a specific purpose: the arrays should be used in a prototype CMUT probe. This meant that the chip should be mounted with electronics in a probe handle and connected to an imaging system. The probe should also be comparable to a standard piezoelectric transducer. This resulted in the following criteria for the CMUT:

- The probe should be comparable to a piezoelectric transducer with the following constraints:
    - Resonant frequency of 5 MHz in immersion.

  - 128-element linear array, λ-pitch → pitch= 300 μm.
  - Element height of 5 mm.

- Fabrication and assembly provided the following requirements:
  - Fusion bonding method.
  - The insulation layer should be a thermally grown, high quality oxide to be able to withstand high voltages even if pull-in occurred.
  - 1 µm thick aluminum bonding pads for wirebonding.
  - The vacuum gap should be large enough for the probe not to operate in pull-in mode when applying 80 % of the pull-in voltage.
  - Outer dimensions should fit within reasonable constraints to a conventional scanner head.

- Requirements from electronics were specified as:
  - Compatible with BK Probe Port.
  - Optimal operation at 190 V DC bias voltage, corresponding to 80 % of pull-in voltage.
  - Functional at up to ±85 V AC transmit voltages.

The plates were made with a square geometry to have the best utilization of area. The silicon plate thickness was 2 µm due to availability of SOI wafers.

From the resonant frequency and the plate thickness specified in the requirements above, the plate side length was calculated to be 49 µm. From the requirements for DC biasing, it was found that a vacuum gap of 360 nm and an insulation layer thickness of 400 nm were suitable for the probe to obtain a pull-in voltage of around 240 V. A thorough description of the design process was included in [73] where it was also described how COMSOL was used to simulate the device performance in immersion, which was not covered by the current analytical models. The final dimensions of the devices is summarized in Table 4.3.

The layout of an array can be seen in Figure 4.4. The bottom contact is a line along the length of the array with bonding pads for every eight element. A zoom in on the array is seen in Figure 4.5. One wafer contained 13 arrays.

Table 4.3: *Device dimensions for 1D arrays fabricated at DTU using the baseline process.*

Parameter	**Value**
Side length, L	24.5 µm
Plate thickness, h	2 µm
Vacuum gap, g	360 nm
Insulation layer thickness, t_{ox}	400 nm
Al layer thickness, h_{Al}	200 nm

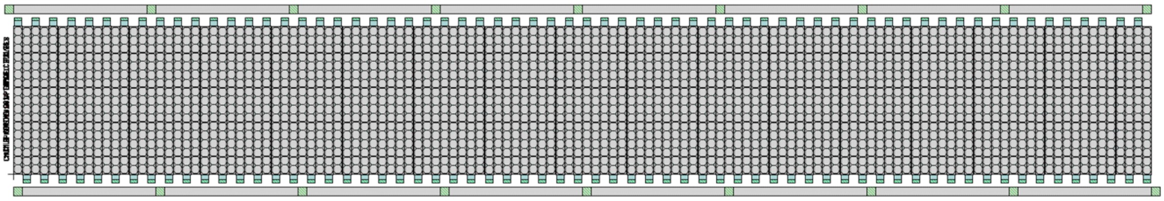

Figure 4.4: *Mask layout for 1D arrays with 128 elements made at DTU. The element pitch is* 300 µm *and elevation height* 5 mm*. The contact for substrate is made on the front side of the device and is seen as the bar along the length of the array.*

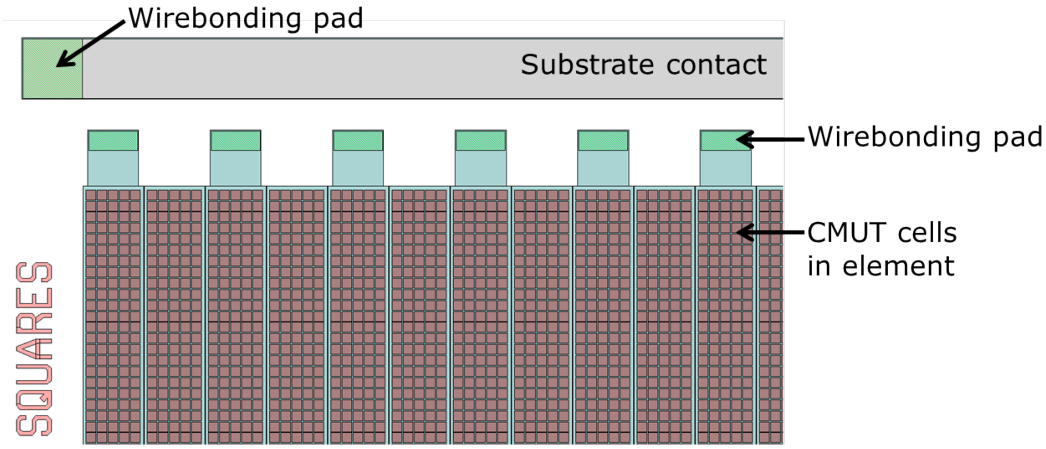

Figure 4.5: *Zoom in on mask layout to show individual elements (seen as vertical bars with red square cells), contact for substrate and bonding pads to be used for wirebonding.*

4.3 Fabrication Process

The devices were fabricated with a fusion bonding process. An overview of the process can be seen in Figure 4.6. The details and results from the fabrication are described in the following. The fabrication is also described in [53, 73] and the full process flow can be seen in appendix B.

Step 1: Oxidation of Support Posts and Insulation Layer

First step of the process was to oxidize the SOI wafer to create the post oxide supporting the plate in the final device, see Figure 4.6a. The oxidation was performed as a dry oxidation at 1100°C for 7 hours. The expected oxide thickness was 360 nm and the actual thickness was measured to be 364±1.6 nm.

In parallel the oxide for the insulation layer was also grown as this was done on separate wafers in this process (opposed to the Stanford process described in chapter 3). The oxidation was performed as a dry oxidation at 1100°C for 8:55 hours. The grown oxide was measured to be 407±2.6 nm.

Figure 4.6: *Process flow overview for the fusion bonding process made at DTU. a) Oxidation of both SOI and substrate wafer; b) defining cavities on SOI wafer by dry etching of the oxide; c) fusion bonding of the two wafers; d) removal of handle and BOX layer of SOI by etching; e) opening up to the bottom electrode by etching; f) defining bonding pads by metal deposition and wet etching; and g) defining top plates and contacts by metal deposition and wet and dry etching. j) The finished device after dicing and wirebonding.*

Step 2: Etching of Cavities

The second step was to etch the cavities in the oxide on the SOI wafer, see Figure 4.6b. This was done by dry etching in the Advanced Oxide Etcher (AOE) for 1 min and 50 s using the standard recipe *m_res_ny* and a chuck temperature of 0°C. The etchants were C_4F_8 with He and H_2 gasses. Figure 4.7 shows a microscope picture of square cells etched in the oxide.

Step 3: Fusion Bonding

The next step was to perform the wafer bonding, see Figure 4.6c. Bonding temperature was 50°C and the piston force 1500 N. The prebonding time was 5 mins and a vacuum of 1.0×10^{-2} mbar was specified. The prebonding was followed by an annealing at 1100°C for 70 min.

Step 4: Etching to Release Plate

After the fusion bonding the plates were released, see Figure 4.6d. First a Buffered HF (BHF, similar to BOE) etch was applied to remove the previously grown oxide from the backside of the SOI wafer, which was now the device front side. Etching time for this step was 6 min. Then the handle layer of the SOI was removed by dry etching using the Advanced Silicon Etcher (ASE). The recipe *cmutaway* was used for 1:05 hours with a chuck temperature of 20°C. This recipe used SF_6 and O_2 for etching and no passivation steps. Every half hour the chamber was purged with Ar to remove any charge build-up which could otherwise break the wafer during de-clamping in the machine. Next, the buried oxide layer was removed by a 20 min BHF etch.

Before any further processing could be performed the wafers were conditioned to an RCA clean as the bonder and annealing furnace were considered dirty. Openings to the alignment marks also needed to be made, as it was not possible to do proper alignment through the 2 µm thick silicon plate. This was done reusing an old mask from a previous process, which just had two openings for the alignment marks and could be used by manual aligning as a first print mask.

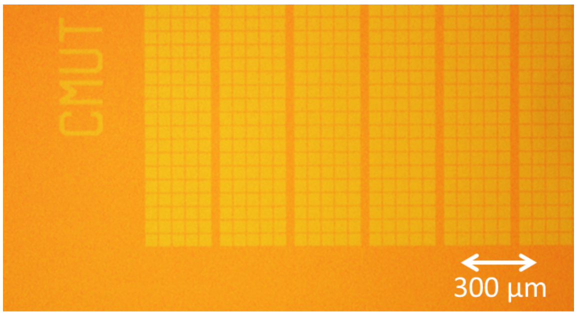

Figure 4.7: *Microscope picture of etched cavities in the SOI wafer. The square cell shape and the elements can be seen.*

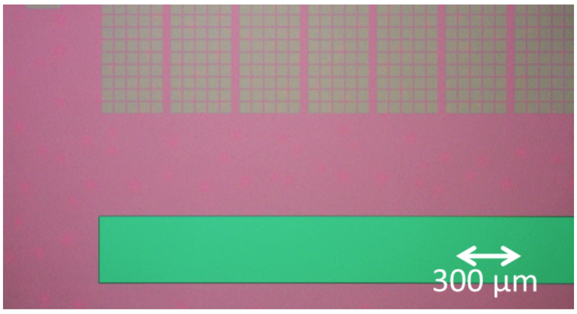

Figure 4.8: *Microscope picture of etched bottom contact openings after fusion bonding. It is seen as a rectangle along the array.*

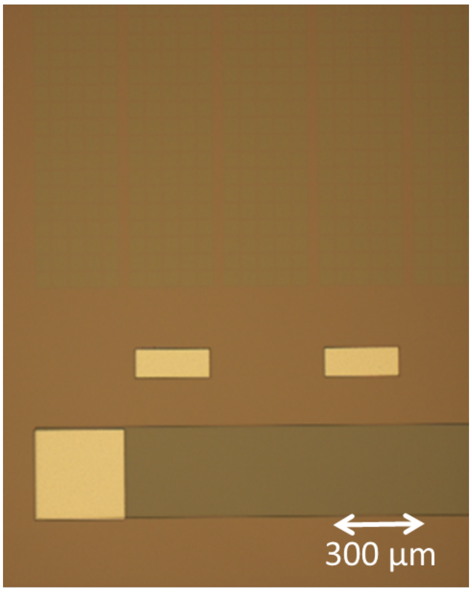

Figure 4.9: *Microscope picture of bonding pads after metal deposition and wet etching.*

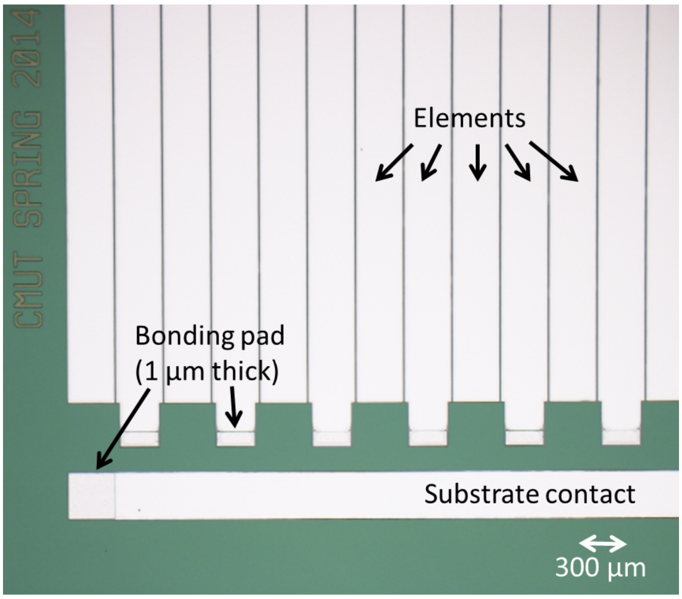

Figure 4.10: *Microscope picture after etching out the elements and contacts. Bonding pads are seen as a thicker aluminum layer in the ends of the elements.*

Step 5: Etching of Bottom Contacts

Next step was opening of the bottom contacts to the substrate wafer, see Figure 4.6e. This was done by dry etching of the silicon device layer and of the support oxide. To avoid notching when etching through the silicon layer a special SOI recipe was used in the Deep Reactive Ion Etcher (DRIE). The process time was 40 s. The oxide etch was performed with the AOE using the recipe *m_res_ny* for 2+2 min (etch depth was checked after the first 2 min). A microscope picture of a device after etching can be seen in Figure 4.8. The cavities was also seen through the device layer.

Step 6: Metallization and Etching of Bonding Pads

The metallization for this process was done in two steps, see Figure 4.6f-g, as the wire bonding partner requested 1 µm of Al on the bonding pads, however, a thinner layer was preferred on the plate area. The first deposition step was of 800 nm Al using e-beam evaporation in the Alcatel, and it was patterned by a wet Al etch. This contained H_2O:H_3PO_4 in the ratio 1:2. The etch was performed at 50°C and etching time was around 8 min. Figure 4.9 shows a microscope picture after defining the bonding pads. The cavities are also seen in the picture.

Step 7: Metallization and Etching of Elements

The last step was to deposit the second metal layer and define the top plates and contacts. A 200 nm thick layer of aluminum was deposited and patterned using wet aluminum etching for around 3 min.

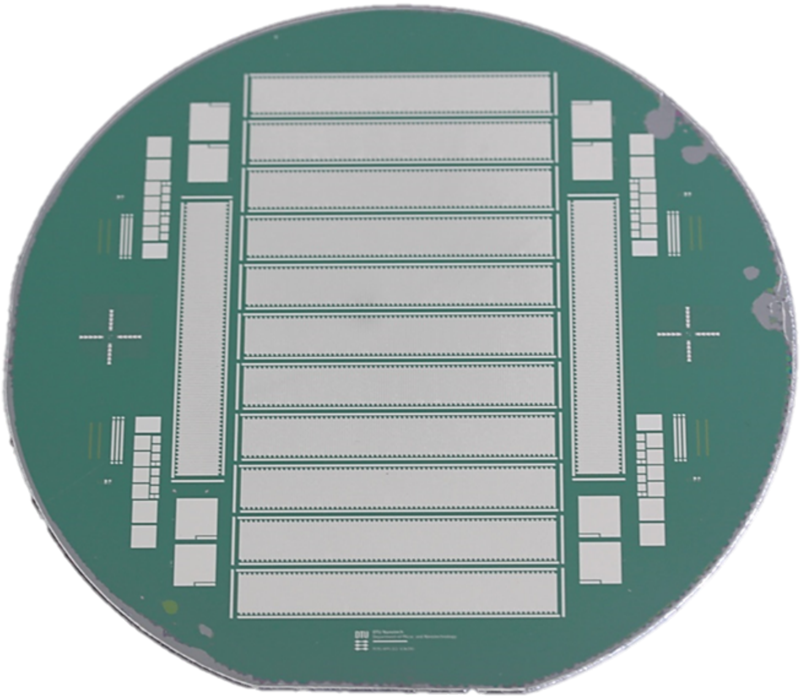

Figure 4.11: *Picture of a finished wafer made with the 1D array baseline process. The wafer contains 13 arrays and some test structures at the edges.*

The pattern was also transferred to the silicon device layer to remove the highly doped material in the regions outside the top plates. The DRIE and the special SOI recipe was used for this, again to avoid notching. Figure 4.10 shows a device after etching out the elements.

Step 8: Post-processing

A picture of a finished wafer can be seen in Figure 4.11. The yield was close to 100 %. There was only a small fault from a resist coating on one of the four wafers that was processed and it affected around 10 elements on one of the arrays. Figure 4.12 shows a picture of a finished CMUT array. During the dicing of the wafer it was found that it was necessary to protect the devices with photoresist. This was to avoid dust from the saw settling on the wafer surface. The resist was easily removed afterwards with acetone.

4.4 Characterization

As for the Stanford arrays both electrical and acoustical characterization were carried out for the arrays made with the baseline process at DTU. The impedance measurements are discussed below and the acoustical characterization is presented in chapter 5 and 6.

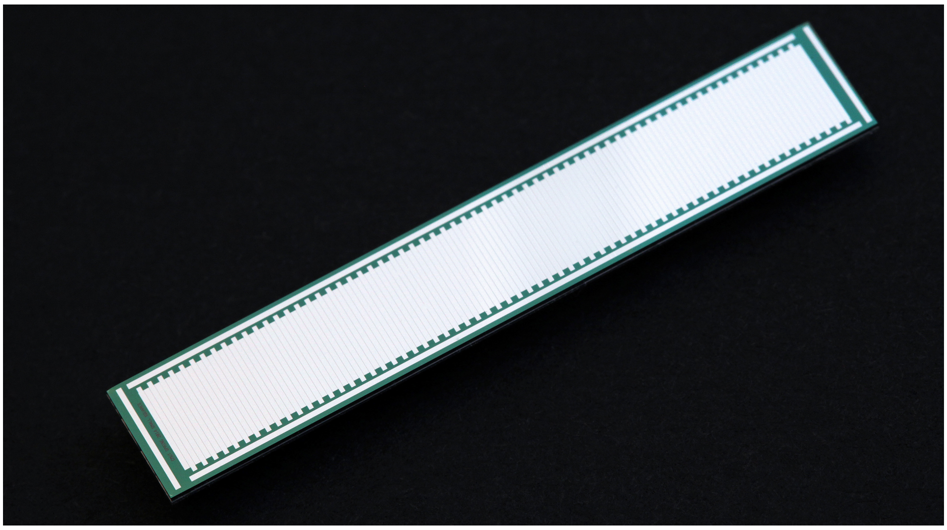

Figure 4.12: *Picture of one finished array. The length of the array is 42 mm and the width is 7 mm*

4.4.1 Impedance Measurements

Initial impedance measurement made on the 1D arrays fabricated at DTU can be seen in Figure 4.13. A bias voltage of 150 V was applied and the frequency was swept from 1-15 MHz with an AC voltage of 50 mV using a HP4191A impedance analyzer (Agilent, Santa Clara, CA, USA) and an external DC supply connected through a bias-T. The capacitive behavior was seen in the impedance measurement. The resonant frequency could be read from the maximum in the phase angle. The device was seen to have resonant frequency in air of 9 MHz. This was lower than the expected value of 11.8 MHz from the design, but could be explained by the theoretical analysis using fixed boundaries. The actual device would have some influence of the support oxide when deflecting, resulting in a sightly higher effective radius and hence lower resonant frequency.

It is noticed that the signal was very weak and to check if this resulted from charging effects in the device structure, the polarity of the bias was switched. New measurements were carried out with -150 V applied. The result can be seen in Figure 4.13b. A significantly higher signal is observed. The signal level in the reverse mode should be enough for making ultrasound images. The two polarities of the bias voltage will be called normal (positive bias) and reverse (negative bias) mode and are illustrated in Figure 4.14.

4.4.2 Charging

An initial investigation of the charging effects was made. This was done through continuous measurement of the impedance on a single element while tracking the maximum phase angle. Figure 4.15 shows a plot of the maximum phase angle where the bias voltage is changed from 0 V $\rightarrow -190$ V $\rightarrow$ 0 V $\rightarrow$ 190 V $\rightarrow$ 0 V $\rightarrow -190$ V and then repeating the same sequence one more time. The change in charging of the device was clearly seen for the two polarities of the bias voltage. Using the normal mode (190 V) the phase increased to around zero degrees after applying 0 V first, but then very quickly

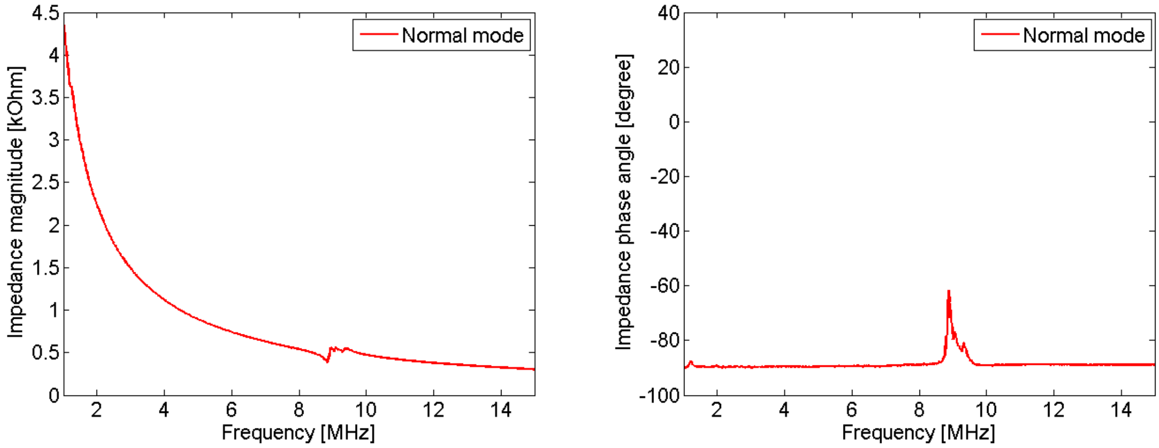

(a) *Bias voltage in normal mode:* 150 V.

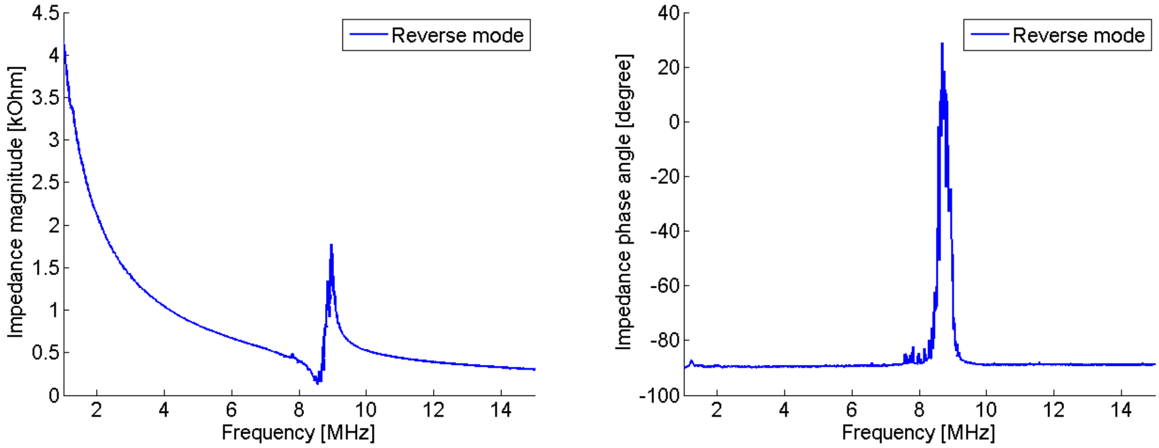

(b) *Bias voltage in reverse mode:* -150 V.

Figure 4.13: *Impedance magnitude and phase angle measured for the DTU arrays with an impedance analyzer. The charging effects are clearly seen for the normal mode (a) as a much lower signal at the resonant frequency is obtained compared to operation in the reverse mode (b).*

reduced to around $-70°$. On the other hand, using the reverse polarity (-190 V) the phase increased to around 60° and then decayed to around 30°. It is noticed that for reverse polarity the same level in phase angle was kept if the bias had just been zero, whereas it went back up to the 60° if the normal polarity had been used in the meantime. Furthermore, it was seen that going from $-190\,\text{V} \rightarrow 0\,\text{V}$ showed a very abrupt shift in phase angle whereas going from $190\,\text{V} \rightarrow 0\,\text{V}$ actually increased the phase angle slightly before slowly decaying back to $-90°$. This indicates that it took longer time to de-charge the device from the normal mode than from the reverse mode. Ideally a short de-charge time is preferred meaning the reverse mode performs better in this regard.

Figure 4.15 shows that it is possible to get much more signal out of the CMUT and circumvent the charging problem to a high degree by changing the bias polarity to the reverse mode. For practical use it was investigated if the reverse mode of operation could give a stable signal level or how much the signal would decrease when performing long term measurements. In the measurements in Figure 4.15 there

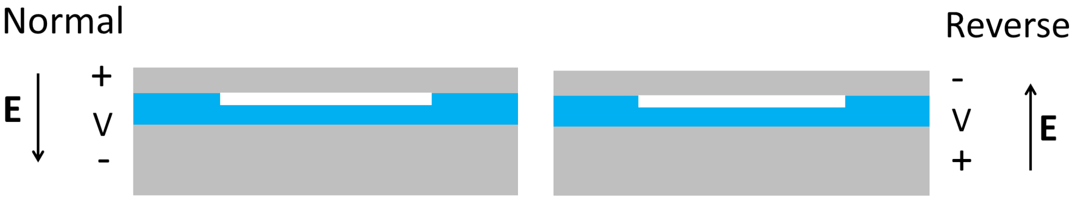

(a) *Bias voltage in normal mode.*

(b) *Bias voltage in reverse mode.*

Figure 4.14: *Illustration of normal and reverse polarity for a CMUT, indicating the direction of the electrical field. a) Normal polarity has ground on the substrate electrode whereas b) reverse mode has ground on the flexible top electrode.*

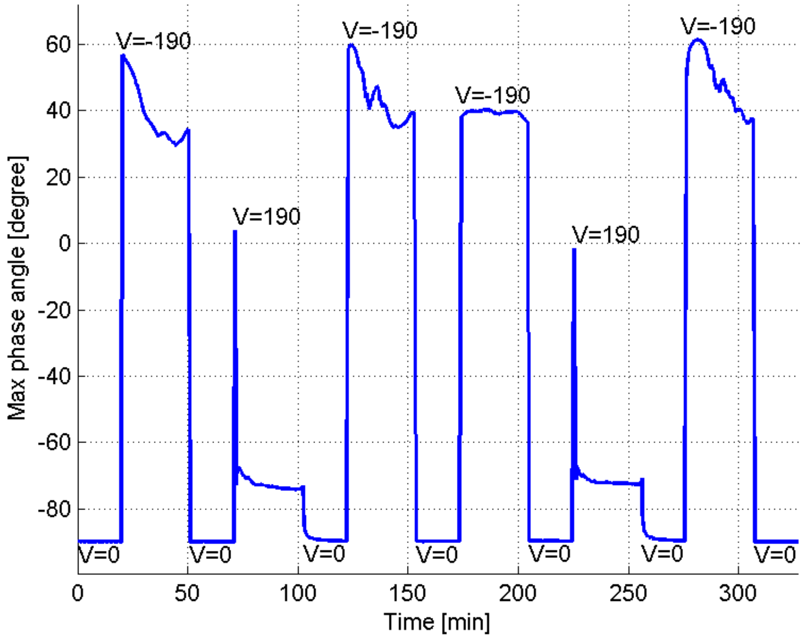

Figure 4.15: *Tracking of maximum impedance phase angle when switching between normal mode (+190 V), zero bias (0 V) and reverse mode (-190 V). The charging effects for the two modes of operation is clearly seen as a lower signal and longer de-charge time when shifting voltage to zero.*

were some indication that a steady level would be reached by just keeping the polarity in the reverse mode. This was tested by two different long term measurements which can be seen in Figure 4.16. On the blue curve in Figure 4.16 a bias voltage of $-190\,\mathrm{V}$ was applied to an element, and the phase angle was tracked for around 23 hours. It is seen to decrease mostly in the beginning and then get more stable towards the end and a high signal was still observed. On the red curve in Figure 4.16 a bias voltage of $-190\,\mathrm{V}$ was applied and for every five hours the bias was set to zero for half an hour before going back to the $-190\,\mathrm{V}$. Again the phase angle was tracked and the same tendency as previous was observed. Both measurements were performed on elements which had not been measured on previously. It can not be concluded that a completely stable level can be reached, however, this signal level should be

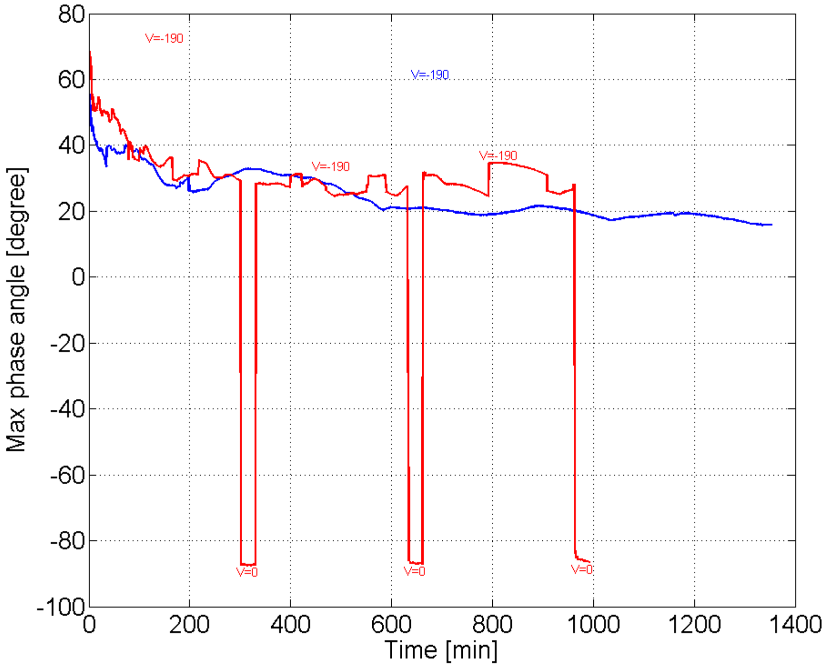

Figure 4.16: *Long term tracking of maximum impedance phase angle when operating in reverse mode (-190 V). The blue curve is when a constant voltage of* $-190\,\mathrm{V}$ *is applied and measurements performed continuously. The red curve is a similar measurement with* $0\,\mathrm{V}$ *applied for 10 min every five hours. An applicable, almost stable signal level is observed over time.*

suitable for making reliable ultrasound imaging.

A second set of long term measurements were performed to learn more about the charging and the results can be seen in Figure 4.17. In Figure 4.17a the bias voltage is changed every half hour from 5 V to 160 V in steps of 5 V for both normal and reverse polarity. It is confirmed that the charging was a lot worse in the normal mode than in the reverse mode. The decreasing signal was visible at around 40 V for the normal mode, whereas it was not observed in the reverse mode measurements. The difference in signal level was clearly seen as well. In Figure 4.17b only reverse mode was measured to see if there was a change in the observed charging over time at different bias voltages. Measurements were made at each voltage for 10 hours with pauses of 10 min at 0 V in between. It was seen that some charging appear at 150 V and continued when the voltage was further increased.

From the long term measurements of the 1D CMUT array with different DC voltage polarity it can be determined where in the CMUT stack the trapped charges are located and the sign of the charges. The charges will under a DC voltage be moved to one of the following interfaces: top silicon plate/vacuum gap, vacuum gap/insulation oxide or insulation oxide/bottom silicon electrode. These interfaces are illustrated in Figure 4.18a and denoted as interface A, B, and C, respectively. The top silicon plate and bottom silicon electrode are both highly doped with a high amount of free charge carriers. If the trapped charges in the CMUT stack were located at either silicon interfaces (A or C) they would be screened by oppositely signed free charges from the silicon. Since this screening effect will cancel out the effect of the trapped charges, it can be concluded that the trapped charges necessarily must be

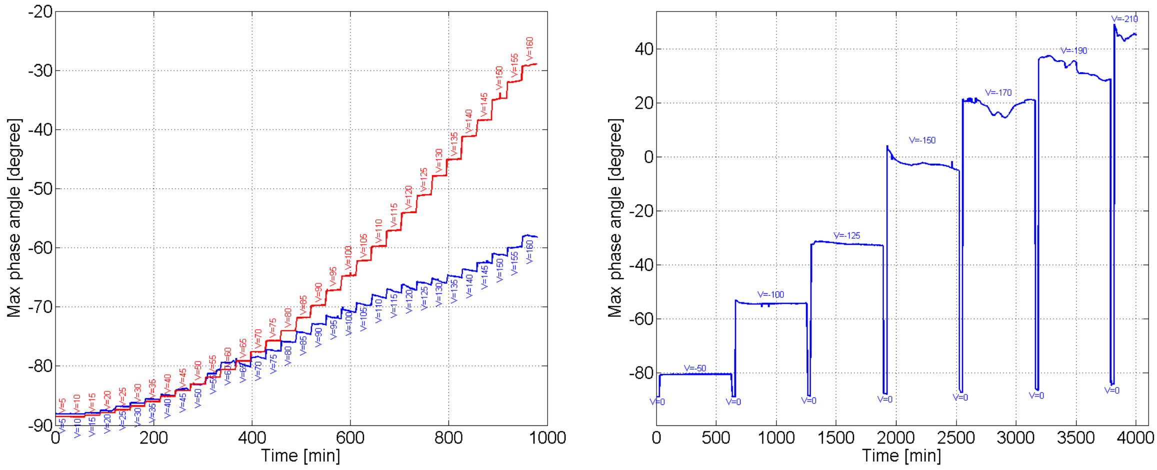

(a) *Increasing bias voltage in steps of* 5 V *for 25 min each.*

(b) *Increasing bias voltage in large steps for 10 hours each.*

Figure 4.17: *Long term tracking of maximum impedance phase angle when operating in normal and reverse mode (a). Charging is clearly seen also for lower voltages in normal mode. For reverse mode it appear around* 150 V *when doing long term measurements only (b).*

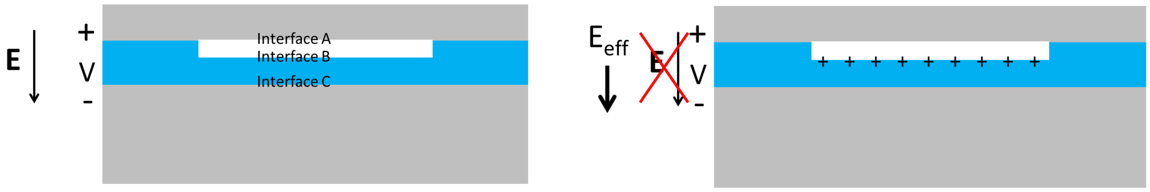

(a) *Possible interfaces for charges to get trapped.*

(b) *Charge build up in normal operation mode.*

Figure 4.18: *Illustration of possible problems with charging when the CMUTs are operated in normal mode. a) Three possiblew interface in the structure for charges to get trapped. b) Positive charges will cause a reduction of the effective bias over the CMUT structure.*

located at the vacuum/oxide interface (B). The measurements showed that the trapped charges primarily affect the CMUT in normal operation mode (Figure 4.14a) by minimizing the effective electric field over the vacuum gap. This means that the trapped charges at the B interface must be positive since negative charges would increase the effective electric field across the gap, see Figure 4.18b.

Further investigations of the origin of these charging effects in the CMUT elements should be performed to find a way to eliminate the charges. It was not carried out in this project due to time constraints.

4.5 Summary

In this chapter the development of the baseline process for fabricating CMUTs at DTU was described. The challenges was explained and guidelines for designing and fabricating the devices was suggested.

The baseline process was used to fabricate 1D arrays which should be used in a prototype probe. The design and layout of the CMUT was explained from the requirements for this prototype. The fabrication process, which is based on separate oxidation of the two wafers used in fusion bonding, was described in details. The connections are made from the front side as for the Stanford devices.

A yield of almost 100 % was also obtained for this process. Impedance measurements showed large charging effects in the device which was found to be reduced drastically by reversing the bias polarity. From investigations of the charging, it was concluded that positive charges were trapped at the interface between insulation oxide and vacuum cavity.

Acoustical testing of the devices was also carried out and will be explained in the two next chapters.

CHAPTER 5

Transducer Packaging and Acoustical Tests

This chapter covers all transducer evaluation that is not the prototype probe. It is important to characterize the fabricated device properly to see how they perform acoustically. For this purpose a flexible platform for testing various designs of transducers was developed in collaboration with BK Medical. The acoustical measurements performed using the experimental Synthetic Aperture Real-time Ultrasound System (SARUS) [70] at CFU.

5.1 Development of Evaluation Platform

For evaluating the transducers with different designs it was a requirement that the evaluation platform was flexible to be able to reuse the expensive electronics parts and easily switch the device. The layout of the system that was developed can be seen in Figure 5.1. The transducer was mounted on and

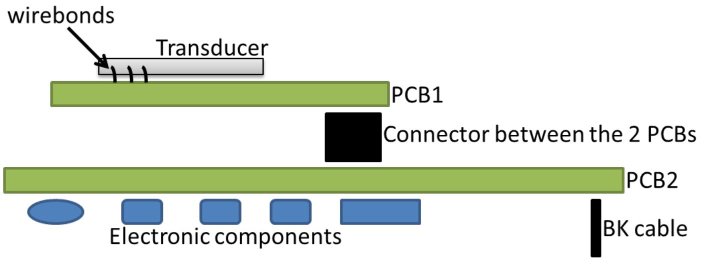

Figure 5.1: *Design of flexible transducer evaluation platform for testing various CMUT designs. The transducer is mounted on a PCB using wirebonding, the PCB is connected to another PCB containing all electronics and a cable for connecting to a scanner is attached to the electronics PCB.*

wirebonded to PCB1, called Chip Carrier Board (CCB). This CCB was clicked onto another PCB containing all the electronics for operating the CMUT and this second PCB was called InterConnect Board (ICB) and could be reused for other devices. A new CCB would be needed for different transducer designs. A transducer cable for a BK Medical scanner was also attached to ICB so the transducer could be connected to an imaging system.

The transducers were made by DTU Nanotech, the wirebonding and mounting on the CCB was done by an external partner, DELTA, and all electronics and layout of the CCB and ICB were made by BK Medical. Another requirement was that the system should be encapsulated in a box to be able to do experiments with the device submerged in water.

The setup can be described as

1. CMUT glued on CCB
2. Wirebonding of all elements
3. Connect CCB with transducer to ICB with electronics
4. Attach transducer cable to ICB
5. Separate cable for DC connections
6. Contained in a waterproof box

Pictures of the final setup can be seen in Figure 5.2 from front and back side of the box.

Figure 5.3 shows a picture of CCBs with different layouts, a chip mounted on a CCB and an ICB. In Figure 5.3a, a 1D and 2D CMUT arrays are seen together with their corresponding CCBs as the top and bottom row, respectively. A 1D array mounted on a CCB with wirebonds covered in glob top is seen to the bottom left and an ICB is seen to the bottom right.

5.2 Acoustical Setup

Two types of acoustical measurement were performed: transmitting into a hydrophone and measuring the output signal plus pulse-echo measurements against a plane reflector, consisting of PVC (Polyvinylchloride), to measure the receive sensitivity. A picture of the transmit setup can be seen in Figure 5.11a, and a picture of the receive setup can be seen in Figure 5.11b. Later another plane reflector of the same material was used. This could fit on top of the evaluation box so the whole box did not have to be submerged in the oil. This setup can be seen in section 5.3 together with the measurements it was used for.

5.2.1 Confirmation of Charging Effects

With the initial configuration of the ICB-CCB setup the polarity of the device was in the normal mode. Using this a decrease in signal was observed over time, see Figure 5.6 which shows RMS of pulse-echo

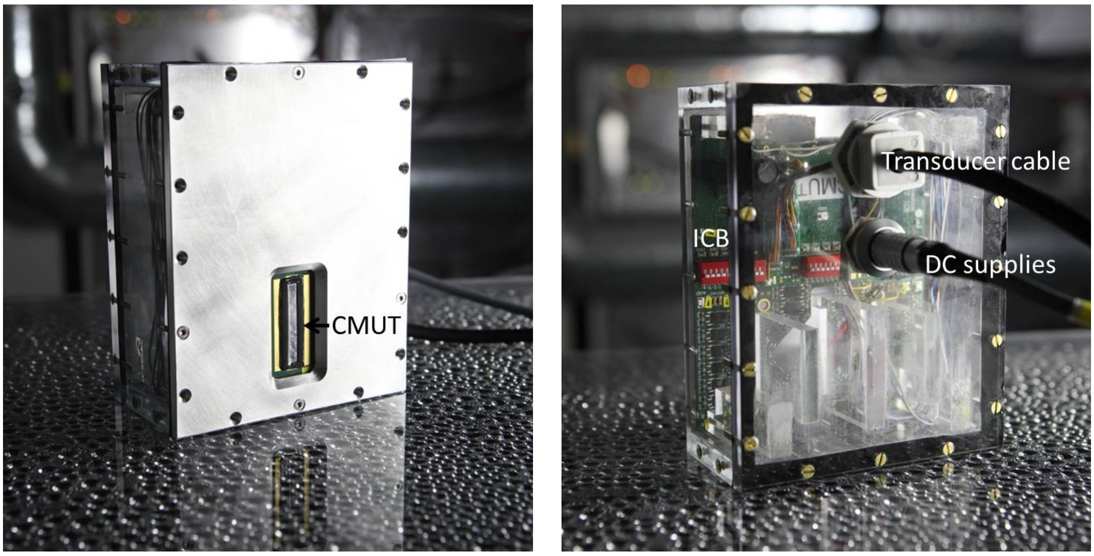

(a) *Front side.* (b) *Backside.*

Figure 5.2: *Flexible transducer evaluation platform developed to test multiple CMUT designs and devices. The front side (a) is open to the CMUT and on the backside (b) the transducer cable and a separate DC supply cable can be seen.*

measurements in voltage measured over time. It is the mean value of all working elements. One element was transmitting at the time and the signal was received with the same element to obtain the two-way sensitivity. The measurement was made with 190 V DC bias and ±60 V AC signal. Ten different white, Gaussian random signals were used for the excitation and averaging was performed over the 10 random signals.

As the charging was discovered during the impedance measurements, shown in chapter 4, the polarity was also switched to reverse mode in this setup. For this a slight modification of the CCB had to be made to be able to put the DC bias on the substrate electrode. This modification is seen in Figure 5.7.

After reversing the bias a much higher signal was obtained as can be seen in Figure 5.8. It was noted that the signal was still decreasing over the time scale that was measured here. However, it was seen for the impedance measurements that an almost stable operating point could be obtained and operating the transducer in the reverse mode was usable for making ultrasound images.

A similar measurement was made for a piezoelectric probe and the results can be seen in Figure 5.9. The two measurements were not directly comparable due to different amplifiers etc. in the setup, however, the level of signal for the CMUT was seen to be in the right order of magnitude after reversing the polarity. All measurements should thus be made in the reverse mode with these devices until a solution to eliminating of the charging completely were found.

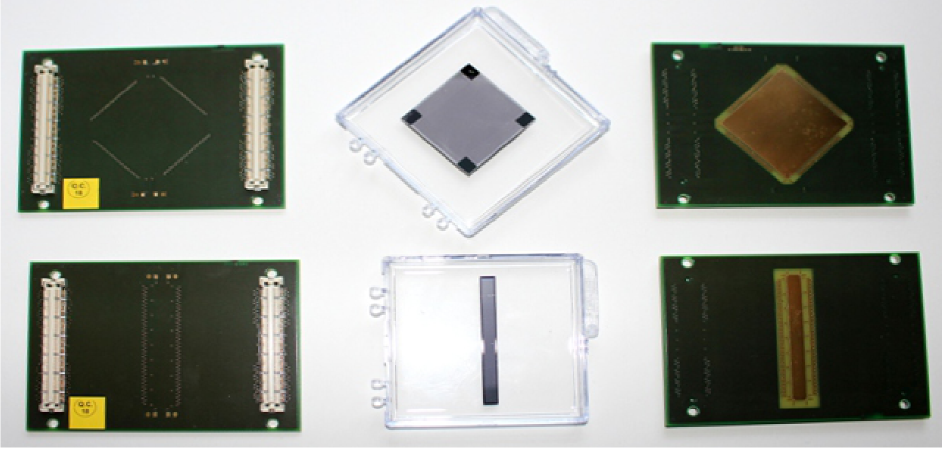

(a) *1D and 2D CMUT arrays and corresponding CCBs. To the left is the backside of the CCBs with connectors seen on each side, in the middle the corresponding devices are seen and to the right the fontside of the CCBs where the devices are glued onto are seen. The top row is for a 2D array and the bottom for a 1D array.*

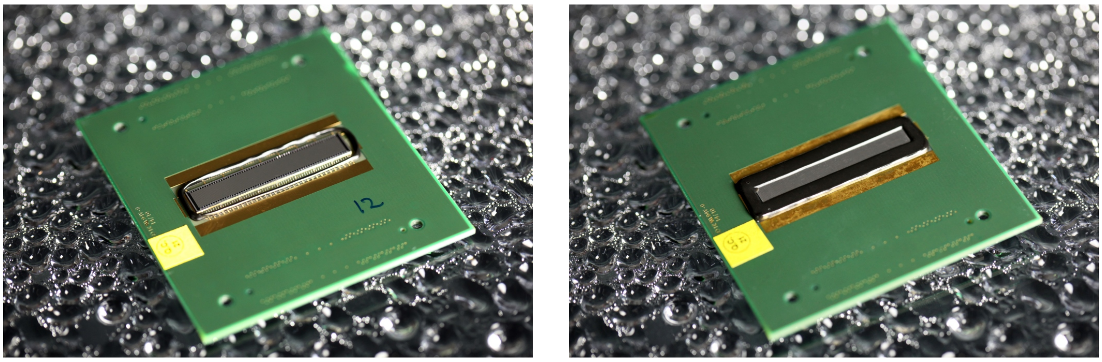

(b) *Mounted 1D array on CCB without glob top.* (c) *Mounted 1D array on CCB with glob top.*

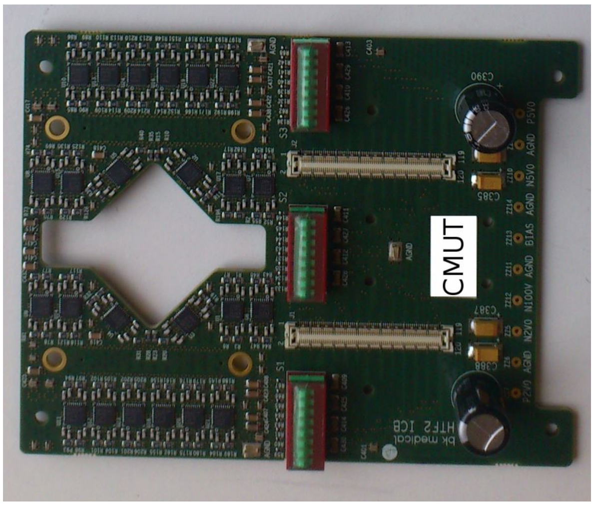

(d) *ICB with electronics for operating the CMUTs. The same ICB is used for both 1D and 2D arrays.*

Figure 5.3: *Different PCBs and devices for the flexible transducer evaluation platform developed to test multiple CMUT designs and devices.*

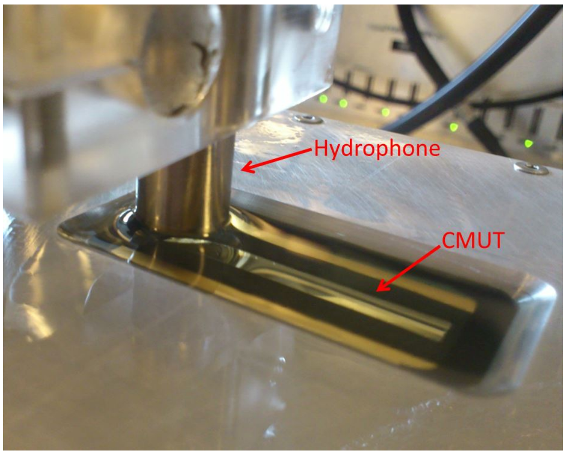

Figure 5.4: *Setup for measuring the transmitted pressure using a hydrophone.*

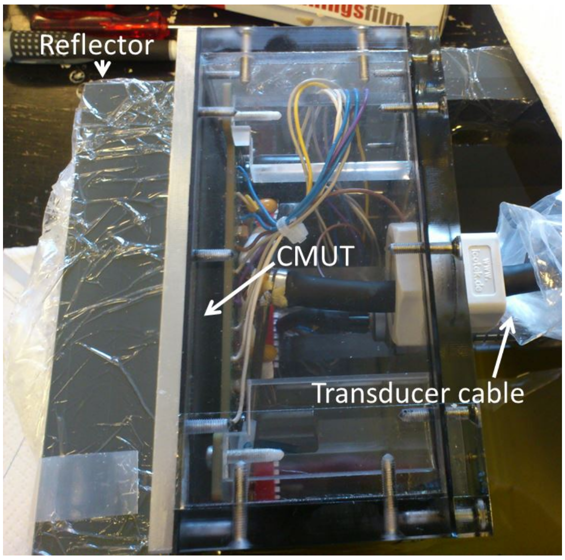

Figure 5.5: *Setup for measuring the receive sensitivity using a plane reflector.*

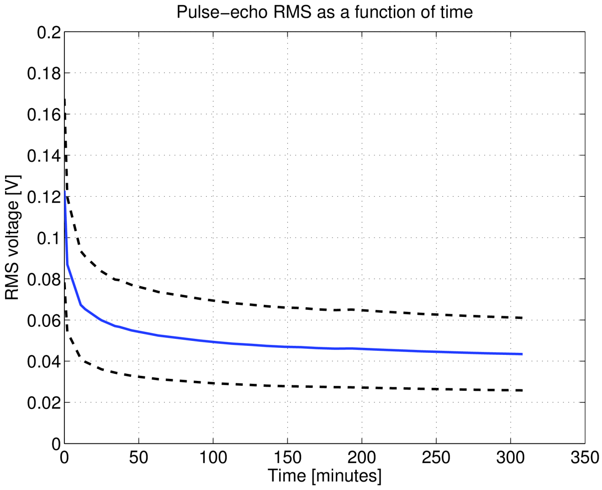

Figure 5.6: *RMS of received signal over time measured using a plane reflector.*

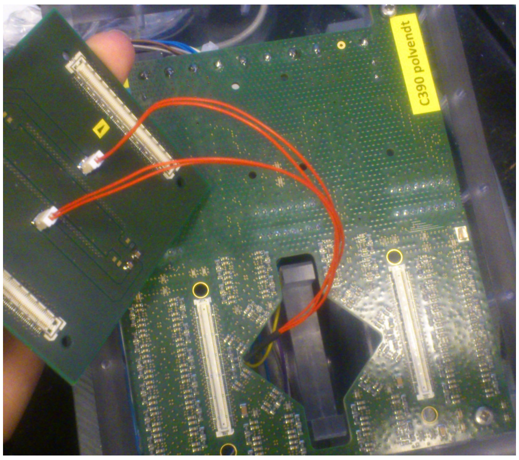

Figure 5.7: *Modification of CCB to allow for bias voltage on the substrate electrode.*

5.3 Device Coating

There are several ways to apply a coating to a transducer e.g. mold-transfer [60], spray coating, VDP [59, 61] and spin coating [61]. For CMUTs insulating layers are usually applied using mold-transfer to integrate a lens at the same time. However, a lens should not be applied for this application as the uncoated devices used for comparison will not be focused. Spray and spin coating are better for wafer scale coating, so instead an alternative method was used. This method will now be described in detail.

To test the PDMS coating, one of the fabricated arrays was mounted on a printed circuit board (PCB)

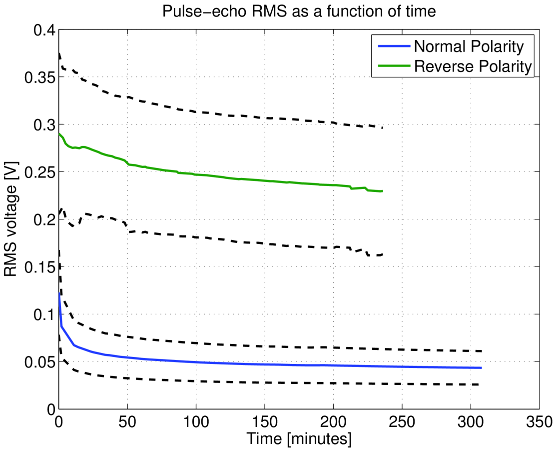

Figure 5.8: *RMS of received signal over time measured using a plane reflector.*

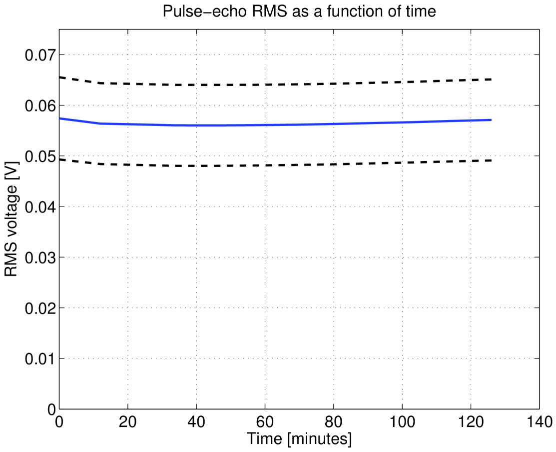

Figure 5.9: *modification of CCB to allow for bias voltage on the substrate electrode.*

and wirebonded. The wirebonds were covered by a protective glob top (CHIPCOAT G8345D) and this was used as a dam when applying the PDMS coating. The dam was filled with liquid PDMS and then cured in vacuum. The procedure for this PDMS coating was

- Mix the two components of Sylgard 170 and de-gas in a vacuum chamber for 20 min
- Apply to device using a syringe with a needle tip by dripping the PDMS onto the surface at a close distance
- De-gas the coated array in a vacuum chamber for 60 min
- Cure in a 70°C oven for at least 1 hour

The height of the glob top dam and thus also the thickness of the coating was estimated to be around 900 μm. Coating thickness have been investigated by Lin et al. [60], who found that the main signal was not affected by the thickness. However, if the coating was thin, the echo from the coating-liquid interface would influence the spectrum. According to their results, this should not be a problem with this thickness of coating.

For this particular experiment of coating evaluation, it was desired to have the coated and uncoated elements as similar to each other as possible. Therefore, half of an array was coated using the described method and the other half was left without coating. A picture of the half coated device can be seen in Figure 5.10.

All measurements were performed in oil for electrical insulation of the uncoated part of the device. Acoustical measurements were made to obtain the transmitted pressure and the receive sensitivity for the two halves of the device. Ten working elements were chosen on each half of the array for the experiments. For all measurements the transducer elements were biased at 190 V, which was 80 % of the calculated pull-in voltage. The AC transmit signal was ±60 V.

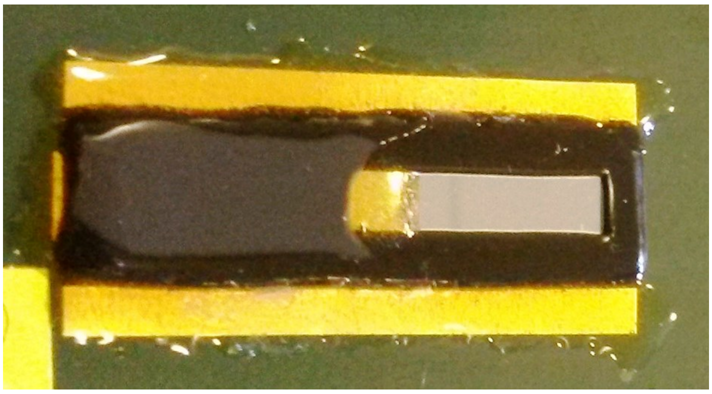

Figure 5.10: *CMUT array mounted on a PCB with PDMS coating applied to half of the array using the glob top and an epoxy as dam.*

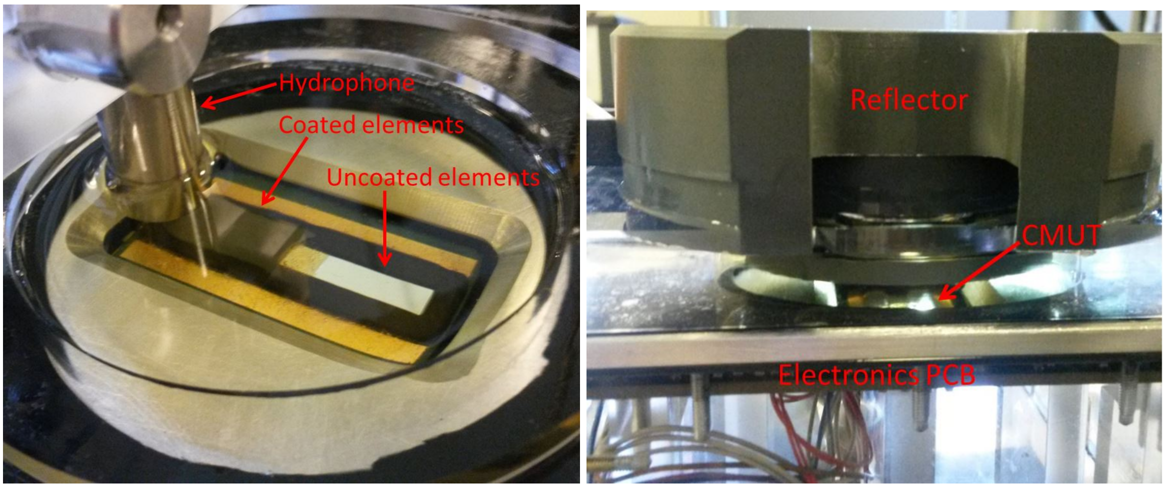

(a) *Hydrophone setup.* (b) *Plane reflector setup.*

Figure 5.11: *Measurement setup using hydrophone (a) and plane reflector (b) in front of the CMUT mounted in the box with electronics.*

5.3.1 Transmit Pressure and Frequency Characteristics

A hydrophone (Optel 5 MHz, Optel, Wroclaw, Poland) placed 10 mm from the transducer surface was used to measure the transmit pressure, as seen in Figure 5.11a. Ten different white, Gaussian random signals were used for the excitation and averaging was done over the 10 random signals. The hydrophone was aligned to the center of all elements when measuring across the array. The values were an average of 10 working elements with or without coating applied. For the transmitted pressure it was found that the array with coating has an output signal of 27% less than the array without coating.

The attenuation in PDMS could be described as [60]

$$L_{\mathrm{dB}} = \alpha f^{\beta} w \qquad \text{or} \qquad \frac{I(w)}{I_0} = 10^{\left(-\frac{\alpha f^{\beta} w}{20}\right)}, \tag{5.1}$$

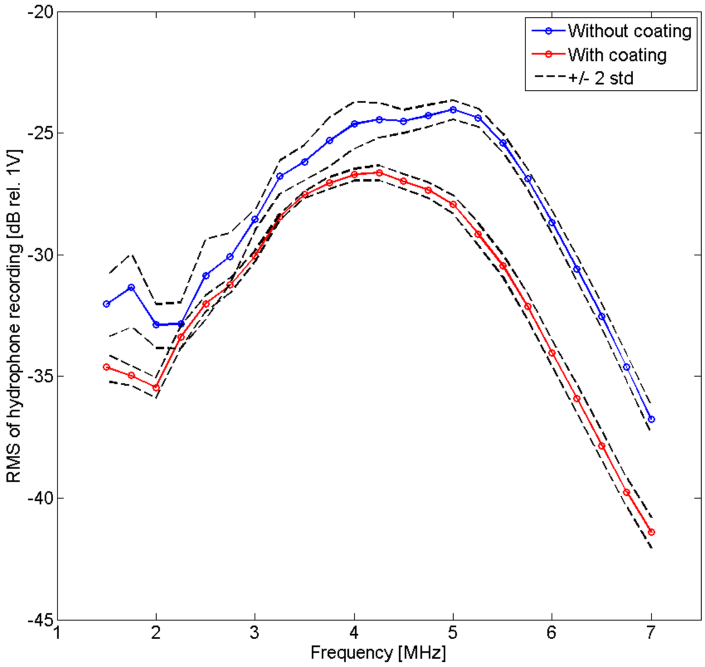

Figure 5.12: *Transfer function in transmit for elements with and without coating found as a mean of 10 elements of each kind. An 8 pulse, narrowband excitation is used for each frequency.*

where I_0 is the original intensity, α the attenuation loss factor (given in dB/MHz/mm), f the frequency, β an empirically found parameter and w the thickness of the coating. For the Sylgard 170 PDMS it was found that $\alpha = 0.37$ dB/MHz/mm and $\beta = 1.4$. Using a frequency of 5 MHz and the estimated coating thickness of 0.9 mm, the expected drop in signal intensity was 31 %, which was comparable to the measured signal loss with a difference of ±13 % respectively for transmit and receive. The differences arose from the estimation of coating thickness.

Hydrophone measurements were also performed for varying frequencies. A narrowband, 8 period, excitation was used at each frequency. The frequency sweep was made from 1.5 MHz to 7 MHz in steps of 250 kHz. The hydrophone was placed in the center of each element at a distance of 10 mm and the average results ±2 standard deviations for 10 elements with and without coating can be seen in Figure 5.12. From this the mean center frequency was found to be 4.5 MHz for the elements without coating and 4.1 MHz for the elements with coating. This means the coating resulted in a decrease in center frequency of around 9 % which was due to the added mass on the plate. Similarly the fractional bandwidth was found to be 77 % for the array without coating and 84 % with the coating. Thus, the PDMS coating slightly increased, 9 %, the fractional bandwidth when transmitting pressure which was explained by the increased damping of the plate. It was also seen that applying this coating with a thickness of 0.9 mm resulted in a loss in signal of around 3.8 dB at the center frequency.

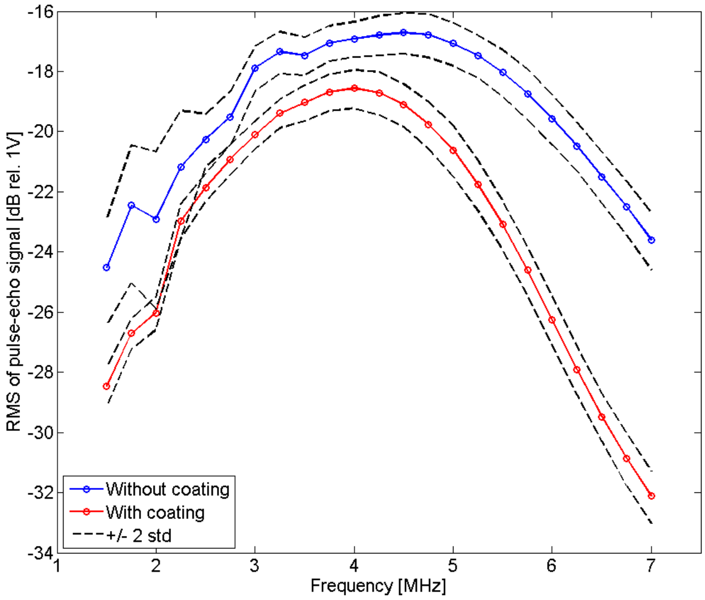

Figure 5.13: *Transfer function in receive for elements with and without coating found as a mean of 10 elements of each kind. An 8 pulse, narrowband excitation is used for each frequency.*

5.3.2 Receive Sensitivity and Pulse-Echo Characteristics

To measure receive sensitivity a plane reflector of 40 mm PVC (Polyvinylchloride) was placed at a distance of 10 mm from the transducer surface as seen in Figure 5.11b. Again ten different white, Gaussian random signals were used for the excitation and averaging was performed over the 10 random signals.

The results from the receive analysis showed a decrease of 35 % for the coated elements compared to the uncoated which matches well with the expected value found from (5.1). The receive sensitivity was found by dividing the measured pulse-echo signal with the measured transmit pressure for the same element to take into account that the coated elements also transmitted less pressure than the elements without coating.

A pulse-echo analysis to find the transfer function using a plane reflector was also carried out. The same method as for the transmit analysis was used and a narrowband, 8 period excitation applied. Again, a frequency sweep was made from 1.5 MHz to 7 MHz in steps of 250 kHz and the average result ±2 standard deviations for 10 elements of each kind can be seen in Figure 5.13. This shows the pulse-echo frequency characteristic. It was seen that the loss in signal was around 3.4 dB. The -6 dB center frequency and fractional bandwidth were found again from the normalized pulse-echo signal. This resulted in the center frequency being 4.4 MHz and 3.9 MHz for the elements without and with coating, respectively. This meant a decrease of 11 %. The measured fractional bandwidths were found to 108 % and 92 %, respectively, resulting in a decrease of 15 %. Again, the coating decreased the center frequency due to the added mass and the fractional bandwidth was decreased as well, which could also be ascribed to the added mass.

The results from the measurements for both transmit and receive are summarized in Table 5.1.

Table 5.1: *Results for center frequency and fractional bandwidth from hydrophone and plane reflector measurements of 10 elements with and 10 elements without coating.*

Measurement	**Without coating**	**With coating**	**Difference**
Center frequency, transmit	4.5 MHz	4.1 MHz	-9 %
Fractional bandwidth, transmit	77 %	84 %	+9 %
Center frequency, receive	4.4 MHz	3.9 MHz	-11 %
Fractional bandwidth, receive	108 %	92 %	-15 %

5.4 Loose Connections

During the measurements another problem was discovered: more and more elements seemed to loose the connection indicated by becoming acoustically dead. An easy way to check if there was connection to an element was to measure the capacitance with the impedance analyzer. For the array used in the longterm acoustical measurements shown above the capacitance was checked right after mounting of the device, and it was found to have 30 missing connections already before use. The capacitance measurements showed that the elements were open not short circuited. This showed that it was not due to short circuiting of the elements, like for the Vermon probe, that they were not emitting ultrasound. During the acoustical measurements 60 elements were not working, and checking the capacitance again afterwards, 80 elements were not connected! The capacitance measurements were performed at 500 kHz by reading the capacitance directly from the impedance analyzer. The capacitance measurements from before and after SARUS measurements can be seen in Figure 5.14.

A lot of tests were performed to find the source of the missing connections to the elements. Computer Tomography (CT) scanning of the mounted devices was tried to see if broken wires or loose wires could be seen. However, since aluminum was used for wire bonding and bonding pads on the device,

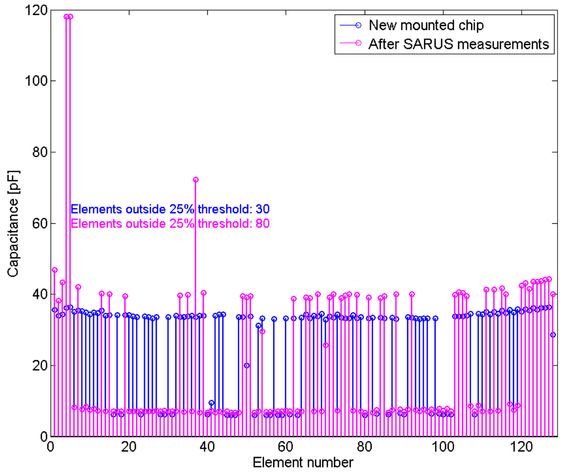

Figure 5.14: *Capacitance check for all elements before and after acoustical measurements on same array.*

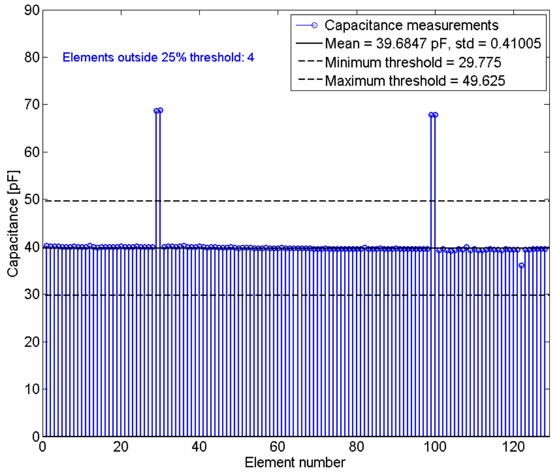

Figure 5.15: *Capacitance check for all elements before using the arrays without covering the wires with glob top.*

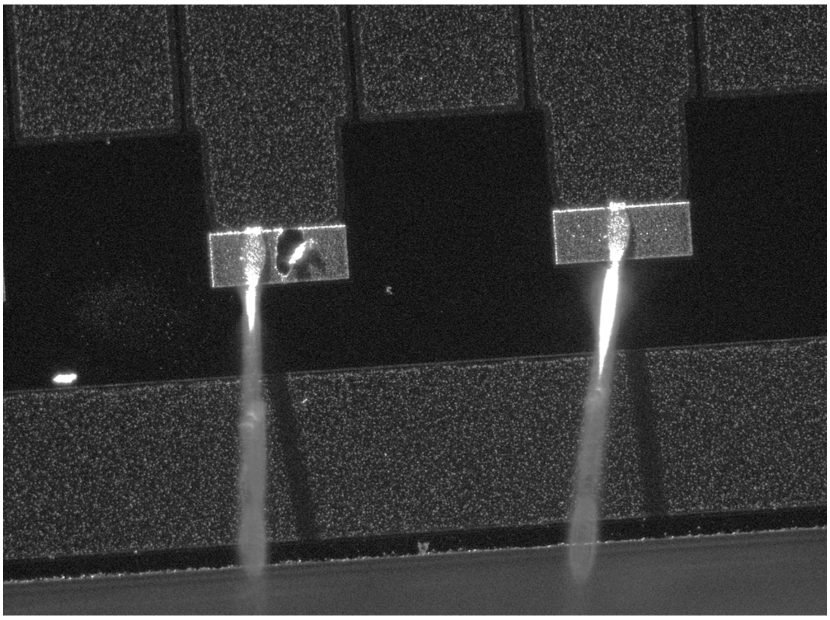

Figure 5.16: *Microscope picture of wirebonding where a previous wire that ripped off the aluminum pads is seen next to one of the wires.*

the wires and pads could not be seen in the CT scanning. An acoustical microscope was tried to again see if the wires were loose or the aluminum bonding pads had loosened from the silicon substrate. Again nothing could be observed to be the reason for the missing connections.

As the problem with the missing connections were not seen to be as severe a problem for the first arrays that was mounted and DELTA changed their bonder since then, it was suspected that the bonder was the origin of the problem. A problem with the bonder could mean that the wires were not properly attached to the bonding pads. Another option could be that the glob top, that was used to protect the wires during experiments, had too much stress so it would either break the wire, pull it off, or pull off the aluminum bonding pads. To test if one of these two options (bonder or glob top) was the problem, a device was mounted in the same way as usual but without the glob top. Checking the capacitance right after mounting, it was found that all elements were connected, see Figure 5.15. As the same bonder was used as for the device in Figure 5.14, it was concluded that it was the glob top causing the problem not the bonder.

Looking in a microscope, there was evidence that the wire bonding had to be redone several places because the aluminum had ripped off. This is seen in Figure 5.16. On another wafer the aluminum was annealed after end processing and this seemed to improve the adhesion to the silicon surface. Alternatively, an adhesion layer of e.g. titanium should be included in the process, however, this requires more modifications of the process flow as titanium is not etched by the wet aluminum etch.

Contact Materials and Annealing

To further evaluate the attachment of bonding wires to the contact pads and the pads themselves, destructive tests of wirebonds on various contact pads were performed. Four samples were prepared with four different metal or treatment conditions:

1. Silicon with 400 nm aluminum pads (Si/Al)
2. Silicon with annealed 400 nm aluminum pads (Si/Al anneal)
3. Silicon with 20 nm titanium and 400 nm aluminum pads (Si/Ti/Al)
4. Silicon with annealed 20 nm titanium and 400 nm aluminum pads (Si/Ti/Al anneal)

The annealing was done at 425°C and the titanium was added as an adhesion layer between the silicon and aluminum. Ten wirebonds were made on each of the substrates and a destructive pull test performed. During this test the bonded wire was pulled and the load for which it broke or got ripped off was a measure of the strength of the wirebond. Normally a wirebond was accepted if the pull test measured above 5.5 g. The mean and standard deviation for the four substrates can be seen in Table 5.2.

A two-sample t-test statistic was used to test the null hypothesis that the difference in mean value between any two destructive tests was zero (against the alternative hypothesis that they were not equal). A level of significance of $\alpha = 0.05$ was used and the degrees of freedom was 18 since the number of measurements in each sample was 10. To perform this test on a relative small number of samples, it was assumed that the populations were normal, and due to independence, so was their difference. It was furthermore assumed that the standard deviations of each pair in the comparisons had a common value. The results from the t-tests can be seen in Table 5.3. If the t-test statistic was less than the table value for a t-distribution with 18 degrees of freedom, $t_{0.025} = 2.1$, the null hypothesis must be accepted. It was therefore only the comparison between Si/Al (sample 1) and Si/Al annealed (sample 2) that resulted in a rejection of the null hypothesis, i.e. there was a difference in the mean breaking strengths for the two treatments. This meant that the wirebonds should be stronger if the aluminum was annealed,

Table 5.2: *Results from a destructive pull test measurements of wirebonds on four different substrates. Mean and standard deviations are found from 10 wirebonds on each.*

Substrate	**Mean load [g]**	**Standard deviation [g]**
Si/Al	6.3	1.30
Si/Al anneal	7.6	1.15
Si/Ti/Al	7.35	0.89
Si/Ti/Al anneal	7.1	0.43

Table 5.3: *Results from t-tests with different combinations of substrates. Only for the Si/Al and the Si/Al anneal a significant difference is observed within the 95 % confidence interval.*

	Si/Al	**Si/Al anneal**	**Si/Ti/Al**	**Si/Ti/Al anneal**
Si/Al	-	2.233	1.987	1.741
Si/Al anneal	2.233	-	0.5124	1.213
Si/Ti/Al	1.987	0.5124	-	0.753
Si/Ti/Al anneal	1.741	1.213	0.753	-

and this was recommended for all future processes. It can not be concluded from these experiments if an adhesion layer is necessary as well.

PDMS as Coating *and* Glob Top

Another alternative for solving the glob top issue was to only apply the outer dam from the standard glob top and then fill it up with PDMS. PDMS was much softer than the standard glob top and the stress should therefore be lower. Furthermore, this solution provided both surface protection/insulation and wire coating at the same time.

A sketch of the wirebonding and possible glob top and coating solutions are seen in Figure 5.17. The wirebonding between device and PCB without any glob top or coating are seen in Figure 5.17a. Figure 5.17b shows the standard glob top procedure performed by DELTA where a two step epoxy was used to protect the wirebonds. A less viscous dam was first applied around the wires and then filled up with a more viscous component before curing. Figure 5.17c shows the proposed method for applying PDMS both as glob top and surface coating at the same time. Here the out dam from the standard glob top was used as a dam which was then filled with PDMS.

This method for protecting the wires were tested on a device mounted on a CCB. The capacitance of 60 elements was measured before any PDMS was applied and all had proper connection afterwards.

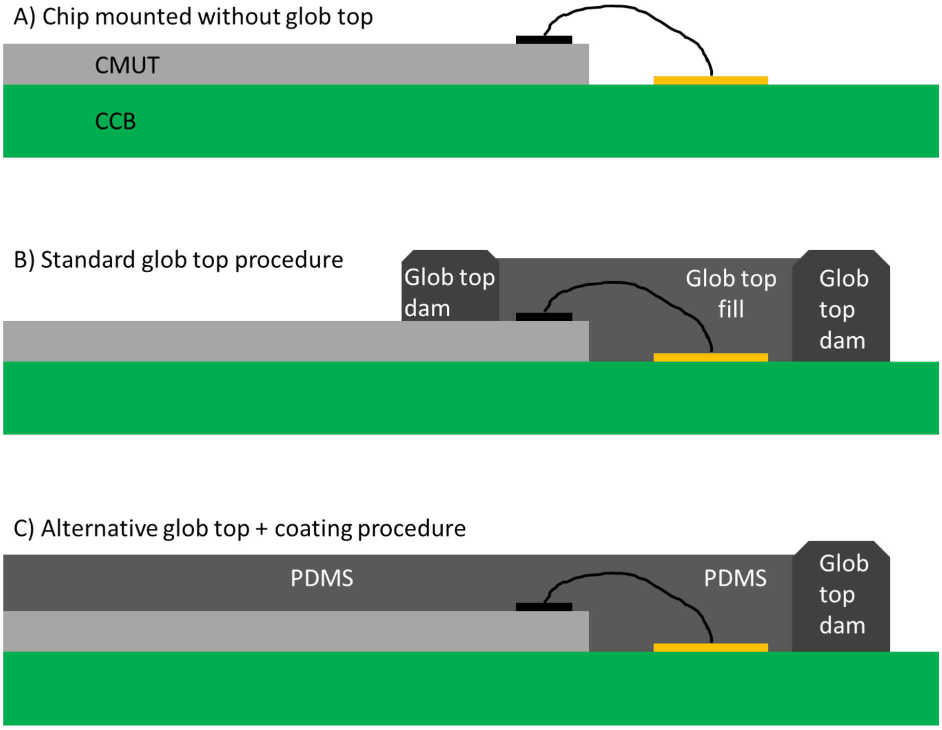

Figure 5.17: *Illustration of possible glob top options. a) The wirebonding between device and PCB, b) the standard glob top procedure performed by DELTA, and c) the alternative protection of both worebonds and device surface with PDMS.*

PDMS was applied using same principle as explained in section 5.3 and all elements still had proper connection. To test whether the PDMS provided sufficient protection of the wires even with a pressure applied on top, a sponge was pushed on the surface of the PDMS. No difference was observed. The transducer was then pushed towards the skin of an arm and as this resulted in no difference as well, a finger was pushed firmly against the surface. Again all elements were still connected to the PCB and it could be concluded that the PDMS would provide a sufficient glob top for the wirebonds.

5.5 Summary

In this chapter the development of a flexible system for testing multiple transducer design was described. The platform is based on wirebonding of the device to a PCB which is connected to a second PCB containing the electronics and a cable to a scanner. It is developed in collaboration with BK Medical.

The charging effects was confirmed acoustically by measuring pulse-echo against a plane reflector. Reversing the bias voltage was again seen to decrease the charging issue.

A thorough investigation of Sylgard 170 PDMS was carried out to evaluate this material as coating for CMUTs. The work was presented at a conference [53], see appendix F, as an evaluation of a device with coating of half of the elements. The initial measurements performed on the coated and uncoated elements showed that the 0.9 mm thick Sylgard 170 PDMS coating had an effect of around 30 % on the performance of the CMUT array regarding transmitted pressure and receive sensitivity. In both transmit and pulse-echo measurements the transfer function was found by sweeping the frequency and a decrease of the center frequency of 9-11 % was found. The fractional bandwidth was found to increase by 9 % in transmit and decrease by 15 % in receive. The losses in dB was found to be around 3.8 dB in transmit and 3.4 dB in pulse-echo. As some effects are always expected from a coating due to the loss in the material the Sylgard 170 PDMS was found to be a good option for coating of CMUTs.

An other problem with the mounted devices was observed: a lot of loose connections which kept increasing in number during operation of the transducer. It was found to be due to too much stress in the glob top, which caused the aluminum to get ripped off the silicon surface on the device. A final solution to this problem was still under investigation at the time of this thesis, but two methods was suggested. The first was to anneal the aluminum after deposition and patterning to improve the adhesion, and the other was to use PDMS or an other softer material as glob top and coating in one.

The challenges found in this chapter and the suggested solutions also apply to the prototype probe described in the next chapter. This probe is built on a similar system as the evaluation platform.

CHAPTER 6

TABLA Prototype Probe

In the last part of the project a new goal was made in the large ultrasound project: make a CMUT prototype probe. The timeline for this was set to 100 day! Within these 100 days new devices should be designed and fabricated, and electronics should be developed to operate the CMUT. Furthermore, packaging and mounting in a probe handle should finalize the prototype probe. The CMUTs were designed and fabricated at DTU, the electronics were made by BK Medical and the assembly by STI.

The probe was named TABLA. The name was inspired by an Indian set of drums with two different sizes, in this case representing the 1D and 2D version of the prototype. The 2D version was out of scope for the 100 days and this thesis, but will be made in the future. A sketch of how the final probe should look is seen in Figure 6.1.

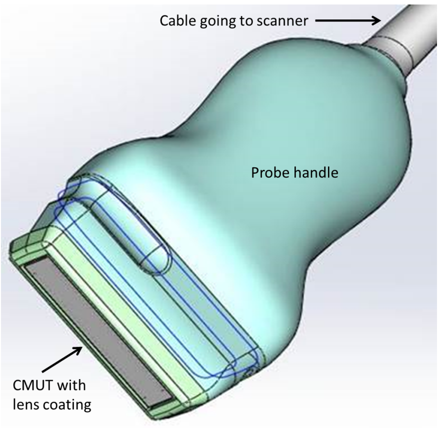

Figure 6.1: *Drawing of the final TABLA prototype probe as it should look after assembly. The grey area is a lens covering the CMUT and the light green part is called the nose piece.*

6.1 Probe Requirements

Certain requirements and restrictions for how the probe should be designed and fabricated arose from the project goal of making a fully working probe. These criteria were also stated in chapter 4 with the description of device design. The CMUTs used for the TABLA probe are the arrays described in chapter 4, and the design and fabrication of the CMUTs can be found there.

For completeness some of the requirements are repeated here. The main idea from a scientific point of view with the TABLA probe, was to make a CMUT probe and compare the performance of this probe with a standard piezoelectric probe. Thus, the parameters affecting imaging performance were chosen to match an 8812 STI piezoelectric probe. Table 6.1 shows the parameters of the TABLA probe and the 8812 probe. The two last parameters are not a requirement, but an observation after producing the TABLA probe.

Table 6.1: *Transducer parameters for a 8812 piezoelectric probe and the TABLA CMUT prototype probe. The CMUT is made to match this piezoelectric probe as much as possible.*

	8812	**TABLA**
Design Center Frequency	5 MHz	5 MHz
Pitch	0.3 mm	0.3 mm
Number of elements	128	128
Active length	38.1 mm	38.1 mm
Elevation	5 mm	5 mm
Geometric focal depth	25 mm	25 mm
Lens material	Plastic	RTV
Lens max thickness	0.584 mm	1.15 mm

The probes were both linear arrays with λ-pitch. The TABLA probe was designed to operate at a DC bias of 190 V which should correspond to 80 % of the pull-in voltage. The transmit signal should be ±85 V AC which is the maximum of the imaging systems. The probe should work with both a BK 2300 commercial scanner and the research scanner, SARUS.

All this was taken into account when designing the TABLA probe devices, electronics and packaging scheme, which will be described in the following section.

6.2 Probe Development

The design and fabrication of the device used in this probe was described in chapter 4. The plate side length was 49 µm, the insulation oxide layer was 400 nm, the vacuum gap height 360 nm and the plate consisted of 2 µm silicon and 200 nm aluminum.

To assemble the TABLA probe, it was desired to have electronics that could be reused if necessary, thus, a flexible system similar to the one described in chapter 5 was developed. A cable should be connected to a PCB which contained the electronic parts, see Figure 6.2, and this PCB should be connected to another PCB which held the CMUT. The connector PCB should in this case, unlike the CCB used in the evaluation platform, be a flexible PCB. This PCB still contained the connections to the individual elements and to ground. The flexibility was necessary to fold the connections backwards and into the probe handle. The chip was mounted by DELTA in the same way as before using wirebonding and a glob top. A CMUT mounted on a flexible PCB, ready for assembly into the probe is seen in Figure 6.3. The PCBs are made by BK Medical.

Figure 6.4 shows the flexible PCB mounted on the electronics PCB. The device is seen facing forward in the photo and the flexible part of the PCB can be seen to bend and connect to the solid PCB. The photo in Figure 6.4 is only for demonstration; for the actual probe the CMUT needs a protective coating and a focusing lens as well.

After the chip was mounted, wirebonded and glob topped it was sent to STI who handled the assembly and packaging into the probe handle. The glob top dam was filled with Room Temperature Vulcanized (RTV) silicone for insulation of the device surface. A lens of RTV for focusing in transmit was applied

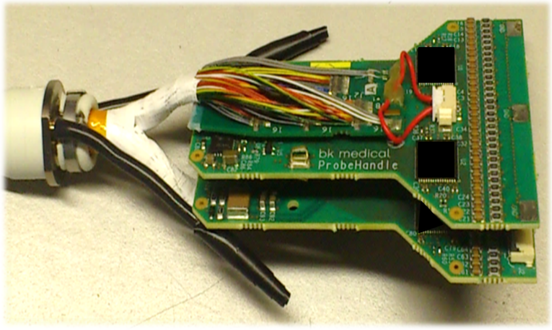

Figure 6.2: *PCBs to be put inside the probe handle of a TABLA prototype. A cable is attached to the outside side of each PCB.*

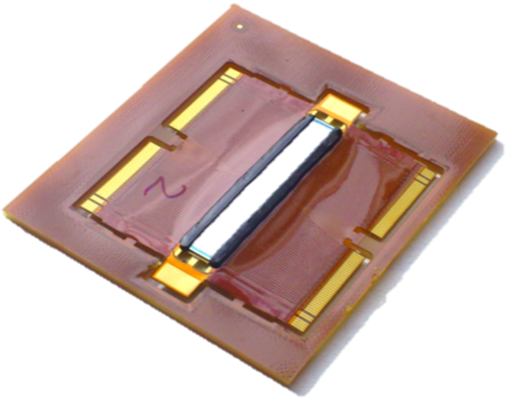

Figure 6.3: *Flexible PCB for mounting CMUTs and connect to the probe handle PCB. A CMUT device is seen as the bright rectangle.*

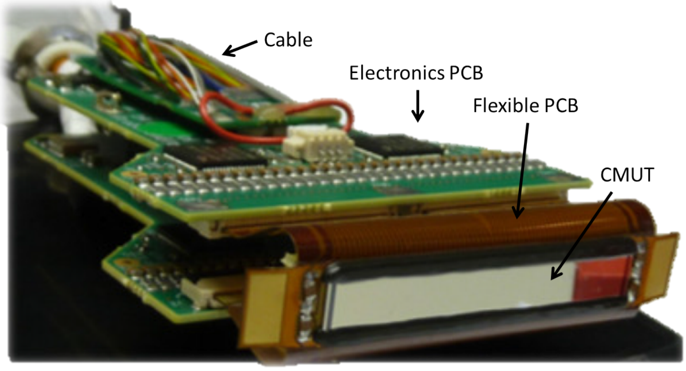

Figure 6.4: *Flexible PCB with a CMUT chip connected to the probe handle PCB for demonstration purpose. The chip mounted on the flexible PCB is seen in the front and the cable toward the back.*

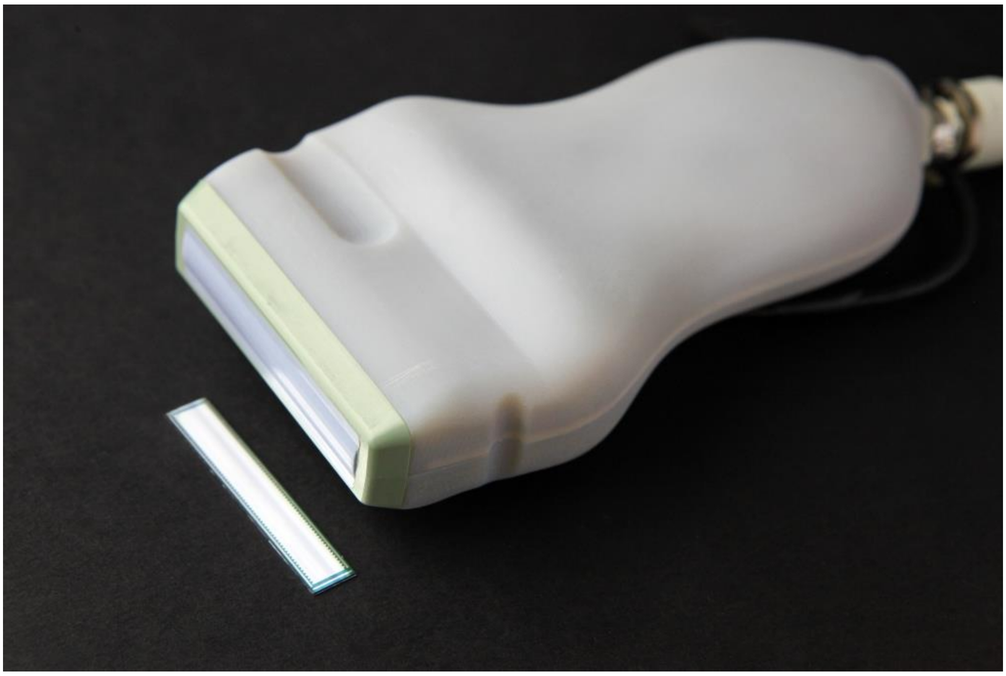

Figure 6.5: *First finished TABLA probe with a similar device in front of it.*

as well. The design also allowed for adding a backing material on the backside of the chip by having a hole in the flexible PCB. Two different materials were tested in the two first prototype assemblies: a standard backing material used for piezoelectric transducers by STI and a piece of FR4 which was the material used for the flexible PCB. Offhand, no difference was observed for the two backing materials so for future probe assemblies the FR4 can be used, however, no quantitative evaluation of the two backing materials has been carried out.

An existing nose piece (tip of the probe) for a piezoelectric probe was used for the assembly of the TABLA probe. The plastic handle was 3D printed for the prototype probes. Figure 6.5 shows a photo of the first finished prototype of the TABLA probe with a CMUT similar to the one inside the probe in front of it.

6.3 Characterization

By the time this PhD project ended, two prototype probes had been assembled. Some initial tests were conducted with a BK 2300 ultrasound scanner and these will now be shown and discussed.

6.3.1 The TABLA 1 Prototype Probe

This was the first successful prototype assembly and the probe was named TABLA 1. This first probe was finished within the 100 days deadline that was originally set for the CMUT prototype probe. Images was successfully made with the probe.

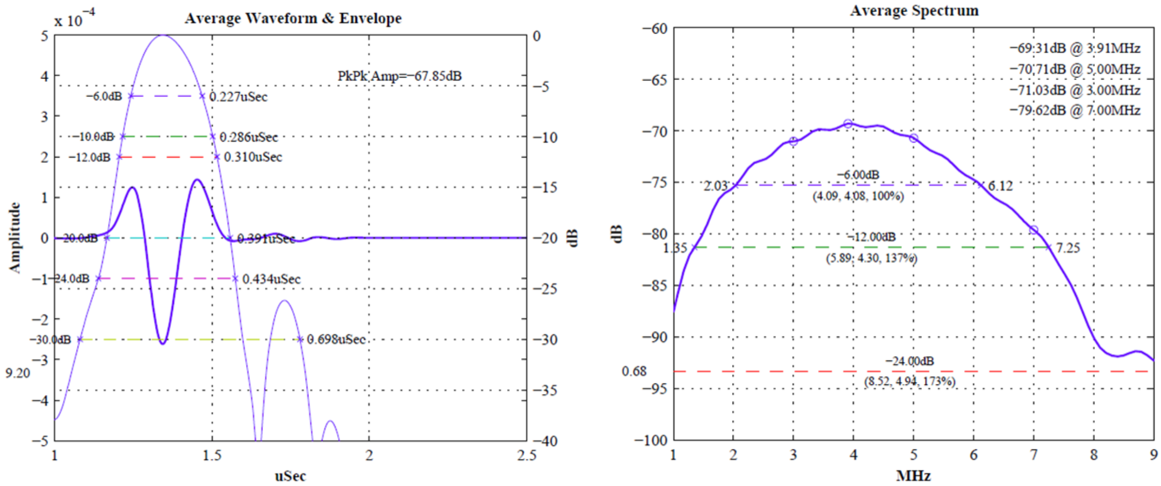

(a) *Average waveform.*

(b) *Average spectrum.*

Figure 6.6: *Initial characterization of working elements after finished assembly of the TABLA 1 probe. a) Average waveform in pulse-echo and b) corresponding average spectrum.*

After the assembly, the individual elements were measured in pulse-echo. The average waveform of the working elements right after assembly can be seen in Figure 6.6a and the average spectrum in Figure 6.6b. This characterization was made by STI as part of their probe production similar to evaluations of their standard piezoelectric probe after manufacturing (a rough comparison to a manufacturing test of a piezoelectric probe will be shown later in this section).

The spectral shape in Figure 6.6b looked Gaussian as it should, and the ringdown characteristic attractive as well. It is seen that the center frequency was measured to be 4.1 MHz and the -6 dB fractional bandwidth to be 100 % which was expected for a CMUT probe. This was found from the average of the working elements. As this probe was assembled before the problem with increasing number of loose connections was discovered. As for the ICB-CCB solution, using glob top resulted in a lot of elements with missing connections and more lost their connections along the way when using the probe. During the assembly the elements were checked after every step in the process and right after the flexible PCB arrived at STI, seven elements were missing connection. The number increased to 17 after first coating, to 21 after applying backing material, to 24 after applying the lens and to 33 at an acoustic test at STI before shipping the probe back to BK Medical. The number of missing elements were not measured after using the probe for imaging, but too many elements are lost to continue imaging with this probe.

A couple of ultrasound images were also made before most of the elements lost the connection. Figure 6.7a shows an image of a tissue mimicking and wire phantom and Figure 6.7b shows an image of a carotic artery on a volunteer. In Figure 6.7a the metal wires are clearly seen as white spots, but no cysts (should be next to the wires) are visible. In Figure 6.7b the round black area a little off-center to the right is the carotic artery. The images looks good and the structures can be identified in the images. However, the sensitivity of the probe was seen to be rapidly decreasing when continuously measuring with the probe. This was due to the previously mentioned polarity of the DC bias which for this probe was in the normal mode of operation, for which charging would cause a large decrease in signal as it

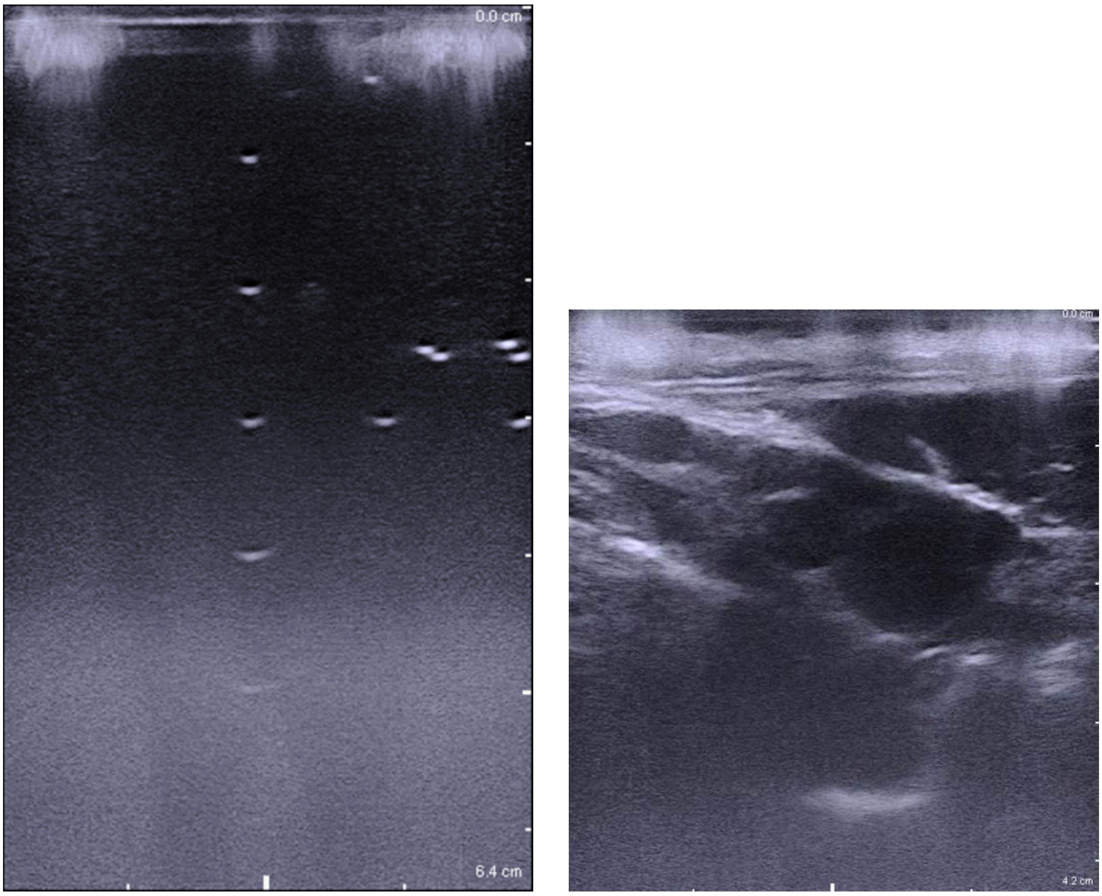

(a) *Phantom image.* (b) *In-vivo image.*

Figure 6.7: *Ultrasound images made with the CMUT TABLA 1 prototype probe. a) Shows a wire phantom and b) shows the carotid artery on a volunteer.*

was observed in the images.

6.3.2 The TABLA 2 Prototype Probe

A second prototype probe was successfully assembled. A couple of changes were made compared to the TABLA 1 probe: FR4 was used as backing material, better connection of shield to ground, a little thicker lens (due to process variations), and the polarity was changed to the reverse mode to avoid the charging issue.

As for the TABLA 1 probe, the individual elements were measured in pulse-echo after the assembly. The average waveform of the working elements can be seen in Figure 6.8a and the average spectrum in Figure 6.8b. Again this characterization was performed by STI.

It was seen that the center frequency was measured to be 3.6 MHz and the -6 dB fractional bandwidth 111 % for this probe. As for the TABLA 1 probe this was also assembled before the problem with

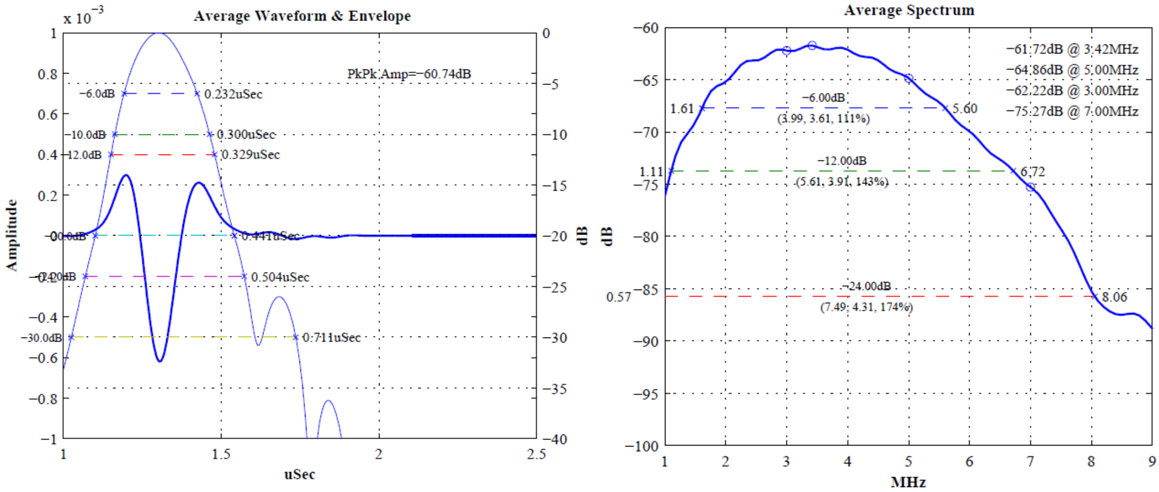

(a) *Average waveform.* (b) *Average spectrum.*

Figure 6.8: *Initial characterization of working elements after finished assembly of the second TABLA probe. a) Average waveform in pulse-echo and b) corresponding average spectrum.*

missing connections was solved and around 30 elements were not connected after the assembly was finished. Thus, it was expected that this probe had a limited life time before too many open connections would make it unsuitable for imaging.

A couple of ultrasound images were made before too many elements lost the connections. The images were made at BK Medical with a 2300 scanner and for an initial comparison similar images were also made using a 9012 piezoelectric probe from STI. This probe did not have the same specifications as the 8812, however, it was the only available for the 2300 scanner at the time of measuring. The images can therefore not be directly compared, but they can provide an initial idea of the CMUT probe performance.

Figure 6.9 shows images of a tissue mimicking phantom with wires and cysts and images of a carotic artery on a volunteer made with both the TABLA 2 probe and the 9012 piezoelectric probe. The images look good for the TABLA probe and the structures could be clearly identified in the images. It should be noted that the gain was a lot higher for the TABLA probe than for the 9012 (93 % compared to 44-50 %) indicating a lower sensitivity of the TABLA probe. However, the operating conditions were not optimal for the TABLA probe, as a frequency of 7 MHz was used, the AC transmit voltage was set to 50 V and not the 85 V the probe was designed for. Furthermore, the 9012 probe has 192 elements which should give a better images than a 128 element probe. A lot of elements had also already lost the connection in the TABLA probe, so the number of active channels for this probe would be even lower than 128. Taking all this into account, the sensitivity would probably still not be as good as for the piezoelectric probe, however, the difference would not be as big.

In contrast to the TABLA 1 probe, the signal of the TABLA 2 probe did not decrease when measuring continuously. This showed that the reverse mode of operation had solved the issue with charging in the CMUT also for the prototype probe. Future assemblies should be made in the reverse mode if the charging issue is not eliminated from the device.

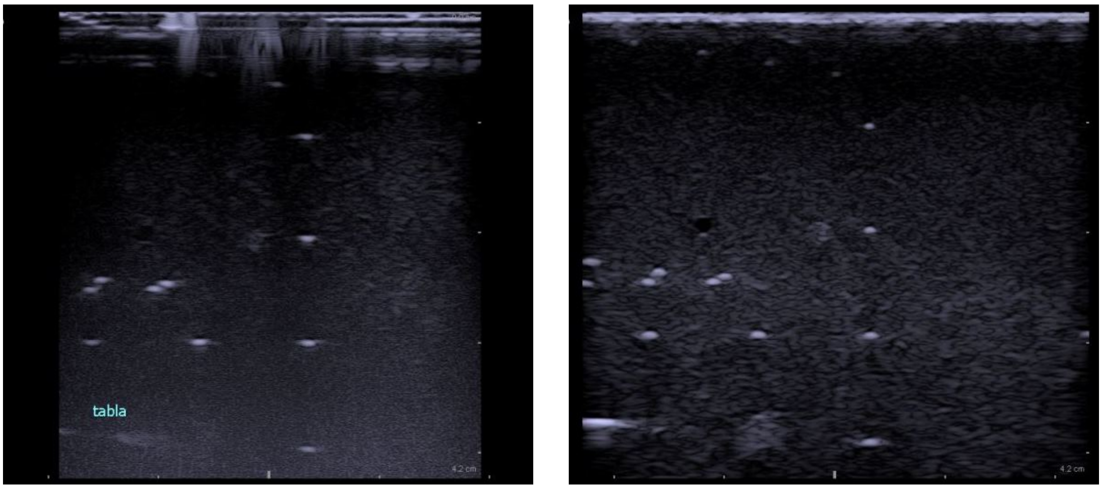

(a) *Phantom image made with TABLA 2.*

(b) *Phantom images made with 9012.*

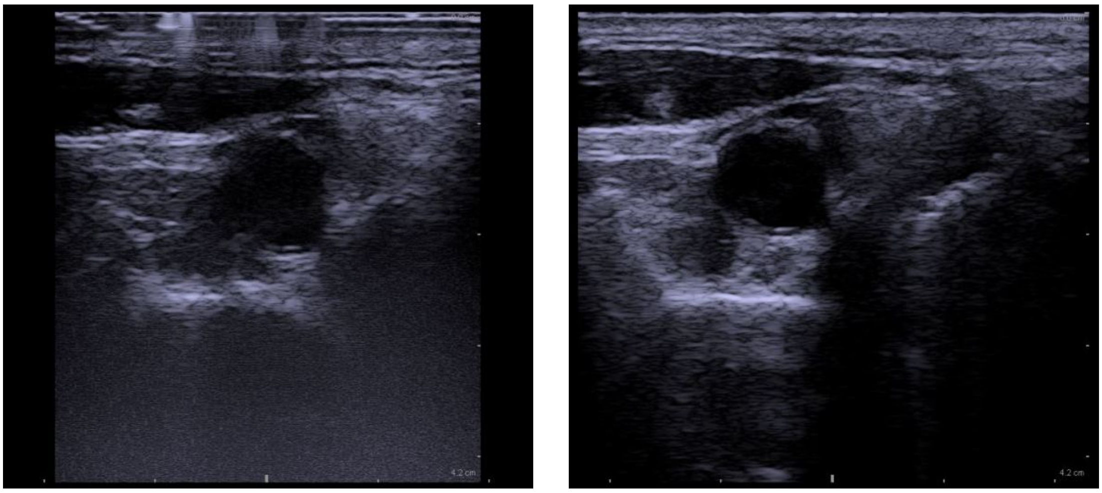

(c) *In vivo image made with TABLA 2.*

(d) *In-vivo image made with 9012.*

Figure 6.9: *Ultrasound images of a multi-purpose phantom (a and b) and a carotic artery (c and d) of a volunteer to test the TABLA 2 probe (a and c) and make an initial comparison to a piezoelectric probe (b and d). The gain for the TABLA probe was 93 % and for the piezoelectric probe it was 44 %.*

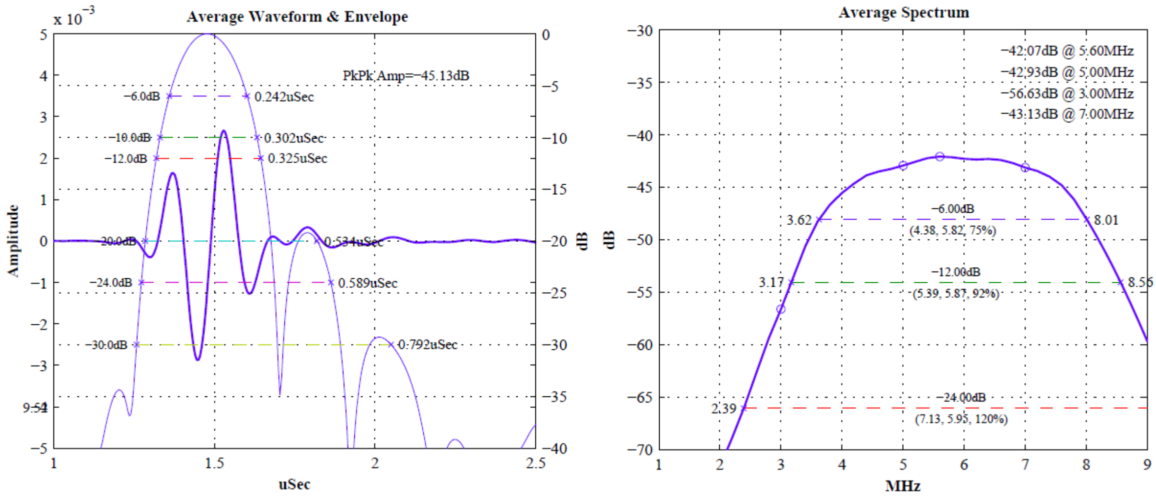

(a) *Average waveform.* (b) *Average spectrum.*

Figure 6.10: *Initial characterization of all elements after finished assembly of a 8812 piezoelectric probe. a) Average waveform in pulse-echo and b) corresponding average spectrum.*

6.3.3 Comparison

An example of a manufacturing test made on a 8812 probe was provided from STI. The average waveform of all elements in such a probe can be seen in Figure 6.10a and the average spectrum in Figure 6.10b.

By extracting data from the measurements an initial comparison of the three probes could be made. The results can be seen in Table 6.2. Comparing the two TABLA probes with the 8812 piezoelectric probe from these measurements, it was seen that the TABLA probes had a lower center frequency which was due to the design of the CMUTs. The TABLA probes both have a higher fractional bandwidth as it was expected for a CMUT probe. Furthermore, it was seen that the amplitude was around 20 dB lower for the CMUT probes showing a lower sensitivity for these probes than for the piezoelectric probe. As seen in Table 6.1, the lens material for the 8812 and the TABLA probes were different and had different attenuations. The following informations about lens design was given from STI: the two-way

Table 6.2: *Summary of measured probe values made by STI for the two first TABLA probes and a 8812 piezoelectric probe. The measurements are seen in Figures 6.6, 6.8 and 6.10.*

	TABLA 1	**TABLA 2**	8812
Center Frequency	4.1 MHz	3.6 MHz	5.8 MHz
Fractional bandwidth	100 %	111 %	75 %
Peak frequency	3.9 MHz	3.4 MHz	5.6 MHz
dB at peak frequency	-66.6 dB	-61.7 dB	-42.1 dB
Peak-peak amplitude	-65.1 dB	-60.7 dB	-45.1 dB

attenuation at 5 MHz in the 8812 array lens was around 1.4 dB. The 5 MHz two-way attenuation in the TABLA 1 lens was estimated to be 6.2 dB and for the TABLA 2 with the thicker lens it might be closer to 8 dB. This meant a difference of around 5 dB due to lens attenuation was expected. The 8812 probe was furthermore tested using a different test system which showed in a test measurement to give around 5 dB lower sensitivity. Even taking both of these 5 dB differences into consideration, it only accounted for some of the lower sensitivity that was measured. The difference in sensitivity which was not accounted for was then 5-10 dB. Possible factors to influence this lower sensitivity could be the glob top approach, which could reduce the active area of the CMUT (if around 10 % it would be -1 dB). It could also be due to the fact that a piezoelectric probe, with a lower center frequency than the 8812, would also have a lower sensitivity due to the lower capacitance (may be around 2-3 dB). Furthermore, it could also arise from the amplifiers only being in their start-up 0 dB gain mode and if they were activated, they would add sensitivity to the CMUT probe. In general it seemed that the CMUT probe lack sensitivity compared to a piezoelectric probe, however, a fair and quantitative comparison should be made with a final, fully working version of the probe.

Comparing the two TABLA probes to each other, it was seen that the sensitivity was markedly higher for the TABLA 2 even with the thicker lens. This was very likely caused by the bias reversal which also showed a higher signal in the impedance measurements in chapter 4.15. The center frequency was slightly reduced which was due to the higher effective bias causing an increased spring softening effect. It could also be partly caused by the thicker coating as seen during the investigations of the effect of a coating on CMUTs (see section 5.3). Furthermore, an increased fractional bandwidth was observed which could also be explained by the increased spring softening which as it meant a lower mechanical impedance of the system, and that the impact of the acoustical impedance would therefore be relatively higher. This resulted in an increased damping of the system, which gave a higher bandwidth of the system.

In total, there were definitely some improvements for the second version of the TABLA probe. Investigation on how to solve the problem with missing connections was still ongoing and hopefully a fully working CMUT probe could be made within this year.

6.4 Summary

In this chapter the development of the CMUT prototype probe called TABLA was described. The probes were made in collaboration with BK Medical who was in charge of electronics and STI who was in charge of packaging and assembly.

The probe was designed similar to the evaluation platform described in the previous chapter with a CMUT device mounted on a carrier PCB which in this case was flexible. The flexibility made it possible to connect the carrier PCB to a PCB with all electronics inside a probe handle. A cable was attached to the electronics PCB as well to connect the transducer to a BK 2300 scanner or SARUS. Two TABLA probes had been assembled so far and the initial characterization showed promising results for the CMUT probe, however, the first version suffered from charging effects. These was solved in the second version, which had issues with loosing connections as seen with the evaluation platform as well.

The TABLA probe was designed to match a standard piezoelectric probe in specifications as much as possible and initial comparisons were carried out. The sensitivity was seen to be lower for the CMUT probe, but the fractional bandwidth larger as expected. A proper quantitative characterization and comparison with a similar piezoelectric probe was not done at the time of this thesis and will be the scope of future work when the issue with lose connection is properly solved. Furthermore, the fully working probe should also make it through tests for approval of images on humans and on a longer perspective a clinical study will be made.

CHAPTER 7

Project Conclusion

The overall purpose of this project was to design, fabricate, and characterize microfabricated capacitive transducers for ultrasound imaging.

Theoretical Modeling of the CMUT

Basic knowledge and understanding of the CMUT device was obtained through analytical modelling. The focus in this project was to include the anisotropic effects of a single crystalline silicon plate in the analytical models. The full anisotropic plate equation was solved for the deflection of both circular and square shaped plates. The solutions for the deflections were compared to FEM showing a maximum deviation of 0.3 %. The theory of multilayer plates is also applied to CMUTs and the result compared to a deflection measurement of a fabricated device showing a difference of only 0.07 %. A full electrostatic analysis based on energy considerations and including the anisotropic effects was carried out for both circular, square, and parallel plate devices. CMUTs are usually operated with a DC bias of 80 % of the pull-in voltage. The stable position of a square plate at 80 % of pull-in was found to only have a deviation of 0.01 % compared to a circular plate whereas the parallel plate had a deviation of 0.3 %. Looking at the spring constant for the three plate types a difference of 0.47 % was found for the square and circular plates opposed to 12.5 % for the circular and parallel plates, both at 80 % of pull-in. The pull-in distance and pull-in voltage was calculated both for zero and non-zero applied pressure for all three plate types. For the parallel plate exact expression can be found and using the same form for the expression for the circular and square plates results in a deviation of 0.6 % and 0.7 %, respectively, for the pull-in distance and 3.9 % and 1.7 %, respectively for the relative pull-in voltage. The capacitance for circular and square plates was found to only have a difference of 1.4 % at a relative deflection of 0.4. To simplify the calculations for the square plate the capacitance for the circular plate was used instead, resulting in a deviation of only 1.6 %. Devices with both circular and square plates were fabricated to compare with the developed theory. The stable position and pull-in voltage was measured and comparing these to the anisotropic theory, it is seen that the theory is within the uncertainty interval of the measurements for both types of plates.

CMUT Fabrication

Fusion bonding was chosen as the process technology for producing CMUTs in this project. Two different processes was carried out with almost 100 % yield in both.

The first 1D arrays were fabricated at Stanford University reusing an existing design. Two versions of the arrays were made: one for linear array imaging at 5 MHz and one for phased array imaging at 2.6 MHz. Both had 132 elements and both circular and square cells were included in the design. Impedance measurements showed signals high enough for imaging with a maximum in phase angle at resonance above 20° for both types of arrays. The resonant frequency in air was measured to be 13.5 MHz and 11.8 MHz, respectively. Increasing the bias voltage the spring softening effect was clearly seen as a lower resonant frequency. The uniformity between two arrays from the same wafer was found to be 0.3 % and the uniformity between all elements within an array was also good with deviations from the mean value of less than 1 % for all elements.

The second version of 1D arrays were made at DTU with the developed baseline process. These arrays were designed to be used in a prototype probe which should be comparable to a piezoelectric probe. The 128 element linear arrays with square shaped cell arrays were designed to have an immersion frequency of 5 MHz. Impedance measurements in air showed a resonant frequency of 9 MHz for these arrays. A large issue with charging was observed in the devices. It was found that the charging effects could be reduced drastically by reversing the bias polarity. Operating in the normal bias polarity with ground on the bottom electrode the maximum phase angle would reduce to around $-60°$ which is not suitable for imaging, however, reversing the bias polarity to having ground on the top electrode, the maximum phase angle increased to around 20°. From investigations of the charging, it was concluded that positive charges were trapped at the interface between insulation oxide and vacuum cavity.

CMUT Acoustical Characterization

Acoutical tests were performed with both Stanford and DTU arrays. For the Stanford version, one of array was mounted into a probe by Vermon and used for the first CMUT ultrasound imaging at DTU. Images were made both of a hydrophone and of a multiwire phantom using both DRF, STA and THI imaging methods. However, the probe suffered from a low breakdown voltage of the support oxide which made proper imaging with these devices impossible and the focus was shifted to the DTU arrays.

As it was expected that several transducer designs should be tested during a longer project period, a flexible platform for evaluating CMUTs was developed. This part was made in close collaboration with BK medical who were in charge of designing PCBs and electronics. The evaluation platform is based on wirebonding of the device to a PCB which is connected to a second PCB containing the electronics and a cable to a scanner. A thorough investigation of Sylgard 170 PDMS was carried out to evalute this material as coating for CMUTs. The initial measurements performed on the coated and uncoated elements show that the 0.9 mm thick Sylgard 170 PDMS coating have an effect of around 30 % on the performance of the CMUT array regarding transmitted pressure and receive sensitivity. In both transmit and pulse-echo measurements the transfer function was found by sweeping the frequency and a decrease of the center frequency of 9-11 % was found. The fractional bandwidth was found to increase by 9 % in transmit and decrease by 15 % in receive. The loss in the coating can, however, be reduced by reducing the thickness of the coating which was not optimized yet.

For the DTU arrays, two of the fabricated devices were also mounted into probe handles. The prototype probes were successfully produced all the way from design and fabrication of new chips (DTU Nanotech), design and production of electronics (BK) and assembly with backing, coating and lens in a probe handle (STI). The first assembled TABLA probe suffered from large charging effects which degraded the image quality to an useless level. The charging issue was solved in the second version by reversing the bias polarity. The second version then had issues with loosing connection to the individual elements. It was found to be due to too much stress in the glob top which caused the aluminum to get ripped off the silicon surface on the device. A final solution to this problem was still under investigation at the time of this thesis, but two methods was suggested. The first was to anneal the aluminum after deposition and patterning to improve the aluminum adhesion. Annealing of the aluminum was tested and showed a significant improvement in a t-test of the mean values for 10 wirebonds of each kind. The other suggestion was to use PDMS or an other softer material as glob top and coating in one and this was tested to provide sufficient protection of the wirebonds even when applying different levels of pressure to the wires through the coating.

The TABLA probe was designed to match a standard piezoelectric probe in specifications as much as possible and initial comparisons were carried out. The sensitivity was seen to be lower for the CMUT probe with around 20 dB. The resonant frequency was around 2-2.5 MHz lower, and the fractional bandwidth larger, 100-110 % versus 75 %, as expected.

7.1 Outlook

With this project the work with CMUTs at DTU was initiated. A lot of experience was gained and 1D arrays was successfully produced. The characterization and optimization of the devices just started and looking ahead this will be the focus of future work.

First of all, a third version of the TABLA probe should be assembled with proper connection to all elements. Using this probe, a proper quantitative characterization and comparison with a similar piezoelectric probe should be carried out. Furthermore, the fully working probe should also make it through tests for approval of images on humans and on a longer perspective a clinical study should be made to complete the evaluation of the CMUT probe.

Having a fully working CMUT probe which is comparable to a piezoelectric probe is good, but really utilizing the advantages with the CMUT technology is of great interest for future projects. The CMUT technology provides much higher design flexibility than the conventional piezoelectric fabrication method and a probe designed specifically for tissue harmonic imaging (THI) could much easier be made with CMUTs. As the technique of THI is to transmit with the fundamental frequency and receive with at the second harmonic frequency, a probe with separate cells optimized for transmitting and receiving can be made with CMUTs.

Bibliography

[1] Ö. Oralkan, A. S. Ergun, J. A. Johnson, M. Karaman, U. Demirci, K. Kaviani, T. H. Lee, and B. T. Kuri-Yakub, "Capacitive micromachined ultrasonic transducers: Next-generation arrays for acoustic imaging?" *IEEE Trans. Ultrason., Ferroelec., Freq. Contr.*, vol. 49, pp. 1596–1610, 2002.

[2] B. T. Khuri-Yakub, "Silicon micromachined ultrasonic transducers," *Japanese Journal of Applied Physics*, vol. 39, no. 5B, pp. 2883–2887, 2000.

[3] B. T. Khuri-Yakub and O. Oralkan, "Capacitive micromachined ultrasonic transducers for medical imaging and therapy," *Journal of Micromechanics and Microengineering*, vol. 21, no. 5, pp. 054 004–054 014, may 2011.

[4] K. Erikson, F. Fry, and J. Jones, "Ultrasound in medicine - a review," *IEEE Transactions on Sonics and Ultrasonics*, vol. 21, no. 3, pp. 144–170, jul 1974.

[5] S. H. Wong, M. Kupnik, R. D. Watkins, K. Butts-Pauly, and B. T. Khuri-Yakub, "Capacitive micromachined ultrasonic transducers for therapeutic ultrasound applications," *IEEE Trans. Biomed. Eng.*, vol. 57, no. 1, pp. 114–123, jan 2010.

[6] M. Kupnik, M.-C. Ho, S. Vaithilingam, and B. Khuri-Yakub, "CMUTs for air coupled ultrasound with improved bandwidth," in *Proc. IEEE Ultrason. Symp.*, 2011, pp. 592–595.

[7] K. K. Park, H. J. Lee, G. G. Yaralioglu, A. S. Ergun, O. Oralkan, M. Kupnik, C. F. Quate, B. T. Khuri-Yakub, T. Braun, J. P. Ramseyer, H. P. Lang, M. Hegner, C. Gerber, and J. K. Gimzewski, "Capacitive micromachined ultrasonic transducers for chemical detection in nitrogen," *Appl. Phys. Lett.*, vol. 91, no. 9, pp. 094 102–094 102, aug 2007.

[8] H. Azhari, "Appendix a: Typical acoustic properties of tissues," in *Basics of Biomedical Ultrasound for Engineers*. John Wiley and Sons, Inc., 2010.

[9] J. A. Jensen, *Estimation of Blood Velocities Using Ultrasound: A Signal Processing Approach*. New York: Cambridge University Press, 1996.

[10] X. Jin, I. Ladabaum, and B. Khuri-Yakub, “The microfabrication of capacitive ultrasonic transducers,” *J. Microelectromech. S.*, vol. 7, no. 3, pp. 295–302, sep 1998.

[11] A. Caronti, G. Caliano, R. Carotenuto, A. Savoia, M. Pappalardo, E. Cianci, and V. Foglietti, “Capacitive micromachined ultrasonic transducer (CMUT) arrays for medical imaging,” *Microelectronics Journal*, vol. 37, no. 8, pp. 770–777, aug 2006.

[12] Y. Huang, A. S. Ergun, E. Hæggström, M. H. Badi, and B. T. Khuri-Yakub, “Fabricating capacitive micromachined ultrasonic transducers with wafer-bonding technology,” *J. Microelectromech. Syst*, vol. 12, no. 2, pp. 128–137, 2003.

[13] B. Legrand and D. Collard, “Electrostatic actuation, electromechanical resonators,” lecture, 2002.

[14] G. Caliano, R. Carotenuto, E. Cianci, V. Foglietti, A. Caronti, A. Iula, and M. Pappalardo, “Design, fabrication and characterization of a capacitive micromachined ultrasonic probe for medical imaging,” *IEEE Trans. Ultrason., Ferroelec., Freq. Contr.*, vol. 52, no. 12, pp. 2259–2269, dec 2005.

[15] D. W. Schindel, D. A. Hutchins, L. Zou, and M. Sayer, “The design and characterization of micromachined air-coupled capacitance transducers,” *IEEE Trans. Ultrason., Ferroelec., Freq. Contr.*, vol. 42, no. 1, pp. 42–50, 1995.

[16] M. Haller and B. T. Khuri-Yakub, “A surface micromachined electrostatic ultrasonic air transducer,” in *Proc. IEEE Ultrason. Symp.*, vol. 2, 1994, pp. 1241–1244.

[17] M. I. Haller and B. T. Khuri-Yakub, “A surface micromachined electrostatic ultrasonic air transducer,” *IEEE Trans. Ultrason., Ferroelec., Freq. Contr.*, vol. 43, no. 1, pp. 1–6, 1996.

[18] X. Cheng, J. Chen, C. Li, J.-H. Liu, I.-M. Shen, and P.-C. Li, “A miniature capacitive ultrasonic imager array,” *IEEE Sensors Journal*, vol. 9, no. 5, pp. 569–577, may 2009.

[19] R. A. Noble, A. D. R. Jones, T. J. Robertson, D. A. Hutchins, and D. R. Billson, “Novel, wide bandwidth, micromachined ultrasonic transducers,” *IEEE Trans. Ultrason., Ferroelec., Freq. Contr.*, vol. 48, no. 6, pp. 1495–1507, nov 2001.

[20] M. Kupnik, A. S. Ergun, Y. Huang, and B. Khuri-Yakub, “Extended insulation layer structure for CMUTs,” in *Proc. IEEE Ultrason. Symp.*, oct 2007, pp. 511–514.

[21] C. H. Cheng, E. M. Chow, X. Jin, S. Ergun, and B. T. Khuri-Yakub, “An efficient electrical addressing method using through-wafer vias for two-dimensional ultrasonic arrays,” in *Proc. IEEE Ultrason. Symp.*, vol. 2, oct 2000, pp. 1179–1182.

[22] C. H. Cheng, A. S. Ergun, and B. T. Khuri-Yakub, “Electrical through-wafer interconnects with sub-picofarad parasitic capacitance,” in *Microelectromechanical Systems Conference*, 2001, pp. 18–21.

[23] M. Kupnik, S. Vaithilingam, K. Torashima, I. Wygant, and B. Khuri-Yakub, “CMUT fabrication based on a thick buried oxide layer,” in *Proc. IEEE Ultrason. Symp.*, 2010, pp. 547–550.

[24] K. K. Park, H. Lee, M. Kupnik, and B. T. Khuri-Yakub, “Fabrication of capacitive micromachined ultrasonic transducers via local oxidation and direct wafer bonding,” *J. Microelectromech. S.*, vol. 20, no. 1, pp. 95–103, 2011.

[25] X. Zhuang, I. O. Wygant, D. S. Lin, M. Kupnik, O. Oralkan, and B. T. Khuri-Yakub, "Wafer-bonded 2-d CMUT arrays incorporating through-wafer trench-isolated interconnects with a supporting frame," *IEEE Trans. Ultrason., Ferroelec., Freq. Contr.*, vol. 56, no. 1, pp. 182–192, jan 2009.

[26] Y. Huang, X. Zhuang, E. O. Hæggström, A. S. Ergun, C.-H. Cheng, and B. T. Khuri-Yakub, "Capacitive micromachined ultrasonic transducers with piston-shaped membranes: Fabrication and experimental characterization," *IEEE Trans. Ultrason., Ferroelec., Freq. Contr.*, vol. 56, pp. 136–145, 2009.

[27] A. Nikoozadeh and P. T. Khuri-Yakub, "CMUT with substrate-embedded springs for non-flexural plate movement," in *Proc. IEEE Ultrason. Symp.*, oct 2010, pp. 1510–1513.

[28] P. C. Eccardt, K. Niederer, T. Scheiter, and C. Hierold, "Surface micromachined ultrasound transducers in CMOS technology," in *Proc. IEEE Ultrason. Symp.*, vol. 2, 1996, pp. 959–962.

[29] J. Knight, J. McLean, and F. L. Degertekin, "Low temperature fabrication of immersion capacitive micromachined ultrasonic transducers on silicon and dielectric substrates," *IEEE Trans. Ultrason., Ferroelec., Freq. Contr.*, vol. 51, no. 10, pp. 1324–1333, oct 2004.

[30] J. Zahorian, M. Hochman, T. Xu, S. Satir, G. Gurun, M. Karaman, and F. L. Degertekin, "Monolithic CMUT-on-CMOS integration for intravascular ultrasound applications," *IEEE Trans. Ultrason., Ferroelec., Freq. Contr.*, vol. 58, no. 12, pp. 2659–2667, dec 2011.

[31] Y. Tsuji, M. Kupnik, and B. T. Khuri-Yakub, "Low temperature process for CMUT fabrication with wafer bonding technique," in *Proc. IEEE Ultrason. Symp.*, oct 2010, pp. 551–554.

[32] N. A. Hall and F. L. Degertekin, "Integrated optical interferometric detection method for micromachined capacitive acoustic transducers," *Appl. Phys. Lett.*, vol. 80, no. 20, pp. 3859–3861, may 2002.

[33] L. L. Liu, O. M. Mukdadi, J. R. Hertzberg, H. B. Kim, V. M. Bright, and R. Shandas, "Atomic layer deposition for fabricating capacitive micromachined ultrasonic transducers: initial characterization," in *Proc. IEEE Int. Symp. Biomed. Imag.*, apr 2004, pp. 512–515.

[34] X. Zhuang, D.-S. Lin, O. Oralkan, and B. T. Khuri-Yakub, "Fabrication of flexible transducer arrays with through-wafer electrical interconnects based on trench refilling with PDMS," *J. Microelectromech. S.*, vol. 17, no. 2, pp. 446–452, apr 2008.

[35] A. Caronti, A. Coppa, A. Savoia, C. Longo, P. Gatta, B. Mauti, A. Corbo, B. Calabrese, G. Bollino, A. Paz, G. Caliano, and M. Pappalardo, "Curvilinear capacitive micromachined ultrasonic transducer (CMUT) array fabricated using a reverse process," in *Proc. IEEE Ultrason. Symp.*, 2008, pp. 2092–2095.

[36] I. Ladabaum, X. Jin, H. T. Soh, A. Atalar, and B. T. Khuri-Yakub, "Surface micromachined capacitive ultrasonic transducers," *IEEE Trans. Ultrason., Ferroelec., Freq. Contr.*, vol. 45, no. 3, pp. 678–690, 1998.

[37] A. Caronti, G. Caliano, A. Iula, and M. Pappalardo, "An accurate model for capacitive micromachined ultrasonic transducers," *IEEE Trans. Ultrason., Ferroelec., Freq. Contr.*, vol. 49, no. 2, pp. 159–168, feb 2002.

[38] A. Lohfink and P.-C. Eccardt, "Linear and nonlinear equivalent circuit modeling of CMUTs," *IEEE Trans. Ultrason., Ferroelec., Freq. Contr.*, vol. 52, no. 12, pp. 2163–2172, 2005.

[39] I. O. Wygant, M. Kupnik, and B. T. Khuri-Yakub, "Analytically calculating membrane displacement and the equivalent circuit model of a circular CMUT cell," in *Proc. IEEE Ultrason. Symp.*, 2008, pp. 2111–2114.

[40] A. Nikoozadeh, B. Bayram, G. Yaralioglu, and B. Khuri-Yakub, "Analytical calculation of collapse voltage of CMUT membrane," in *Proc. IEEE Ultrason. Symp.*, vol. 1, 2004, pp. 256–259.

[41] H. Koymen, A. Atalar, E. Aydogdu, C. Kocabas, H. K. Oguz, S. Olcum, A. Ozgurluk, and A. Unlugedik, "An improved lumped element nonlinear circuit model for a circular CMUT cell," *IEEE Trans. Ultrason., Ferroelec., Freq. Contr.*, vol. 59, no. 8, pp. 1791–1799, 2012.

[42] B. Ahmad and R. Pratap, "Elasto-electrostatic analysis of circular microplates used in capacitive micromachined ultrasonic transducers," *IEEE Sensors Journal*, vol. 10, no. 11, pp. 1767–1773, 2010.

[43] S. Timoshenko and S. Woinowsky-Krieger, *Theory of Plates and Shells*, 2nd ed. Mcgraw-Hill College, jun 1959.

[44] R. L. Taylor and S. Govindjee, "Solution of clamped rectangular plate problems," *Communications in Numerical Methods in Engineering*, vol. 20, no. 10, pp. 757–765, 2004.

[45] M. Rahman, J. Hernandez, and S. Chowdhury, "An improved analytical method to design CMUTs with square diaphragms," *IEEE Trans. Ultrason., Ferroelec., Freq. Contr.*, vol. 60, no. 4, pp. 834–845, apr 2013.

[46] P. C. Eccardt, P. Wagner, and S. Hansen, "Analytical models for micromachined transducers - an overview," in *Proc. IEEE Ultrason. Symp.*, 2006, pp. 572–581.

[47] G. G. Yaralioglu, B. Bayram, A. Nikoozadeh, and B. T. P. Khuri-Yakub, "Finite element modeling of capacitive micromachined ultrasonic transducers," *Proc. SPIE Med. Imag.*, vol. 5750, pp. 77–86, 2005.

[48] M. F. la Cour, T. L. Christiansen, J. A. Jensen, and E. V. Thomsen, "Modelling of CMUTs with anisotropic plates," in *Proc. IEEE Ultrason. Symp.*, 2012, pp. 588–591.

[49] M. F. la Cour, T. L. Christiansen, C. Dahl-Petersen, K. Reck, O. Hansen, J. A. Jensen, and E. V. Thomsen, "Modeling and measurements of CMUTs with square anisotropic plates," in *Proc. IEEE Ultrason. Symp.*, 2013, pp. 2187–2190.

[50] E. Ventsel and T. Krauthammer, *Thin plates and shells: theory, analysis, and applications*. Dekker, 2001.

[51] K. S. Pister and S. B. Dong, "Elastic bending of layered plates," *Journal of the Engineering Mechanics Division*, vol. 85, no. 4, pp. 1–10, oct 1959.

[52] S. B. Dong, K. S. Pister, and R. L. Taylor, "On the theory of laminated anisotropic shells and plates," *Journal of the Aerospace Sciences*, vol. 29, no. 8, pp. 969–975, aug 1962.

[53] M. F. la Cour, M. B. Stuart, M. B. Laursen, S. E. Diederichsen, E. V. Thomsen, and J. A. Jensen, "Investigation of PDMS as a coating on CMUTs for imaging," in *Proc. IEEE Ultrason. Symp.* IEEE, 2014, pp. 2584–2587.

[54] O. Oralkan, X. C. Jin, K. Kaviani, A. S. Ergun, F. L. Degertekin, M. Karaman, and B. T. Khuri-Yakub, "Initial pulse-echo imaging results with one-dimensional capacitive micromachined ultrasonic transducer arrays," in *Proc. IEEE Ultrason. Symp.*, vol. 1, 2000, pp. 959–962.

[55] D. M. Mills, "Medical imaging with capacitive micromachined ultrasound transducer (cMUT) arrays," in *Proc. IEEE Ultrason. Symp.*, vol. 1, aug 2004, pp. 384–390.

[56] M. Legros, C. Meynier, R. Dufait, G. Ferin, and F. Tranquart, "Piezocomposite and CMUT arrays assessment through in vitro imaging performances," in *Proc. IEEE Ultrason. Symp.*, nov 2008, pp. 1142–1145.

[57] A. Bhuyan, J. W. Choe, B. C. Lee, P. Cristman, O. Oralkan, and B. T. Khuri-Yakub, "Miniaturized, wearable, ultrasound probe for on-demand ultrasound screening," in *Proc. IEEE Ultrason. Symp.*, oct 2011, pp. 1060–1063.

[58] A. S. Savoia, G. Caliano, and M. Pappalardo, "A CMUT probe for medical ultrasonography: From microfabrication to system integration," *IEEE Trans. Ultrason., Ferroelec., Freq. Contr.*, vol. 59, no. 6, pp. 1127–1138, 2012.

[59] E. Jeanne, C. Meynier, J. Terry, M. Roy, L. Haworth, and D. Alquier, "Evaluation of parylene as protection layer for capacitive micromachined ultrasonic transducers," *ECS Transactions*, vol. 11, no. 16, pp. 25–33, mar 2008.

[60] D.-S. Lin, X. Zhuang, S. H. Wong, M. Kupnik, and B. T. Khuri-Yakub, "Encapsulation of capacitive micromachined ultrasonic transducers using viscoelastic polymer," *J. Microelectromech. S.*, vol. 19, no. 6, pp. 1341–1351, dec 2010.

[61] X. Zhuang, A. Nikoozadeh, M. A. Beasley, G. G. Yaralioglu, B. T. Khuri-Yakub, and B. L. Pruitt, "Biocompatible coatings for CMUTs in a harsh, aqueous environment," *Journal of Micromechanics and Microengineering*, vol. 17, no. 5, pp. 994–1001, may 2007.

[62] E. Jeanne, C. Meynier, F. Teston, D. Certon, N. Felix, M. Roy, and D. Alquier, "Protection layer influence on capacitive micromachined ultrasonic transducers performance," *MRS Online Proceedings Library*, vol. 1052, 2007.

[63] M. F. la Cour, T. L. Christiansen, J. A. Jensen, and E. V. Thomsen, "Electrostatic analysis of cmuts with circular and square anisotropic plates," *IEEE Trans. Ultrason., Ferroelec., Freq. Contr.*, p. Submitted, 2014.

[64] E. V. Thomsen, K. Reck, G. Skands, C. Bertelsen, and O. Hansen, "Silicon as an anisotropic mechanical material: Deflection of thin crystalline plates," *Sensors and Actuators*, p. submitted, 2014.

[65] S. Holgate, "The transverse flexure of perforated aeolotropic plates," *Proceedings of the Royal Society A: Mathematical, Physical and Engineering Science*, vol. 185, no. 1000, pp. 50–69, jan 1946.

[66] J. J. Hall, "Electronic effects in the elastic constants of n-type silicon," *Phys. Rev.*, vol. 161, no. 3, pp. 756–761, sep 1967.

[67] F. Mbakogu and M. Pavlovic, "Bending of clamped orthotropic rectangular plates: a variational symbolic solution," *Computers and Structures*, vol. 77, no. 2, pp. 117–128, jun 2000.

[68] T. L. Christiansen, O. Hansen, M. D. Johnsen, J. N. Lohse, J. A. Jensen, and E. V. Thomsen, "Void-free direct bonding of CMUT arrays with single crystalline plates and pull-in insulation," *Proc. IEEE Ultrason. Symp.*, pp. 1737–1740, 2013.

[69] A. Lei, M. F. l. C. S. E. Diederichsen and, M. B. Stuart, T. L. Christiansen, J. A. Jensen, and E. V. Thomsen, "Dimensional scaling for optimized CMUT operations," in *Proc. IEEE Ultrason. Symp.* IEEE, 2014, pp. 2595–2598.

[70] J. A. Jensen, H. Holten-Lund, R. T. Nilsson, M. Hansen, U. D. Larsen, R. P. Domsten, B. G. Tomov, M. B. Stuart, S. I. Nikolov, M. J. Pihl, Y. Du, J. H. Rasmussen, and M. F. Rasmussen, "SARUS: A synthetic aperture real-time ultrasound system," *IEEE Trans. Ultrason., Ferroelec., Freq. Contr.*, vol. 60, no. 9, pp. 1838–1852, 2013.

[71] T. Pedersen, G. Fragiacomo, O. Hansen, and E. V. Thomsen, "Highly sensitive micromachined capacitive pressure sensor with reduced hysteresis and low parasitic capacitance," *Sensors and Actuators*, vol. 154, no. 1, pp. 35–41, 2009.

[72] G. Fragiacomo, "Micromachined capacitive pressure sensor with signal conditioning electronics," Ph.D. dissertation, Technical University of Denmark, 2012.

[73] S. E. Diederichsen, "Capacitive micromachined ultrasonic transducers (CMUTs): Theory, design, fabrication and characterization," Master's thesis, Technical University of Denmark, 2014.

APPENDIX A

Process Flow - Stanford Arrays

Step	description	Machine	Recipe	Time	comment
1	oxidation	wbnonmetal	piranha clean	20 min	
		wbdiff	RCA cleaning	30 min	fresh chemicals
		thermco1/2	wet O2 1000C	1h15m/52 m	targeted thickness 0.4 and 0,3 µm
		nanospec	measure thickness		
2	Litho	singe oven			if done immediately after oxidation this not needed
		yes oven	HMDS	30 min	
		svg coat track 1	1 µm resist with 2 mm EBR w/o VP		
		Karlsuss	hard contact, oxide mask 1	1.1 s	
		svg dev	60 s postbake (prog #3)		
		Drytek2	descum prog 1	1.5 min	
		wbnonmetal	6:1 BOE oxide etch	4.5 min or 5.7 min	fresh chemicals
		wbnonmetal	Piranha resist strip	20 min	fresh chemicals
3	2nd oxidation	wbdiff	RCA cleaning	30 min	fresh chemicals, NO HF DIP!
		thermco1/2	wet O2 1000C	1h45m + 30m	target 2 µm
		nanospec	measure thickness		
4	Litho	yes oven	HMDS	30 min	
		svg coat track 1	1.6 µm resist with 2 mm EBR w/o VP		
		Karlsuss2	hard contact, oxide mask 2	1.7 s	40 µm alignment gab, Critical alignment, Karlsuss2 better focusing
		svg dev	120 s postbake (prog #4)		
		Drytek2	descum prog 1	1.5 min	
		AMTetcher	season etch prog. 3	10 min	
		AMTetcher	season etch prog. 3	3.5 min	~1200Å
		Drytek2	descum prog 1	1.5 min	
		wbnonmetal	Piranha resist strip	20 min	fresh chemicals
		nanospec	measure thickness, and gap height		
5	Bonding	wbdiff	RCA cleaning		
		special rinse			
		Ksbonder	recipe: kupnik50		
	Annealling	Thermco2	2wetox at 1050C	4h	
6	Grinding	Tim, crystal shop	remove 300 µm +/-20 µm of 525 µm		
		IR camera	check bonding quality		
7	removing box	wbnonmetal	piranha clean	20 min	no fresh chemicals

		wbgen	Heated TMAH	~9 hours	strip handle took about 9h at 95-98C, started at 70C
		wbnonmetal	piranha clean		
		wbnonmetal	6:1BOE oxide etc	6 min	overetched, still color but hydrophobic surface
8	Litho (bot. Contact)	singe oven	prebake	10 min	
		yes oven	HMDS	30 min	
		svg coat track 1	1.6 µm resist with 2 mm EBR w/o VP		
		Karlsuss1/2	hard contact, mask3	1.7 s	
		svg dev	120 s postbake (prog #4)		
		Drytek2	descum prog 1	1.5 min	
		sts1	Si etch recipe	10 min	
		AMTetcher	season etch prog. 3	15 min	
		Drytek2	descum prog 1	1.5 min	
		wbnonmetal	Piranha resist strip	20 min	fresh chemicals
9	Contacts	Al deposition	Give wafers to Tom, crystal shop		400 nm Al, 15s HF dip before
		Rinse+Singe oven	Dumprinse, SRD wbmetal+Singe oven	30 min	
		yes oven	HMDS	30 min	
		svg coat track 1	1.6 µm resist with 2 mm EBR w/o VP		
		Karlsuss1/2	hard contact, mask 4	1.7 s	
		svg dev	120 s postbake (prog #4)		
		Drytek2	descum prog 1	1.5 min	
		Al etch	wbmetal	1.5-2.5 min	
		sts1	Si etch recipe	10-12 min	
		wbmetal	PRX127 resist strip	20 min	Piranha will remove metal!

APPENDIX B

Process Flow - DTU Arrays

Step #	Process	Equipment	Recipe	Comments	Processed on wafer #
1	**RCA cleaning**				
1.1	RCA1	RCA 1 bath	10 min	Prepare RCA 1 and RCA 2 before this step. Wash baths with water gun before adding new chemicals. Turn on heater for RCA 1 30 min before this step and turn on heater for RCA 2 when beginning this step.	All wafers: Four DSP SOI (N^+ device layer) Four SSP OP422 (P+) Two Danchip test wafers (n- and p-type, respectively)
1.2	Quickdump	Quickdump bath in front of RCA 1	3 min		
1.3	HF	5 % HF bath	30 s		
1.4	Rinse	Water bath in front of HF bath	20 s		
1.5	Quickdump	Quickdump bath in front of RCA 1	3 min		
1.6	RCA2	RCA 2 bath	10 min		
1.7	Quickdump	Quickdump bath in front of RCA 1	3 min	Turn off heater for RCA 1 and RCA 2	
1.8	HF	5 % HF bath	30 s		
1.9	Rinse	Water bath in front of HF bath	20 s		
1.10	Quickdump	Quickdump bath in front of RCA 1	5 min		
1.11	Spin dry	Spin dryer at RCA bench			
2a	**Grow oxide layer 1 (top wafer)**			**Figure a**	
2a.1	Thermal oxidation	Furnace: A3 Phosphorus drive-in	Recipe: dry1100, time: 7h 0min, 20 min anneal	Expected thickness from logbook: 360 nm	SOI wafers: T1, T2, T3, T4, test wafer (n-type)
2a.2	Inspection	Filmtek	Measure oxide thickness, 5 points	Measured: 364 +- 1.6 nm	test wafer
2b	**Grow oxide layer 2 (bottom wafer)**				
2b.1	Thermal oxidation	Furnace: A1 Boron drive-in	Recipe: dry1100, time: 8h 55min, 20 min anneal	Expected thickness from logbook: 400 nm	SSP wafers: B1, B2, B3, B4, test wafer (p-type)
2b.2	Inspection	Filmtek	Measure oxide thickness, 5 points	Measured: 407 +- 2.6 nm	test wafer
3	**Create CMUT cavities**			**Figure b**	
3.1	Adhesion promotion, spin on photoresist	Spin Track 1	Recipe: T1 MiR 701 1.5µm with HDMS		SOI wafers: T1, T2, T3, T4 (process on device layer side)
3.2	Exposure	KS Aligner	23 s @ 7 mW/cm2, hard contact	Mask: 1-D CMUT arrays - Cavities (Optimized) Rotate aligner to zero and set both wheels to 10 before exposing.	T1, T2, T3, T4
3.3	Post exposure bake	Spin Track 2	Recipe: T2 MiR 701 PEB		T1, T2, T3, T4
3.4	Development/rinse	Automatic Developer-TMAH	Recipe: DUV 60s or MiR 701 60s	Important: Make sure that the rinse step runs after the TMAH step. If not, run the "UTIL-DR" recipe for a DI water rinse	T1, T2, T3, T4
3.5	Dry	Spin dryer	Spin dry		T1, T2, T3, T4
3.6	Inspection	Optical microscope	Check for errors in lithography	Errors with MISSING resist are most severe!	T1, T2, T3, T4
3.7	Oxide etch	AOE	Recipe: m_res_ny, Time: 1min 50s	Let AOE cool to 0-1 degC for roughly 20-30 minutes before etching	T1, T2, T3, T4
3.8	Strip photoresist	Plasma asher 2	O2/N2: 400/70 ml/min, 1000 W, 45 min.	Alternatively use acetone	T1, T2, T3, T4
3.9	Inspection	Optical microscope	Measure etched CMUT cavity side length		T1, T2, T3, T4
4	**RCA Cleaning without second HF dip**				
4.1	RCA1	RCA 1 bath	10 min	Prepare RCA 1 and RCA 2 before this step. Wash baths with water gun before adding new chemicals. Turn on heater for RCA 1 30 min before this step and turn on heater for RCA 2 when beginning this step.	All wafers: T1, T2, T3, T4, B1, B2, B3, B4
4.2	Quickdump	Quickdump bath in front of RCA 1	3 min		

4.3	HF	5 % HF bath	15 s		
4.4	Rinse	Water bath in front of HF bath	20 s		
4.5	Bubble rinse	Bubbler in front of BHF bath	3 min		
4.6	RCA2	RCA 2 bath	10 min		
4.7	Quickdump	Quickdump bath in front of RCA 1	3 min	Turn off heater for RCA 1 and RCA 2	
4.8	Spin dry	Spin dryer at RCA bench			
5	**Wafer bonding**			**Figure c**	
5.1	Fusion bonding	EVG NIL	Recipe: CMUT (temp: 50 C, piston force: 1500 N, bond time 5 min, vacuum: 1.0E-2 mbar)	Transport wafers in dedicated box from RCA. Minimize ambient exposure and handling time. Use RCA cleaned tweezers.	All wafers: T1, T2, T3, T4, B1, B2, B3, B4
5.2	Inspection	Infrared camera	Inspect for pre-anneal voids		T1+B1, T2+B2, T3+B3, T4+B4
5.3	Annealing	Anneal-bond	Recipe: ann1110, Time 1h 10min		T1+B1, T2+B2, T3+B3, T4+B4
5.4	Inspection	Infrared camera	Inspect for post-anneal voids		T1+B1, T2+B2, T3+B3, T4+B4
6	**Remove grown oxide, handle layer and BOX**			**Figure d**	
6.1	Oxide etch	BHF	6 min (80 nm/min)	Dip wafers in water first to fill out potential voids, and blow dry the side to be etched before dipping into BHF. Check that the oxide is removed by confirming that the membrane is water repellant	T1+B1, T2+B2, T3+B3, T4+B4
6.2	Silicon etch	ASE	Recipe: cmutaway, Time: 1h 5m	Chuck temperature: 20C. While proccessing: It can easily be seen when the oxide is completely removed (then give it 30-60 seconds more and abort the proccess). Make sure to rinse the wafers with a water gun before next step.	T1+B1, T2+B2, T3+B3, T4+B4
6.3	Oxide etch	BHF	20 min (80 nm/min)	Dip wafers in water first to fill out potential voids, and blow dry the side to be etched before dipping into BHF. Check that the oxide is removed by confirming that the membrane is water repellant	T1+B1, T2+B2, T3+B3, T4+B4
6.4	Rinse/dry	Wet bench/Spin dryer	5 min. in DI water, spin dry		T1+B1, T2+B2, T3+B3, T4+B4
7	**RCA cleaning**				
7.1	RCA1	RCA 1 bath	10 min	Prepare RCA 1 and RCA 2 before this step. Wash baths with water gun before adding new chemicals. Turn on heater for RCA 1 30 min before this step and turn on heater for RCA 2 when beginning this step.	All wafer pairs: T1+B1, T2+B2, T3+B3, T4+B4
7.2	Quickdump	Quickdump bath in front of RCA 1	3 min		
7.3	HF	5 % HF bath	30 s		
7.4	Rinse	Water bath in front of HF bath	20 s		
7.5	Bubble rinse	Bubbler in front of BHF bath	3 min		
7.6	RCA2	RCA 2 bath	10 min		
7.7	Quickdump	Quickdump bath in front of RCA 1	3 min	Turn off heater for RCA 1 and RCA 2	
7.8	HF	5 % HF bath	30 s		
7.9	Rinse	Water bath in front of HF bath	20 s		
7.10	Rinse 2	Bubbler in front of BHF bath	5 min		
7.11	Spin dry	Spin dryer at RCA bench			
8	**Etch opening for alignment marks**			**Figure e**	
8.1	Adhesion promotion, spin on photoresist	Spin Track 1	Recipe: T1 MiR 701 1.5µm with HDMS		All wafer pairs: T1+B1, T2+B2, T3+B3, T4+B4

8.2	Exposure	KS Aligner	23 s @ 7 mW/cm2, hard contact	Mask: Opening for alignment marks Rotate aligner to zero and set both wheels to 10 before exposing.	T1+B1, T2+B2, T3+B3, T4+B4
8.3	Post exposure bake	Spin Track 2	Recipe: T2 MiR 701 PEB		T1+B1, T2+B2, T3+B3, T4+B4
8.4	Development/rinse	Automatic Developer-TMAH	Recipe: DUV 60s or MiR 701 60s	Important: Make sure that the rinse step runs after the TMAH step. If not, run the "UTIL-DR" recipe for a DI water rinse	T1+B1, T2+B2, T3+B3, T4+B4
8.5	Dry	Spin dryer	Spin dry		T1+B1, T2+B2, T3+B3, T4+B4
8.6	Inspection	Optical microscope	Check for errors in lithography	Errors with MISSING resist are most severe!	T1+B1, T2+B2, T3+B3, T4+B4
8.7	Silicon etch	DRIE Pegasus	Recipe: CMUT/tlehr/SOI_membrane_2um, proccess time: 40 sec	Visually check color in openings after etch to confirm that the oxide has been reached.	T1+B1, T2+B2, T3+B3, T4+B4
8.8	Strip photoresist	Plasma asher 2	O2/N2: 400/70 ml/min, 1000 W, 45 min.	Alternatively use acetone	T1+B1, T2+B2, T3+B3, T4+B4
8.9	Inspection	Optical microscope			T1+B1, T2+B2, T3+B3, T4+B4
9	**Etch access to bottom electrode**			**Figure e**	
9.1	Adhesion promotion, spin on photoresist	Spin Track 1	Recipe: T1 MiR 701 1.5µm with HDMS		All wafer pairs: T1+B1, T2+B2, T3+B3, T4+B4
9.2	Exposure	KS Aligner	23 s @ 7 mW/cm2, hard contact	Mask: 1-D CMUT arrays - etch to bottom contacts Rotate aligner to zero and set both wheels to 10 before exposing.	T1+B1, T2+B2, T3+B3, T4+B4
9.3	Post exposure bake	Spin Track 2	Recipe: T2 MiR 701 PEB		T1+B1, T2+B2, T3+B3, T4+B4
9.4	Development/rinse	Automatic Developer-TMAH	Recipe: DUV 60s or MiR 701 60s	Important: Make sure that the rinse step runs after the TMAH step. If not, run the "UTIL-DR" recipe for a DI water rinse	T1+B1, T2+B2, T3+B3, T4+B4
9.5	Dry	Spin dryer	Spin dry		T1+B1, T2+B2, T3+B3, T4+B4
9.6	Inspection	Optical microscope	Inspect for errors		T1+B1, T2+B2, T3+B3, T4+B4
9.7	Silicon etch	DRIE Pegasus	Recipe: CMUT/tlehr/SOI_membrane_2um, proccess time: 40 sec	Visually check color in openings after etch to confirm that the oxide has been reached.	T1+B1, T2+B2, T3+B3, T4+B4
9.8	Oxide etch	AOE	Recipe: m_res_ny, Time: 2+2 min (230 nm/min)	Visually check color in openings after etch to confirm that the silicon has been reached. Only etch for 2 min at a time (2 min removes around 400 nm)	T1+B1, T2+B2, T3+B3, T4+B4
9.9	Strip photoresist	Plasma asher 2	O2/N2: 400/70 ml/min, 1000 W, 45 min.	Alternatively use acetone	T1+B1, T2+B2, T3+B3, T4+B4
10	**Metallization of wire bond pads**			**Figure f/g**	
10.1	Adhesion promotion (optional)	BHF dip	Approx. 20 sec BHF dip (alternatively go directly from step 8.7 to 10.3)	Dip wafers in water first to fill out potential voids, and blow dry the side to be etched before dipping into BHF. Check that the oxide is removed by confirming that the membrane is water repellant	All wafer pairs: T1+B1, T2+B2, T3+B3, T4+B4
10.2	Rinse/dry	Wet bench/Spin dryer	5 min. in DI water, spin dry		T1+B1, T2+B2, T3+B3, T4+B4
10.3	Deposit Al	Alcatel	800 nm	Al is deposited over the whole wafer	T1+B1, T2+B2, T3+B3, T4+B4
10.4	Spin on photoresist	SSE spinner	2.2 µm AZ5214e, bake for 90s@90 deg	Or use spin track.	T1+B1, T2+B2, T3+B3, T4+B4
10.5	Exposure	KS Aligner	9 s @ 7 mW/cm2, hard contact	Mask: 1-D CMUT arrays - wire-bond pads	T1+B1, T2+B2, T3+B3, T4+B4
10.6	Development	Developer bath	70 s in AZ351 developer	Maybe slightly overdevelop to ensure good wet Al etch	T1+B1, T2+B2, T3+B3, T4+B4
10.7	Rinse/dry	Wet bench/Spin dryer	5 min. in DI water, spin dry		T1+B1, T2+B2, T3+B3, T4+B4

10.8	Al etch	Aluminium etch 1	H2O:H3PO4 1:2, 50 degC, (100 nm/min)	Thoroughly mix the solution using an empty wafer boat. Temperature control is very unstable, so manually ensure that the temperature is kept at approx. 50C before etching. It can be clearly seen when the etch is done through visual inspection - leave the boat in the mix for another 5-10 seconds.	T1+B1, T2+B2, T3+B3, T4+B4
10.9	Rinse/dry	Wet bench/Spin dryer	5 min. in DI water, spin dry		T1+B1, T2+B2, T3+B3, T4+B4
10.10	Strip photoresist	Plasma asher 1	O2/N2: 400/70 ml/min, 1000 W, 45 min.		T1+B1, T2+B2, T3+B3, T4+B4
11	**Metallization and etch of contacts/top electrodes**			**Figure h/i**	
11.1	Deposit Al	Alcatel	200 nm	Al is deposited over the whole wafer	All wafer pairs: T1+B1, T2+B2, T3+B3, T4+B4
11.2	Spin on photoresist	SSE spinner	2.2 µm AZ5214e, bake for 90s@90 deg	Or use spin track.	T1+B1, T2+B2, T3+B3, T4+B4
11.3	Exposure	KS Aligner	9 s @ 7 mW/cm2, hard contact	Mask: 1-D CMUT arrays - top electrode	T1+B1, T2+B2, T3+B3, T4+B4
11.4	Development	Developer bath	70 s in AZ351 developer	Maybe slightly overdevelop to ensure good wet Al etch	T1+B1, T2+B2, T3+B3, T4+B4
11.5	Rinse/dry	Wet bench/Spin dryer	5 min. in DI water, spin dry		T1+B1, T2+B2, T3+B3, T4+B4
11.6	Al etch	Aluminium etch 1	H2O:H3PO4 1:2, 50 degC, (100 nm/min)	Thoroughly mix the solution using an empty wafer boat. Temperature control is very unstable, so manually ensure that the temperature is kept at approx. 50C before etching. It can be clearly seen when the etch is done through visual inspection - leave the boat in the mix for another 5-10 seconds.	T1+B1, T2+B2, T3+B3, T4+B4
11.7	Rinse/dry	Wet bench/Spin dryer	5 min. in DI water, spin dry		T1+B1, T2+B2, T3+B3, T4+B4
11.8	Si etch	DRIE Pegasus	Recipe: CMUT/tlehr/SOI_membrane_2um, proccess time: 40 sec	Visually check color in openings after etch to confirm that the oxide has been reached	T1+B1, T2+B2, T3+B3, T4+B4
11.9	Strip photoresist	Plasma asher 1	O2/N2: 400/70 ml/min, 1000 W, 45 min.		T1+B1, T2+B2, T3+B3, T4+B4
12	**Protective resist layer**				
12.1	Spin on photoresist	SSE spinner	Recipe: AZ4562_4inch_10um		All wafer pairs: T1+B1, T2+B2, T3+B3, T4+B4
13	**Dicing and resist removal (outside cleanroom)**				
13.1	Dice out chips	Saw	Set to program 8, then use semiautomatic cut. Align wafer with the x/y buttons. Press start/stop two times	Dicing must be performed in several independent runs as the wafer design does not allow dicing of the whole wafer at once.	All wafer pairs: T1+B1, T2+B2, T3+B3, T4+B4
13.2	Remove resist	Laboratory outside the cleanroom	Acetone bath, water bath, water gun/sprayer and air gun	Place individual arrays in acetone bath until all resist is gone (leave it for a few minutes but make sure arrays are covered with acetone). Then, transfer arrays to a water bath to prevent the acetone from drying on the arrays. Finally the arrays are flushed with DI water using a water spray and dried with an air gun.	All arrays

APPENDIX C

Paper - Modelling of CMUTs with Anisotropic Plates

In Conference proceedings of the International Ultrasonics Symposium, Dresden, October 2012.

10.1109/ULTSYM.2012.0146

Modelling of CMUTs with Anisotropic Plates

Mette Funding la Cour*†, Thomas Lehrmann Christiansen†, Jørgen Arendt Jensen* and Erik V. Thomsen†
*Center for Fast Ultrasound Imaging, Department of Electrical Engineering, Technical University of Denmark,
DK-2800 Kgs. Lyngby, Denmark
†Department of Micro and Nanotechnology, Technical University of Denmark, DK-2800 Kgs. Lyngby, Denmark

***Abstract*—Traditionally, CMUTs are modelled using the isotropic plate equation and this leads to deviations between analytical calculations and FEM simulations. In this paper, the deflection profile and material parameters are calculated using the anisotropic plate equation. It is shown that the anisotropic calculations match perfectly with FEM while an isotropic approach causes up to 10% deviations in deflection profile. Furthermore, we show how commonly used analytic modelling methods such as static calculations of the pull-in voltage and dynamic modelling through an equivalent circuit representation can be adjusted to include the correct anisotropic behaviour by using an effective flexural rigidity. The anisotropic caluclations are also compared to experimental data from actual CMUTs showing an error of maximum 3%.**

I. INTRODUCTION

Capacitive micromachined ultrasonic transducers (CMUT) are a promising alternative to piezoelectric transducers and receive considerable attention due to their advantages such as wider bandwidth, higher sensitivity, ease of array fabrication and integration [1], [2]. Analytical and finite element calculations are important for efficient design of CMUTs and much has been put into modelling the behavior of the CMUT using mostly lumped element calculations [1] or finite element modelling [3]. Currently, the analytical approach to modelling the CMUT is based on the isotropic plate equation from which the deflection profile $w(x, y)$ can be obtained.

With the fusion bonding fabrication technology [4], the plate usually consists of crystalline silicon which is an anisotropic material. This leads to differences between analytical deflection profiles calculated with the isotropic plate equation and deflection profiles calculated by finite element programs that uses the correct anisotropic approach.

In this paper, the performance of CMUTs will be analytically calculated using the correct anisotropic approach. Utilising the anisotropic plate equation with fixed boundary conditions, the exact solution for the deflection profile can be obtained. The anisotropic solution is compared to the isotropic solution and FEM simulations. By combining the isotropic and anisotropic deflection profiles an effective flexural rigidity can be found. Using this, the pull in condition is found for a generalised case through energy considerations and the resonance frequency is found by lumped element modelling and compared to measurements. The objective is thus to show that using the anisotropic plate equation gives results matching FEM simulations and to demonstrate how this can easily be implemented into commonly used methods for calculating the performance of CMUTs.

II. THE ISOTROPIC PLATE EQUATION

In some cases, the CMUT devices have a thin plate made of an isotropic material, such as silicon nitride, and the static deflection profile, $w(x, y)$, is calculated by solving the isotropic plate equation [5]

$$\frac{\partial^4 w}{\partial x^4} + 2\frac{\partial^4 w}{\partial x^2 \partial y^2} + \frac{\partial^4 w}{\partial y^4} = \frac{p}{D_\mathrm{i}} \tag{1}$$

where p is the applied pressure difference across the plate and the flexural rigidity is given by

$$D_\mathrm{i} = \frac{E}{12\,(1-\nu^2)} h^3 \tag{2}$$

where E is the Young's modulus, ν is the Poisson's ratio, and h is the thickness of the plate. The plate equation is then solved using appropriate boundary conditions.

The plate material, however, is not always isotropic. Crystalline silicon is an anisotropic material with a diamond cubic crystal structure. For plates made on silicon (111) substrates, Young's modulus and Poisson's ratio are constant and the isotropic plate equation can be used. However, for other silicon substrates, such as silicon (001) and silicon (011), Young's modulus and Poisson's ratio are strongly anisotropic, and (1) and (2) are therefore no longer valid.

III. THE ANISOTROPIC PLATE EQUATION

The differential equation for the deflection, $w(x, y)$, of a thin, anisotropic plate exposed to a uniform load p is [6]

$$\frac{\partial^4 w}{\partial x^4} + k_1\frac{\partial^4 w}{\partial x^3 \partial y} + k_2\frac{\partial^4 w}{\partial x^2 \partial y^2} + k_3\frac{\partial^4 w}{\partial x \partial y^3} + k_4\frac{\partial^4 w}{\partial y^4} = \frac{p}{D_\mathrm{h}} \tag{3}$$

where

$$k_1 = \tfrac{4\hat{c}_{16}}{\hat{c}_{11}} \quad k_2 = \tfrac{2(\hat{c}_{12}+2\hat{c}_{66})}{\hat{c}_{11}} \quad k_3 = \tfrac{4\hat{c}_{26}}{\hat{c}_{11}}$$
$$k_4 = \tfrac{\hat{c}_{22}}{\hat{c}_{11}} \quad D_\mathrm{h} = \tfrac{1}{12}h^3\hat{c}_{11} \tag{4}$$

and $\hat{c}_{pq}$ are the elements of the reduced stiffness tensor in the plate coordinate system (using the engineering strain convention) given by [6]

$$\hat{c}_{pq} = c'_{pq} - \frac{c'_{p3}c'_{3q}}{c'_{33}} \tag{5}$$

Here, c'_{ij} are the elements of the stiffness tensor in the plate coordinate system.

By aligning the plate coordinate system to the crystallographic coordinate system the expressions in (4) can be

TABLE I
ROOM TEMPERATURE (300K) STIFFNESS COEFFICIENTS FOR CRYSTALLINE SILICON [7].

c_{11}	c_{12}	c_{44}
165.6 GPa	63.9 GPa	79.5 GPa

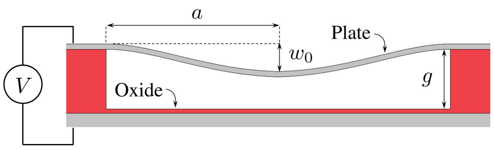

Fig. 1. Cross sectional view of CMUT cell with applied voltage.

expressed through the stiffness coefficients of silicon shown in Table I [7].

For a thin circular plate on a (100) substrate, we obtain

$$k_1 = k_3 = 0 \tag{6}$$

$$k_2 = \frac{2c_{12}}{c_{11}+c_{12}} + \frac{4c_{11}c_{44}}{c_{11}^2 - c_{12}^2} = 2.81 \tag{7}$$

$$k_4 = 1 \tag{8}$$

$$D_\mathrm{h} = \frac{1}{12}\left(c_{11} - \frac{c_{12}^2}{c_{11}}\right) h^3 = 11.75\ \mathrm{GPa} \cdot h^3 \tag{9}$$

The solution to (3) for a circular plate of radius a fixed at the boundary is easily obtained using polar coordinates. The deflection at a point a distance r from the center is given by [5]

$$w(r) = w_0 \left(1 - \left(\frac{r}{a}\right)^2\right)^2 \tag{10}$$

This equation is similar to the deflection profile for the isotropic case, however, the center deflections are different

$$w_{0,\mathrm{isotropic}} = \frac{1}{64}\frac{a^4 p}{D_\mathrm{i}} \tag{11}$$

$$w_{0,\mathrm{anisotropic}} = \frac{1}{8\,(3+k_2+3k_4)}\frac{a^4 p}{D_\mathrm{h}} \tag{12}$$

Fig. 1 shows a cross sectional view of a CMUT cell with an applied voltage with parameters shown.

By equating (11) and (12) and isolating D_i it is possible to find an effective flexural rigidity

$$D_\mathrm{eff} = \frac{3+k_2+3k_4}{8} D_\mathrm{h} \tag{13}$$

This can be used to change from the isotropic equation to the anisotropic equation in commonly used analytical models of CMUTs. Examples of this will be shown in the following sections.

Fig. 2 shows the normalised deflection profiles, using (10) to (12), of a CMUT exposed to a pressure difference. Using Young's modulus and Poisson's ratio along the [100] direction (E_{100}=130 GPa, ν_{100}=0.278) gives the solid green curve and using Young's modulus and Poisson's ratio along the [110] direction (E_{110}=169 GPa, ν_{110}=0.062) gives the dashed blue curve. The anisotropic solution is shown as a dotted red curve and is on top of the FEM simulation shown for comparison. The FEM simulations were performed in COMSOL 4.2a using the full anisotropic stiffness tensor. Excellent agreement between the anisotropic solution and the finite element calculation is seen. The figure also shows that Young's modulus and Poisson's ratio corresponding to [100] or [110] directions leads to errors in the center deflection of around 10%. To reduce this error, it is common practice to use mean values of Young's modulus and Poisson's ratio (E_ave=148 GPa, ν_ave=0.177) which decreases the error to around 1.5%. However, using the anisotropic approach gives the exact result. The error between the anisotropic calculation and FEM is less than 0.3%.

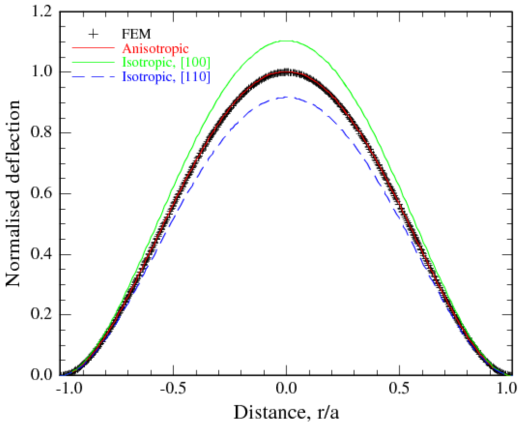

Fig. 2. Normalised deflection profile of a thin circular plate of silicon (001) as calculated by (10), (12), (11) and FEM.The anisotropic profile is on top of the FEM simulations.

IV. ANALYTICAL MODELLING

As mentioned previously, the behavior of CMUTs are in most cases modelled using lumped element analysis or finite element analysis. In the following, an analytical model for CMUTs based on energy and force considerations will be presented. By investigating the energies of the system it is possible to estimate pull-in voltage and distance [8]. This approach also applies when using the anisotropic plate equation and an example will be given in the end of the section.

The total potential energy of the plate, U_t, has three terms

$$U_\mathrm{t} = U_\mathrm{p} + U_\mathrm{e} + U_\mathrm{s} \tag{14}$$

where U_p is the energy associated with pressure, U_e is the electrostatic energy due to the capacitor and U_s is the strain energy stored in the deflected plate. Equation (10) is the solution to the plate equation when a uniform pressure is applied. The electrostatic pressure is not uniform but as observed by [8] it is a very good approximation.

The energy contribution from the pressure difference is calculated as the work performed (i.e. force times length, here pressure times area times length) when deflecting the plate

$$U_\mathrm{p} = -\int_0^a 2\pi p r w dr = -\frac{1}{3}a^2 p \pi w_0 \tag{15}$$

The electrostatic energy for an applied voltage V is given by

$$U_\mathrm{e} = -\frac{1}{2} C_\mathrm{t} V^2 \tag{16}$$

where the total capacitance C_t is given from the capacitance of the plate C_pl and of the insulating oxide C_ox

The potential energy associated with the plate acting as a spring is given by

$$U_\mathrm{s} = \frac{1}{2} D_\mathrm{eff} \int_0^a \left(\frac{\partial_r \left(r \partial_r w \right)}{r} \right)^2 2\pi r \, dr = \frac{32 D_\mathrm{eff} \pi w_0^2}{3a^2} \tag{17}$$

The flexural rigidity appears in this equation, making it possible to switch between isotropic and anisotropic cases.

By taking the derivative of the total potential energy with respect to the center deflection, the total equivalent force on the center of the plate can be found

$$\begin{aligned} F_\mathrm{t} = -\frac{\partial U_\mathrm{t}}{\partial w_0} = \frac{1}{3} a^2 p \pi - \frac{64 D_\mathrm{eff} \pi w_0}{3a^2} + \\ \frac{C_0 C_\mathrm{ox}^2 \sqrt{g} V^2 \left(\sqrt{g} w_0 + \sqrt{w_0} \left(-g + w_0 \right) \mathrm{ArcTanh} \left[\sqrt{\frac{w_0}{g}} \right] \right)}{4 \left(g - w_0 \right) w_0^2 \left(C_\mathrm{ox} + C_0 \sqrt{\frac{g}{w_0}} \mathrm{ArcTanh} \left[\sqrt{\frac{w_0}{g}} \right] \right)^2} \end{aligned} \tag{18}$$

where g is the gap distance. The stable position of the plate is found when $F_\mathrm{t} = 0$. Thus, this equation can in principle be solved numerically to obtain the center deflection w_0 for a given design (C_0, g, a, D_eff) and operating conditions (V and p).

V. PULL IN VOLTAGE

To simplify the calculation, we normalise by using the following expressions

$$x_{00} = \frac{p a^4}{64 g D_\mathrm{eff}}, x_0 = \frac{g}{w_0}, k_\mathrm{ox} = \frac{C_0}{C_\mathrm{ox}} \quad , V_\mathrm{A}^2 = V^2 \frac{3a^2 C_0}{256 D_\mathrm{eff} g^2 \pi} \tag{19}$$

x_{00} is the normalised deflection due to the external pressure, x_0 is the normalised center deflection, k_ox is the ratio of capacitances at zero voltage and V_A is the normalised applied voltage. This way (18) becomes

$$\begin{aligned} F_\mathrm{tn} = -x_0 + x_{00} - \\ \frac{V_\mathrm{A}^2 \left(\sqrt{x_0} + \left(-1 + x_0 \right) \mathrm{ArcTanh} \left[\sqrt{x_0} \right] \right)}{\left(-1 + x_0 \right) \sqrt{x_0} \left(\sqrt{x_0} + k_\mathrm{ox} \mathrm{ArcTanh} \left[\sqrt{x_0} \right] \right)^2} \end{aligned} \tag{20}$$

The pull in voltage V_PI and the pull in point x_PI of the CMUT cell can be found from the expression of the force as $\partial F_\mathrm{tn} / \partial x_0 = 0$ and $F_\mathrm{tn} = 0$ apply. By isolating V_A in the first equation and substituting this result into the second, x_PI can be obtained and then afterwards V_PI.

For the special case where both the oxide thickness and the applied pressure is zero, the pull in distance becomes $x_\mathrm{PI} = 0.46$. For a parallel plate capacitor, this distance is $x_\mathrm{PI,parallel} = 1/3$. With the corrected pull in distance, the pull in voltage becomes

$$V_\mathrm{PI} = \sqrt{\frac{89.4459 D_\mathrm{eff} g^2}{a^2 C_0}} \tag{21}$$

TABLE II
PULL IN VOLTAGES AND RESONANCE FREQUENCIES FOR THE SPECIAL CASE OF ZERO APPLIED PRESSURE AND ZERO OXIDE THICKNESS.

	V_PI	ω_0 (0 V)
Anisotropic	179 V	9.6 MHz
Isotropic [001]	172 V	9.1 MHz
Isotropic [011]	188 V	10.0 MHZ
Isotropic average	179 V	9.5 MHz

To compare calculations using the isotropic and anisotropic approaches, the pull in voltage for the special case (21) is found and shown in Table II. The calculation is performed with $a = 20$ μm, $h = 1$ μm and $g = 0.5$ μm. A difference of more than 10 V is observed so using different parameters for the calculations can make a considerable difference in the expected pull in voltage. Using the average values for Young's modulus and Poisson's ratio gives a result close to the correct anisotropic result.

VI. RESONANCE FREQUENCY

When modelling the dynamic behaviour of transducers, such as CMUTs, it is common practice to set up a lumped parameter equivalent circuit representation [9], [10], [11], [1]. Using the center displacement of the CMUT plate, w_0, and the equivalent charge on the plate, Q, as state variables, the state equations of the system are given by (18) and the three relations $V = Q/C_\mathrm{t}$, $i = dQ/dt$ and $v = dw_0/dt$. The system can then be linearized around a bias point $(w_{0,\mathrm{b}}, Q_\mathrm{b})$ by using the Jacobian of the system [11], [9], [10]

$$\begin{bmatrix} dV \\ dF_\mathrm{t} \end{bmatrix} = \begin{bmatrix} \left. \frac{\partial V}{\partial Q} \right|_{w_{0,\mathrm{b}}, Q_\mathrm{b}} & \left. \frac{\partial V}{\partial w_0} \right|_{w_{0,\mathrm{b}}, Q_\mathrm{b}} \\ \left. \frac{\partial F_\mathrm{t}}{\partial Q} \right|_{w_{0,\mathrm{b}}, Q_\mathrm{b}} & \left. \frac{\partial F_\mathrm{t}}{\partial w_0} \right|_{w_{0,\mathrm{b}}, Q_\mathrm{b}} \end{bmatrix} \begin{bmatrix} dQ \\ dw_0 \end{bmatrix} \tag{22}$$

The linearized system can then be transformed into the complex frequency domain by Lapace transform. Denoting the matrix in (22) as A, we get the following in the frequency domain

$$\begin{bmatrix} dV \\ dF_\mathrm{t} \end{bmatrix} = A \begin{bmatrix} dQ \\ dw_0 \end{bmatrix} = A \begin{bmatrix} \frac{1}{s} di \\ \frac{1}{s} dv \end{bmatrix} = B \begin{bmatrix} di \\ dv \end{bmatrix} \tag{23}$$

The lumped system components, the transformer factor and the coupling coefficient of the transducer can then easily be extracted from the matrix B [11]. The effective mass of the plate is attached to the terminals of the mechanical domain to complete the equivalent circuit as shown in Fig. 3, where k^* is the spring constant including spring softening. The effective mass is found through the relation $m_\mathrm{eff} = k_\mathrm{eff} / \omega_0^2$, where $k_\mathrm{eff} = \partial^2 U_\mathrm{s} / \partial w_0^2$ and ω_0 is the fundamental resonance frequency of the plate. The effect on the resonance frequency of using different flexural rigidities is demonstrated in Table II. Note that the velocity of the system in this calculation is

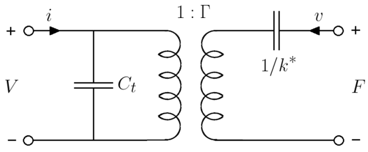

Fig. 3. Equivalent circuit diagram for a CMUT.

the velocity of the center of the plate. For correct coupling to the acoustic domain, a second transformer relation should be added to the equivalent circuit [9], [10]. Only the coupling between the electric and the mechanical domain is shown here for simplicity.

In such an equivalent circuit, the full anisotropic behaviour of the silicon plate is described by simply using the effective flexural rigidity as given in (13). This demonstrates that existing CMUT models can easily be accommodated to include the actual behaviour of single crystalline silicon plates.

VII. COMPARISON WITH MEASUREMENTS

To see how well the analytical model describes the behavior of CMUTs, measurements have been performed on fabricated devices. The impedance was measured with a HP 8752A network analyzer for varying bias voltages and the resonance frequency was found from the phase. The measurements were performed on two types of devices, half of them meant for phased array imaging with a frequency of 2.6 MHz ($a = 24.5\ \mu\text{m}$, $h = 1.5\ \mu\text{m}$, $g = 0.37\ \mu\text{m}$ and $t_{\text{ox}} = 0.21\ \mu\text{m}$) and the others for linear array imaging with a frequency of 5 MHz ($a = 24.5\ \mu\text{m}$, $h = 1.77\ \mu\text{m}$, $g = 0.29\ \mu\text{m}$ and $t_{\text{ox}} = 0.21\ \mu\text{m}$). Fig. 4 shows the resonance frequency as a function of applied voltage calculated for our two types of devices (red and green curve, circles). The corresponding analytical calculations are shown for comparison (blue and black curves, diamonds). Phased array device has solid curves and linear array device has dashed curves. The model is seen to match well with the measurements. The calculated values for the linear array device (dashed curves) has an average deviation from the measurements of $3\% \pm 0.7$ while for the phased array device (solid curves) it is only $2\% \pm 0.4$. The deviation can be explained by the metal electrode layer on top of the membrane causing a change in effective mass and flexural rigidity which is not included in the analytical calculations.

VIII. CONCLUSION

We have here demonstrated how wafer bonded CMUTs can be analytically modelled using the full anisotropic properties of single crystalline silicon. Using this approach, the analytic plate deflection profile shows excellent correspondence with FEM calculations. We have used a circular CMUT as an example to show how the anisotropic behaviour is easily incorporated into both static modelling of the pull-in voltage and dynamic equivalent circuit modelling by simply introducing an effective flexural rigidity. Using the anisotropic equivalent circuit model, the resonance frequency as a function of bias voltage has been compared to measurements on wafer bonded CMUTs in order to evaluate the accuracy of the model.

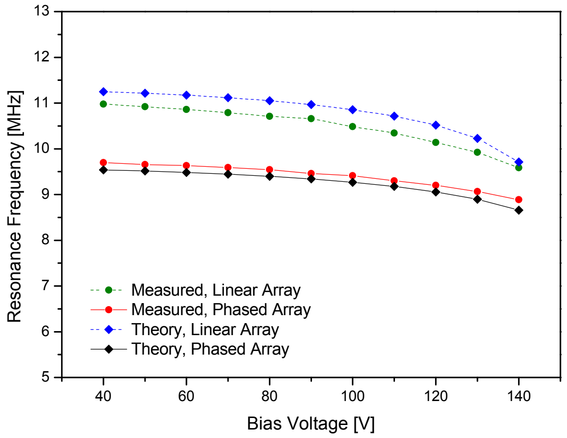

Fig. 4. Resonance frequency vs. applied voltage for measurement on two different devices and corresponding analytical curves.

REFERENCES

[1] I. Ladabaum, X. Jin, H. T. Soh, A. Atalar, and B. t. Khuri-Yakub, "Surface micromachined capacitive ultrasonic transducers," *IEEE Transactions on Ultrasonics, Ferroelectrics and Frequency Control*, vol. 45, no. 3, pp. 678–690, May 1998.

[2] O. Oralkan, A. Ergun, J. Johnson, M. Karaman, U. Demirci, K. Kaviani, T. Lee, and B. Khuri-Yakub, "Capacitive micromachined ultrasonic transducers: next-generation arrays for acoustic imaging?" *IEEE Transactions on Ultrasonics, Ferroelectrics and Frequency Control*, vol. 49, no. 11, pp. 1596 –1610, Nov. 2002.

[3] A. Lohfink, P.-C. Eccardt, W. Benecke, and H. Meixner, "Derivation of a 1D CMUT model from FEM results for linear and nonlinear equivalent circuit simulation," in *2003 IEEE Symposium on Ultrasonics*, vol. 1, Oct. 2003, pp. 465 – 468 Vol.1.

[4] Y. Huang, A. Ergun, E. Haeggstrom, M. Badi, and B. Khuri-Yakub, "Fabricating capacitive micromachined ultrasonic transducers with wafer-bonding technology," *Journal of Microelectromechanical Systems*, vol. 12, no. 2, pp. 128 – 137, Apr. 2003.

[5] S. Timoshenko and S. Woinowsky-Krieger, *Theory of Plates and Shells,*, 2nd ed. Mcgraw-Hill College, Jun. 1959.

[6] S. Holgate, "The transverse flexure of perforated aeolotropic plates," *Proceedings of the Royal Society A: Mathematical, Physical and Engineering Sciences*, vol. 185, no. 1000, pp. 50–69, Jan. 1946. [Online]. Available: http://adsabs.harvard.edu/abs/1946RSPSA.185...50H

[7] J. J. Hall, "Electronic effects in the elastic constants of n-type silicon," *Physical Review*, vol. 161, no. 3, pp. 756–761, Sep. 1967. [Online]. Available: http://link.aps.org/doi/10.1103/PhysRev.161.756

[8] H. Koymen, A. Atalar, E. Aydogdu, C. Kocabas, H. Oguz, S. Olcum, A. Ozgurluk, and A. Unlugedik, "An improved lumped element nonlinear circuit model for a circular CMUT cell," *IEEE transactions on ultrasonics, ferroelectrics, and frequency control*, vol. 59, no. 8, pp. 1791–1799, Aug. 2012, PMID: 22899125. [Online]. Available: http://www.ncbi.nlm.nih.gov/pubmed/22899125

[9] H. A. C. Tilmans, "Equivalent circuit representation of electromechanical transducers: I. lumped-parameter systems," *Journal of Micromechanics and Microengineering*, vol. 6, no. 1, pp. 157–176, Mar. 1996. [Online]. Available: http://iopscience.iop.org/0960-1317/6/1/036

[10] ——, "Equivalent circuit representation of electromechanical transducers: II. distributed-parameter systems," *Journal of Micromechanics and Microengineering*, vol. 7, no. 4, pp. 285–309, Dec. 1997. [Online]. Available: http://iopscience.iop.org/0960-1317/7/4/005

[11] S. D. Senturia, *Microsystem Design*. Springer, Nov. 2000.

APPENDIX D

Paper - Modeling and Measurements of CMUTs with Square Anisotropic Plates

In Conference proceedings of the International Ultrasonics Symposium, Prague, July 2013.

10.1109/ULTSYM.2013.0559

Modeling and Measurements of CMUTs with Square Anisotropic Plates

Mette Funding la Cour*†, Thomas Lehrmann Christiansen†, Christian Dahl-Petersen†, Kasper Reck†,
Ole Hansen†, Jørgen Arendt Jensen* and Erik Vilain Thomsen†
*Center for Fast Ultrasound Imaging, Department of Electrical Engineering, Technical University of Denmark,
DK-2800 Kgs. Lyngby, Denmark
†Department of Micro and Nanotechnology, Technical University of Denmark, DK-2800 Kgs. Lyngby, Denmark

***Abstract*—The conventional method of modeling CMUTs use the isotropic plate equation to calculate the deflection, leading to deviations from FEM simulations including anisotropic effects of around 10% in center deflection. In this paper, the deflection is found for square plates using the full anisotropic plate equation and the Galerkin method. Utilizing the symmetry of the silicon crystal, a compact and accurate expression for the deflection can be obtained. The deviation from FEM in center deflection is <0.1%. The deflection was measured on fabricated CMUTs using a white light interferometer. Fitting the anisotropic calculated deflection to the measurement a deviation of 0.5-1.5% is seen for the fitted values. Finally it was also measured how the device behaved under increasing bias voltage and it is observed that the model including anisotropic effects is within the uncertainty interval of the measurements.**

I. INTRODUCTION

Precise modeling of capacitive micromachined ultrasonic transducers (CMUT) is important for an efficient design process. The deflection $w(x,y)$ is an important parameter that influences several basic CMUT parameters such as pull-in voltage and capacitance. Most existing analytical approaches use the isotropic plate equation to calculate the deflection [1], [2]. However, when using fusion bonding fabrication technology the plate usually consists of crystalline silicon, which is an anisotropic material. The isotropic approach is then invalidated and this results in deviations in the deflection compared to finite element modeling (FEM) and measurements. Therefore, to get precise modeling of these CMUTs the anisotropy of silicon needs to be taken into account.

For circular plates a simple and exact solution for the deflection exists, but this is not the case for square plates. Existing solutions for the deflection of square plates is based on series expansions with either trigonometric [3] or polynomial basis functions [4]. None of these, however, take the anisotropy of the plate into account.

Previously a model was made for calculating the deflection for an anisotropic plate with circular geometry [5], and in this paper the model is expanded to include square plates as well. The approach used to solve the full anisotropic plate equation is the Galerkin method [6]. Utilizing the symmetry of the silicon crystal, a compact and accurate approximation of the deflection can be obtained. The calculated deflection is compared to the solution for corresponding isotropic cases, a finite element model (FEM) and measurements performed on fabricated devices. Furthermore, the calculated deflection is used to find the stable position of the CMUT plate for a given bias voltage. Equivalent measurements are performed as well and the theory is compared to these.

II. THE ISOTROPIC PLATE EQUATION

Conventionally the deflection $w(x,y)$ of a CMUT with a thin plate is modeled using the isotropic plate equation [3]

$$\frac{\partial^4 w}{\partial x^4}+2\frac{\partial^4 w}{\partial x^2\partial y^2}+\frac{\partial^4 w}{\partial y^4}=\frac{p}{D_\mathrm{i}}, \qquad (1)$$

where p is the applied pressure difference across the plate. The flexural rigidity is given by

$$D_\mathrm{i}=\frac{E}{12(1-\nu^2)}h^3 \qquad (2)$$

with E being Young's modulus, ν being Poisson's ratio, and h being the thickness of the plate. For clamped rectangular and square plates no simple exact solution exists to this equation and approximate methods have to be used. The traditional isotropic approach is based on a series expansion of the deflection and the center deflection for a thin clamped square plate having side length $2L$ is [3]

$$w_{0,\mathrm{isotropic}}=0.020245\frac{L^4 p}{D_\mathrm{i}}. \qquad (3)$$

However, the plate material is often not isotropic and (1) and (2) are therefore no longer valid. Using the fusion bonding fabrication technique the plate usually consist of silicon which is an anisotropic material with a diamond cubic crystal structure. Having a silicon (001) substrate, which are most often used, Young's modulus and Poisson's ratio are strongly anisotropic, and this leads to inaccurate deflection expressions.

III. ANISOTROPIC PLATE EQUATION

To be able to take the anisotropy of the plate into account and avoid the inaccuracy from isotropic modeling, the stiffness of the plate needs to be described through the stiffness matrix of the material instead of Young's modulus and Poisson's ratio. The starting point is the relation between stress and strain [7]

$$\sigma^\mathrm{c}=\mathbf{c}^\mathrm{c}\varepsilon^\mathrm{c}, \text{ or } \varepsilon^\mathrm{c}=\mathbf{s}^\mathrm{c}\sigma^\mathrm{c}. \qquad (4)$$

Here superscript c denotes the crystallographic coordinate system, so $\mathbf{c}^\mathrm{c}$ is the stiffness matrix and $\mathbf{s}^\mathrm{c}=(\mathbf{c}^\mathrm{c})^{-1}$ the compliance matrix in this coordinate system. Having a thin plate the stresses in the z direction can be ignored and plane

TABLE I. ROOM TEMPERATURE (300K) COMPLIANCE COEFFICIENTS FOR LOW DOPED N-TYPE CRYSTALLINE SILICON [8].

s^{c}_{11}	s^{c}_{12}	s^{c}_{44}
$7.69 \times 10^{-12}\ \mathrm{Pa}^{-1}$	$-2.14 \times 10^{-12}\ \mathrm{Pa}^{-1}$	$12.58 \times 10^{-12}\ \mathrm{Pa}^{-1}$

stress assumed. The relation between strain and stress then becomes

$$\begin{pmatrix} \varepsilon_1 \\ \varepsilon_2 \\ \varepsilon_6 \end{pmatrix} = \begin{pmatrix} s_{11} & s_{12} & s_{16} \\ s_{12} & s_{22} & s_{26} \\ s_{16} & s_{26} & s_{66} \end{pmatrix} \begin{pmatrix} \sigma_1 \\ \sigma_2 \\ \sigma_6 \end{pmatrix} = \mathbf{S}_{\mathrm{eff}} \begin{pmatrix} \sigma_1 \\ \sigma_2 \\ \sigma_6 \end{pmatrix} \quad (5)$$

and we can define an effective stiffness matrix, $\mathbf{C}_{\mathrm{eff}} = (\mathbf{S}_{\mathrm{eff}})^{-1}$. For silicon the effective compliance matrix becomes

$$\mathbf{S}^{\mathrm{c}}_{\mathrm{eff}} = \begin{pmatrix} s^{\mathrm{c}}_{11} & s^{\mathrm{c}}_{12} & 0 \\ s^{\mathrm{c}}_{12} & s^{\mathrm{c}}_{11} & 0 \\ 0 & 0 & s^{\mathrm{c}}_{44} \end{pmatrix}. \quad (6)$$

The compliance elements in this matrix are known from measurements and shown in Table I [8]. It is noted that the elements in (6) are known in the crystallographic coordinate system. An equation describing plate deflection on the other hand is valid in the plate coordinate system which is not necessarily the same. To illustrate this further the crystallographic and the plate coordinate systems can be seen in Fig. 1. The solid coordinate system aligned to the $\langle 100 \rangle$ directions is where the compliance values for silicon are known and the dashed system shows the rotated coordinate system for the plate where the compliance values needs to be calculated. Having silicon as plate material and performing standard cleanroom fabrication, the plate will usually be on a (001) substrate and aligned to the primary wafer flat. Flat alignment is to the $\langle 110 \rangle$ direction and the plate coordinate system will be rotated $\psi = 45°$ and a transformation of the compliance matrix between the two coordinate systems is needed. The resulting effective stiffness matrix for the present case becomes (taking the inverse of the transformed compliance matrix) [9]

$$C^{\mathrm{eff}}_{\mathrm{Si(001),[110]}} = \begin{pmatrix} \frac{1}{s^{\mathrm{c}}_{44}} + \frac{1}{2(s^{\mathrm{c}}_{11}+s^{\mathrm{c}}_{12})} & \frac{1}{2(s^{\mathrm{c}}_{11}+s^{\mathrm{c}}_{12})} - \frac{1}{s^{\mathrm{c}}_{44}} & 0 \\ \frac{1}{2(s^{\mathrm{c}}_{11}+s^{\mathrm{c}}_{12})} - \frac{1}{s^{\mathrm{c}}_{44}} & \frac{1}{s^{\mathrm{c}}_{44}} + \frac{1}{2(s^{\mathrm{c}}_{11}+s^{\mathrm{c}}_{12})} & 0 \\ 0 & 0 & \frac{1}{2s^{\mathrm{c}}_{11}-2s^{\mathrm{c}}_{12}} \end{pmatrix}. \quad (7)$$

It is seen that the stiffness matrix now has an orthotropic symmetry.

Now having the effective stiffness matrix the generalized plate equation can be used. This is a differential equation for the deflection, $w(x,y)$, of a thin anisotropic plate exposed to a uniform load p given by [10], [9]

$$\frac{\partial^4 w}{\partial x^4} + k_1 \frac{\partial^4 w}{\partial x^3 \partial y} + k_2 \frac{\partial^4 w}{\partial x^2 \partial y^2} + k_3 \frac{\partial^4 w}{\partial x \partial y^3} + k_4 \frac{\partial^4 w}{\partial y^4} = \frac{p}{D_{\mathrm{a}}}. \quad (8)$$

The plate coefficients k_1-k_4 and the anisotropic flexural rigidity, D_{a}, depend on the elastic constants of the plate material

$$k_1 = \frac{4C^{\mathrm{eff}}_{13}}{C^{\mathrm{eff}}_{11}} \quad k_2 = \frac{2\left(C^{\mathrm{eff}}_{12}+2C^{\mathrm{eff}}_{33}\right)}{C^{\mathrm{eff}}_{11}} \quad k_3 = \frac{4C^{\mathrm{eff}}_{23}}{C^{\mathrm{eff}}_{11}}$$
$$k_4 = \frac{C^{\mathrm{eff}}_{22}}{C^{\mathrm{eff}}_{11}} \quad D_{\mathrm{a}} = \frac{1}{12} h^3 C^{\mathrm{eff}}_{11} \quad (9)$$

where C^{eff}_{pq} are elements in the effective stiffness matrix. Notice that the stiffness of the plate is no longer expressed through Young's modulus and Poisson's ratio but directly through the stiffness values.

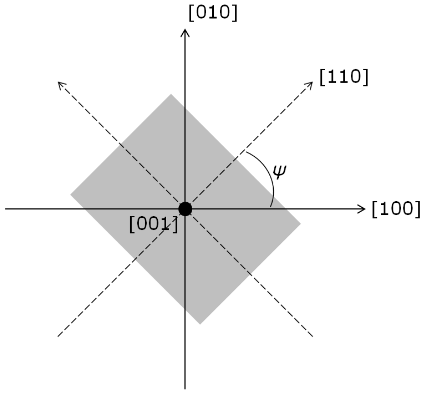

Fig. 1. The two coordinate systems, solid lines are the crystallographic system aligned to the $\langle 100 \rangle$ direction and the dashed lines the plate system aligned to the $\langle 110 \rangle$ direction.

TABLE II. SELECTED VALUES FOR THE PLATE COEFFICIENTS AND ANISOTROPIC FLEXURAL RIGIDITY FOR PLATES ON A SILICON (001) SUBSTRATE [9].

Orientation	ψ	k_1	k_2	k_3	k_4	$12D_a/h^3$[GPa]
[100]	0	0	2.8133	0	1	140.96
[110]	$\pi/4$	0	1.3241	0	1	169.62

Using the compliance values for silicon in Table I and inserting the stiffness elements in (7) into (9) it follows that $k_1 = k_3 = 0$ and $k_4 = 1$. Thus, aligning the plate to the primary flat simplifies the anisotropic plate equation (8) to

$$\frac{\partial^4 w}{\partial x^4} + k_2 \frac{\partial^4 w}{\partial x^2 \partial y^2} + \frac{\partial^4 w}{\partial y^4} = \frac{p}{D_{\mathrm{a}}}. \quad (10)$$

The same is the case for aligning the plate along the [100] direction where the inverse of (6) is used instead of (7), giving the same values for k_1, k_3 and k_4. For these two special cases the coefficients in the plate equation are summarized in Table II.

IV. SOLVING THE PLATE EQUATION

Having a rectangular or square plate makes analytical deflection calculations complicated and approximate methods must be used to solve the generalized plate equation. With the anisotropic approach the Galerkin method [6] can be used to find approximate expressions for the deflection of a thin anisotropic square plate. In the most common case for CMUTs the plate is fabricated on a silicon (001) substrate and aligned to the [110] direction. For this orthotropic square plate with sidelengths $2L$ the relative deflection is found to [9], [11]

$$\frac{w(x,y)}{w_0} = \left[1 - \left(\frac{x}{L}\right)^2\right]^2 \left[1 - \left(\frac{y}{L}\right)^2\right]^2 \times \left[1 + \beta\left(\frac{x}{L}\right)^2 + \beta\left(\frac{y}{L}\right)^2\right], \quad (11)$$

where the plate parameter is defined as

$$\beta = \frac{182 + 143k_2}{1432 + 91k_2}. \quad (12)$$

The center deflection can be written

$$w_{0,\mathrm{Si}(001)} = \frac{77(1432+91k_2)}{256(16220+11k_2(329+13k_2))}\frac{L^4 p}{D_\mathrm{a}}. \qquad (13)$$

Eqn. (11)-(13) are also valid when the plate is aligned to the [100] direction on a silicon (001) substrate. Note that the center deflection depends only on the k_2 coefficient. For primary flat alignment it is found by inserting k_2 into (12) that $\beta = 0.23920$. This results in a normalized deflection surface for the plate aligned to the $\langle 110\rangle$ direction given by

$$\left.\frac{w(x,y)}{w_0}\right|_{\mathrm{Si}(001),\langle 110\rangle} = \left[1-(x/L)^2\right]^2\left[1-(y/L)^2\right]^2 \times \left[1+0.239207\left[(x/L)^2+(y/L)^2\right]\right] \qquad (14)$$

and the center deflection becomes

$$w_0|_{\mathrm{Si}(001),\langle 110\rangle} = 0.02196\frac{L^4 p}{D_\mathrm{a}}. \qquad (15)$$

Comparing (3) and (15) it is seen that they are very similar containing the same parameters but different coefficients and the anisotropic instead of the isotropic flexural rigidity.

Fig. 2 shows the deflection cross section through $y = 0$ of a square plate of silicon (001)

$$w_{y=0} = w_0\left[1-(x/L)^2\right]^2\left[1+\beta(x/L)^2\right]. \qquad (16)$$

The deflection calculated with the anisotropic approach uses $k_2 = 1.3241$ in (12) and center deflection (15). This is compared to the isotropic approach using $k_2 = 2$ in (12) and center deflection (3), with Young's modulus and Poisson's ratio in the [100] and [110] directions, and to a finite element (FEM) simulation made using the full anisotropic compliance matrix (compliance coefficients from Table I) in COMSOL. The calculated deflections are normalized to the FEM center deflection. Excellent agreement is shown between the anisotropic curve and FEM with a deviation of less than 0.1 % whereas the isotropic approach leads to deviations in the center deflection of around 10 % for both [100] and [110] directions.

V. CMUT APPLICATION

Many important design parameters for CMUTs depend on the deflection of the plate. By using static analysis it is possible to find the stable position of the plate when applying a certain bias voltage. The stable position is easiest expressed through the center deflection and is the position where the strain force balance the electrostatic and pressure forces. The center deflection is found from energy considerations. The total potential energy of the system consists of three terms:

1) Strain energy. Calculated by integrating the strain energy density using (5), (7) and (11) and the result is

$$U_\mathrm{s} = \frac{1}{2}\int_{-h/2}^{h/2}\int_{-L}^{L}\int_{-L}^{L}(\sigma_1\varepsilon_1+\sigma_2\varepsilon_2+\sigma_6\varepsilon_6)\,\mathrm{d}x\mathrm{d}y\mathrm{d}z \qquad (17)$$

$$U_{\mathrm{s,Si}(001),[110]} = 3.91172\times 10^{11}\frac{h^3 w_0^2}{L^2}. \qquad (18)$$

2) Energy due to applied pressure. This is found from the pressure load on the plate

$$U_\mathrm{p} = -\int_{-L}^{L}\int_{-L}^{L} pw(x,y)\;dxdy \qquad (19)$$

$$U_{\mathrm{p,Si}(001),[110]} = -1.216pw_0L^2. \qquad (20)$$

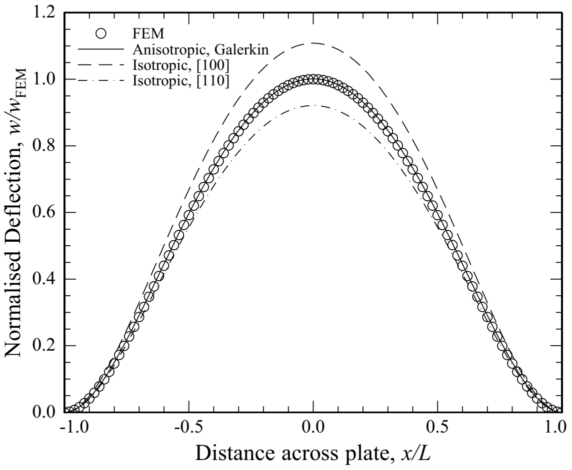

Fig. 2. Normalized deflection cross section ($y = 0$) of a square plate of silicon (001) calculated using both the isotropic approach with Young's modulus and Poisson's ratio in the [100] and [110] directions and the anisotropic approach. The circles represent the deflection calculated by FEM.

3) Electrostatic energy. Expressed through the charge Q or applied voltage V, the vacuum permittivity ε_0, gap height g and the total capacitance C_t of the device which for a square plate is found using a Taylor expansion of the integrant with the deflection in (11)

$$U_\mathrm{e} = Q^2/(2C_\mathrm{t}) = \frac{1}{2}V^2C_\mathrm{t}. \qquad (21)$$

$$= \frac{1}{2}V^2\int_{-L}^{L}\int_{-L}^{L}\frac{\varepsilon_0}{g-w(x,y)}dxdy \qquad (22)$$

The total force on the system is then found by differentiating the total potential energy with respect to the center deflection. From this the stable center position of the plate can be found for a given applied voltage as the point where the total force is zero.

VI. COMPARISON TO MEASUREMENTS

CMUTs with square silicon plates have been fabricated using fusion bonding. The fabricated devices have a 65x65 μm wide and 2.37 μm thick silicon plate with a gap height of 405 nm and a 198 nm thick insulating oxide at the bottom of the cavity. The deflection was measured with a Sensofar PLu Neox 3D Optical Profiler using white light interferometry.

Fig. 3 shows a measured cross section of the normalized deflection for the fabricated device. It is normalized in both center deflection and distance across the plate to compare the shape of the measured deflection with the calculated deflection. The red curve is a fit made to the measurements using the anisotropic model (16). Both the center deflection and the plate parameter β is fitted. As it is seen in the figure the fitted value for β is 0.243 which matches very well, with a deviation of 1.5%, compared to the calculated value of 0.23920 for this type of plate (silicon (001) substrate aligned to [110] direction). The center deflection found from the fit has a deviation of 0.5% compared to the measurement.

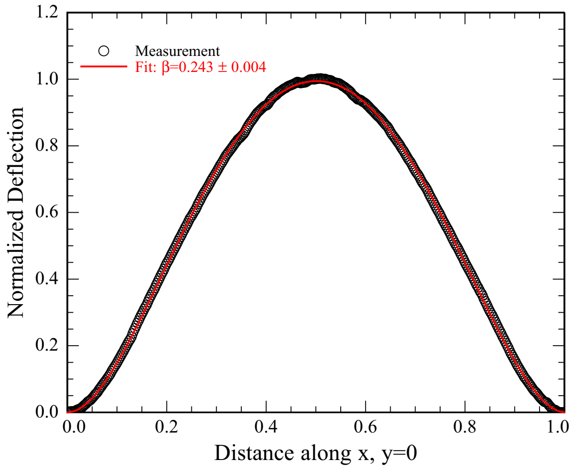

Fig. 3. Normalized deflection cross section from measurement on a fabricated CMUT. The red curve is a fit made with (16).

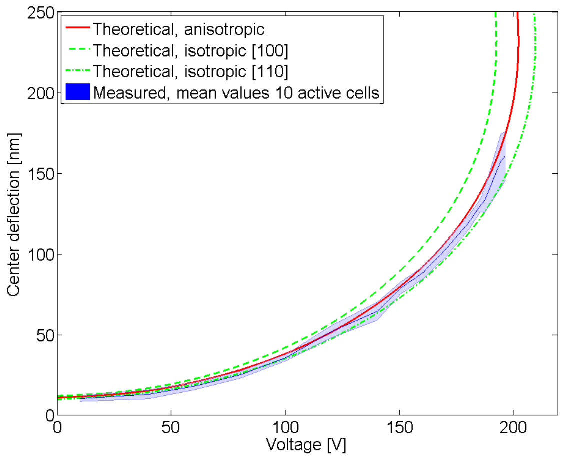

Fig. 4. Measured center deflection for increasing bias voltage together with theoretical curves using anisotropic and isotropic approaches.

Measurements with a DC voltage applied were also performed and the results are shown in Fig. 4. Here it is seen how the center deflection varies with the applied voltage and how it deflects more when approaching the pull-in voltage as expected. The center deflection for the measurements is found as the average of 10 cells. The errorbars corresponds to plus/minus two standard deviations. A theoretical curve made from the stable position analysis described in section V is plotted as well for both anisotropic and isotropic [100] and [110] approaches. The thickness of the plate is adjusted to 2.48, 2.49 and 2.47 μm respectively with the correction found by FEM to take the 200 nm Al layer on top of the Si into account. It is seen that the anisotropic theory matches well with the measurement as it is within the error margin and the isotropic curves show similar behavior as in Fig. 2. Also the pull-in voltage is in good agreement as it was measured to be 206 V, compared to an expected value of 202 V from the anisotropic model.

VII. CONCLUSION

Using isotropic plate theory to calculate the deflection of anisotropic silicon plates results in deviations from FEM or measurements of up to 10%. The full anisotropic plate equation was solved using the Galerkin method. It is seen that the deflection simplifies by utilizing the symmetry of the silicon crystal and a compact solution is obtained for square CMUT plates on a (001) silicon substrate aligned to the [110] direction. The maximum deviation is less than 0.1% compared to FEM. Furthermore, the deflection was measured on fabricated devices and fitting the anisotropic calculated deflection to the measurement a deviation of 0.5-1.5% is observed in the fitted parameters. The stable position for varying bias voltage was also found using the anisotropic theory and comparing this to measurements it is seen that the theory is within the uncertainty interval of the measurements.

ACKNOWLEDGEMENT

This work was financially supported by the Danish National Advanced Technology Foundation (024-2008-3) and (82-2012-4).

REFERENCES

[1] I. O. Wygant, M. Kupnik, and B. T. Khuri-Yakub, “Analytically calculating membrane displacement and the equivalent circuit model of a circular CMUT cell,” in *IEEE Ultrasonics Symposium, 2008. IUS 2008*. IEEE, Nov. 2008, pp. 2111–2114.

[2] A. Lohfink and P.-C. Eccardt, “Linear and nonlinear equivalent circuit modeling of CMUTs,” *IEEE Transactions on Ultrasonics, Ferroelectrics and Frequency Control*, vol. 52, no. 12, pp. 2163 –2172, Dec. 2005.

[3] R. L. Taylor and S. Govindjee, “Solution of clamped rectangular plate problems,” *Communications in Numerical Methods in Engineering*, vol. 20, no. 10, p. 757765, 2004. [Online]. Available: http://onlinelibrary.wiley.com/doi/10.1002/cnm.652/abstract

[4] M. Rahman, J. Hernandez, and S. Chowdhury, “An improved analytical method to design CMUTs with square diaphragms,” *IEEE Transactions on Ultrasonics Ferroelectrics and Frequency Control*, vol. 60, no. 4, pp. 834–845, Apr. 2013, WOS:000317010200020.

[5] M. F. la Cour, T. L. Christiansen, J. A. Jensen, and E. V. Thomsen, “Modelling of CMUTs with anisotropic plates,” *Proceedings of IEEE International Ultrasonics Symposium*, pp. 588–591, 2012.

[6] E. Ventsel and T. Krauthammer, *Thin Plates and Shells: Theory: Analysis, and Applications*. Taylor & Francis, Aug. 2001.

[7] R. E. Newnham, *Properties of Materials: Anisotropy, Symmetry, Structure*. Oxford University Press, USA, Jan. 2005.

[8] J. J. Hall, “Electronic effects in the elastic constants of n-type silicon,” *Physical Review*, vol. 161, no. 3, pp. 756–761, Sep. 1967. [Online]. Available: http://link.aps.org/doi/10.1103/PhysRev.161.756

[9] E. V. Thomsen, K. Reck, G. Skands, C. Bertelsen, and O. Hansen, “Silicon as an anisotropic mechanical material: Deflection of thin crystalline plates,” submitted to Journal of Microelectromechanical Systems.

[10] S. Holgate, “The transverse flexure of perforated aeolotropic plates,” *Proceedings of the Royal Society A: Mathematical, Physical and Engineering Sciences*, vol. 185, no. 1000, pp. 50–69, Jan. 1946. [Online]. Available: http://adsabs.harvard.edu/abs/1946RSPSA.185...50H

[11] F. Mbakogu and M. Pavlovi, “Bending of clamped orthotropic rectangular plates: a variational symbolic solution,” *Computers & Structures*, vol. 77, no. 2, pp. 117–128, Jun. 2000. [Online]. Available: http://www.sciencedirect.com/science/article/pii/S0045794999002175

APPENDIX E

Paper - Electrostatic Analysis of CMUTs with Circular and Square Anisotropic Plates

Submitted to IEEE Transactions on Ultrasonics Ferroelectrics and Frequency Control, May 2014.

Electrostatic Analysis of CMUTs with Circular and Square Anisotropic Plates

Mette Funding la Cour*†, Thomas Lehrmann Christiansen† Jørgen Arendt Jensen* and Erik Vilain Thomsen†
*Center for Fast Ultrasound Imaging, Department of Electrical Engineering, Technical University of Denmark, DK-2800 Kgs. Lyngby, Denmark
†Department of Micro and Nanotechnology, Technical University of Denmark, DK-2800 Kgs. Lyngby, Denmark

Abstract—**Traditionally, CMUTs are modeled using the isotropic plate equation and this leads to deviations between analytical calculations and FEM simulations. In this paper, the deflection is calculated for both circular and square plates using the full anisotropic plate equation. It is shown that the anisotropic calculations match perfectly with FEM while an isotropic approach causes up to 10% deviations in deflection. For circular plates an exact solution can be found and for square plates using the Galerkin method and utilizing the symmetry of the silicon crystal, a compact and accurate expression for the deflection can be obtained. The deviation from FEM in center deflection is $< 0.1\%$. The theory of multilayer plates is also applied to the CMUT. The deflection of a square plate was measured on fabricated CMUTs using a white light interferometer. Fitting the plate parameter for the anisotropic calculated deflection to the measurement a deviation of 0.07 % is seen. Furthermore, electrostatic analysis is performed using energy considerations and the calculated deflections to include the anisotropy. The stable position, effective spring constant, pull-in distance and pull-in voltage are found for both circular and square anisotropic plates and the pressure dependence is also included by comparing to the corresponding analysis for a parallel plate. Finally, it was also measured how fabricated devices with both circular and square plates behaved under increasing bias voltage and it is observed that the models including anisotropic effects are within the uncertainty interval of the measurements.**

I. INTRODUCTION

Precise modeling of capacitive micromachined ultrasonic transducers (CMUT) is important for an efficient design process. A CMUT consists of two plates where one of them is fixed and the other can deflect. The deflection $w(x, y)$ of the movable plate is an important parameter that influences several basic CMUT parameters such as pull-in voltage and capacitance. Most existing analytical approaches use the isotropic plate equation to calculate the deflection i.e. [1], [2]. However, when using fusion bonding fabrication technology [3], the plate usually consists of crystalline silicon. Having a silicon (001) substrate, which are most often used, Young's modulus and Poisson's ratio are strongly anisotropic. The isotropic approach is then invalid, and this results in deviations in the deflection compared to finite element modeling (FEM) and measurements. Therefore, to get precise modeling of these CMUTs, the anisotropy of silicon needs to be taken into account.

The first decade after CMUTs were invented, various analytical models were presented for circular cells, which included more and more features of the device behaviour [4], [5], [6]. However, all of them were based on parallel plate approximations for the deflection leading only to estimates of the critical CMUT parameters. Later, the actual deflection of the movable plate clamped at the edges was taken into account [2], [7], [8], where it was used for calculating pull-in voltage and derivation of an equivalent circuit model. The effect from having a non-uniform load on the plate was included in solving the plate equation by [7] who used superposition and a concentrically loaded plate, and by [9] who used the Galerkin method. The non-uniform load occurs when the bias voltage is increased, as the electrostatic force will be greater where the gap is smaller, an effect getting more distinct when the deflection is larger. However, it is not necessary to include for the typical CMUT case, where the plate never deflect more than half the gap due to pull-in.

All of these models assumes a circular plate geometry of the CMUT cells. For circular plates, a simple and exact solution for the deflection exists [10], but this is not the case for square plates. Existing solutions for the deflection of square plates is based on series expansions with either trigonometric [11] or polynomial basis functions [12]. None of these, however, take the anisotropy of the plate into account.

For the first fabricated CMUTs there was no need for using anisotropic plate theory, as the plate usually consisted of silicon nitride or polysilicon when fabricated with the sacrificial release method. After the fusion bonding fabrication method was applied to CMUTs, the anisotropy of the plate, which now consisted of crystalline silicon, was considered [13]. However, instead of solving the problem analytically, finite element modeling (FEM) was used to estimate a set of material parameters (Young's modulus and Poisson's ratio) to use in the models to get an approximation as close as possible to the correct anisotropic solution.

This paper presents solutions to the full anisotropic plate equation for both circular and square plates used in fusion bonded CMUTs. The models were initially presented in [14] for an anisotropic plate with circular geometry, and this was then modified and expanded to include square plates as well in [15]. For the circular cells the symmetry reduces the plate equation and an exact solution for the anisotropic case can be obtained similarly to the isotropic solution. The approach used to solve the equation for the square plate is the Galerkin method [16]. Utilizing the symmetry of the silicon crystal, a compact and precise approximation of the deflection of a square plate can be obtained for the anisotropic case.

The plate usually also consists of more than one material. The theory of laminar plates is described in [17], [18] and in this paper, the multilayer plate theory including anisotropy is applied to calculate important parameters for a two layer silicon/metal plate typically used for CMUTs.

Having found the deflection of the CMUT plate, a model for the electrostatic behavior of the transducer can be set up. Circular cells have been investigated thoroughly during the years and a full model for this plate geometry has recently been presented [8], whereas the full electrostatic analysis for the square plate has not been investigated previously. Furthermore, none of the existing models include the anisotropy.

The isotropic plate equation and solutions for circular and square plates can be found in Section II. It is followed by the anisotropic plate equation and how to utilize the symmetry of the silicon crystal to reduce and solve the problem in Section III for both circular and square plates. The calculated deflection is compared to the solution for corresponding isotropic cases, a finite element model (FEM) and measurements performed on fabricated devices. Furthermore, in Section VI the calculated deflection is used to find the stable position, effective spring constant, pull-in distance and pull-in voltage of the CMUT plates. The pressure dependence is also included. Measurements of the stable position are performed on devices with both circular and square plates and the theory is compared to these in Section VII.

II. THE ISOTROPIC PLATE EQUATION

Conventionally, the deflection $w(x,y)$ of a CMUT with a thin plate is modeled using the isotropic plate equation [11]

$$\frac{\partial^4 w}{\partial x^4} + 2\frac{\partial^4 w}{\partial x^2 \partial y^2} + \frac{\partial^4 w}{\partial y^4} = \frac{p}{D_\mathrm{i}}, \tag{1}$$

where p is the applied pressure difference across the plate and the flexural rigidity is given by

$$D_\mathrm{i} = \frac{E}{12\left(1-\nu^2\right)}h^3, \tag{2}$$

with E being Young's modulus, ν being Poisson's ratio, and h being the thickness of the plate.

For thin clamped circular plates, an exact solution exists. For such a plate with radius a, the center deflection is given by [10]

$$w_{0,\mathrm{iso,circ}} = \frac{1}{64}\frac{a^4 p}{D_\mathrm{i}}. \tag{3}$$

For clamped rectangular and square plates, no simple exact solution exists and approximate methods have to be used. The conventional isotropic approach is based on a series expansion of the deflection, and the center deflection for a thin clamped square plate having side length $2L$ is [11]

$$w_{0,\mathrm{iso,sq}} = 0.020245\frac{L^4 p}{D_\mathrm{i}}. \tag{4}$$

Fig. 1 shows a cross sectional view of a CMUT cell with an applied voltage. The device parameters are illustrated for both circular and square plates.

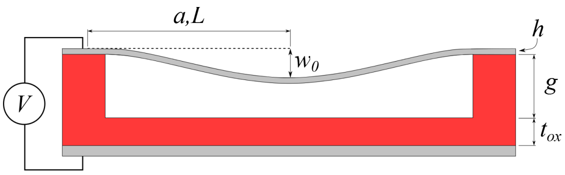

Fig. 1. Cross sectional view of CMUT cell with applied voltage.

TABLE I

ROOM TEMPERATURE (300K) COMPLIANCE COEFFICIENTS FOR N-TYPE CRYSTALLINE SILICON MEASURED BY [21] FOR A SUBSTRATE WITH LOW DOPING LEVEL (150 Ω-CM, $\sim 2.8\times10^{13}$ CM^{-3}) AND HIGH DOPING LEVEL (3.26 MΩ-CM, $\sim 2.1\times10^{19}$ CM^{-3}).

	Low doping	High doping
s^c_{11}	7.691×10^{-12} Pa^{-1}	7.858×10^{-12} Pa^{-1}
s^c_{12}	-2.1420×10^{-12} Pa^{-1}	-2.2254×10^{-12} Pa^{-1}
s^c_{44}	12.577×10^{-12} Pa^{-1}	12.628×10^{-12} Pa^{-1}

III. THE ANISOTROPIC PLATE EQUATION

To take the anisotropy of the plate into account and avoid the inaccuracy from isotropic modeling, the stiffness of the plate needs to be described through the stiffness matrix of the material instead of Young's modulus and Poisson's ratio. The starting point is the relation between stress, σ, and strain, ϵ, [19]

$$\sigma^\mathrm{c} = \mathbf{c}^\mathrm{c}\epsilon^\mathrm{c}, \text{ or } \epsilon^\mathrm{c} = \mathbf{s}^\mathrm{c}\sigma^\mathrm{c}. \tag{5}$$

Here superscript c denotes the crystallographic coordinate system, so $\mathbf{c}^\mathrm{c}$ is the stiffness matrix and $\mathbf{s}^\mathrm{c} = (\mathbf{c}^\mathrm{c})^{-1}$ the compliance matrix in this coordinate system. Having a thin plate, the stresses in the z direction can be ignored and plane stress assumed. Using the voigt notation, the relation between strain and stress then becomes [20]

$$\begin{pmatrix}\varepsilon_1\\ \varepsilon_2\\ \varepsilon_6\end{pmatrix} = \begin{pmatrix} s_{11} & s_{12} & s_{16}\\ s_{12} & s_{22} & s_{26}\\ s_{16} & s_{26} & s_{66}\end{pmatrix}\begin{pmatrix}\sigma_1\\ \sigma_2\\ \sigma_6\end{pmatrix} = \mathbf{S}_\mathrm{eff}\begin{pmatrix}\sigma_1\\ \sigma_2\\ \sigma_6\end{pmatrix}, \tag{6}$$

and we can define an effective stiffness matrix from the effective compliance matrix

$$\mathbf{C}_\mathrm{eff} = \left(\mathbf{S}_\mathrm{eff}\right)^{-1}. \tag{7}$$

For silicon the effective compliance matrix is

$$\mathbf{S}^\mathrm{c}_\mathrm{eff} = \begin{pmatrix} s^\mathrm{c}_{11} & s^\mathrm{c}_{12} & 0\\ s^\mathrm{c}_{12} & s^\mathrm{c}_{11} & 0\\ 0 & 0 & s^\mathrm{c}_{44}\end{pmatrix}. \tag{8}$$

The elements in this matrix are known from measurements and shown in Table I [21]. It is noted that the elements in (8) are known in the crystallographic coordinate system, which is not necessarily the same as the coordinate system of the plate. To illustrate this further, the crystallographic and the plate coordinate systems can be seen in Fig. 2. The solid coordinate system aligned to the $\langle 100\rangle$ directions is where the compliance values for silicon are known and the dashed system shows the rotated coordinate system for the plate where the compliance values needs to be calculated. Having silicon as plate material and performing standard cleanroom fabrication, the plate will usually be on a (001) substrate and aligned to the primary wafer flat. Flat alignment is to the [110] direction, so the plate coordinate system will be rotated $\psi = 45°$ with respect to the crystallographic coordinate system. A transformation of the compliance matrix between the two coordinate systems is therefore needed. As it is the stiffness matrix elements that are to be used in the plate equation, the resulting effective stiffness matrix for the present case can be expressed through (7) [20]

$$C^{\mathrm{eff}}_{\mathrm{Si(001),[110]}} = \begin{pmatrix} \frac{1}{s^{\mathrm{c}}_{44}} + \frac{1}{2(s^{\mathrm{c}}_{11}+s^{\mathrm{c}}_{12})} & \frac{1}{2(s^{\mathrm{c}}_{11}+s^{\mathrm{c}}_{12})} - \frac{1}{s^{\mathrm{c}}_{44}} & 0 \\ \frac{1}{2(s^{\mathrm{c}}_{11}+s^{\mathrm{c}}_{12})} - \frac{1}{s^{\mathrm{c}}_{44}} & \frac{1}{s^{\mathrm{c}}_{44}} + \frac{1}{2(s^{\mathrm{c}}_{11}+s^{\mathrm{c}}_{12})} & 0 \\ 0 & 0 & \frac{1}{2s^{\mathrm{c}}_{11}-2s^{\mathrm{c}}_{12}} \end{pmatrix}. \quad (9)$$

It is seen that the stiffness matrix has an orthotropic symmetry.

Having the effective stiffness matrix, the generalized plate equation can be used. This is a differential equation for the deflection, $w(x, y)$, of a thin anisotropic plate exposed to a uniform load p given by [20], [22]

$$\frac{\partial^4 w}{\partial x^4} + k_1 \frac{\partial^4 w}{\partial x^3 \partial y} + k_2 \frac{\partial^4 w}{\partial x^2 \partial y^2} + k_3 \frac{\partial^4 w}{\partial x \partial y^3} + k_4 \frac{\partial^4 w}{\partial y^4} = \frac{p}{D_{\mathrm{a}}}. \quad (10)$$

The plate coefficients k_1-k_4 and the anisotropic flexural rigidity, D_{a}, depend on the elastic constants of the plate material

$$k_1 = \tfrac{4C^{\mathrm{eff}}_{13}}{C^{\mathrm{eff}}_{11}} \quad k_2 = \tfrac{2\left(C^{\mathrm{eff}}_{12}+2C^{\mathrm{eff}}_{33}\right)}{C^{\mathrm{eff}}_{11}} \quad k_3 = \tfrac{4C^{\mathrm{eff}}_{23}}{C^{\mathrm{eff}}_{11}} \quad (11)$$

$$k_4 = \tfrac{C^{\mathrm{eff}}_{22}}{C^{\mathrm{eff}}_{11}} \quad D_{\mathrm{a}} = \tfrac{1}{12} h^3 C^{\mathrm{eff}}_{11},$$

where C^{eff}_{pq} are elements in the effective stiffness matrix (9). Note that the stiffness of the plate is no longer expressed through Young's modulus and Poisson's ratio but directly through the stiffness values.

Using the compliance values for silicon (Table I) and inserting the stiffness elements in (9) into (11), it follows that $k_1 = k_3 = 0$ and $k_4 = 1$. Thus, aligning the plate to the primary flat simplifies the anisotropic plate equation (10) to

$$\frac{\partial^4 w}{\partial x^4} + k_2 \frac{\partial^4 w}{\partial x^2 \partial y^2} + \frac{\partial^4 w}{\partial y^4} = \frac{p}{D_{\mathrm{a}}}. \quad (12)$$

The same is the case for aligning the plate along the [100] direction where the inverse of (8) is used instead of (9), resulting in the same values for k_1, k_3 and k_4. For these two special cases, the coefficients in the plate equation are summarized in Table II for both high and low doping levels of the substrate.

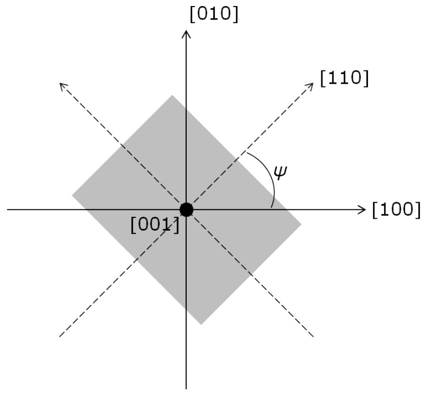

Fig. 2. The two coordinate systems, solid lines are the crystallographic system aligned to the $\langle 100\rangle$ direction and the dashed lines the plate system aligned to the $\langle 110\rangle$ direction.

TABLE III
YOUNG'S MODULUS AND POISSON'S RATIO FOR SILICON (001).

	Young's modulus	Poisson's ratio
[100] direction	130 GPa	0.278
[110] direction	169 GPa	0.062
Mean value	148 GPa	0.177

A. Deflection of Circular plates

The solution to (10) for a circular plate of radius a fixed at the boundary is easily obtained using polar coordinates. The deflection at a point a distance r from the center is given by [10]

$$\frac{w(r)}{w_0} = \left(1 - \left(\frac{r}{a}\right)^2\right)^2. \quad (13)$$

This expression is similar to the deflection for the isotropic case, however, the center deflection is different

$$w_{0,\mathrm{circ}} = \frac{1}{8\,(3 + k_2 + 3k_4)} \frac{a^4 p}{D_{\mathrm{a}}}. \quad (14)$$

By combining (3) and (14) it is possible to find an effective flexural rigidity

$$D_{\mathrm{eff}} = \frac{3 + k_2 + 3k_4}{8} D_{\mathrm{a}}. \quad (15)$$

This can be used to easily change from the isotropic plate equation to the anisotropic plate equation in already existing analytical models of CMUTs. An example of this will be shown in section VI. Using the plate coefficient values from Table II for a highly doped (001) silicon plate aligned to the $\langle 110\rangle$ direction, the effective flexural rigidity becomes $D_{\mathrm{eff}} = 0.91551 D_{\mathrm{a}}$.

To compare the anisotropic model with the isotropic approach and FEM simulations, the normalized deflection of a CMUT exposed to a pressure difference is shown in Fig. 3. The FEM simulations were performed in COMSOL Multiphysics version 4.2a using the full anisotropic stiffness tensor and the curves are normalized to the center deflection of this. The isotropic curves are made using (13) and (3) and Young's modulus and Poisson's ratio along the [100] and [110] directions (see Table III) to give the dash and dashdot lines, respectively. The anisotropic solution is made using (13)

TABLE II

SELECTED VALUES FOR THE PLATE COEFFICIENTS AND ANISOTROPIC FLEXURAL RIGIDITY FOR PLATES ON A SILICON (001) SUBSTRATE [20]. UPPER VALUES IN BRACKETS ARE FOR LOW DOPING LEVEL AND LOWER VALUES FOR HIGH DOPING LEVEL.

Orientation	ψ	k_1	k_2	k_3	k_4	$12D_a/h^3$[GPa]
[100]	0	0	2.8133 ± 0.0006 2.8559 ± 0.0006	0	1	140.96 ± 0.03 138.35 ± 0.03
[110]	$\pi/4$	0	1.3241 ± 0.0004 1.2949 ± 0.0004	0	1	169.62 ± 0.03 167.96 ± 0.03

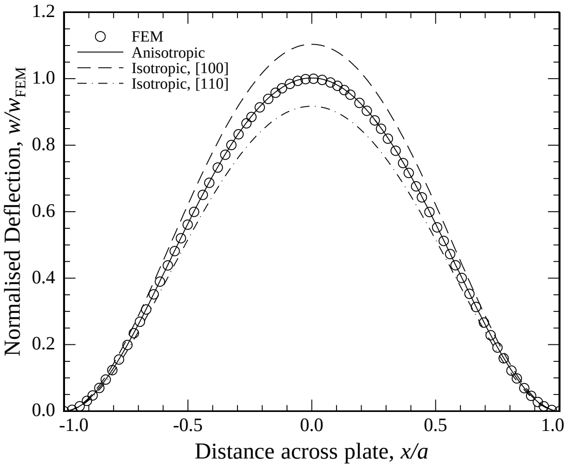

Fig. 3. Normalized deflection cross section ($y = 0$) of a thin circular plate of silicon (001) calculated with (13) using both the isotropic approach (3) with Young's modulus and Poisson's ratio in the [100] and [110] directions and the anisotropic approach (14). The circles represent the deflection calculated by FEM.

and (14) and is shown as a solid curve. This is on top of the FEM simulation (circles). Due to the symmetry of the circular plate, any set of parameters from Table II can be used. Excellent agreement between the anisotropic solution and the finite element calculation is seen with an error of less than 0.3%. The figure also shows that using Young's modulus and Poisson's ratio corresponding to [100] or [110] directions leads to errors in the center deflection of around 10%. To reduce this error, it is common practice to use mean values of Young's modulus and Poission's ratio (see Table III) which decreases the error to around 1.5%.

As it is seen, using the anisotropic approach for a thin circular CMUT plate on a (001) silicon substrate is simple and the result is exact.

B. Deflection of Square Plates

Having a square plate makes analytical deflection calculations complicated and approximate methods must be used to solve the anisotropic plate equation. With the anisotropic approach, the Galerkin method [16] can be used to find approximate expressions for the deflection of a thin anisotropic square plate. As previously stated, in the most common case for CMUTs, the plate is fabricated on a silicon (001) substrate and aligned to the [110] direction. For this orthotropic square plate with sidelengths $2L$, the relative deflection is found to be [20], [23]

$$\begin{aligned}\frac{w(x,y)}{w_0} &= \left[1-\left(\frac{x}{L}\right)^2\right]^2\left[1-\left(\frac{y}{L}\right)^2\right]^2\\ &\times\left[1+\beta\left(\frac{x}{L}\right)^2+\beta\left(\frac{y}{L}\right)^2\right],\end{aligned} \tag{16}$$

where the plate parameter β is defined as

$$\beta = \frac{182+143k_2}{1432+91k_2}. \tag{17}$$

The center deflection can be written

$$w_{0,\mathrm{sq,Si(001)}} = \frac{77(1432+91k_2)}{256(16220+11k_2(329+13k_2))}\frac{L^4p}{D_\mathrm{a}}. \tag{18}$$

Equations (16)-(18) are also valid when the plate is aligned to the [100] direction on a silicon (001) substrate. Note that the center deflection depends only on the k_2 coefficient. For primary flat alignment, it is found by inserting k_2 into (17) and using the low doping values $\beta_\mathrm{low} = 0.23920$ and using the high doping values $\beta_\mathrm{high} = 0.23691$. For the low doping case, this results in a normalized deflection for the plate aligned to the $\langle 110\rangle$ direction given by

$$\begin{aligned}\left.\frac{w(x,y)}{w_0}\right|_{\mathrm{sq,Si(001)},\langle 110\rangle} &= \left[1-(x/L)^2\right]^2\left[1-(y/L)^2\right]^2\\ &\times\left[1+0.23920\left[(x/L)^2+(y/L)^2\right]\right],\end{aligned} \tag{19}$$

and the center deflection becomes

$$w_{0,\mathrm{sq,Si(001)},\langle 110\rangle} = 0.02196\frac{L^4p}{D_\mathrm{a}}. \tag{20}$$

For the high doping case, the factor in front becomes 0.02204 for the center deflection. Comparing (4) and (20), it is seen that they are very similar containing the same parameters but different coefficients and the anisotropic instead of the isotropic flexural rigidity.

Fig. 4 shows the deflection cross section through $y = 0$ of a square plate of silicon (001) given by the reduced version of (16)

$$w_{y=0,\mathrm{sq}} = w_0\left[1-(x/L)^2\right]^2\left[1+\beta\left(x/L\right)^2\right]. \tag{21}$$

The deflection calculated with the anisotropic approach uses $k_2 = 1.3241$ in (17) and center deflection (20) (solid curve). This is compared to the isotropic approach using $k_2 = 2$

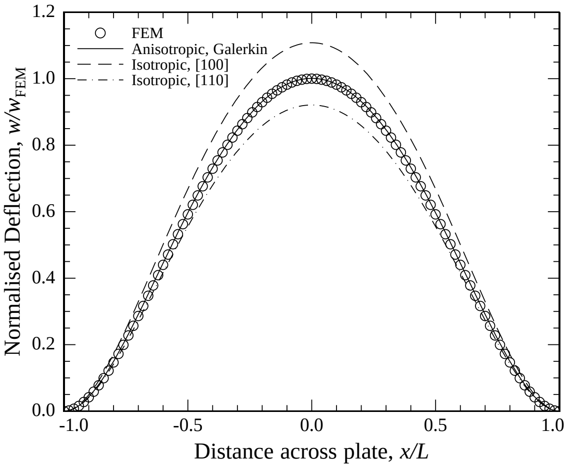

Fig. 4. Normalized deflection cross section ($y = 0$) of a square plate of silicon (001) calculated with (21) using both the isotropic approach (4) with Young's modulus and Poisson's ratio in the [100] and [110] directions and the anisotropic approach (20). The circles represent the deflection calculated by FEM.

in (17) and center deflection (4), with Young's modulus and Poisson's ratio in the [100] and [110] directions (dash and dashdot curves), and to a finite element (FEM) simulation made using the full anisotropic compliance matrix (compliance coefficients from Table I) in COMSOL (circles). The calculated deflections are normalized to the FEM center deflection. Excellent agreement is shown between the anisotropic curve and FEM with a deviation of less than 0.1 % whereas the isotropic approach leads to deviations in the center deflection of around 10 % for both [100] and [110] directions.

IV. MULTILAYER PLATES

Following the method by [17], [18] the anisotropic plate theory can be expanded to also include plates consisting of more than one layer. Starting from equations for the moment and stress resultants, it can be found that the general plate equation including anisotropic effects has the same form as for the single layer plate (10), however, the plate coefficients $k_1 - k_4$ and the plate stiffness D_{a} will be different to capture effects from having a multilayer plate.

For the CMUT application, the multilayer plate will often consist of two layers with silicon as the main part and a thin aluminum layer on top for contacts. The aluminum is an isotropic material and the silicon is, as seen on (8), an orthotropic material (when aligned to [110] direction on a (001) substrate). For this two-layer plate, the total thickness is called h and the ratio $\alpha = h_{\mathrm{Al}}/h$ is defined from the thickness of the aluminum, h_{Al}. When the plate is all silicon $\alpha = 0$ and when the plate is only aluminum $\alpha = 1$. Again utilizing the symmetry of the materials, it can be found that $k_1 = k_3 = 0$ and $k_4 = 1$ so again only k_2 and D_{a} need to be taken into account for the usual CMUT plates.

The expressions for k_2 and the plate stiffness becomes quite long even for the simplified case. Using the compliance values for highly doped silicon in Table I and Young's modulus of $E = 70$ GPa and Poisson's ratio of $\nu = 0.35$ for aluminum in the expressions, they become

$$D_{\mathrm{AlSi}} = (13.9963\ \mathrm{GPa} - 22.0458\ \mathrm{GPa} \cdot \alpha)h^3 \tag{22}$$

$$k_{2,\mathrm{AlSi}} = 1.29493 + 1.00464\alpha. \tag{23}$$

TABLE IV

EXAMPLES ON k_2, STIFFNESS AND CENTER DEFLECTION WHEN USING SINGLE OR MULTILAYER PLATE THEORY.

	α	k_2	$12D_{\mathrm{a}}/h^3$	w_0
Circ., multi	0.10	1.3954	141.50 GPa	29.4 nm
Circ., Si	-	1.2949	167.96 GPa	25.7 nm
Sq., multi	0.08	1.3753	146.79 GPa	12.5 nm
Sq., Si	-	1.2949	167.96 GPa	11.2 nm

Furthermore, it can also be found that when having a sufficiently thin aluminum layer, $\alpha < 0.2$, a series expansion can be used and simple correction formulas can be found. This way, the flexural rigidity of the combined aluminum and silicon plate compared to the flexural rigidity for a plate of only silicon with the same thickness as the total thickness can be expressed as

$$\frac{D_{\mathrm{AlSi}}}{D_{\mathrm{Si}}} = 1 - 1.575\alpha. \tag{24}$$

Similarly, for the plate parameter k_2 it is found that

$$\frac{k_{2,\mathrm{AlSi}}}{k_{2,\mathrm{Si}}} = 1 - 0.775822\alpha. \tag{25}$$

Equations (24) and (25) both use the stiffness values for highly doped silicon from Table I.

For a circular plate, the relative center deflection using the same method as above can be found to be

$$\frac{w_{0,\mathrm{AlSi,circ}}}{w_{0,\mathrm{Si,circ}}} = 1 + 1.437\alpha. \tag{26}$$

Doing the same for square plates the relation becomes

$$\frac{w_{0,\mathrm{AlSi,Sq}}}{w_{0,\mathrm{Si,Sq}}} = 1 + 1.445\alpha. \tag{27}$$

The error between the series expansion and the full result for the center deflection is less than 2 % for $\alpha = 0.2$ for both plate geometries. An example of a typical thicknesses of the layers of the CMUT multilayer plate is $\sim$2 μm silicon and $\sim$0.2 μm aluminum. This gives $\alpha = 0.1$ and the error when using the series expansion is less than 0.5%.

As examples on how the aluminum layer influences the plate parameter, stiffness and center deflection of the circular and square plates, calculations using single and multilayer plate theory can be seen in Table IV. Here, calculations are made with dimensions as the fabricated devices found in Table V. It is seen that including the aluminum layer in the calculations affects k_2 with around 7 %, the stiffness of the plate with around 18 % and the center deflection with around 12 % in this case.

TABLE V

DIMENSIONS OF DEVICES FABRICATED WITH CIRCULAR AND SQUARE PLATES USING WAFER BONDING.

	Circular	Square
Size (a, L)	36 μm	32.5 μm
Plate thickness, Si h_{Si}	1.8 μm	2.3 μm
Al thickness h_{Al}	200 nm	200 nm
Gap height (vacuum) g	(uncertain)	405 nm
Insulation layer t_{ox}	195 nm	198 nm

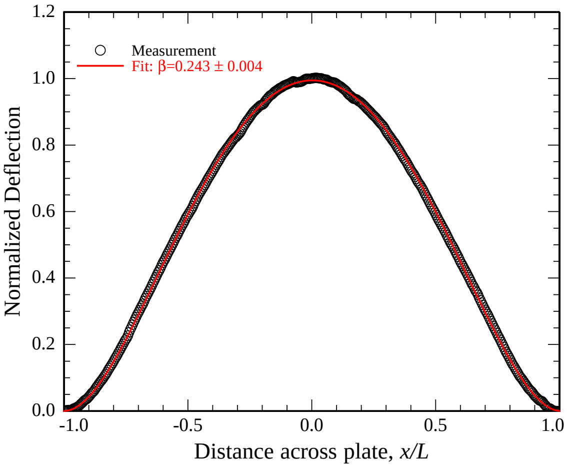

Fig. 5. Normalized deflection cross section ($y = 0$) from measurement on a fabricated CMUT with square plate of silicon (001) aligned to [110]. The red curve is a fit made from (21).

V. DEFLECTION MEASUREMENT

To further validate the deflection of the square plate, CMUTs with square silicon plates have been fabricated using fusion bonding [24]. The dimensions of the fabricated device can be seen in Table V. The deflection was measured with a Sensofar PLu Neox 3D Optical Profiler using white light interferometry. Fig. 5 shows a measured cross section of the normalized deflection for a fabricated device. It is normalized in both center deflection and distance across the plate to compare the shape of the measured deflection with the calculated deflection. The red curve is a fit made to the measurements using the anisotropic model (21). The plate parameter β is fitted to the measurements. As it is seen in the figure, the fitted value for β is 0.243. Using (23) for calculating β for this multilayer plate (2 μm highly doped silicon (001) substrate aligned to [110] direction with 200 nm Al) a deviation of only 0.07 % is obtained.

VI. ELECTROSTATIC ANALYSIS

Many important design parameters for CMUTs depend on the deflection of the plate. By using the solutions found in the previous sections and performing electrostatic analysis, it is possible to find the stable position of the plate, when applying a certain bias voltage. The stable position is the position where the spring force balances the electrostatic and pressure forces. From this the pull-in distance and pull-in voltage can be found.

The analysis in the following is based on energy considerations. The total potential energy U_{t} consists of three terms, the strain energy U_{s}, the electrostatic energy U_{e}, and the energy from applying a pressure U_{p}

$$U_{\mathrm{t}} = U_{\mathrm{s}} + U_{\mathrm{p}} + U_{\mathrm{e}}. \tag{28}$$

The method is valid for all systems where the total potential energy is of the form

$$U_{\mathrm{t}} = \frac{k_0 w_0^2}{2} - pA_{\mathrm{eff}} w_0 - \frac{1}{2} V^2 C_{\mathrm{t}}(w_0), \tag{29}$$

where k_0 is the generalized spring constant that comes from the calculation of the strain energy, A_{eff} is the effective area of the plates i.e. the area that goes into calculation of the work performed by deflecting the plate due to applied pressure, V is the applied voltage, p the atmospheric pressure, C_{t} the total capacitance of the device and w_0 the center deflection of the plate. For the parallel plate $k_0 = k$ and $A_{\mathrm{eff}} = A$.

The total force on the system, F_{t}, is found by differentiating the total potential energy with respect to the center deflection, which is used as a reference in this work (any deflection could be used as a reference)

$$F_{\mathrm{t}} = \frac{\partial U_{\mathrm{t}}}{\partial w_0} = k_0 w_0 - pA_{\mathrm{eff}} - \frac{1}{2} V^2 C_{\mathrm{t}}'(w_0), \tag{30}$$

where $C_{\mathrm{t}}'(w_0)$ denotes the capacitance differentiated with respect to w_0. The stable position of the plate can be found for a given applied voltage as the point where the total force is zero, so solving

$$k_0 w_0 = pA_{\mathrm{eff}} + \frac{1}{2} V^2 C_{\mathrm{t}}'(w_0). \tag{31}$$

The effective spring constant, k_{eff}, can be found as the second derivative of the total potential energy or by differentiating the total force

$$k_{\mathrm{eff}} = \frac{\partial F_{\mathrm{t}}}{\partial w_0} = k_0 - \frac{1}{2} V^2 C_{\mathrm{t}}''(w_0). \tag{32}$$

Pull-in occurs when the effective spring constant is zero and the pull-in voltage V_{PI} can be expressed as

$$V_{\mathrm{PI}} = \frac{2k_0}{C_{\mathrm{t}}''(w_0)}. \tag{33}$$

Inserting the pull-in voltage (33) into the equation for the stable position (31) the pull-in distance can be found by solving the equation

$$k_0 w_0 = pA_{\mathrm{eff}} + \frac{k_0 C_{\mathrm{t}}'(w_0)}{C_{\mathrm{t}}''(w_0)}. \tag{34}$$

This can then be inserted into (33) to obtain the pull-in voltage. Finding pull-in distance and voltage is therefore a question of solving the two equations (31) and (34) for the two variables.

In the following, this analysis is shown for both circular and square plates including the anisotropic effects and for a parallel plate capacitor as well for comparison. Similar analysis has previously been shown by others for circular plates i.e. [2], [8] and is therefore shown here in compact form with focus on the anisotropy of the plate.

A. Capacitance

An important variable in the electrostatic analysis for CMUTs is the capacitance. The capacitance at zero deflection, C_0, of the plate can for both the circular and square plates be divided into two contributions: The capacitance from the vacuum gap $C_0 = \epsilon_0 A/g$ and the capacitance from the insulation oxide between in electrodes $C_{\mathrm{ox}} = \epsilon_0 \epsilon_{\mathrm{ox}} A/t_{\mathrm{ox}}$. A is the area of the plates, g the vacuum gap, ϵ_0 the vacuum permittivity, t_{ox} the thickness of the insulation oxide layer, and ϵ_{ox} the relative permittivity of the oxide. The effect from having both contributions can be collected in an effective gap height

$$g_{\mathrm{eff}} = g + \frac{t_{\mathrm{ox}}}{\epsilon_{\mathrm{ox}}}. \tag{35}$$

The total capacitance at zero deflection can then be written

$$C_{\mathrm{t0}} = \left(\frac{1}{C_0} + \frac{1}{C_{\mathrm{ox}}}\right)^{-1} = \frac{\epsilon_0 A}{g_{\mathrm{eff}}}. \tag{36}$$

Taking the deflection of the plate into account, the total capacitance of the device is

$$C_{\mathrm{t}} = \frac{1}{g_{\mathrm{eff}}} \iint \frac{\epsilon_0}{1 - \eta f(x,y)} \,\mathrm{d}x\,\mathrm{d}y \tag{37}$$

where $\eta = w_0/g_{\mathrm{eff}}$ is the normalized center deflection and $f(x,y)$ is a function describing the shape of the deflection. For circular plates, this function will be (13), for square plates it is (19), and for the parallel plate $f = 1$.

The total capacitance of a parallel plate capacitor is given by

$$C_{\mathrm{t,parallel}} = C_{\mathrm{t0}} \frac{1}{1-\eta}. \tag{38}$$

For the circular plate, the integral can be solved analytically and the total capacitance becomes

$$C_{\mathrm{t,circ}} = C_{\mathrm{t0}} \sqrt{\frac{1}{\eta}}\ \operatorname{arctanh}\sqrt{\eta}. \tag{39}$$

For the square plate, there is no analytical solution. The integration in (37) is performed numerically and is stored using the interpolation function in Wolfram Mathematica 9. The relative error between the interpolation function and the numerical integration is less than 4×10^{-6} and this function can be used like a normal expression for further calculations. The total capacitance can be written

$$C_{\mathrm{t,sq}} = C_{\mathrm{t0}} f_i(\eta). \tag{40}$$

where $f_i(\eta)$ is the interpolation function. Alternatively, a Taylor expansion can be used, however, at least 8 terms is needed to get sufficient accuracy.

Fig. 6 shows the total capacitance normalized to the total capacitance with no deflection, $C_{\mathrm{t}}/C_{\mathrm{t0}}$, versus the relative deflection, η, for all three cases. It is seen that when normalized, the circular and square plates have similar capacitance responses. For example, at a relative deflection of 0.4 the deviation is 1.4% between the square and circular capacitance, whereas using the parallel plate approximation results in a much larger difference as seen in the figure.

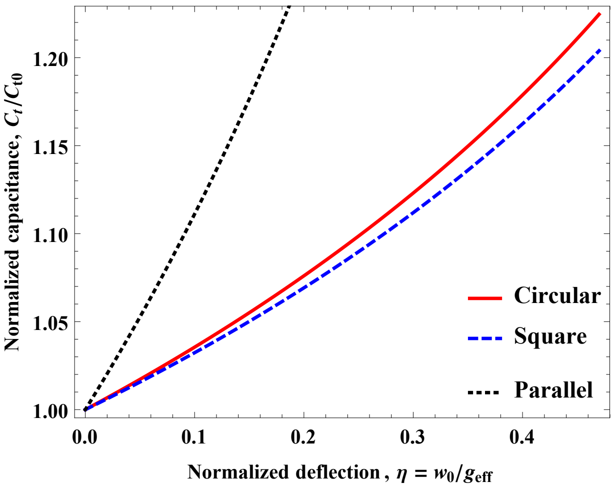

Fig. 6. Normalized total capacitance versus normalized deflection for a circular (39) and a square plate (40). The parallel plate solution (38) shown for comparison.

B. Energy calculations

The total strain energy is calculated by integrating the strain energy density using (6) and (9). Having a thin plate, we can assume plane stress and the expression becomes

$$U_{\mathrm{s}} = \frac{1}{2} \iiint \left(\sigma_1 \varepsilon_1 + \sigma_2 \varepsilon_2 + \sigma_6 \varepsilon_6\right) \mathrm{d}x\,\mathrm{d}y\,\mathrm{d}z, \tag{41}$$

where the strains are given by

$$\epsilon_1 = -z\frac{\partial^2 w(x,y)}{\partial x^2}, \epsilon_2 = -z\frac{\partial^2 w(x,y)}{\partial y^2}, \epsilon_6 = -2z\frac{\partial^2 w(x,y)}{\partial x \partial y}. \tag{42}$$

The energy due to the externally applied pressure is calculated as minus the work performed (i.e. force times length, here pressure times area times length) when deflecting the plate

$$U_{\mathrm{p}} = -\iint p w(x,y)\,\mathrm{d}x\,\mathrm{d}y. \tag{43}$$

The electrostatic energy is expressed through the charge Q or applied voltage V, the vacuum permittivity ϵ_0, gap height g_{eff} and the total capacitance C_{t} of the device

$$\begin{aligned} U_{\mathrm{e}} &= -\frac{1}{2}V^2 C_{\mathrm{t}} \\ &= -\frac{1}{2}V^2 \iint \frac{\epsilon_0}{g_{\mathrm{eff}} - w(x,y)}\,\mathrm{d}x\,\mathrm{d}y \end{aligned} \tag{44}$$

The capacitance inserted during the second equalization in (44) is valid for all plate geometries, if the right expression for the deflection is used in each case. It can be seen how the deflection of the plate appears, and therefore, the plate geometry and the anisotropy of the plate is included through the deflection.

For a circular plate (41), (43) and (44) become

$$\begin{aligned} U_{\mathrm{s,circ}} &= \frac{1}{2}\int_{-h/2}^{h/2}\int_{0}^{2\pi}\int_{0}^{a} r\left(\sigma_1\varepsilon_1+\sigma_2\varepsilon_2+\sigma_6\varepsilon_6\right)\,\mathrm{d}r\,\mathrm{d}\theta\,\mathrm{d}z \\ &= \frac{h^3\pi w_0^2\left(3C_{11}^{\mathrm{eff}}+2C_{12}^{\mathrm{eff}}+3C_{22}^{\mathrm{eff}}+4C_{33}^{\mathrm{eff}}\right)}{9a^2} \end{aligned} \tag{45}$$

$$U_{\mathrm{p,circ}} = -\int_{0}^{a} 2\pi prw dr = -\frac{1}{3}\pi pa^2 w_0 \tag{46}$$

$$U_{\mathrm{e,circ}} = -\frac{1}{2}C_{\mathrm{t}}V^2 = -\frac{1}{2}V^2 C_{\mathrm{t0}}\sqrt{\frac{1}{\eta}}\ \mathrm{arctanh}\sqrt{\eta}. \tag{47}$$

Using (11) it can be seen that the strain energy can be written in terms of the effective flexural rigidity

$$U_{\mathrm{s,circ}} = \frac{h^3\pi w_0^2}{9a^2}\left(3+k_2+3k_4\right)\frac{12D_{\mathrm{a}}}{h^3} = \frac{32\pi D_{\mathrm{eff}}w_0^2}{3a^2} \tag{48}$$

By changing the flexural rigidity, it is possible to easily switch between isotropic and anisotropic calculations in (48).

Comparing (48), (45), and (46) with (29) it can be seen that for the circular plate the general spring constant and the effective area are given by

$$k_{0,\mathrm{circ}} = \frac{2\cdot 32D_{\mathrm{eff}}\pi}{3a^2} = \frac{64D_{\mathrm{eff}}\pi}{3a^2} \tag{49}$$

$$A_{\mathrm{eff,circ}} = \frac{1}{3}\pi a^2. \tag{50}$$

For the square plate, only the most common case with a highly doped plate on silicon (001) substrate aligned to the $\langle 110\rangle$ direction is considered. Using the deflection from (19), the strain energy for the square plate becomes

$$\begin{aligned} U_{\mathrm{s,sq}} &= \frac{1}{2}\int_{-h/2}^{h/2}\int_{-L}^{L}\int_{-L}^{L}\left(\sigma_1\varepsilon_1+\sigma_2\varepsilon_2+\sigma_6\varepsilon_6\right)\,\mathrm{d}x\,\mathrm{d}y\,\mathrm{d}z \\ &= \frac{4096h^3w_0^2}{4729725L^2}\left(\gamma_1C_{11}^{\mathrm{eff}}+2\gamma_2C_{12}^{\mathrm{eff}}+\gamma_1C_{22}^{\mathrm{eff}}+4\gamma_2C_{33}^{\mathrm{eff}}\right), \end{aligned} \tag{51}$$

$$\gamma_1 = \left(1001+468\beta+476\beta^2\right),\quad \gamma_2 = 26\left(11+2\beta^2\right).$$

Using the value for β_{high}, $\gamma_1 = 1138.5$ and $\gamma_2 = 288.9$. Inserting the plate coefficients from (11) into (51), it can be seen that the strain energy can be written in terms of the plate coefficients and the anisotropic flexural rigidity

$$U_{\mathrm{s,sq}} = \frac{49152}{4729725}\left(\gamma_1+\gamma_2k_2+\gamma_1k_4\right)\frac{D_{\mathrm{a}}w_0^2}{L^2}, \tag{52}$$

Using the values from Table II the strain energy for the square plate of silicon (001) aligned to the $\langle 110\rangle$ direction becomes

$$U_{\mathrm{s,sq,Si(001),[110]}} = \xi_{\mathrm{s}}\frac{h^3w_0^2}{L^2}, \tag{53}$$

where the constant is $\xi_{\mathrm{s}} = 385.637$ GPa.

The energy contribution from applied pressure (43) is for this case given by

$$U_{\mathrm{p,sq}} = -\int_{-L}^{L}\int_{-L}^{L} pw(x,y)\ dxdy \tag{54}$$

$$U_{\mathrm{p,sq,Si(001),[110]}} = -\xi_{\mathrm{p}}pL^2w_0. \tag{55}$$

where $\xi_{\mathrm{p}} = 1.215$.

The electrostatic energy can in this square plate case not be found exact as an approximation is needed for the total capacitance. Using the result from (40) this energy contribution can be expressed as

$$U_{\mathrm{e,sq}} = -\frac{1}{2}V^2C_{\mathrm{t0}}f(\eta). \tag{56}$$

Comparing (53) and (55) with (29) it is seen that for the square plate the general spring constant and the effective area are given by

$$k_{0,\mathrm{sq}} = \frac{2\cdot\xi_{\mathrm{s}}h^3}{L^2} = \frac{2h^3\xi_{\mathrm{s}}}{L^2} \tag{57}$$

$$A_{\mathrm{eff,sq}} = \xi_{\mathrm{p}}L^2. \tag{58}$$

C. Stable position

Using the expressions (48)-(47) for the energies and the equation for the stable position (31), the stable position for the circular plate becomes

$$V_{\mathrm{stable,circ}} = \sqrt{\frac{-256g_{\mathrm{eff}}\eta^{3/2}(-a^4p\pi/64+D_{\mathrm{eff}}\pi\eta g_{\mathrm{eff}})(-1+\eta)}{3a^2C_{\mathrm{t0}}\left(-\mathrm{arctanh}\left[\sqrt{\eta}\right]+\eta\ \mathrm{arctanh}\left[\sqrt{\eta}\right]+\sqrt{\eta}\right)}}. \tag{59}$$

A comparison of the stable position found using the anisotropic approach, (59), and measurements on a fabricated device can be found in Section VII.

For the square plate, combining the expressions in (53), (55) and (56), the stable position for the highly doped square plate on silicon (001) substrate aligned to the $\langle 110\rangle$ direction can be found by (31)

$$V_{\mathrm{stable,sq}} = \sqrt{\frac{2g_{\mathrm{eff}}\left(-L^4p\xi_{\mathrm{p}}+2h^3\eta\xi_{\mathrm{s}}g_{\mathrm{eff}}\right)}{C_{\mathrm{t0}}L^2f(\eta)}}. \tag{60}$$

Devices with square plates were also fabricated and a comparison of the stable position found using the anisotropic approaches compared to the measured center deflection can be found in Section VII.

Originally, the CMUT was modelled by use of a parallel plate approximation [4], [5]. The parallel plate case is also included here for comparison and in this case, the stable position is

$$V_{\mathrm{stable,parallel}} = \sqrt{\frac{2(-1+\eta)^2g_{\mathrm{eff}}(-Ap+k\eta g_{\mathrm{eff}})}{C_{\mathrm{t0}}}}. \tag{61}$$

From the static analysis, it is possible to present a set of general design plots for CMUTs by using adequate normalizations. Hereby, the results for circular, square and parallel plates can be compared. For specific device behavior, the equations for zero applied pressure or voltage can be used to eliminate the normalizations. These expressions are derived in section VI-E.

Fig. 7 shows the stable position of the plate for varying bias voltages. The bias voltage is normalized to the pull-in voltage at zero applied pressure $V/V_{\mathrm{PI,p0}}$ and the deflection to the pull-in distance at zero applied pressure $\eta/\eta_{\mathrm{PI,p0}}$. It is seen that the circular and square plate give almost identical results, whereas the parallel plate has a slight deviation. At 80 %

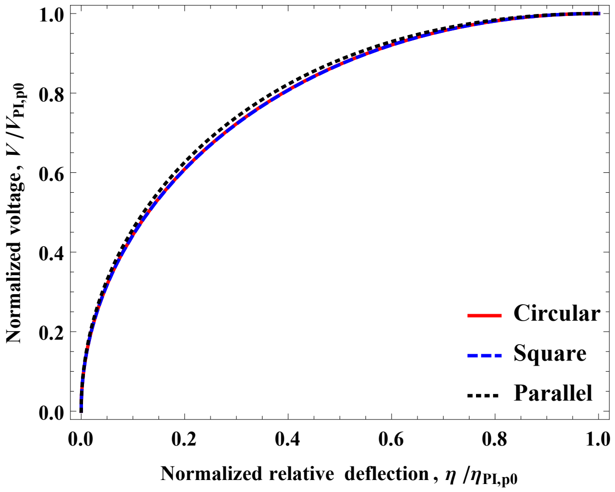

Fig. 7. Stable voltage normalized to pull-in voltage at zero applied pressure versus relative center deflection normalized to the pull-in distance at zero applied pressure for circular (59), square (60) and parallel plates (61).

of pull-in, which is where the CMUT is usually designed to operate, the deviation of the square plate result compared to the circular plate result is only 0.01 %. For the parallel plate the deviation is 0.3 % compared to the circular plate result.

D. Spring constant

As mentioned earlier, the effective spring constant can be found by performing the double differentiation of the total potential energy with respect to center deflection, see (32). The generalized spring constant can be identified from the strain energy for both circular and square plates, (49) and (57), and for the parallel plate the spring constant is simply just k. All these expressions can be inserted into the generalized effective spring constant (32) to obtain the effective spring constant for each plate type. The effect of spring softening is easily seen in (32) as the second term and it is seen to depend on the capacitance. Furthermore, it is seen that the spring constant at zero applied voltage is the generalized spring constant.

In Fig. 8, the effective spring constant relative to the spring constant at zero applied voltage k_{eff}/k_0 is shown versus the normalized relative deflection $\eta/\eta_{\mathrm{PI,p0}}$ (lower axis) or normalized voltage (upper axis). The spring softening effect is clearly seen as the effective spring constant becomes smaller when the deflection and bias voltage increases. Again the circular and square plate behave almost identical and the parallel plate approximation differs from the two. Operating at 80% of pull-in the deviation between square and circular plate results is 0.47% and for the parallel plate it is 12.5%.

In general, it is seen from Figs. 7 and 8 that the overall behaviour of the CMUT is well captured by both the more accurate results for the circular and square plates but also by the parallel plate approximation. The difference lies in the normalizations i.e. the pull-in point calculation which is different for each case when using the actual shape of the deflection. The anisotropic effects are included through these as well. This means that practically the simple expressions can be used to model the CMUTs with good approximations, if using the specific de-normalizations for each plate type.

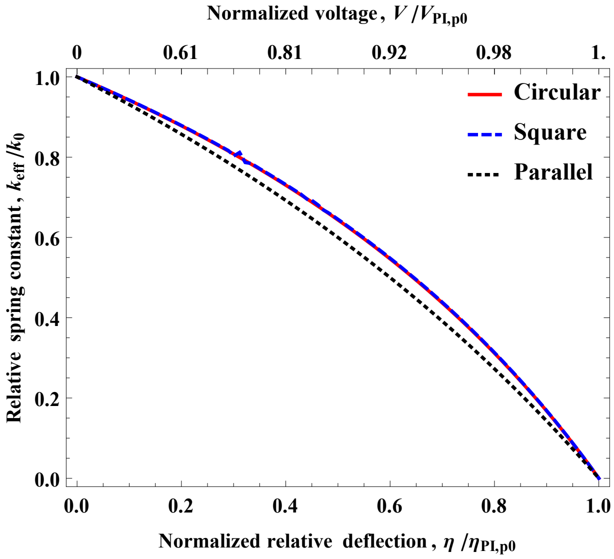

Fig. 8. Normalized effective spring constant versus relative center deflection normalized to the pull-in distance for circular, square and parallel plates.

E. Pull-in

For the parallel plate, the pull-in distance at zero applied pressure is given by $\eta_{\mathrm{PI,p0,parallel}} = 1/3$. The corresponding pull-in voltage is

$$V_{\mathrm{PI,p0,parallel}} = \sqrt{\frac{8kg_{\mathrm{eff}}^2}{27C_{\mathrm{t0}}}}. \tag{62}$$

The pressure dependence on the pull-in distance can be found analytically for this plate type and is given by

$$\eta_{\mathrm{PI,parallel}} = 1/3 + 2/3p_{\mathrm{r}}, \tag{63}$$

where the relative pressure is given by $p_{\mathrm{r}} = pA/(g_{\mathrm{eff}}k)$. The relative pressure is the applied pressure normalized to the pressure it takes to deflect the plate the size of the effective gap, p_{g}. Fig. 9 shows the linear dependence of the pressure on the pull-in distance, (63), as the black dotted curve. The pressure dependent pull-in voltage can for the parallel plate also be calculated analytically and is given by

$$V_{\mathrm{PI,parallel}} = \frac{(-Ap + kg_{\mathrm{eff}})^3}{27C_{\mathrm{t0}}k^2g_{\mathrm{eff}}}. \tag{64}$$

It is seen that the influence of the pressure on the pull-in distance, and thus also the pull-in voltage, is dependent on the geometry of the device. Defining the relative pull-in voltage as $V_{\mathrm{rel}} = V_{\mathrm{PI}}/V_{\mathrm{PI,p0}}$ and using (64) and (62), the relative pull-in voltage for the parallel plate yields

$$V_{\mathrm{rel,parallel}} = (1 - p_{\mathrm{r}})^{(3/2)}. \tag{65}$$

Fig. 10 shows a comparison of the relative voltage versus the relative pressure with a black dotted curve for the parallel plate.

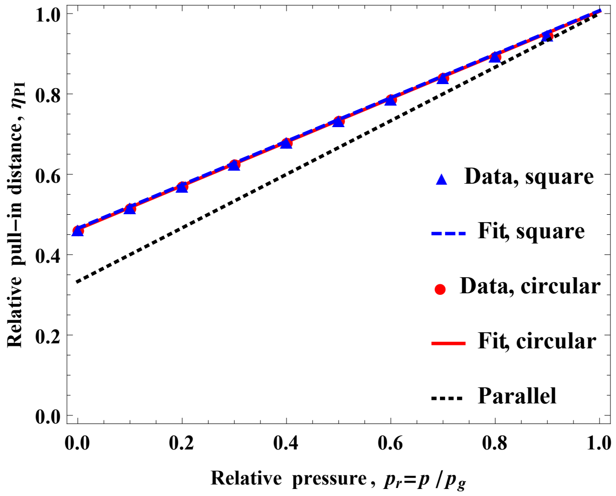

Fig. 9. Pull-in distance versus relative pressure. Circles are the full calculation for circular plates, triangles the full model for square plates, the red solid curve a fit for the circular plate (68), blue dashed curve a fit for the square plate (71) and black dotted the analytical expression for the parallel plate (63).

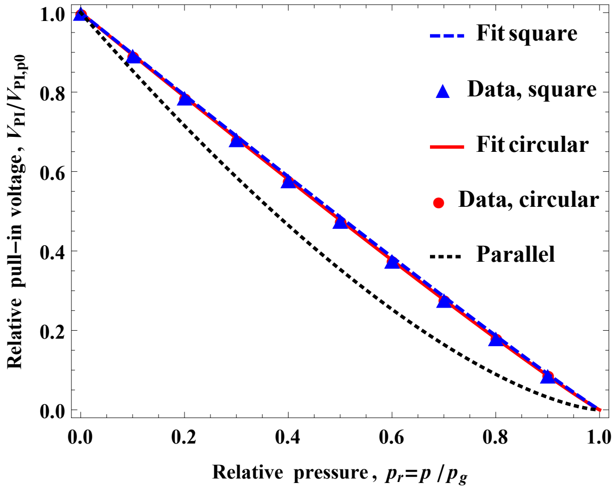

Fig. 10. Pull-in voltage relative to pull-in voltage for zero applied pressure versus relative pressure. Circles are the full calculation for circular plates, triangles the full model for square plates, the red solid curve a fit for the circular plate (69), blue dashed curve a fit for the square plate (72) and black dotted the analytical expression for the parallel plate (65).

Looking at the circular plate and the special case where the applied pressure is zero, the relative pull-in distance becomes $\eta_{\mathrm{PI,p0,circ}} = 0.463$ from (34). With this pull-in distance inserted into (59), the pull in voltage at zero applied pressure for the circular plate becomes

$$V_{\mathrm{PI,p0,circ}} = \sqrt{\frac{89.4459 D_{\mathrm{eff}} g_{\mathrm{eff}}^2}{a^2 C_{\mathrm{t0}}}}. \tag{66}$$

To find the influence of the pressure on the pull-in distance, (34) is evaluated for varying values of the pressure. The result can be seen as red points in Fig. 9. As also observed by [2], [8], the influence of the pressure on the pull-in distance is found to be linear as for the parallel plate. The expression can be found by considering the boundary conditions $\eta_{\mathrm{PI}}(0) = \eta_{\mathrm{PI,p0}}$ and $\eta_{\mathrm{PI}}(1) = 1$. Using these conditions the expression for the pressure dependent relative pull-in distance becomes

$$\eta_{\mathrm{PI}} = \eta_{\mathrm{PI,p0}} + (1 - \eta_{\mathrm{PI,p0}})p_{\mathrm{r}}, \tag{67}$$

where the relative pressure is given by $p_{\mathrm{r}} = p/p_{\mathrm{g}} = pa^4/(64 g_{\mathrm{eff}} D_{\mathrm{eff}})$ for the circular plate. Inserting $\eta_{\mathrm{PI,p0,circ}} = 0.463$ for the circular plate yields

$$\eta_{\mathrm{PI,circ}} = 0.463 + 0.537 p_{\mathrm{r}}. \tag{68}$$

Eqn. (68) is plotted as the red solid curve in Fig. 9. The maximum deviation between the expression and the data points is 0.6 %. Compared to the parallel plate solution the difference in pull-in distance at zero applied pressure is clearly observed. Furthermore, note that (67) also applies for the parallel plate as seen in (63).

To see how the pressure affects the pull-in voltage for the circular plate the relative pull-in voltage is again considered. For simplicity, the equation for the pressure dependent pull-in voltage is not shown, but it is found from the pull-in distance, (68), inserted into the stable position, (59). The resulting equation is evaluated for varying values of pressure and this is shown as red dots in Fig. 10. It is seen that the pull-in voltage decreases for increasing external pressure as expected, since the plate is deflected due to the applied pressure. To follow the analytical expression obtained for the parallel plate, a fit was made to an expression having the same form as this analytical result $V_{\mathrm{rel}} = (1 - p_{\mathrm{r}})^{(K \cdot 3/2)}$, where K is the fitted parameter. The result from fitting is

$$V_{\mathrm{rel,circ}} = (1 - p_{\mathrm{r}})^{(0.710 \cdot 3/2)}, \tag{69}$$

Using this fit a maximum deviation of only 3.9 % is obtained. Also for the pull-in voltage, a difference is observed between the the parallel and circular plate.

To expand this pull-in investigation to square plates as well, the same procedure as for the circular plates is followed. For the square case, the pull-in distance in the special case of zero applied pressure becomes $\eta_{\mathrm{PI,p0,sq}} = 0.466$ which is very close to the circular plate pull-in distance. The corresponding pull-in voltage is

$$V_{\mathrm{PI,p0,sq}} = \sqrt{\frac{2.95118 g_{\mathrm{eff}}^2 h^3 \xi_{\mathrm{s}}}{C_{\mathrm{t0}} L^2}}. \tag{70}$$

To find the influence of the pressure on the pull-in distance for the square plate it was calculated for different pressures and plotted as triangular points in Fig. 9. A linear fit to the data points are shown as a dashed blue line. As for the two other plate geometries, the influence of the pressure on the pull-in distance is found to be linear and using (67) it can be described as

$$\eta_{\mathrm{PI,sq}} = 0.466 + 0.534 p_{\mathrm{r}}, \tag{71}$$

where the relative pressure for the square plate is given by $p_{\mathrm{r}} = 0.021961 pL^4/(g_{\mathrm{eff}} D_{\mathrm{a}})$. The maximum deviation between the fit and the data points for the square plate is 0.7%.

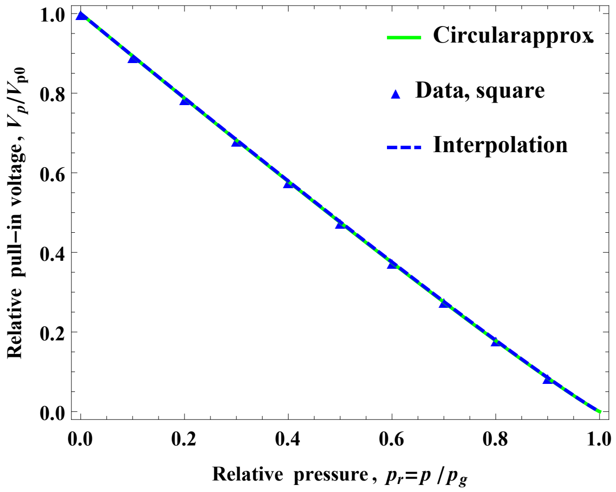

Fig. 11. Pull-in voltage relative to pull-in voltage for zero applied pressure versus relative pressure for a square plate using the interpolating function (blue, dashed) and an approximation of the capacitance using the circular expression (green, solid). The triangles are the original data points calculated from the full solution.

In Fig. 10 it is seen how the pressure affects the pull-in voltage for the square plate shown as triangular points and a fit with a dashed blue line. The calculation method is the same as for the circular plate, and the same behavior is also observed. A fit of the data points to an expression of the same form as for the parallel plate case yields

$$V_{\mathrm{rel,sq}} = (1 - p_{\mathrm{r}})^{(0.712 \cdot 3/2)}, \tag{72}$$

resulting in a maximum deviation of 1.7%.

As it can be difficult for others to use the interpolation function in (40), and since the results for a circular and square plate are close to each other, the expression for the total capacitance of the circular plate (37) can be used for the square plate instead of the interpolation function due to the similarity of the results. If the same pull-in analysis is carried out, the same pull-in distance is obtained and the result for the relative pull-in voltage versus relative pressure can be seen in Fig. 11. The data points show the result using the interpolation function. The fit to the expression in (65) when using the circular capacitance is shown together with the previous fit for the square plate using the interpolating function. The fit of the data points in this approximation case case yields

$$V_{\mathrm{rel,sq}} = (1 - p_{\mathrm{r}})^{(0.715 \cdot 3/2)}, \tag{73}$$

The two curves look the same and the maximum deviation from the data points is only 1.6 %. The deviation is highest for higher relative pressure and realistic values for CMUTs would be in the lower end. The relative pressure for the fabricated square device, see Table V, is 0.02 which gives a deviation of only 0.01 % when using the circular plate capacitance.

VII. MEASUREMENTS

To compare the anisotropic approach for modeling CMUTs to measurements for further validation of the theory for both circular and square plates, devices with both plate types were fabricated using a fusion bonding method [24]. The dimensions of the devices can be seen in Table V.

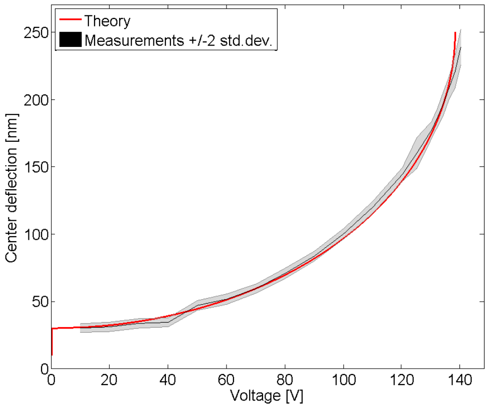

Fig. 12. Measured center deflection for increasing bias voltage together with theoretical curves for a circular plate (59).

Measurements of the stable position (presented as the deflection in the center of the plate) for increasing bias voltage were performed on the fabricated devices. The deflections were measured as area scans with a Sensofar PLu Neox 3D Optical Profiler using white light interferometry.

Fig. 12 shows the measurements of the circular plate device. It is seen how the center deflection varies with the applied voltage and how it deflects more when approaching the pull-in voltage as expected. The center deflection for the measurements is found as the average of 10 cells and gray shaded areas corresponds to plus/minus two standard deviations. For the circular device there was some uncertainty in the final gap height due to the fabrication method. Because of this it was not possible to plot the theoretical stable position for a circular plate, (59), together with the measurements. Instead a fit was made which is shown as the theoretical curve in Fig. 12. From the fit a gap height of 457 nm was found and it is seen that the expression captures the behavior of the device very well. With this gap, the theoretical curve is within the uncertainty interval of the measurements. Also, the pull-in voltage is in good agreement with the experimentally found value, as it was measured to be 140 V, compared to an expected value of 138 V from the anisotropic model (69).

Measurements with a DC voltage applied were also performed for the square plate and the results are shown in Fig. 13. The center deflection for the measurements is found as the average of 10 cells and the gray shaded areas correspond to plus/minus two standard deviations. The theoretical curve is made from the stable position analysis and is for this case plotted directly as the gap height was known from this fabrication run. It is seen that the anisotropic theory matches well with the measurement as it is within the error margin. Also, the pull-in voltages are in good agreement as it was measured to be 206 V, compared to an expected value of 201 V from the anisotropic model (72).

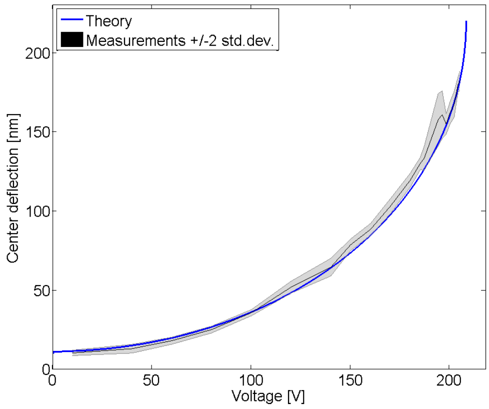

Fig. 13. Measured center deflection for increasing bias voltage together with theoretical curves for a square plate (60).

VIII. CONCLUSION

In this paper it was demonstrated how wafer bonded CMUTs with both circular and square plates can be analytically modelled using the full anisotropic properties of single crystalline silicon. For the circular plate an exact solution to the plate equation was obtained and for the square plate, the full anisotropic plate equation was solved using the Galerkin method. In this case, it is seen that the deflection simplifies by utilizing the symmetry of the silicon crystal and a compact solution is obtained for square CMUT plates on a (001) silicon substrate aligned to the [110] direction. Using this approach, the analytic plate deflections show excellent correspondence with FEM calculations and measurements. Using isotropic plate theory to calculate the deflection of anisotropic silicon plates results in deviations from FEM or measurements of up to 10 %. Using the anisotropic theory reduces the deviation from FEM to less than 0.3 % for the circular plate and 0.1 % for the square plate. Fitting the anisotropic calculated deflection for the square plate to the measurement, a deviation of only 0.07 % is observed for the fitted plate parameter. The theory of multilayer plates is also applied to CMUTs, however, only a small difference will be obtained in the deflection for the typical CMUT case.

A full electrostatic analysis including the anisotropic effects was carried out for both circular, square, and parallel plate devices. The analysis is based on energy considerations and capacitance, effective spring constant, stable position, pull-in distance, and pull-in voltage are all calculated. In the pull-in analysis the pressure dependence is also included. The circular and square plate devices are seen to behave very similar with a difference of 0.01% for stable position and 0.47% for effective spring constant at 80% of pull-in. Using the parallel plate approximation will results in deviations of 0.3% and 12.5%, respectively, at 80% of pull-in. The pressure dependence is expressed through linear fits for the pull-in distance with a maximum deviation of only 0.6% for the circular plate and 0.7% for the square plate. The pressure dependent pull-in voltage was seen to follow an exponentiation expression with maximum deviations of 3.9% and 1.7% for the circular and square plate, respectively. Using the capacitance function of the circular plate for the square plate the maximum deviation is 1.6%.

Devices with both circular and square plates were fabricated and the stable position and pull-in voltage measured. Comparing this to to the anisotropic theory, it is seen that the theory is within the uncertainty interval of the measurements in both cases.

ACKNOWLEDGEMENT

This work was financially supported by the Danish National Advanced Technology Foundation through grants 024-2008-3 and 82-2012-4.

REFERENCES

[1] P. C. Eccardt, P. Wagner, and S. Hansen, “Analytical models for micromachined transducers - an overview,” in *IEEE Ultrasonics Symposium, 2006*, 2006, pp. 572–581.

[2] I. O. Wygant, M. Kupnik, and B. T. Khuri-Yakub, “Analytically calculating membrane displacement and the equivalent circuit model of a circular CMUT cell,” in *IEEE Ultrasonics Symposium, 2008. IUS 2008*. IEEE, Nov. 2008, pp. 2111–2114.

[3] Y. Huang, A. Ergun, E. Haeggstrom, M. Badi, and B. Khuri-Yakub, “Fabricating capacitive micromachined ultrasonic transducers with wafer-bonding technology,” *Journal of Microelectromechanical Systems*, vol. 12, no. 2, pp. 128 – 137, Apr. 2003.

[4] I. Ladabaum, X. Jin, H. T. Soh, A. Atalar, and B. t. Khuri-Yakub, “Surface micromachined capacitive ultrasonic transducers,” *IEEE Transactions on Ultrasonics, Ferroelectrics and Frequency Control*, vol. 45, no. 3, pp. 678–690, May 1998.

[5] A. Caronti, G. Caliano, A. Iula, and M. Pappalardo, “An accurate model for capacitive micromachined ultrasonic transducers,” *IEEE Transactions on Ultrasonics, Ferroelectrics and Frequency Control*, vol. 49, no. 2, pp. 159–168, Feb. 2002.

[6] A. Lohfink and P.-C. Eccardt, “Linear and nonlinear equivalent circuit modeling of CMUTs,” *IEEE Transactions on Ultrasonics, Ferroelectrics and Frequency Control*, vol. 52, no. 12, pp. 2163 –2172, Dec. 2005.

[7] A. Nikoozadeh, B. Bayram, G. Yaralioglu, and B. Khuri-Yakub, “Analytical calculation of collapse voltage of CMUT membrane [capacitive micromachined ultrasonic transducers],” in *2004 IEEE Ultrasonics Symposium*, vol. 1, 2004, pp. 256–259 Vol.1.

[8] H. Koymen, A. Atalar, E. Aydogdu, C. Kocabas, H. Oguz, S. Olcum, A. Ozgurluk, and A. Unlugedik, “An improved lumped element nonlinear circuit model for a circular CMUT cell,” *IEEE transactions on ultrasonics, ferroelectrics, and frequency control*, vol. 59, no. 8, pp. 1791–1799, Aug. 2012, PMID: 22899125. [Online]. Available: http://www.ncbi.nlm.nih.gov/pubmed/22899125

[9] B. Ahmad and R. Pratap, “Elasto-electrostatic analysis of circular microplates used in capacitive micromachined ultrasonic transducers,” *IEEE Sensors Journal*, vol. 10, no. 11, pp. 1767–1773, 2010.

[10] S. Timoshenko and S. Woinowsky-Krieger, *Theory of Plates and Shells,*, 2nd ed. Mcgraw-Hill College, Jun. 1959.

[11] R. L. Taylor and S. Govindjee, “Solution of clamped rectangular plate problems,” *Communications in Numerical Methods in Engineering*, vol. 20, no. 10, p. 757765, 2004. [Online]. Available: http://onlinelibrary.wiley.com/doi/10.1002/cnm.652/abstract

[12] M. Rahman, J. Hernandez, and S. Chowdhury, “An improved analytical method to design CMUTs with square diaphragms,” *Ieee Transactions on Ultrasonics Ferroelectrics and Frequency Control*, vol. 60, no. 4, pp. 834–845, Apr. 2013, WOS:000317010200020.

[13] G. G. Yaralioglu, B. Bayram, A. Nikoozadeh, and B. T. P. Khuri-Yakub, “Finite element modeling of capacitive micromachined ultrasonic transducers,” vol. 5750, 2005, pp. 77–86. [Online]. Available: http://dx.doi.org/10.1117/12.595619

[14] M. F. la Cour, T. L. Christiansen, J. A. Jensen, and E. V. Thomsen, “Modelling of CMUTs with anisotropic plates,” *Proceedings of IEEE International Ultrasonics Symposium*, 2012.

[15] M. F. la Cour, T. L. Christiansen, C. Dahl-Petersen, K. Reck, O. Hansen, J. A. Jensen, and E. V. Thomsen, "Modeling and measurements of CMUTs with square anisotropic plates," *Proceedings of the 2013 IEEE International Ultrasonics Symposium*, 2013.

[16] E. Ventsel and T. Krauthammer, *Thin Plates and Shells: Theory: Analysis, and Applications*. Taylor & Francis, Aug. 2001.

[17] K. S. Pister and S. B. Dong, "Elastic bending of layered plates," *Journal of the Engineering Mechanics Division*, vol. 85, no. 4, pp. 1–10, Oct. 1959. [Online]. Available: http://cedb.asce.org/cgi/WWWdisplay.cgi?11861

[18] S. B. Dong, Pister, K. S., and Taylor, R. L., "On the theory of laminated anisotropic shells and plates," *Journal of the Aerospace Sciences*, vol. 29, no. 8, pp. 969–975, Aug. 1962. [Online]. Available: http://arc.aiaa.org/doi/pdf/10.2514/8.9668

[19] R. E. Newnham, *Properties of Materials: Anisotropy, Symmetry, Structure*. Oxford University Press, USA, Jan. 2005.

[20] E. V. Thomsen, K. Reck, G. Skands, C. Bertelsen, and O. Hansen, "Silicon as an anisotropic mechanical material: Deflection of thin crystalline plates," submitted to Sensors and Actuators.

[21] J. J. Hall, "Electronic effects in the elastic constants of n-type silicon," *Physical Review*, vol. 161, no. 3, pp. 756–761, Sep. 1967. [Online]. Available: http://link.aps.org/doi/10.1103/PhysRev.161.756

[22] S. Holgate, "The transverse flexure of perforated aeolotropic plates," *Proceedings of the Royal Society A: Mathematical, Physical and Engineering Sciences*, vol. 185, no. 1000, pp. 50–69, Jan. 1946. [Online]. Available: http://adsabs.harvard.edu/abs/1946RSPSA.185...50H

[23] F. Mbakogu and M. Pavlovi, "Bending of clamped orthotropic rectangular plates: a variational symbolic solution," *Computers & Structures*, vol. 77, no. 2, pp. 117–128, Jun. 2000. [Online]. Available: http://www.sciencedirect.com/science/article/pii/S0045794999002175

[24] T. Christiansen, O. Hansen, M. Dahl Johnsen, J. Lohse, J. Jensen, and E. Thomsen, *Void-Free Direct Bonding of CMUT Arrays with Single Crystalline Plates and Pull- In Insulation*. IEEE, 2013, pp. 1737–1740.

APPENDIX F

Paper - Investigation of PDMS as coating on CMUTs for imaging

In Conference proceedings of the International Ultrasonics Symposium, Chicago, September 2014.

Investigation of PDMS as coating on CMUTs for imaging

Mette Funding la Cour*†, Matthias Bo Stuart*, Mads Bjerregaard Laursen†,
Søren Elmin Diederichsen†, Erik Vilain Thomsen† and Jørgen Arendt Jensen*
*Center for Fast Ultrasound Imaging, Department of Electrical Engineering, Technical University of Denmark,
DK-2800 Kgs. Lyngby, Denmark
†Department of Micro and Nanotechnology, Technical University of Denmark, DK-2800 Kgs. Lyngby, Denmark

***Abstract*—A protective layer is necessary for Capacitive Micromachined Ultrasonic Transducers (CMUTs) to be used for imaging purpose. The layer should both protect the device itself and the patient while maintaining the performance of the device. In this work Sylgard 170 PDMS is tested as coating material for CMUTs through comparison of transmit pressure and receive sensitivity in immersion of coated and uncoated elements. It is seen that the transmitted pressure decreases with 27% and the receive sensitivity decreases 35 % when applying the coating using a dam and fill principle. This matches well with the estimated value of 31 %. With the coating, the center frequency was found to be decreased from 4.5 MHz to 4.1 MHz and the fractional bandwidth was increased from 77 % to 84 % in transmit. In receive the center frequency was found to decrease from 4.4 MHz to 3.9 MHz and the fractional bandwidth was decreased from 108 % to 92 %, when applying the PDMS coating.**

I. INTRODUCTION

Coating of Capacitive Micromachined Ultrasonic Transducers (CMUTs) is important for insulation between the surface of the elements and the patient, when applying the high voltages required for operating CMUTs. Furthermore it also protects the surface of the device against environmental factors and e.g. degradation of the electrodes [1].

A possible coating material should have good acoustical properties such that the impedance matches with the medium for high energy transfer and a glass transition temperature below room temperature providing a low static Young's modulus for preserving the CMUT's pull-in voltage [2]. Furthermore, the coating needs to be biocompatible. Polydimethylsiloxane (PDMS), Sylgard 170, is chosen as coating material in this work since it fulfills these requirements. Its acoustical properties match well with water and tissue (acoustical impedance 1.5 MRayls for water, 1.63 MRayls for tissue and 1.37 MRayls for Sylgard 170).

Other coating materials have previously been investigated e.g. Parylene C [1], [3], which gives good results and has the advantage of being cleanroom compatible, but is deposited using Vapor Deposition Polymerization (VDP). Silicon nitride has also been proposed due to cleanroom compatibility, however, the stress in the nitride highly affects the device performance [4]. Different types of PDMS have also been investigated, and it is seen that some will increase the output signal, due to increased mass loading, and others will decrease the influence of the echo from the coating-water interface, due to better impedance matching [2], [3]. Many of the experiments regarding coating have been conducted in air using a vibrometer, and thus need further testing to check the influence on performance for imaging.

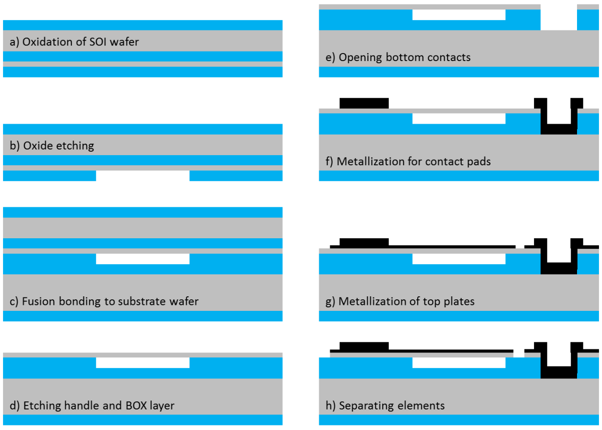

Fig. 1. Process steps for fabricating 1D arrays using fusion bonding and oxidation of both SOI and substrate wafer. Both top and bottom electrode can be contacted from the front side of the device.

The objective for this work is to investigate how the Sylgard 170 PDMS coating affects the CMUT performance through comparison of the transmit pressure and receive sensitivity for devices with and without coating.

II. TRANSDUCER FABRICATION

To test whether the Sylgard 170 PDMS is a suitable coating material for CMUTs, 128 element 1D arrays were fabricated with a fusion bonding process. The overall process flow can be seen in Fig. 1. This process is developed to minimize the number of process steps, while avoiding bumps at the corners [5]. Bumps on the oxide surface often arise from having two oxidations of the substrate wafer to form cavities and an insulation layer separately. However, the bumps can ruin the fusion bonding quality and the double oxidation method then requires an extra etching step to etch back the bumps. The first step is to oxidize the silicon-on-insulator (SOI) wafer and etch cavities in the oxide. An oxidation is performed on the substrate wafer as well to obtain an insulation layer in the bottom of the cavities. Fusion bonding is performed and followed by high temperature annealing. The handle layer and buried oxide layer are etched away before opening up to the bottom electrode. A thick aluminum layer (800 μm) is deposited for bonding pads

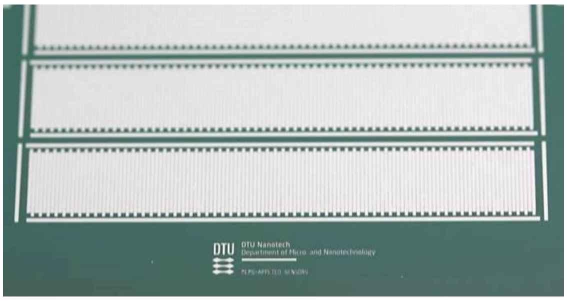

Fig. 2. Photo of fabricated 1D CMUT arrays after end of fabrication. The arrays have 128 elements and are designed to operate at 5 MHz.

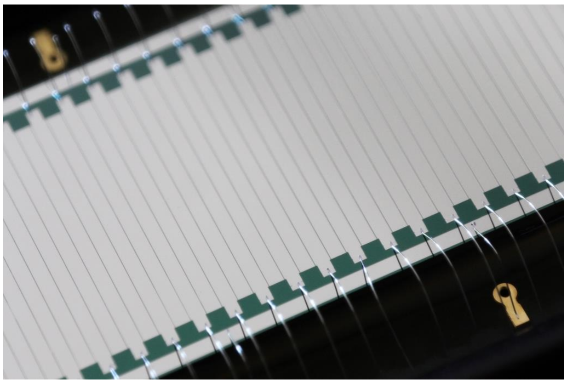

Fig. 3. Photo of finished 1D array mounted on and wirebonded to a PCB. The elements are seen as the vertical metal lines where every second has a contact pad to the same side of the array. The bottom contact is seen as a metal bar along the array.

and a thin aluminum layer (200 μm) is deposited to completely cover the top electrodes. The top plates and elements are defined by etching aluminum and silicon. A picture of a finished array can be seen in Fig. 2. The elements have contact pads at the ends and the bottom contact for reaching the substrate is running along the length of the array. Fig. 3 shows a microscope picture of an array, where the elements can be seen as vertical lines, and every second element has contact pads to the same side. The thicker aluminum layer at the pads improves the wirebonding.

The arrays are aimed at an immersion resonant frequency of 5 MHz. They are linear arrays with a λ pitch i.e. 300 μm. Each element consists of 460 square shaped cells with a side length of 49 μm and is 5 mm long.

III. DEVICE COATING AND MEASUREMENT SETUP

There are several ways to apply a coating to a transducer: mold-transfer [2], spray coating, VDP [1], [3], and spin coating [3]. For CMUTs insulating layers are usually applied using mold-transfer to integrate a lens at the same time. However, a lens should not be applied for this application as the uncoated devices used for comparison will not be focused. Spray and spin coating are better for wafer scale coating, so instead an alternative method was used. This method will now be described in detail.

To test the PDMS coating, one of the fabricated arrays was mounted on a printed circuit board (PCB) and wirebonded. The wirebonds are covered by a protective glob top (CHIPCOAT G8345D) and this is used as a dam when applying the PDMS coating. The dam is filled with liquid PDMS and then cured in vacuum. The procedure for this PDMS coating is

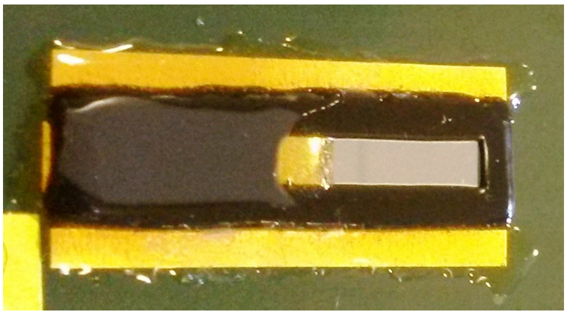

Fig. 4. CMUT array mounted on a PCB with PDMS coating applied to half of the array using the glob top and an epoxy as a dam.

- Mix the two components of Sylgard 170 and de-gas in a vacuum chamber for 20 min
- Apply to device using a syringe with a needle tip by dripping the PDMS onto the surface at a close distance
- De-gas the coated array in a vacuum chamber for 60 min
- Cure in a 70°C oven for at least 1 hour

The height of the glob top dam and thus also the thickness of the coating is estimated to be ~ 900 μm. Coating thickness have been investigated by Lin et al. [2], who found that the main signal is not affected by the thickness. However, if the coating is thin, the echo from the coating-liquid interface will influence the spectrum. According to their results, this should not be a problem with this thickness of coating.

For this particular experiment of coating evaluation, it was desired to have the coated and uncoated elements as similar to each other as possible. Therefore, half of an array was coated using the described method and the other half was left without coating. A picture of the half coated device can be seen in Fig. 4.

For evaluating the transducers with and without coating, a flexible platform developed for testing different CMUTs was used. The layout of the setup can be seen in Fig. 5, where the transducer is mounted on and wirebonded to PCB1. This PCB is clicked onto another PCB containing all the electronics for operating the CMUT, and this second PCB can be reused for other devices. A transducers cable for a BK Medical scanner is also attached to PCB2, so the transducer can be connected to an imaging system. A picture of the setup can be seen in Fig. 6.

IV. MEASUREMENTS AND DISCUSSION

The measurements are performed with the experimental Synthetic Aperture Real-time Ultrasound System (SARUS) [6]. All measurements are performed in oil for electrical insulation of the uncoated part of the device. Acoustical

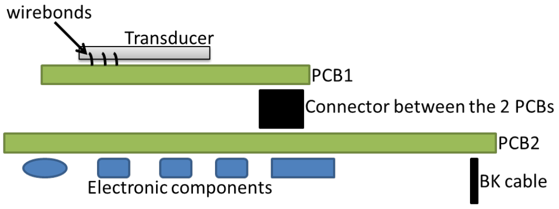

Fig. 5. Sketch of principle of transducer evaluation platform for testing various CMUT designs and chips. The CMUT is wirebonded to a PCB, which is connected to a second PCB with a transducer cable attached.

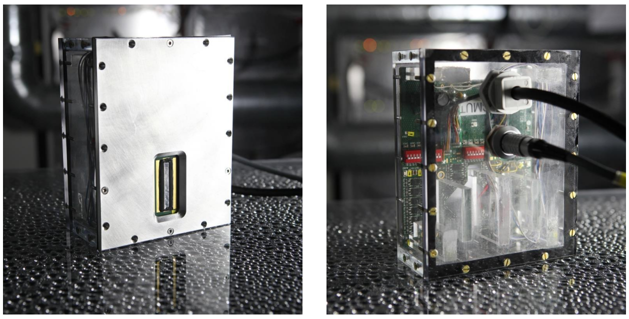

(a) *Frontside.* (b) *Backside.*

Fig. 6. Flexible transducer evaluation platform developed to test multiple CMUT designs and devices. The front side is open to the CMUT and on the backside the transducer cable and a separate DC supply cable can be seen.

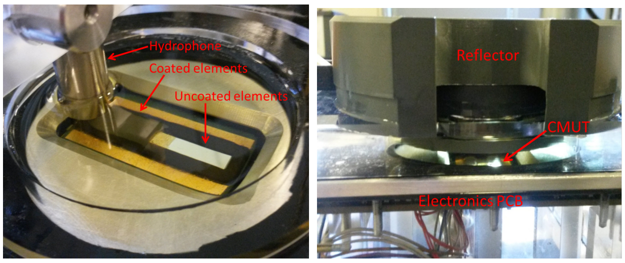

(a) *Hydrophone setup.* (b) *Plane reflector setup.*

Fig. 7. Measurement setup using hydrophone and plane reflector in front of the CMUT mounted in the box with electronics.

measurements are made to obtain the transmitted pressure and the receive sensitivity for the two halves of the device. Ten working elements are chosen on each half of the array for the experiments. For all measurements the transducer elements are biased at 190 V, which is 80 % of the calculated pull-in voltage. The AC transmit signal is ±60 V.

A. Transmit pressure

A hydrophone (Optel 5 MHz, Optel, Wroclaw, Poland) placed 10 mm from the transducer surface is used to measure the transmit pressure, as seen in Fig. 7a. Ten different white, Gaussian random signals are used for the excitation. The RMS of the sampled signals is calculated and averaging is done over the 10 random signals. The hydrophone is aligned to the center of all elements when measuring across the array. The values are an average of 10 working elements with or without coating applied. For the transmitted pressure it was found that the array with coating has an output signal of 27% less than the array without coating.

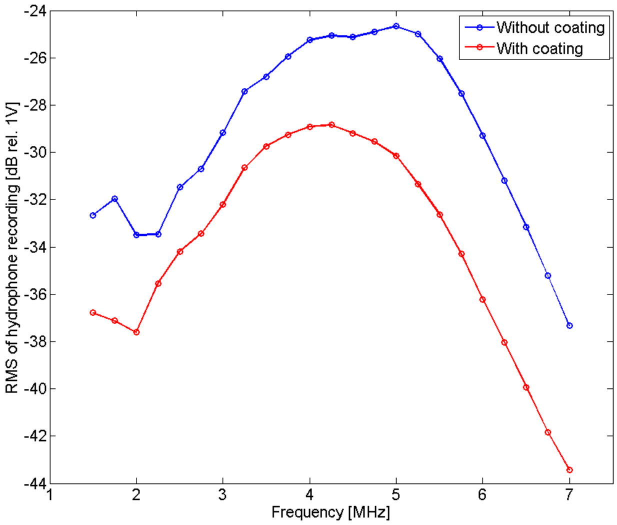

Fig. 8. Transfer function in transmit for elements with and without coating found as a mean of 10 elements of each kind. An 8 pulse, narrowband excitation is used for each frequency.

The attenuation in PDMS can be described as [2]

$$L_{\mathrm{dB}} = \alpha f^{\beta} w \text{ or } \frac{V(w)}{V_0} = 10^{\left(-\frac{\alpha f^{\beta} w}{20}\right)}, \qquad (1)$$

where I_0 is the original intensity, α the attenuation loss factor (given in dB/MHz/mm), f the frequency, β an empirically found parameter and w the thickness of the coating. For the Sylgard 170 PDMS, $\alpha = 0.37$ dB/MHz/mm and $\beta = 1.4$. Using a frequency of 5 MHz and the estimated coating thickness of 0.9 mm, the expected drop in signal amplitude is 31 %, which is comparable to the measured signal loss with a difference of ±13 % respectively for transmit and receive. The differences could arise from the estimation of coating thickness.

Hydrophone measurements were also performed for varying frequencies. A narrowband, 8 period, excitation was used at each frequency. The frequency sweep was made from 1.5 MHz to 7 MHz in steps of 250 kHz. The hydrophone was placed at the center of each element at a distance of 10 mm and the average results for 10 elements with and without coating can be seen in Fig. 8. From this the mean center frequency is found to be 4.5 MHz for the elements without coating and 4.1 MHz for the elements with coating. The coating results in a decrease in center frequency of around 9 %, which is due to the added mass on the plate. Similarly the fractional bandwidth is found to be 77 % for the array without coating and 84 % with the coating. Thus, the PDMS coating slightly increases, 9 %, the fractional bandwidth when transmitting pressure, which is explained by the increased dampening of the plate. It is also seen that applying this coating with a thickness of 0.9 mm results in a loss in signal of around 3.8 dB at the center frequency.

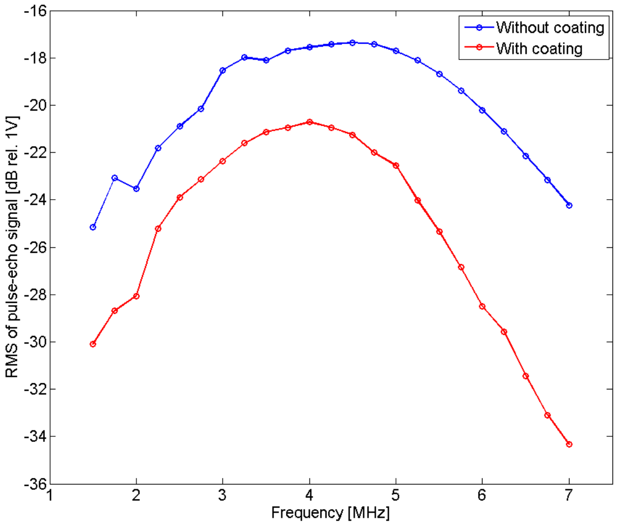

Fig. 9. Transfer function in receive for elements with and without coating found as a mean of 10 elements of each kind. An 8 pulse, narrowband excitation is used for each frequency.

B. Receive sensitivity

To measure receive sensitivity a plane reflector of 40 mm PVC (Polyvinylchloride) was placed at a distance of 10 mm from the transducer surface as seen in Fig. 7b. Again ten different white, Gaussian random signals are used for the excitation and the RMS of the sampled signal is calculated. Averaging is done over the 10 random signals.

The results from the receive analysis showed a decrease of 35 % for the coated elements compared to the uncoated which matches well with the expected value found from (1). The receive sensitivity is found by dividing the measured pulse-echo signal with the measured transmit pressure for the same element to take into account that the coated elements also transmit less pressure than the elements without coating.

A pulse-echo analysis to find the transfer function using a plane reflector was also carried out. The same method as for the transmit analysis was used and a narrowband, 8 period excitation applied. Again, a frequency sweep was made from 1.5 MHz to 7 MHz in steps of 250 kHz, and the average result for 10 elements of each kind can be seen in Fig. 9. This shows the pulse-echo frequency characteristic. It is seen that the loss in signal is around 3.4 dB. The -6 dB center frequency and fractional bandwidth were found again from the normalized pulse-echo signal. This resulted in the center frequency being 4.4 MHz and 3.9 MHz for the elements without and with coating, respectively. This means a decrease of 11 %. The measured fractional bandwidths were found to be 108 % and 92 %, respectively, resulting in a decrease of 15 %. Again, the coating decreases the center frequency due to the added mass and the fractional bandwidth is decreased as well, which can also be ascribed to the added mass.

The results from the frequency sweep measurements for both transmit and receive are summarized in Table I.

Table I. RESULTS FOR CENTER FREQUENCY AND FRACTIONAL BANDWIDTH FROM HYDROPHONE AND PLANE REFLECTOR MEASUREMENTS OF 10 ELEMENTS WITH AND 10 ELEMENTS WITHOUT COATING.

Measurement	Without coating	With coating	Difference
Center frequency, transmit	4.5 MHz	4.1 MHz	-9 %
Fractional bandwidth, transmit	77 %	84 %	+9 %
Center frequency, receive	4.4 MHz	3.9 MHz	-11 %
Fractional bandwidth, receive	108 %	92 %	-15 %

V. CONCLUSION

The initial measurements performed on the two devices show that the 0.9 mm thick Sylgard 170 PDMS coating decrease the performance of the CMUT array around 30 % regarding transmitted pressure and receive sensitivity. In both transmit and pulse-echo measurements the transfer function was found by sweeping the frequency and a decrease of the center frequency of 9-11 % was found. The fractional bandwidth was found to increase by 9 % in transmit and decrease by 15 % in receive. The losses in dB was found to be around 3.8 dB in transmit and 3.4 dB in pulse-echo. In conclusion, some effects are always expected from a coating due to the loss in the material and with the measured influence of the Sylgard 170 PDMS, this is a good option for coating of CMUTs.

ACKNOWLEDGEMENT

This work was financially supported by the Danish National Advanced Technology Foundation (024-2008-3) and (82-2012-4).

REFERENCES

[1] E. Jeanne, C. Meynier, J. Terry, M. Roy, L. Haworth, and D. Alquier, “Evaluation of parylene as protection layer for capacitive micromachined ultrasonic transducers,” *ECS Transactions*, vol. 11, no. 16, pp. 25–33, Mar. 2008.

[2] D.-S. Lin, X. Zhuang, S. H. Wong, M. Kupnik, and B. T. Khuri-Yakub, “Encapsulation of capacitive micromachined ultrasonic transducers using viscoelastic polymer,” *Journal of microelectromechanical systems : a joint IEEE and ASME publication on microstructures, microactuators, microsensors, and microsystems*, vol. 19, no. 6, pp. 1341–1351, Dec. 2010.

[3] X. Zhuang, A. Nikoozadeh, M. A. Beasley, G. G. Yaralioglu, B. T. Khuri-Yakub, and B. L. Pruitt, “Biocompatible coatings for CMUTs in a harsh, aqueous environment,” *Journal of Micromechanics and Microengineering*, vol. 17, no. 5, p. 994, May 2007.

[4] E. Jeanne, C. Meynier, F. Teston, D. Certon, N. Felix, M. Roy, and D. Alquier, “Protection layer influence on capacitive micromachined ultrasonic transducers performance,” *MRS Online Proceedings Library*, vol. 1052, 2007.

[5] T. L. Christiansen, O. Hansen, M. D. Johnsen, J. N. Lohse, J. A. Jensen, and E. V. Thomsen, “Void-free direct bonding of CMUT arrays with single crystalline plates and pull-in insulation,” in *Ultrasonics Symposium (IUS), 2013 IEEE International*, Jul. 2013, pp. 1737–1740.

[6] J. A. Jensen, H. Holten-Lund, R. T. Nilsson, M. Hansen, U. D. Larsen, R. P. Domsten, B. G. Tomov, M. B. Stuart, S. I. Nikolov, M. J. Pihl, Y. Du, J. H. Rasmussen, and M. F. Rasmussen, “SARUS: A synthetic aperture real-time ultrasound system,” *IEEE Transactions on Ultrasonics, Ferroelectrics, and Frequency Control*, vol. 60, no. 9, pp. 1838–1852, Sep. 2013.

APPENDIX G

Paper - Dimensional Scaling for Optimized CMUT Operations

In Conference proceedings of the International Ultrasonics Symposium, Chicago, September 2014.
Co-author.

Dimensional Scaling for Optimized CMUT Operations

Anders Lei*, Søren Elmin Diederichsen*, Mette Funding la Cour*†, Matthias Bo Stuart†
Thomas Lehrmann Christiansen*, Jørgen Arendt Jensen† and Erik Vilain Thomsen*
*Department of Micro and Nanotechnology, Technical University of Denmark, DK-2800 Kgs. Lyngby, Denmark
†Center for Fast Ultrasound Imaging, Department of Electrical Engineering, Technical University of Denmark,
DK-2800 Kgs. Lyngby, Denmark

***Abstract*—This work presents a dimensional scaling study using numerical simulations, where gap height and plate thickness of a CMUT cell is varied, while the lateral plate dimension is adjusted to maintain a constant transmit immersion center frequency of 5 MHz. Two cell configurations have been simulated, one with a single square cell and one with an infinite array of square cells. It is shown how the radiation impedance from neighboring cells has a significant impact on the design process. For transmit optimization, both plate dimensions and gap height should be increased. For receive mode, the gap height should be increased while the effect of plate dimensions is ambiguous depending on if the array design is closest to a single cell or infinite array of cells. The findings of the simulations are verified by acoustical measurements on two CMUT arrays with different plate dimensions.**

I. INTRODUCTION

The potential benefits of utilizing capacitive micromachined ultrasonic transducer (CMUT) arrays in ultrasonic transducers are well discussed in the literature: large bandwidth, ease of fabrication, compatibility with CMOS, design flexibility, etc. All of these properties are nevertheless of secondary concern for imaging purposes, if the CMUT array is not capable of providing the necessary transmit pressure and receive sensitivity. It is therefore essential to understand how the transmit and receive sensitivity scales with the dimensions of the CMUT cell.

In the most basic configuration, there are three adjustable dimensional parameters for a CMUT cell: gap height, plate thickness and side length for a square cell. The two latter parameters determine the mechanical properties of the CMUT and are linked if a fixed resonant frequency of the CMUT cell is desired. The gap height determines the electrical properties of the CMUT, i.e. the capacitance and pull-in voltage; and thereby the required DC biasing and AC excitation voltage. The CMUT will typically be biased and operated at fixed fractions of the pull-in voltage. The result is that for a fixed immersion frequency, only two dimensional parameters can be adjusted independently: gap height and either plate thickness or side length. The aim of this work is to investigate the scaling properties between these parameters.

Numerous lumped element models of CMUTs are presented in the literature with varying degrees of complexity [1], [2]. The conventional advantage of the lumped model is that closed-form expressions can potentially be attained. This provides easy insight in how the performance scales with parameters and direct evaluation of a specific design. To achieve closed-form expressions, several assumptions are required [3]. The radiation impedance, and thus the overall damping of the system, is often assumed to equal the plane-wave radiation impedance. This assumption is valid for situations where the transducer is large relative to the wavelength. The element width of the CMUT array is typically on the order of maximum one wavelength (λ-pitch), and consists of several individual CMUT cells across; the plane wave assumption is hence not suitable for most CMUT designs.

Another way of analyzing the performance of a CMUT is to use numerical simulations such as finite element analysis (FEA) [4], [5]. FEA allows accurate simulation of the CMUT and in particular the medium loading and mutual radiation impedance for multiple cells. The disadvantage of FEA is that the computation time reaches a critical level, if more than just a few CMUT cells are to be analyzed.

This work will utilize two different FEA models to investigate the dimensional scaling: a single CMUT cell with no neighbors, and a CMUT cell in an infinite array of cells with a fixed spacing. Any actual CMUT array design will have characteristics that are in-between these two cell configurations. Since the transducer center frequency is determined by the medical imaging purpose, it is a fundamental requirement for the dimensional scaling analysis that the center frequency of the CMUT in immersion is constant. In this study, the center frequency in transmit is set to 5 MHz. The simulated results will be compared to experimental results from two fabricated CMUT arrays with different designs.

II. FINITE ELEMENT ANALYSIS

The FEA simulations are performed using the software COMSOL Multiphysics V4.4 (COMSOL AB, Sweden). The FEA model is a full electro-mechanical-acoustical setup with the physics/interfaces *Electromechanics (emi)* and *Pressure Acoustics, Frequency Domain (acpr)*. The first interface models the electro-mechanical interaction and deformation of the CMUT cell. The latter interface models the propagation of acoustic waves in the medium. COMSOL's own internal variables are used for coupling between the two interfaces.

The CMUT cell consists of a 2 µm thick mechanical silicon support representing the fixed bottom plate of the CMUT structure. The suspended top silicon plate of the CMUT with thickness t is separated from the bottom plate by a distance g. The top and bottom plate with a vacuum gap in-between has a side length of a. Both top and bottom plate extend further

2.5 μm outside the vacuum gap representing half the spacing (2.5 μm) to the neighboring cell. The material between the top and bottom plates in this cell spacing is silicon dioxide. To emulate realistic anchoring conditions, the model is only mechanically fixed at the lower boundary of the bottom plate and at the vertical boundary half distance to the neighboring cell.

The square geometry requires a 3D model, but only ¼ of the cell is simulated with symmetry boundaries to minimize the computation. The difference between the two configurations with either a single cell (SC), or an infinite array of cells (IAC) is the medium. A hemisphere medium with a perfectly matched layer (PML) as outer rim is used for SC. The PML layer absorbs all incoming pressure waves, so that no radiated waves are reflected. For IAC, a tube medium is used with the same footprint as the CMUT cell including the cell spacing. The walls of the tube have hard boundary conditions giving full reflections corresponding to the incoming pressure waves from neighboring cells. At the top of the tube, a PML block prevents reflections of waves, which corresponds to an infinite medium.

The essential condition of a constant 5 MHz immersion transmit center frequency required a feedback loop between dimensional parameters and the simulated transmit spectrum. This feedback was achieved by controlling COMSOL through MATLAB (MathWorks, Inc., Natick, MA, USA). A simulation sequence was thus conducted by setting a gap height, plate thickness and side length. The pull-in voltage was determined for this design and fixed fractions of the pull-in voltage were used for the DC and AC voltages, 80% and 50%, respectively. The transmit spectrum was simulated and the center frequency extracted. The feedback loop then changed the plate side length and the simulation sequence was repeated until a transmit center frequency of 5 MHz in immersion was achieved.

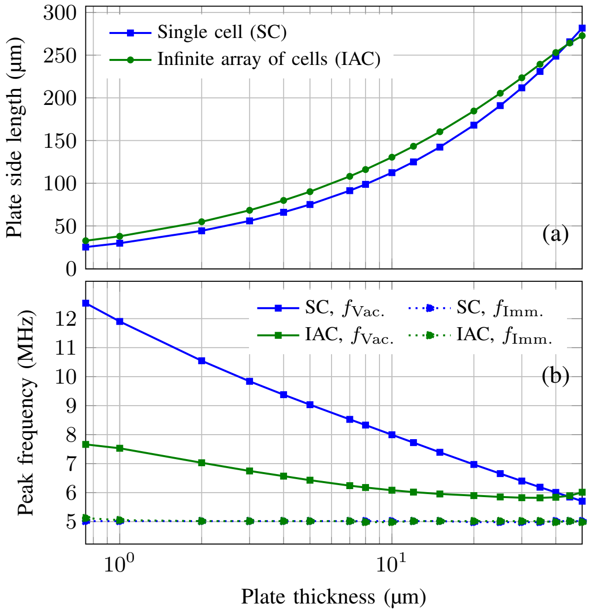

Fig. 1. (a) Plate side length and (b) Vacuum ($f_{\mathrm{Vac.}}$) and immersion ($f_{\mathrm{Imm.}}$) peak frequencies for single and infinite array of cells as function of plate thickness. The feedback loop in the FEA adjust the plate side length to ensure a constant immersion frequency of 5 MHz.

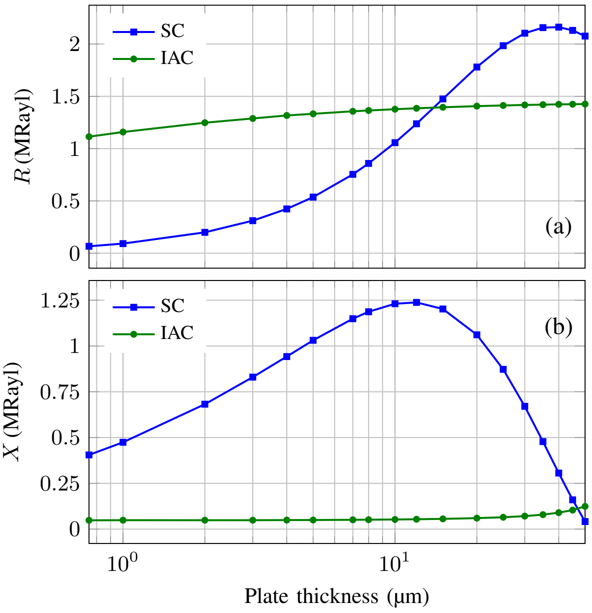

Fig. 2. (a) Real/resistive and (b) imaginary/reactive part of the simulated radiation impedance as function of plate thickness at 5 MHz.

A. *FEA Results*

The feedback effect of the FEA simulations is seen in Fig. 1(a) where the plate side length is plotted as function of the logarithmic plate thickness. One plate thickness thus results in different plate side lengths depending on SC or IAC configuration. This difference is further emphasized in Fig. 1(b), where the simulated peak frequencies for both vacuum and immersion are plotted. While the feedback loop ensures the required immersion frequency of 5 MHz, the frequency shift from vacuum to immersion differs significantly between the two configurations. The frequency shift between vacuum and immersion is due to the interaction with the medium, and it is thus clear that the impact of the medium is depending on neighboring cells.

The difference in interaction with the medium for the two cell configurations is analyzed in Fig. 2, where the real/resistive (R) and imaginary/reactive (X) parts of the simulated radiation impedance ($Z_{\mathrm{a}} = R + iX$) at 5 MHz are plotted as function of plate thickness. For thick plates with side lengths comparable to or larger than the wavelength ($\lambda \approx 480$ μm), the radiation impedance is expected to approach the plane wave impedance. For a plane wave, the impedance is purely real and equals the characteristic impedance (Z_0) of the medium. Water is used as medium in the simulation with $Z_0 \approx 1.5$ MRayl. With a resistive part close to Z_0 and a small reactive part relative to SC, the impedance for IAC is close to that of a plane wave. The smaller reactive part for IAC compared to SC is what mainly causes the difference in frequency shift from vacuum to immersion between the two configurations in Fig. 1(b). Where the reactive part gives a frequency shift, the resistive part of Z_{a} mainly affects the overall damping of the CMUT.

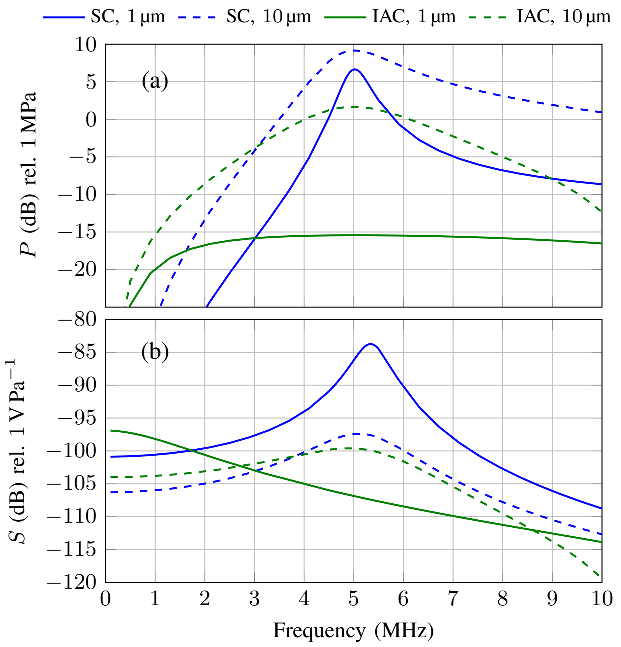

Fig. 3. (a) Transmit and (b) receive sensitivity spectrum for both single and infinite array of cells with 200 nm gap height and plate thicknesses of 1 µm and 10 µm.

This is illustrated in Fig. 3(a) where the simulated average cell surface pressure is plotted as function of frequency for two different plate thicknesses with a gap height of 200 nm. The two solid lines are for a plate thickness of 1 µm. The considerably higher resistive impedance for IAC compared to SC seen in Fig. 2(a), causes a damping effect with lower peak pressure amplitude as consequence. The high medium loading relative to the mechanical impedance for IAC with thin plates causes the CMUT to become over-damped. The transmitted pressure approaches zero for low frequencies since there can exist no static pressure in the medium. The plate deflection however increases for decreasing frequency according to an over-damped oscillator. For a 10 µm thick plate (dashed lines) the mechanical impedance is increased and the difference in resistive impedance between IAC and SC is less (see Fig. 2(a)). The result is that IAC becomes under-damped with a resonance peak, and the difference in pressure amplitude relative to SC is lower.

The receive sensitivity in voltage readout ($\mathrm{d}V/\mathrm{d}P$) for the same CMUT designs as in Fig. 3(a) is seen in Fig. 3(b). The small upwards shift ($\approx$ 0.3 MHz) in center frequency for SC with $t = 1\,\mu\mathrm{m}$ compared to transmit is due to a change in mechanical impedance caused by the difference in force distribution from the electrostatic force in transmit to a uniform incoming pressure distribution in receive. The over-damping for the IAC with thin plate is more clearly seen in the receive sensitivity since it follows the deflection characteristics of an over-damped system. For thicker plates, the IAC becomes under-damped and exhibits a resonance peak around the transmit center frequency.

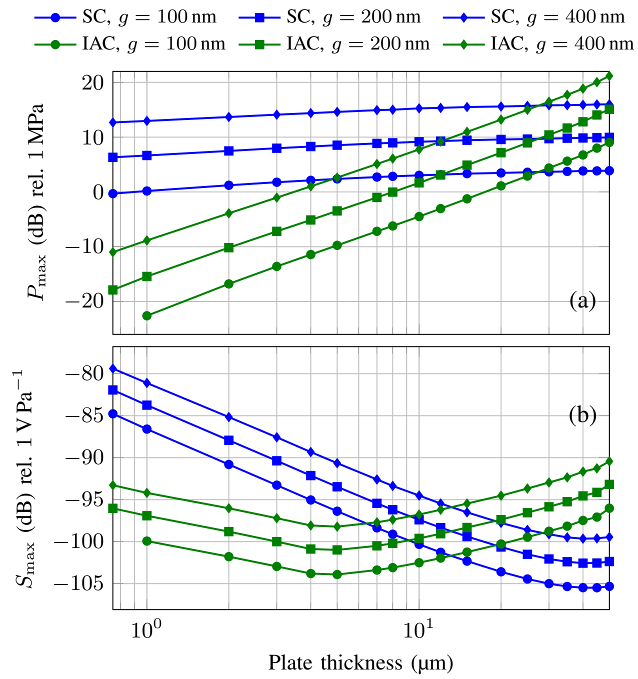

Fig. 4. (a) Peak transmit pressure and (b) peak receive sensitivity for SC and IAC with three different gap heights as function of plate thickness.

The full dimensional FEA scaling study is seen in Fig. 4, where the extracted peak surface pressure and peak receive sensitivity, are plotted as function of plate thickness for three different gap heights. The pressure scaling in Fig. 4(a) shows similar tendency for both SC and IAC with increasing pressure for thicker plates and larger gap height. This scaling follows intuition as thicker plates with larger area equals higher mass and more inertia. Increasing the gap height means one can apply a higher voltage and thereby increase the potential energy of the system.

The dimensional scaling of the receive sensitivity is seen in Fig. 4(b). The sensitivity for both SC and IAC is as expected improved for increasing gap height due to higher applicable voltages and hence charge on the plates. For SC, the sensitivity is increasing for decreasing plate thickness. This is expected, since a lower thickness means less mass and therefore lower mechanical impedance. The decreasing sensitivity tendency levels off for thick plates due the maximum in resistive impedance for SC seen in Fig. 2(a). For IAC, the sensitivity is also decreasing with thickness until $\approx 5\,\mu\mathrm{m}$ where it begins to increase. The turning point corresponds to the thickness

TABLE I. SUMMARIZED SCALING TRENDS FROM FIG. 4.

	Single cell		Infinite array of cells	
	TX	RX	TX	RX
Scaling plate thickness (dB) 1 µm → 2 µm	0.8	-4.2	5.3	-1.9
Scaling gap height (dB) 200 nm → 400 nm	6.2	2.8	6.3	3.8

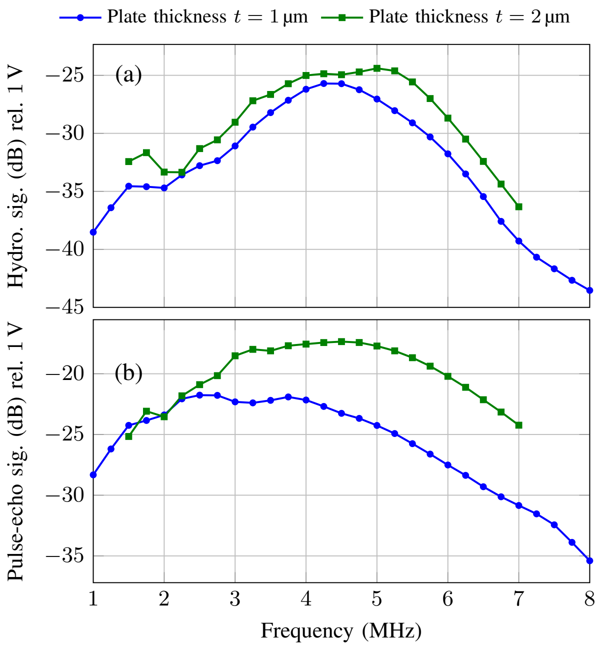

Fig. 5. (a) Hydrophone and (b) pulse-echo measurements for two CMUT arrays with different plate thicknesses.

where the mechanical impedance reaches the critical value that changes the CMUT from under-damped to over-damped. The thickness where the SC and IAC receive scaling lines with same gap height intersect, corresponds to the thickness where the resistive impedance of SC and IAC intersects in Fig. 2(a). A summary of the scaling trends is listed in Table I.

III. EXPERIMENTAL RESULTS

Two different square cell CMUT arrays with plate thicknesses of $1\,\mu\text{m}$ and $2\,\mu\text{m}$ and plate side lengths of $35\,\mu\text{m}$ and $49\,\mu\text{m}$, respectively, were fabricated using the process described in [6]. Both arrays have the same element area. The acoustic measurements were carried out using the experimental Synthetic Aperture Real-time Ultrasound System (SARUS) [7] and performed in vegetable oil for electrical insulation of the uncoated device. Hydrophone and pulse-echo measurements were performed at a $10\,\text{mm}$ distance from the transducer surface. The hydrophone used was an Optel 5 MHz hydrophone (Optel, Wroclaw, Poland) and the plane reflector a $40\,\text{mm}$ thick Polyvinylchlorid plate. A narrowband, 8 periods excitation was used with a frequency step of $250\,\text{kHz}$ with the RMS signal taken as the average of 16 center array elements.

TABLE II. SUMMARIZED RESULTS FROM HYDROPHONE AND PULSE-ECHO SPECTRUM IN FIG. 5.

	$t = 1\,\mu\text{m}$		$t = 2\,\mu\text{m}$	
	TX	TX→RX	TX	TX→RX
Peak values (dB)	-25.7	-21.8	-24.4	-17.4
Center frequency (MHz)	4.43	3.57	4.51	4.41
Fractional bandwidth (%)	70	140	77	108

The measured spectra for the two arrays are seen in Fig. 5 with summarized results in Table II. The difference in peak hydrophone signal amplitude of $1.3\,\text{dB}$ between the two arrays is within the expected range of $0.8\,\text{dB}$ to $5.3\,\text{dB}$ in Table I for SC and IAC, respectively. The pulse-echo center frequency decreases $\approx 0.9\,\text{MHz}$ for the $1\,\mu\text{m}$ thick plate. This follows the FEA simulations in Fig. 3(b) and Fig. 4(b) where plates with thicknesses less than $\approx 5\,\mu\text{m}$ becomes increasingly over-damped due to a lower mechanical impedance. The peak pulse-echo signal amplitude is more than $4\,\text{dB}$ higher for the thicker plate due to an increase in the total product of both the transmit and receive sensitivity spectrum. This result is in agreement with the FEA scaling trends in Table I.

IV. CONCLUSION

A dimensional scaling study using numerical simulations of square CMUT cells with a constant transmit immersion frequency of $5\,\text{MHz}$ has been presented. Two cell configurations have been studied: a single cell and an infinite array of cells. Any real CMUT array design will behave within these two extremes. It is demonstrated how the mutual radiation impedance from neighboring cells affects both the transmit and receive sensitivity spectrum. To optimize the transmit sensitivity, the plate size and gap height should be increased. For the receive sensitivity, the gap height should be increased while the scaling on plate size is dependent on the actual CMUT array design. The conclusions from the numerical simulations are validated by acoustical measurements on two fabricated CMUT arrays with plate thicknesses of $1\,\mu\text{m}$ and $2\,\mu\text{m}$, respectively.

ACKNOWLEDGMENT

This work was financially supported by the Danish National Advanced Technology Foundation (82-2012-4).

REFERENCES

[1] I. Wygant, M. Kupnik, and B. Khuri-Yakub, “Analytically calculating membrane displacement and the equivalent circuit model of a circular CMUT cell,” in *IEEE Ultrasonics Symposium, 2008. IUS 2008*, Nov. 2008, pp. 2111–2114.

[2] H. Koymen, A. Atalar, E. Aydogdu, C. Kocabas, H. Oguz, S. Olcum, A. Ozgurluk, and A. Unlugedik, “An improved lumped element nonlinear circuit model for a circular CMUT cell,” *IEEE Transactions on Ultrasonics, Ferroelectrics, and Frequency Control*, vol. 59, no. 8, pp. 1791–1799, Aug. 2012.

[3] I. Wygant, M. Kupnik, and B. Khuri-Yakub, “CMUT design equations for optimizing noise figure and source pressure,” in *IEEE Ultrasonics Symposium, 2009. IUS 2009*, 2009.

[4] K. K. Park and B. T. Khuri-Yakub, “Dynamic response of an array of flexural plates in acoustic medium,” *The Journal of the Acoustical Society of America*, vol. 132, no. 4, pp. 2292–2303, Oct. 2012.

[5] H. Oguz, A. Atalar, and H. Koymen, “Equivalent circuit-based analysis of CMUT cell dynamics in arrays,” *IEEE Transactions on Ultrasonics, Ferroelectrics, and Frequency Control*, vol. 60, no. 5, pp. 1016–1024, May 2013.

[6] M. F. la Cour, M. B. Stuart, M. B. Laursen, S. E. Diederichsen, E. V. Thomsen, and J. A. Jensen, “Investigation of PDMS as coating on CMUTs for imaging,” in *IEEE Ultrasonics Symposium, 2014. IUS 2014*, 2014.

[7] J. A. Jensen, H. Holten-Lund, R. Nilsson, M. Hansen, U. Larsen, R. Domsten, B. Tomov, M. Stuart, S. Nikolov, M. Pihl, Y. Du, J. Rasmussen, and M. Rasmussen, “SARUS: A synthetic aperture real-time ultrasound system,” *IEEE Transactions on Ultrasonics, Ferroelectrics, and Frequency Control*, vol. 60, no. 9, pp. 1838–1852, Sep. 2013.